

THE EFFECT OF AMMONIUM NITRATE AND ETHYLENE GLYCOL IN
CARBOXYMETHYL CELLULOSE SOLID POLYMER ELECTROLYTES
FOR RECHARGEABLE PROTON BATTERY

KHADIJAH HILMUN KAMARUDIN

Thesis submitted in fulfillment of the requirement for the degree of
Doctor of Philosophy in Physics in the School of Fundamental Science
Universiti Malaysia Terengganu

February 2016

ABSTRACT

Abstract of thesis presented to the Senate of Universiti Malaysia Terengganu in fulfilment of the requirement for the degree of Doctor of Philosophy

THE EFFECT OF AMMONIUM NITRATE AND ETHYLENE GLYCOL IN CARBOXYMETHYL CELLULOSE SOLID POLYMER ELECTROLYTES FOR RECHARGEABLE PROTON BATTERY

KHADIJAH HILMUN KAMARUDIN

February 2016

Main Supervisor : Associate Professor Mohd Ikmar Nizam Mohamad Isa, Ph.D.

School : School of Fundamental Science

Solid polymer electrolytes (SPEs) have been recognised as promising electrolytes to overcome the limitation in gel/liquid counterparts. In this research, the potential of carboxymethyl cellulose (CMC)-based SPEs was studied. Two systems, namely System I which comprised of CMC doped ammonium nitrate (NH_4NO_3) salt and System II which comprised of CMC- NH_4NO_3 plasticized ethylene glycol (EG) are prepared via solution casting technique. The interactions between polymer, salt and plasticizer in both systems are observed by FTIR analysis. The amorphousness and thermal behaviour of both systems are obtained by XRD and TGA-DTG analyses, respectively. The incorporation of 45 wt.% NH_4NO_3 salt in System I has optimized the ambient temperature ionic conductivity to $(7.71 \pm 0.04) \times 10^{-3} \text{ Scm}^{-1}$. Ionic conductivity is enhanced to $(3.80 \pm 0.06) \times 10^{-2} \text{ Scm}^{-1}$ on the addition of 20 wt.% EG plasticizer in System II. The temperature-dependent ionic conductivity for both electrolyte systems is Arrhenian and thermally activated. The activation energy did

not show the significant effect to the enhancement of ionic conductivity in both systems. However, the activation energy in System I is higher than in System II. Ionic conductivity is observed to be influenced by the number density (n), mobility (μ) and diffusion coefficient (D) of mobile charge carriers in System I. Whereas, ionic conductivity in System II is affected only by n and inversely proportional to μ and D . These transport parameters are affected by the fraction of ionic species in both systems. The majority of mobile charge carriers is recognized to be ions as evidenced by transference number measurement via DC polarization technique. This analysis also supported that the mobile charge carriers in both systems are H^+ cations or protons. Conduction mechanism in both systems is described by the relation of Jonscher's universal power law and hopping mechanism models. Quantum mechanical tunneling model was identified to represent the ionic conduction mechanism in both systems. Electrical studies show that the SPEs are ionic conductors. The electrical behaviour of SPEs is attributed to the conductivity relaxation process. The highest conducting SPEs in both systems were applied in the fabrication of rechargeable proton batteries. Based on the batteries performance, it can be concluded that the rechargeable proton batteries in the present work are suitable to be applied in low current based electrochemical device applications.

ABSTRAK

Abstrak tesis yang dikemukakan kepada Senat Universiti Malaysia Terengganu sebagai memenuhi keperluan untuk ijazah Doktor Falsafah

KESAN AMONIUM NITRAT DAN ETILENA GLIKOL DALAM ELEKTROLIT PEPEJAL POLIMER KARBOKSILMETIL SELULOSA UNTUK BATERI PROTON CAS SEMULA

KHADIJAH HILMUN KAMARUDIN

Februari 2016

Penyelia Utama : Profesor Madya Mohd Ikmar Nizam Mohamad Isa, Ph.D.

Pusat Pengajian : Pusat Pengajian Sains Asas

Elektrolit pepejal polimer (SPEs) telah dikenalpasti sebagai elektrolit yang berupaya untuk mengatasi kekurangan yang dialami oleh elektrolit gel/cecair. Dalam kajian ini, potensi karboksilmetil selulosa (CMC) berasaskan SPEs telah dikaji. Dua sistem iaitu Sistem I terdiri daripada CMC berdop garam ammonium nitrat (NH_4NO_3) dan Sistem II terdiri daripada CMC- NH_4NO_3 berpemplastik etilena glikol (EG) telah disediakan melalui teknik penuangan larutan. Interaksi-interaksi diantara polimer, garam dan pemplastik dalam kedua-dua sistem telah dicerap melalui analisis IR. Keamorfusan dan perlakuan haba kedua-dua sistem diperolehi daripada analisis XRD dan TGA-DTG. Dengan penambahan 45 wt.% garam NH_4NO_3 dalam Sistem I telah mengoptimumkan kekonduksian ion suhu ambien/sekeliling pada $(7.71 \pm 0.04) \times 10^{-3} \text{ Scm}^{-1}$. Kekonduksian ion dipertingkatkan kepada $(3.80 \pm 0.06) \times 10^{-2} \text{ Scm}^{-1}$ dengan penambahan 20 wt.% pemplastik EG dalam Sistem II. Analisis kebergantungan kekonduksian ion terhadap suhu menunjukkan kedua-dua sistem

elektrolit adalah Arrhenian dan diaktifkan secara terma. Tenaga pengaktifan tidak menunjukkan kesan yang ketara terhadap penambahan kekonduksian ion dalam kedua-dua sistem. Walau bagaimanapun, tenaga pengaktifan bagi Sistem I didapati lebih tinggi berbanding Sistem II. Kekonduksian ion dipengaruhi oleh kepadatan nombor (n), mobiliti (μ) dan pekali peresapan (D) pembawa cas bergerak dalam Sistem I. Manakala, kekonduksian ion dalam Sistem II hanya dipengaruhi oleh n dan berkadar songsang dengan μ dan D . Parameter-parameter angkutan ini dipengaruhi oleh pecahan spesies-spesies ion. Majoriti pembawa cas bergerak dikenalpasti sebagai ion seperti yang telah dibuktikan oleh pengukuran jumlah pemindahan melalui teknik pengkutuban DC. Analisis ini juga menyokong bahawa pembawa cas bergerak dalam kedua-dua sistem adalah H^+ kation atau proton. Mekanisma kekonduksian untuk kedua-dua sistem diterangkan berdasarkan hukum kuasa sejagat Jonscher dan model-model mekanisme lompatan. Model penerowongan mekanik kuantum telah dikenalpasti untuk mewakili mekanisme kekonduksian ion dalam kedua-dua sistem. Kajian elektrik menunjukkan bahawa SPEs adalah pengalir/konduktor ion. Perlakuan elektrik SPEs adalah disebabkan oleh proses kekonduksian relaksasi/kekenduran. SPEs dengan kekonduksian tertinggi dalam kedua-dua sistem telah digunakan dalam fabrikasi bateri proton cas semula. Berdasarkan prestasi daripada bateri-bateri tersebut, ia boleh disimpulkan bahawa bateri proton cas semula dalam kajian ini sesuai untuk diaplikasikan dalam penggunaan peranti elektrokimia berarus rendah.

ACKNOWLEDGEMENTS

Alhamdulillah. In the name of Allah, the Most Beneficent, the Most Merciful, Praise be to Allah for His blessing in my life.

I would like to take this opportunity to express my gratitude to all those that contributed to my PhD journey. Foremost, I would like to sincerely thank to my supervisor, Assoc. Prof. Dr. Mohd Ikmar Nizam Haji Mohamad Isa for his endless encouragement, wisdom, assistance, support and most importantly his patience throughout this journey.

My profound appreciation goes to Prof. Emeritus Dato' Dr. Noor Azhar Mohamed Shazili, Director of Institute of Oceanography and Environment (the former Deputy Vice Chancellor (Academic and International Affairs)), Universiti Malaysia Terengganu and Prof. Dr. Tengku Sifzizul Tengku Muhammad, Director of Institute of Marine Biotechnology (the former Dean of Faculty of Science and Technology), Universiti Malaysia Terengganu for giving me the golden opportunity to pursue my PhD studies in UMT. Thank you for the trust!

I would like to extend my sincere appreciation to Assoc. Prof. Dr. Wan Mohd Khairul Wan Mohamed Zin, Deputy Dean (Talent and Research), School of Fundamental Science (PPSA) and Ms. Nooraisah Moidu, Assistant Registrar, Centre of Academic Talent and Innovation, UMT for their endless courage and help throughout this journey. I would also like to thank the panel of thesis examiners, Prof. Dr. Wan Mohd Norsani Wan Nik and Assoc. Prof. Dr. Ab Malik Marwan Ali for the insightful comments and reviews of my thesis.

I would like to thank all the fellow Advanced Materials Team members, especially Dr. Ahmad Salihin Samsudin and Ms. Chai Mui Nyuk for experimental assistance and insightful discussions. My thank also goes to Mr. Maswadi Mustafa and Mr. Mohd. Jamaluddin Jusoh from Inorganic Chemistry Laboratory, PPSA for their invaluable effort and help in TGA-DSC experiments. Also not to forget PPSA and PPKK colleagues as well as PPKK lab staffs for their fruitful discussions and kind assistances, which I greatly appreciate.

My deepest thanks to my family, my wonderful parents and siblings, who have been unstinting sources of understanding, prayer, patience and unconditional support, for who always be there for me, I would not have come this far without my family's support. It is to them that I dedicate this thesis.

Last but not least, I would like to acknowledge GRA skim under FRGS Vot. 59319 from Malaysia Minister of Education (MOE) for funding and financial support.

Khadijah Hilmun Kamarudin

18 Rabiul Awal 1437H

29th December 2015

APPROVAL

I certify that an Examination has met on 21st February 2016 to conduct the final examination of Khadijah Hilmun Kamarudin, on her Doctor of Philosophy thesis entitled "The Effect of Ammonium Nitrate and Ethylene Glycol in Carboxymethyl Cellulose Solid Polymer Electrolytes for Rechargeable Proton Battery" in accordance with the regulations approved by the Senate of Universiti Malaysia Terengganu. The Committee recommends that the candidate be awarded the relevant degree. The members of the Examination Committee are as follows:

Wan Mohd Khairul Bin Wan Mohamed Zin, Ph.D.
Associate Professor
School of Fundamental Science
Universiti Malaysia Terengganu
(Chairperson)

Wan Mohd Norsani Bin Wan Nik, Ph.D.
Professor
School of Ocean Engineering
Universiti Malaysia Terengganu
(Internal Examiner)

Ab Malik Marwan Bin Ali, Ph.D.
Associate Professor
Faculty of Applied Sciences
Universiti Teknologi MARA
(External Examiner)

HAMDAN BIN SUHAIMI
Ph.D.
Professor/Dean
School of Fundamental Science
Universiti Malaysia Terengganu

Date:

APPROVAL

This thesis has been accepted by the Senate of Universiti Malaysia Terengganu as fulfilment of the requirements for the degree of Doctor of Philosophy.

HAMDAN BIN SUHAIMI
Ph.D.
Professor/Dean
School of Fundamental Science
Universiti Malaysia Terengganu

Date:

DECLARATION

I hereby declare that the thesis is based on my original work except for quotations and citations which have been duly acknowledged. I also declare that it has not been previously or concurrently submitted for any other degree at Universiti Malaysia Terengganu or other institutions.

khilmun .

KHADIJAH HILMUN KAMARUDIN

Date: 29th December 2015

TABLE OF CONTENTS

| | Page |
|---|-------------|
| Abstract | ii |
| Abstrak | iv |
| Acknowledgements | vi |
| Approval | viii |
| Declaration | x |
| Table of Contents | xi |
| List of Figures | xiii |
| List of Tables | xxi |
| Abbreviations | xxii |
| Symbols | xxiii |
| List of Publications | xxv |
| | |
| Chapter 1 Introduction | |
| 1.1 Research background | 1 |
| 1.2 Problem statement | 4 |
| 1.3 Research objectives | 6 |
| 1.4 Scope of the research | 6 |
| 1.5 Research significance | 7 |
| 1.6 Thesis outline | 8 |
| | |
| Chapter 2 Literature Review | |
| 2.1 Biodegradable polymers | 11 |
| 2.2 Solid polymer electrolytes | 15 |
| 2.2.1 Types of solid polymer electrolytes | 16 |
| 2.2.2 Basic properties of solid polymer electrolytes | 17 |
| 2.2.3 Ion-conduction mechanism | 19 |
| 2.3 Solid-state electrochemical cell | 34 |
| 2.3.1 Fundamental theories of battery | 34 |
| 2.3.2 Battery characteristics | 36 |
| | |
| Chapter 3 Methodology | |
| 3.1 Method of research | 38 |
| 3.2 Phase I: Preparation of solid polymer electrolytes | 39 |
| 3.3 Phase II: Characterization of solid polymer electrolytes | 42 |
| 3.3.1 Fourier transform infrared spectroscopy | 42 |
| 3.3.2 X-ray diffraction | 43 |
| 3.3.3 Thermogravimetric analyzer | 44 |
| 3.3.4 Electrical impedance spectroscopy | 44 |
| 3.3.5 Transference number measurement | 46 |
| 3.3.6 Potentiostat-galvanostat | 47 |

| | Page | |
|------------------|--|-----|
| 3.4 | Phase III: Fabrication of battery | 48 |
| 3.4.1 | Preparation of electrodes | 49 |
| 3.4.2 | Battery assembly | 50 |
| 3.5 | Phase IV: Characterization of battery | 51 |
| Chapter 4 | Vibrational, Structural and Thermal Properties of Solid Polymer Electrolytes | |
| 4.1 | Physical appearance of solid polymer electrolytes | 53 |
| 4.2 | FTIR analysis | 54 |
| 4.2.1 | Molecular interaction of CMC and NH ₄ NO ₃ salt | 54 |
| 4.2.2 | Molecular interaction of CMC-NH ₄ NO ₃ and EG plasticizer | 61 |
| 4.2.3 | Proton transfer mechanism | 67 |
| 4.3 | XRD analysis | 70 |
| 4.4 | Thermal behaviour | 73 |
| Chapter 5 | Ionic Conductivity, Transport and Electrical Properties of Solid Polymer Electrolytes | |
| 5.1 | Ionic conductivity studies | 81 |
| 5.1.1 | Nyquist plots | 81 |
| 5.1.2 | Ionic conductivity | 88 |
| 5.2 | Transport studies | 95 |
| 5.2.1 | Ionic species analysis | 95 |
| 5.2.2 | Transport parameters | 103 |
| 5.2.3 | Transference number | 106 |
| 5.3 | Electrical studies | 110 |
| 5.3.1 | Dielectric and modulus | 110 |
| 5.3.2 | Hopping mechanism | 119 |
| Chapter 6 | Electrochemical Cell Performance | |
| 6.1 | Linear sweep voltammetry | 123 |
| 6.2 | Solid-state rechargeable proton batteries | 125 |
| 6.2.1 | Open-circuit voltage | 125 |
| 6.2.2 | Charge-discharge characteristics | 127 |
| Chapter 7 | Conclusion and Future Work | |
| 7.1 | Conclusion | 137 |
| 7.2 | Recommendations for future work | 139 |
| | References | 142 |
| | Appendices | 156 |
| | Biodata of the Author | 169 |

LIST OF FIGURES

| | | Page |
|------------|---|-------------|
| Figure 1.1 | The schematic cross-sectional view of a liquid battery and a solid-state battery. | 2 |
| Figure 1.2 | Statistics of publications on SPEs recorded between 1980 and August 2015. Data derived from (a) SciFinder scholar and (b) ScienceDirect online databases (Accessed on August 10, 2015). | 3 |
| Figure 2.1 | The physical appearance of pure CMC, (a) powder, (b) liquid, and (c) solid film. | 14 |
| Figure 2.2 | The chemical structure of pure CMC. | 15 |
| Figure 2.3 | The chemical structure of NH_4NO_3 salt. | 23 |
| Figure 2.4 | The chemical structure of EG plasticizer. | 25 |
| Figure 2.5 | A diagram of the secondary solid-state electrochemical cell. | 35 |
| Figure 3.1 | Flow chart of research methodology. | 39 |
| Figure 3.2 | (a) The FTIR spectrometer used in this study and (b) the enlargement of SPE film position during measurement. | 43 |
| Figure 3.3 | The MiniFlex II Rigaku X-ray diffraction spectrometer used in this study. | 43 |
| Figure 3.4 | The thermogravimetric analyzer used in this study. | 44 |
| Figure 3.5 | The EIS (HIOKI 3532–50 LCR Hi Tester) equipped with a MEMMERT oven and interfaced to a personal computer. | 45 |
| Figure 3.6 | (a) The experimental arrangement of TNM apparatus, (b) the illustration of a SPE film sandwiched between two blocking electrodes inside the blue pail, and (c) the block diagram of the experimental arrangement in Figure 3.7(a). | 47 |
| Figure 3.7 | The potentiostat-galvanostat Autolab PGSTAT302. | 48 |
| Figure 3.8 | The preparation of electrodes. (a) A stand mixer was used to mix electrode slurry, (b) electrode slurry was cast on a flat glass using a Biuge film applicator, (c) dried electrodes were soaked and rinsed in methanol to remove DBP, and dried electrodes were then hot pressed on treated Al mesh for cathode (d) and Cu grid for anode (e). | 50 |

| | | Page |
|-------------|--|-------------|
| Figure 3.9 | (a) The arrangement of components inside a coin cell-type rechargeable proton battery and (b) the actual size of that completely assembled battery. | 51 |
| Figure 3.10 | Experimental set up for OCV test. | 52 |
| Figure 3.11 | Experimental set up for charge/discharge characteristics using NEWARE high accuracy battery tester. | 52 |
| Figure 4.1 | A highly translucent and flexible SPE films obtained at room temperature. | 54 |
| Figure 4.2 | FTIR spectra of (a) pure CMC film and System I films incorporated with (b) 5 wt.% NH_4NO_3 , (c) 10 wt.% NH_4NO_3 , (d) 15 wt.% NH_4NO_3 , (e) 20 wt.% NH_4NO_3 , (f) 25 wt.% NH_4NO_3 , (g) 30 wt.% NH_4NO_3 , (h) 35 wt.% NH_4NO_3 , (i) 40 wt.% NH_4NO_3 , (j) 45 wt.% NH_4NO_3 , (k) 50 wt.% NH_4NO_3 , and (l) pure NH_4NO_3 salt. | 55 |
| Figure 4.3 | Gaussian fit for FTIR spectra between 1700 cm^{-1} and 1500 cm^{-1} for System I films incorporated with (a) (5 wt.% NH_4NO_3), (b) (10 wt.% NH_4NO_3), (c) (15 wt.% NH_4NO_3), (d) (20 wt.% NH_4NO_3), (e) (25 wt.% NH_4NO_3), (f) (30 wt.% NH_4NO_3), (g) (35 wt.% NH_4NO_3), (h) (40 wt.% NH_4NO_3), (i) (45 wt.% NH_4NO_3), and (j) (50 wt.% NH_4NO_3). Note: Green solid line - vibrational bands from CMC polymer, orange dash line - vibrational bands from NH_4NO_3 salt, red open circles - experimental data and black solid line - fitted sum data. | 57 |
| Figure 4.4 | Deconvoluted FTIR spectra between 1200 cm^{-1} and 900 cm^{-1} for System I films incorporated with (a) (5 wt.% NH_4NO_3), (b) (10 wt.% NH_4NO_3), (c) (15 wt.% NH_4NO_3), (d) (20 wt.% NH_4NO_3), (e) (25 wt.% NH_4NO_3), (f) (30 wt.% NH_4NO_3), (g) (35 wt.% NH_4NO_3), (h) (40 wt.% NH_4NO_3), (i) (45 wt.% NH_4NO_3), and (j) (50 wt.% NH_4NO_3). Note: Green solid line - vibrational bands from CMC polymer, orange dash line - vibrational bands from NH_4NO_3 salt, red open circles - experimental data and black solid line - fitted sum data. | 59 |
| Figure 4.5 | FTIR spectra within $870 - 800\text{ cm}^{-1}$ wavenumber for System I films incorporated with (a) (5 wt.% NH_4NO_3), (b) (10 wt.% NH_4NO_3), (c) (15 wt.% NH_4NO_3), (d) (20 wt.% NH_4NO_3), (e) (25 wt.% NH_4NO_3), (f) (30 wt.% NH_4NO_3), (g) (35 wt.% NH_4NO_3), (h) (40 wt.% NH_4NO_3), (i) (45 wt.% NH_4NO_3), and (j) (50 wt.% NH_4NO_3). | 61 |

| | | Page |
|-------------|--|-------------|
| Figure 4.6 | FTIR spectra of System II films incorporated with (a) 5 wt.% EG, (b) 10 wt.% EG, (c) 15 wt.% EG, (d) 20 wt.% EG, (e) 25 wt.% EG, (f) 30 wt.% EG and (g) 35 wt.% EG, and (h) pure EG plasticizer. | 62 |
| Figure 4.7 | Gaussian fit for FTIR spectra between 1700 cm^{-1} and 1500 cm^{-1} for System II films incorporated with (a) (5 wt.% EG), (b) (10 wt.% EG), (c) (20 wt.% EG), (d) (25 wt.% EG), (e) (30 wt.% EG), and (f) (35 wt.% EG). Note: Green solid line - vibrational bands from CMC polymer, orange dash line - vibrational bands from NH_4NO_3 salt, open circles - experimental data and black solid line - fitted sum data. | 64 |
| Figure 4.8 | Deconvoluted FTIR spectra between 1200 cm^{-1} and 950 cm^{-1} for System II films incorporated with (a) (5 wt.% EG), (b) (10 wt.% EG), (c) (20 wt.% EG), (d) (25 wt.% EG), (e) (30 wt.% EG), and (f) (35 wt.% EG). Note: Green solid line - vibrational bands from CMC polymer, red solid line - vibrational bands from EG plasticizer, orange dash line - vibrational bands from NH_4NO_3 salt, red open circles - experimental data and black solid line - fitted sum data. | 65 |
| Figure 4.9 | FTIR spectra of within 920 – 800 cm^{-1} wavenumber for System II films incorporated with (a) (5 wt.% EG), (b) (10 wt.% EG), (c) (20 wt.% EG), (d) (25 wt.% EG), (e) (30 wt.% EG), and (f) (35 wt.% EG). | 66 |
| Figure 4.10 | Possible interactions of CMC- NH_4NO_3 in System I. | 69 |
| Figure 4.11 | Possible interactions of CMC- NH_4NO_3 -EG in System II. | 69 |
| Figure 4.12 | XRD patterns of pure CMC and System I films incorporating 5 - 50 wt.% NH_4NO_3 | 70 |
| Figure 4.13 | XRD patterns of System II films incorporating 5 - 40 wt.% EG. | 71 |
| Figure 4.14 | (a-f) TGA and (g-l) DTG curves for System I films obtained at room temperature to 400°C. | 75 |
| Figure 4.15 | (a-d) TGA and (e-h) DTG curves for System II films obtained at room temperature to 400°C. | 78 |

| | | Page |
|------------|--|-------------|
| Figure 5.1 | Nyquist plots of the real impedance, Z_r versus imaginary impedance, $-Z_i$ of (a) pure CMC film, and System I films incorporated with (b) 5 wt.% NH_4NO_3 , (c) 10 wt.% NH_4NO_3 and 15 wt.% NH_4NO_3 , (d) 20 wt.% NH_4NO_3 and 25 wt.% NH_4NO_3 , (e) 30 wt.% NH_4NO_3 and 35 wt.% NH_4NO_3 , (f) 40 wt.% NH_4NO_3 and 45 wt.% NH_4NO_3 (Inset: Enlargement of (f) in high-frequency region), and (g) 50 wt.% NH_4NO_3 , measured at ambient temperature. | 82 |
| Figure 5.2 | The corresponding electrical equivalent circuit for Nyquist plots in Figure 5.1. | 84 |
| Figure 5.3 | Nyquist plots of the real impedance, Z_r versus imaginary impedance, $-Z_i$ of System II films incorporated with (a) 5 wt.% EG and 10 wt.% EG, (b) 15 wt.% EG and 20 wt.% EG, (c) 25 wt.% EG and 30 wt.% EG, and (d) 35 wt.% EG and 40 wt.% EG obtained at ambient temperature. | 85 |
| Figure 5.4 | Nyquist plots of temperature dependence for System I films at elevated temperatures of 303K - 353K. (a) 15 wt.% NH_4NO_3 , (b) 25 wt.% NH_4NO_3 , (c) 35 wt.% NH_4NO_3 , and (d) 45 wt.% NH_4NO_3 , with a magnified high-frequency region (inset) for (c) and (d). | 86 |
| Figure 5.5 | Nyquist plots of temperature dependence for System II films at elevated temperatures of 303K - 353K. (a) 10 wt.% EG, (b) 20 wt.% EG, (c) 30 wt.% EG, and (d) 40 wt.% EG, with a magnified high-frequency region (inset) for (d). | 87 |
| Figure 5.6 | The salt-dependent ionic conductivity of System I films measured at ambient temperature. | 89 |
| Figure 5.7 | The plasticizer-dependent ionic conductivity of System II films measured at ambient temperature. | 91 |
| Figure 5.8 | The temperature-dependent ionic conductivity of (a) pure CMC film, and System I films incorporated with (b) 5 wt.% NH_4NO_3 , (c) 10 wt.% NH_4NO_3 , (d) 15 wt.% NH_4NO_3 , (e) 20 wt.% NH_4NO_3 , (f) 25 wt.% NH_4NO_3 , (g) 30 wt.% NH_4NO_3 , (h) 35 wt.% NH_4NO_3 , (i) 40 wt.% NH_4NO_3 , (j) 45 wt.% NH_4NO_3 , and (k) 50 wt.% NH_4NO_3 . | 92 |
| Figure 5.9 | The temperature-dependent ionic conductivity of System II films incorporated with (a) 5 wt.% EG, (b) 10 wt.% EG, (c) 15 wt.% EG, (d) 20 wt.% EG, (e) 25 wt.% EG, (f) 30 wt.% EG, (g) 35 wt.% EG, and (h) 40 wt.% EG. | 92 |

| | | Page |
|-------------|---|-------------|
| Figure 5.10 | Deconvoluted FTIR spectra within 1500 – 1200 cm^{-1} wavenumber for System I films at varied NH_4NO_3 concentration. (a) 5 wt.% NH_4NO_3 , (b) 10 wt.% NH_4NO_3 , (c) 15 wt.% NH_4NO_3 , (d) 20 wt.% NH_4NO_3 , (e) 25 wt.% NH_4NO_3 , (f) 30 wt.% NH_4NO_3 , (g) 35 wt.% NH_4NO_3 , (h) 40 wt.% NH_4NO_3 , (i) 45 wt.% NH_4NO_3 , and (j) 50 wt.% NH_4NO_3 . Note: Green solid line (left) - (C-H) and (right) - (C-OH) characteristic bands of CMC. Blue dot line - free ions, dash line - ion pairs, and purple dash dot dot line - ion aggregates of NH_4NO_3 salt. Red open circles - experimental data and black solid line - fitted sum data. | 97 |
| Figure 5.11 | The percentage of ionic species of System I films at varied NH_4NO_3 salt concentration. | 99 |
| Figure 5.12 | Deconvoluted FTIR spectra within 1500 – 1200 cm^{-1} wavenumber for System II films at varied EG concentration. (a) 5 wt.% EG, (b) 10 wt.% EG, (c) 20 wt.% EG, (d) 25 wt.% EG, (e) 30 wt.% EG, and (f) 35 wt.% EG. Note: Green solid line (left) - (C-H) and (right) - (C-OH) characteristic bands of CMC. Blue dot line - free ions, dash line - ion pairs, and purple dash dot dot line - ion aggregates of NH_4NO_3 salt. Red open circles - experimental data and black solid line - fitted sum data. | 100 |
| Figure 5.13 | The percentage of ionic species of System II films at varied EG concentration. | 102 |
| Figure 5.14 | Transport parameters against NH_4NO_3 concentration of System I films. (a) Ionic conductivity, σ_{DC} , (b) number density of mobile ions, n , (c) mobility of ions, μ , and (d) diffusion coefficient, D . | 104 |
| Figure 5.15 | Transport parameters against EG concentration of System II films. (a) Ionic conductivity, σ_{DC} , (b) number of mobile ions, n , (c) mobility of ions, μ , and (d) diffusion coefficient, D . | 105 |
| Figure 5.16 | Normalized polarization current, I vs. time, t for the highest conducting SPE film incorporating (a) 45 wt.% NH_4NO_3 ($\Gamma_{ion} = 0.67$) and, (b) 20 wt.% EG ($\Gamma_{ion} = 0.84$) measured at room temperature. | 107 |
| Figure 5.17 | The relation of (a) mobility and, (b) diffusion coefficient of cations and anions against NH_4NO_3 concentration for System I films. | 109 |

| | | Page |
|-------------|---|-------------|
| Figure 5.18 | The relation of (a) mobility and, (b) diffusion coefficient of cations and anions against EG concentration for System II films. | 110 |
| Figure 5.19 | The dependence of ε_r and ε_i on frequency for (a-b) pure CMC, (c-d) System I, and (e-f) System II films at ambient temperature, 303K. | 112 |
| Figure 5.20 | The dependence of ε_r and ε_i on frequency for (a-b) pure CMC film, and the highest conducting SPE film in (c-d) System I, and (e-f) System II at selected temperatures, 303K - 353K. | 114 |
| Figure 5.21 | The dependence of M_r and M_i on frequency for (a-b) pure CMC, (c-d) System I, and (e-f) System II films at ambient temperature, 303K. | 116 |
| Figure 5.22 | The dependence of M_r and M_i on frequency for (a-b) pure CMC film, and the highest conducting SPE film in (c-d) System I, and (e-f) System II at selected temperatures, 303K - 353K. | 119 |
| Figure 5.23 | Plots of σ_{AC} , $\ln \sigma_{AC}$ and power law exponent s for (a-c) 45 wt.% NH_4NO_3 film in System I and (d-f) 20 wt.% EG film in System II obtained at elevated temperatures. | 121 |
| Figure 6.1 | LSV for (a) 45 wt.% NH_4NO_3 and (b) 20 wt.% EG films measured at room temperature. | 124 |
| Figure 6.2 | The OCV of Cell I and Cell II for 24 hours. | 126 |
| Figure 6.3 | Discharge curves of Cell I for (a) cycle 1, (b) cycle 2, and (c) cycle 4, cycle 6 and cycle 8, measured at 0.02 mA constant current. | 128 |
| Figure 6.4 | Discharge curves of Cell I for (a) cycle 1 and cycle 2, and (b) cycle 4, cycle 6 and cycle 8, measured at 0.04 mA constant current. | 128 |
| Figure 6.5 | Discharge curves of Cell I for (a) cycle 1 and cycle 2, and (b) cycle 4, cycle 6 and cycle 8, measured at 0.06 mA constant current | 129 |
| Figure 6.6 | Discharge curves of Cell II for (a) cycle 1 and 2, and (b) cycle 4, cycle 6, and cycle 8 at 0.02 mA constant current. (Inset: Enlargement of the plateau region). | 130 |
| Figure 6.7 | Discharge curves of Cell II for (a) cycle 1 and 2, and (b) cycle 4, cycle 6, and cycle 8 at 0.04 mA constant current. (Inset: Enlargement of the plateau region). | 130 |

| | | Page |
|-------------|---|-------------|
| Figure 6.8 | Discharge curves of Cell II for (a) cycle 1 and 2, (b) cycle 4, (c) cycle 6, and (d) cycle 8 at 0.06 mA constant current. | 132 |
| Figure 6.9 | Discharge specific capacity of Cell I at different constant current of (a) 0.02 mA, and (b) 0.04 mA and 0.06 mA. | 133 |
| Figure 6.10 | Discharge specific capacity of Cell II at different constant current of (a) 0.02 mA, and (b) 0.04 mA and 0.06 mA. | 133 |
| Figure 6.11 | Charge-discharge characteristics of Cell I for 1 to 10 cycles at 0.02 mA constant current. | 134 |
| Figure 6.12 | Charge-discharge characteristics of Cell II for 1 to 10 cycles at 0.02 mA constant current | 134 |

LIST OF TABLES

| | | Page |
|-----------|---|-------------|
| Table 2.1 | The properties of cellulose derivatives. | 13 |
| Table 2.2 | Ionic conductivity of SPEs based on CMC-ammonium salt/acid systems as reported in the literature. | 26 |
| Table 2.3 | Ionic conductivity of SPEs based on single polymer-NH ₄ NO ₃ salt systems from literature compared to the present work. | 27 |
| Table 3.1 | The designation and NH ₄ NO ₃ concentration of pure CMC film and System I films. *Calculation to obtain weight percentage of NH ₄ NO ₃ concentration. | 41 |
| Table 3.2 | The designation and EG concentration of System II films. **Calculation to obtain weight percentage of EG concentration. | 41 |
| Table 4.1 | Centre peak, FWHM and crystallite size for single polymer, System I and System II films. | 73 |
| Table 4.2 | The total weight loss and degradation temperatures of pure CMC film, System I and System II films obtained from TG analysis. | 79 |
| Table 5.1 | The thickness, regression values and activation energies of pure CMC film, and System I and System II films. | 94 |
| Table 5.2 | Transference numbers of System I and System II films. | 108 |
| Table 6.1 | The LSV values of different electrolyte systems as reported in literature compared to the present work. | 125 |
| Table 6.2 | The OCV value of proton batteries as reported by previous authors. | 127 |
| Table 6.3 | Cell parameters calculated in the plateau region at 0.02 mA discharge current for Cell II. | 131 |
| Table 6.4 | Cell parameters calculated in the plateau region at 0.04 mA discharge current for Cell II. | 131 |

ABBREVIATIONS

| | |
|------|---|
| AC | alternating current |
| CBH | correlated barrier hopping |
| CMC | carboxymethyl cellulose |
| CPE | constant phase element |
| D.S. | degree of substitution |
| DC | direct current |
| DTG | 1 st derivative of TGA |
| EG | ethylene glycol |
| EIS | electrical impedance spectroscopy |
| FTIR | Fourier transform infrared |
| FWHM | full-width at half maximum |
| LSV | linear sweep voltametry |
| M.W. | molecular weight |
| OCV | open-circuit voltage |
| OLPT | overlapping large polaron tunneling |
| QMT | quantum mechanical tunneling |
| SPE | solid polymer electrolyte |
| SPH | small polaron hopping |
| TGA | thermogravimetric analysis |
| TNM | transference (transport) number measurement |
| WL | weight loss |
| XRD | X-ray diffraction |

SYMBOLS

| | |
|-----------------|---|
| μ | mobility of charge carrier |
| τ | relaxation time |
| σ | conductivity |
| ε_i | dielectric loss |
| ε_r | dielectric constant |
| D | diffusion coefficient of charge carrier |
| E | energy density |
| E_a | activation energy |
| H^+ | hydrogen ion/proton |
| I_f | final residual current |
| I_i | initial current |
| k_b | Boltzmann's constant |
| L | crystallite size |
| M_i | imaginary part of electrical modulus |
| M_r | real part of electrical modulus |
| n | number density of charge carrier |
| NH_4NO_3 | ammonium nitrate |
| P | power density |
| Q | capacity |
| R_b | bulk resistance |
| s | power law exponent |
| T | temperature |
| T_g | glass transition temperature |
| T_p | peak temperature |
| Z_i | imaginary part of impedance |
| Z_r | real part of impedance |
| Γ_{ele} | electronic transference number |
| Γ_{ion} | ionic transference number |

LIST OF PUBLICATIONS

This thesis is in part based on the research that led to the following publications:

Journal Articles

1. Kamarudin, K. H. and Isa, M. I. N. *Ionic conductivity via quantum mechanical tunneling in NH_4NO_3 doped carboxymethyl cellulose solid biopolymer electrolytes*. *Advanced Materials Research*, **2015**, 1107, 236-241.
2. Kamarudin, K. H., Abdul Rani, M. S. A and Isa, M. I. N. *Ionic conductivity and conduction mechanism of biodegradable dual polysaccharides blend electrolytes*. *American-Eurasian Journal of Sustainable Agriculture*, **2015**, 9(2), 8-14.
3. Ramlli, M. A., Kamarudin, K. H. and Isa, M. I. N. *Ionic conductivity and structural analysis of carboxymethyl cellulose doped with ammonium fluoride as solid biopolymer electrolytes*. *American-Eurasian Journal of Sustainable Agriculture*, **2015**, 9(2), 46-51.
4. Kamarudin, K. H. and Isa, M. I. N. *Structural and DC ionic conductivity studies of carboxy methylcellulose doped with ammonium nitrate as solid polymer electrolytes*. *International Journal of Physical Sciences*, **2013**, 8(31), 1581-1587.

Proceeding and Book Chapter

1. Kamarudin, K. H. and Isa, M. I. N. *Transport properties of biodegradable cellulose biopolymer electrolytes*. **2015**. To be published as a book chapter in a research book entitled Eastern Corridor Renewable Energy.
2. Kamarudin, K. H. and Isa, M. I. N. *Investigation on conductivity and complexation of NH_4NO_3 based cellulose complexes*, 2013, 12th UMT International Annual Symposium UMTAS **2013** Proceeding, p. 867-873.

Conference and Exhibition Attended

1. Oral Presenter. *Ionic conductivity and transport studies of CMC-based solid biopolymer electrolytes*. PPSA Postgraduate Colloquium (PCPPSA2015), 17th Oct. **2015**, Kompleks Kuliah Berpusat, Universiti Malaysia Terengganu, Terengganu.
2. Oral Presenter. *Ionic conductivity and conduction mechanism of biodegradable dual polysaccharides blend electrolytes*. International Postgraduate Conference on Physics and Mathematical Sciences (IPCPMS2015), 10th – 11th Feb. **2015**, Seaview Hotel, Langkawi, Kedah.

3. Oral Presenter. *Ionic conductivity and structural analysis of carboxymethyl cellulose doped with ammonium fluoride as solid biopolymer electrolytes.* International Postgraduate Conference on Physics and Mathematical Sciences (IPCPMS2015), 10th – 11th Feb. **2015**, Seaview Hotel, Langkawi, Kedah.
4. Poster Presenter. *Transport properties of CMC-NH₄NO₃ proton conducting solid polymer electrolytes.* XIV International Symposium on Polymer Electrolytes (ISPE-14), 24th - 29th August **2014**, The Pier Geelong, Geelong, Australia.
5. Oral Presenter. *Transport properties of biodegradable cellulose biopolymer electrolytes.* Eastern Corridor Renewable Energy Symposium 2014 (ECRES2014), "Exploring The Renewable Energy For Future Earth", 3th Nov. **2014**, Universiti Malaysia Terengganu, Terengganu.
6. Oral Presenter. *Ionic conductivity via quantum mechanical tunneling in NH₄NO₃ doped carboxymethyl cellulose solid biopolymer electrolytes.* 27th Regional Conference on Solid State Science & Technology (RCSSST27), "Solid State Science & Technology Towards an Immense Breakthrough", 20-22 Dec. **2013**, Magellan Sutera Harbour, Kota Kinabalu, Sabah.
7. Poster Presenter. *Investigation on conductivity and complexation of NH₄NO₃ based cellulose complexes.* 12th UMT International Annual Symposium UMTAS 2013, "Advancements in Marine and Freshwater Sciences", 8-10 Oct. **2013**, Permai Inn Hotel, Kuala Terengganu, Terengganu.
8. Participant. *Eco-friendly rechargeable cell with cellulose based solid biopolymer electrolyte.* INOVASI@UMT 2014, 3rd June **2014**. Foyer PPDSNZ, Universiti Malaysia Terengganu.
9. Participant. *CAMNIT biopolymer electrolytes.* INOVASI@UMT 2013, 29th May **2013**. Dewan Sultan Mizan, Universiti Malaysia Terengganu, Terengganu.

Awards

1. Best Presenter Award. *Ionic conductivity and structural analysis of carboxymethyl cellulose doped with ammonium fluoride as solid biopolymer electrolytes.* International Postgraduate Conference on Physics and Mathematical Sciences (IPCPMS2015), 10 – 11th Feb. **2015**, Seaview Hotel, Langkawi, Kedah.
2. Silver Medal. *CAMRATE rechargeable green cell: An aspiration of greener renewable energy.* 25th International Invention, Innovation & Technology Exhibition (ITEX2014), 8 - 10th May **2014**. KLCC, Kuala Lumpur.

CHAPTER 1

INTRODUCTION

1.1 Research background

In the modern world, the inevitable power sources for portable electric and electronic devices are energy storage systems. The high demand for clean, smart, small size, lightweight, low cost, sustainable and longer shelf-life with power-hungry features, has accelerated immense research on advanced energy storage systems (Holmberg et al., 2014). One of the major technological challenges lies in the innovation and development of rechargeable batteries. In information and communication technology, rechargeable batteries are like the heart to most portable gadgets such as smartphones, laptops, tablets, GPS navigators/receivers and digital cameras. These gadgets mostly rely on rechargeable batteries to generate and restore electrical power.

In recent years, attempts were focused on developing all-solid-state-batteries since this approach offers attractive features such as being leak-proof, safe operation, flexibility in design and packaging (different shapes and sizes), light, ease of handling, as well as low-cost production and distribution (Kato et al., 2016; Ogawa et al., 2012; Notten et al., 2007). Conventional rechargeable batteries such as lithium-ion batteries contain liquid electrolytes, which are based on highly volatile and flammable organic solvents that trigger the risk of explosion and fire (Nguyen et al., 2014; Quartarone and Mustarelli, 2011; Baggetto et al., 2008). In order to hinder

the risk of electrolyte leakage and to rectify this safety concern, substituting the liquid with a safer and stable solid-state electrolyte is a stringent requirement. This can be achieved by using solid electrolytes in the construction of solid-state rechargeable batteries. Figure 1.1 shows a schematic cross-sectional view of a liquid battery and a solid-state battery as reported by Ogawa et al. (2012).

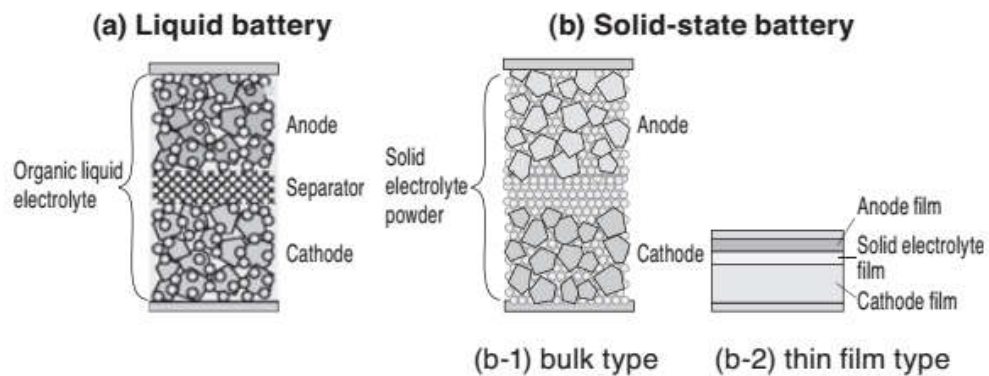


Figure 1.1 The schematic cross-sectional view of a liquid battery and a solid-state battery.

Solid polymer electrolytes (SPEs) or solvent-free polymer electrolytes are a new class of solid state ionic conductors. They are also known as 'superionic solids' or 'fast ion conductors' with a considerably high room temperature ionic conductivity close to that of liquid/aqueous electrolytes (Di Noto et al., 2011; Sequeira et al., 2010). An impressive growth of research related to SPEs was evidenced by the increment of a number of publications per year in scientific literature, particularly books and journal articles. This robust trend is mainly driven by their practical applications in electrochemical devices. Figure 1.2 shows the growth in research activity of SPEs in the past until recent years.

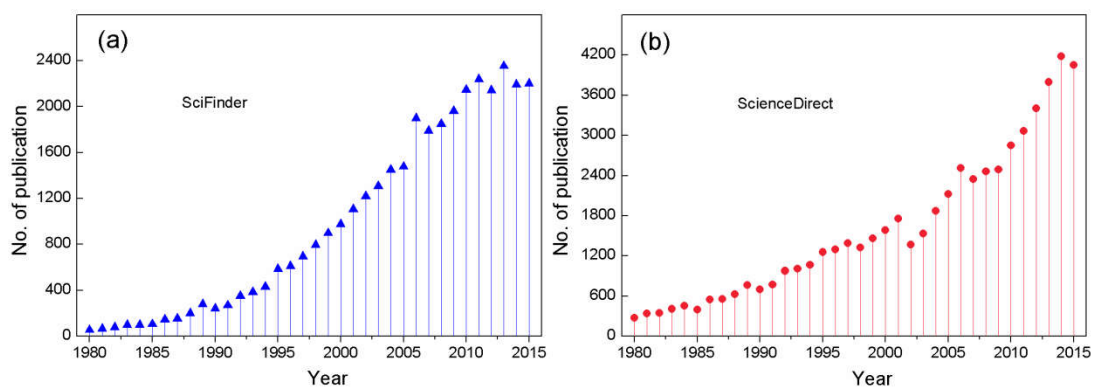


Figure 1.2 Statistics of publications on SPEs recorded between 1980 and August 2015. Data derived from (a) SciFinder scholar and (b) ScienceDirect online databases (Accessed on August 10, 2015).

Polymer electrolytes were studied for over five decades since the initial discovery by Peter V. Wright and his co-workers (Wright, 1975; Fenton et al., 1973) and its technological potential was further investigated by Michel B. Armand and co-workers (Armand and Trascon, 2008; Armand, 1994). Polymer electrolytes are formed by dispersing a salt in a polymer host/matrix to produce an ionically conducting solution (Shuhaimi et al., 2010b). The dispersion or dissolution of the salt in a polymer matrix renders ions as charge carriers that contribute to ionic conductivity under the influence of an electric field.

Recently, most host polymers studies for polymer electrolytes were derived from petroleum-based synthetic polymers such as polyethylene oxides and polyvinyl alcohols which are expensive, non-biodegradable and harmful to the environment. Therefore, naturally occurring polysaccharide polymers such as cellulose can be an initiative to the synthetic polymers. Cellulose is crystalline in nature. Carboxymethyl cellulose (CMC), which is a cellulose derivative, is among the most abundant polymers worldwide, as well as being economical, non-toxic, compatible with various salts, and principally biodegradable (Vroman and Tighzert, 2009;

Finkenstadt, 2005; Adinugraha et al., 2005). Pure CMC exhibits as being high in mechanical strength, transparent, good film forming ability, good thermal and dimensional stabilities and compatible with electrodes (Rani et al., 2015; Hallinan and Balsara, 2013; Kumar and Sekhon, 2002). Pure CMC has low conductivity owing to its slower segmental chain mobility in the crystalline phase (Varshney and Gupta, 2011). CMC consists of hydrophobic polysaccharide backbone and many hydrophilic carboxyl groups. Chemical modification by ion-donating salts or a doping approach further increased the ionic conductivity of CMC. This is due to the carboxyl functional groups of CMC providing more active sites for ions to move or coordinate, leading to the increment of ionic conductivity (Rudhzhiah et al., 2015).

1.2 Problem statement

SPEs can be an alternative to overcome the limitations of liquid/gel counterparts. SPEs based carboxymethyl cellulose utilize 'green' material as a host polymer. However, one of the major drawbacks possessed by SPEs based carboxymethyl cellulose is low ionic conductivity (10^{-8} - 10^{-6} Scm^{-1}) at room temperature (Ramlli and Isa, 2015; Sohaimy and Isa, 2015; Ng et al., 2014; Rozalli and Isa, 2014), which hampers its practical applications in rechargeable proton batteries.

Optimizing the ionic conductivity is among the most crucial goals in SPEs. Hence, the high room temperature ionic conductivity of $\sigma \geq 10^{-4}$ Scm^{-1} is one of the basic requirements of SPEs (Agrawal and Pandey, 2008; Dias et al., 2000). The ionic conduction mechanism in SPEs mainly depends on the segmental motion/mobility of the polymer chain and ionic transport mechanism (Ulaganathan et al., 2013; Varshney and Gupta, 2011; Andrev and Bruce, 2000; Vincent, 1995). The segmental

motion of polymer chain creates free volume for ions to migrate, thus allowing them to propagate. To achieve this condition, a large population of ions or electrons is required to prevent problems associated with ion migration and Ohmic resistance. The other factor that governs the ionic conductivity is ionic transport in SPEs which are attributed to the degree of salt dissociation/concentration, the degree of ion aggregation, the dielectric constant of the host polymer and the mobility of polymer chains. Ammonium salts such as ammonium nitrate (NH_4NO_3) consists of a smaller size cation (H^+) with a larger size anion, which can easily dissociate and render higher protonic conduction (Rudhziah et al., 2015; Pandey et al., 2013), and thus can be a good choice for an ionic dopant.

The addition of plasticizer in SPEs is one of the most effective approaches to enhance the ionic conductivity of SPEs using high dielectric constant, low viscosity and low vapour pressure of organic molecules (Pandey et al., 2013; Varshney and Gupta, 2011; Pradhan et al., 2007). Plasticization improves the mobility of ionic and/or the interfacial interaction among ionic and polar groups in polymer chains which can affect the permeability of film and its mechanical properties. This approach helps to modify the polymer matrix by increasing the salt-solvating force which leads to an increase in the amorphous phase content, dissociating ion aggregates into free cations and anions and lowers the glass transition temperature, T_g (Pandey et al., 2013; Kumar and Sekhon, 2002), therefore, leading to an enhancement in ionic conductivity. High dielectric constant and low viscosity additives such as ethylene glycol (EG) is a good plasticizer and can be used to modify the permeability of SPE film.

To date, various spectroscopic studies were carried out to understand the conduction mechanism of ions in different SPE systems. However, the study on ionic transport mechanisms in these systems is still scarce (Choi and Jang, 2010; Ramya and Selvasekarapandian, 2007) and mostly centred to lithium battery application. Therefore, more research on SPEs, especially for solid-state rechargeable proton batteries, is needed for a better understanding of these mechanisms.

1.3 Research objectives

This research comprises of four (4) main objectives:

- i. To prepare two (2) SPE systems consisting of CMC incorporated with NH_4NO_3 salt (System I) and CMC- NH_4NO_3 plasticized with EG (System II) in varied weight percentages.
- ii. To verify the vibrational, structural, and thermal properties of SPEs in System I and System II.
- iii. To determine the ionic conductivity, electrical and ionic transport properties of SPEs in System I and System II.
- iv. To develop solid-state rechargeable proton battery incorporating with the highest conducting SPEs in System I and System II, and validate its electrochemical performance.

1.4 Scope of the research

The main goal of this research is to discover the potential of CMC as a promising SPE towards the development of solid-state rechargeable proton battery. In this research, CMC acts as a host polymer, NH_4NO_3 salt as a dopant and EG as a

plasticizer. Two (2) SPE systems that consist of a CMC-NH₄NO₃ system (System I) and a CMC-NH₄NO₃-EG system (System II) in varied weight percentages were prepared at room temperature via solution casting technique.

The effect of NH₄NO₃ and EG was studied on the vibrational, structural and thermal properties of SPEs. The molecular interaction/complexation of both systems were investigated using FTIR spectroscopy at room temperature. The amorphousity and thermal stability of both systems were observed using XRD and TGA methods, respectively. The ionic conductivity, electrical and transport properties of both systems were determined using EIS technique and FTIR deconvolution approach.

For practical applications, the highest conducting SPEs in System I and II were applied to the solid-state rechargeable proton battery using Zn-MnO₂ as electrodes. The performance of the battery was observed using multimeter and battery tester to obtain open-circuit voltage and charge-discharge characteristics at room temperature.

1.5 Research significance

One of the greatest challenges encountered by modern society today is the demand for smart, clean and sustainable energy storage devices. Besides power requirements, the evolution of these devices also considers several aspects such as size, weight, cost and environmental impact. From the environmental impact point of view, the method to manage and recycle battery materials is still controversial and scarce owing to the disposable issue of toxic and hazardous materials used. Therefore, using natural polymers as a prime material in the development of SPEs can be an advantage.

The replacement of conventional synthetic polymers with natural polymers such as CMC for SPEs may hinder the use of non-renewable resources and reduces the waste disposal issues through biological cycling. It also can assist in reducing electronic waste contribution and eliminating the issues that arise related to the toxicity and hazardous materials in commercial batteries nowadays.

1.6 Thesis outline

This thesis is organized into seven (7) chapters. As for the introductory of the research, Chapter 1 briefly explains the general overview of the research, problem statement, scope of research and research significance. Thesis outline is described at the end of chapter.

In the following chapter, Chapter 2 discusses the literature review of the properties of biodegradable polymers, types and basic properties of SPEs and the fundamentals of solid-state electrochemical cell. Details of proton-conducting materials, the improvement of ionic conductivity and transport properties and hopping mechanism of SPEs are detailed out and discussed. Besides, the fundamental theories or principles of batteries are also well elucidated.

In Chapter 3, the methodology of the research is explained in detail, which includes the preparation of SPE films and fabrication of proton batteries. The physical-chemical properties of SPEs and battery characteristics have been performed using a variety of characterization techniques. A quick sample preparation is asserted at the end of each technique. The batteries have been fabricated based on standard battery preparation using the most conductive as-prepared SPEs. This achieves the goals for the first and fourth objectives of this research.

Results and discussion have been conferred into three (3) main chapters. Chapter 4 discusses the findings of the vibrational, structural and thermal properties of SPEs. This achieved the second objective of the research. Objective 3 is presented as Chapter 5. Chapter 5 demonstrates the investigation on the ionic conductivity, transport, and electrical properties of SPEs. Objective 4 is presented and discussed in Chapter 6. The electrochemical performance of SPEs employed in the electrochemical devices, namely proton batteries, has been deliberately discussed in this chapter.

As the final chapter, Chapter 7 concludes the outcomes of the research, contributions and future works. A few suggestions have been made to improve the present research and future plan have been proposed in advance.

CHAPTER 2

LITERATURE REVIEW

This chapter discusses a general overview of biodegradable polymers, types and basic properties of solid polymer electrolytes, and the crucial factors that govern the ionic conduction mechanism in solid polymer electrolytes as previously reported by several authors. At the end of the chapter, the theories and characteristics of all solid-state electrochemical cell by utilizing solid polymer electrolytes are briefly explained.

2.1 Biodegradable polymers

Polymers form the basis in our daily life. A polymer is a large/complex molecule (macromolecule), built-up by the repetition of small chemical units (Charles, 2013; Young and Lovell, 2011). The word *polymer* is originated from the classical Greek *poly* and *meros*, meaning 'many' and 'parts' (Charles, 2013; Osswald and Menges, 2010). Polymers are the most important materials currently in use in a broad variety of fields and applications (Li, 2015; Yu et al., 2014; Charles, 2013; Ravve, 2012; Pasparakis et al., 2012)

In recent years, there is increasing concern in the use of natural-based polymers to replace synthetic polymers due to its low toxicity, biocompatibility and biodegradability capabilities. These biodegradable polymers can be categorized into

four (4) main groups depending on the sources and synthesis (Avérous and Pollet, 2012; Vieira et al., 2011; Vroman and Tighzert, 2009; Bordes et al., 2009).

- i. Polymers from biomass such as the agro-polymers from agro-resources;
 - a) polysaccharides, e.g., starch, cellulose, chitin/chitosan,
 - b) protein and lipids, e.g., plant (soy, zein and gluten), and animals (casein, whey, and collagen/gelatin).
- ii. Polymers attained by microbial production (extraction of micro-organisms), e.g., polyhydroxyalkanoates.
- iii. Polymers chemically synthesized using monomers (bio-derived monomers) obtained from agro-resources, e.g., poly(lactic acid).
- iv. Polymers whose monomers and polymers are both obtained by chemical synthesis from fossil resources (petrochemical products), e.g., polycaprolactones.

The first group is considered as agro-polymers, enzymatically degradable polymers. The remaining of the groups is known as biodegradable polyesters (biopolyesters), hydrolytically degradable polymers. Out of these groups, (iv) is derived from non-renewable resources.

The extensive research and exploration of polymer science by scientist and industries are driven by the increasing demands on biopolymer-based films or bio-based materials, particularly for practical applications in food industries and medical fields. This also includes a vast number of polysaccharide polymers have been studied as polymer host in electrolyte preparation as promising materials for solid-state electrochromic and electrochemical device applications (Shukur and Kadir,

2015, Kumar et al., 2012c; Varshney and Gupta, 2011; Shuhaimi et al., 2010b; Ng and Mohamad, 2008). These polysaccharide polymers based electrolytes were reported to exhibit a high ionic conductivity of $\sim 10^{-3} \text{ Scm}^{-1}$ (Alias et al., 2014; Shukur et al., 2013b).

One of the interesting polysaccharide polymers is cellulose. Carboxymethyl cellulose (CMC or known as NaCMC), methyl cellulose (MC), ethyl cellulose (EC), hydroxyethyl cellulose (HEC) and hydroxypropyl cellulose (HPC) are water-soluble cellulose derivatives obtained by etherification of cellulose and distinguish by the functional group and the degree of substitution (D.S.) (Varshney and Naithani, 2011; Zugenmaier, 2008) as exemplified in Table 2.1. Among these ether derivatives of cellulose, CMC exhibits a strong polyelectrolyte which shows sensitivity to pH and ionic strength variations (Akar et al., 2012). In a polyelectrolyte, positive or negative charged groups are covalently attached to a polymer chain and solvated by a high dielectric constant solvent such as water (Dias et al., 2000).

Table 2.1 The properties of cellulose derivatives.

| Cellulose derivatives | Functional group | D.S. | Solubility |
|------------------------------|---|-------------|-------------------|
| CMC | -CH ₂ COONa | 0.5-2.9 | Water |
| MC | -CH ₃ | 1.5-2.4 | Hot water |
| EC | -CH ₂ CH ₃ | 2.3-2.6 | Organic solvents |
| HEC | -CH ₂ CH ₂ OH | 0.5-0.7 | Water |
| HPC | -CH ₂ CH ₂ CH ₂ OH | 1.5-2.0 | Water |

CMC, a naturally abundant polymer with desirable attributes such as renewable, biodegradable, biofunctional, non-toxic, inexpensive and environmentally/ecologically friendly materials (Adinugraha et al., 2005). CMC can be found vastly in plants from wood to renewable agricultural waste or

biomass feedstock resources. CMC is a linear anionic polysaccharide of anhydroglucose units linked by C-1 and C-4 ether bonds known as β -1,4 glycosidic linkages with extensive intramolecular hydrogen bonding, a cellulose derivative prepared from alkaline cellulose and chloroacetic acid by etherification and usually used as its sodium salt (cellulose gum) (Lin et al., 2013). Due to its highly hydrophilic properties, CMC can easily dissolve in cold/hot water. It is widely used in many industrial sectors including food, textiles, paper, adhesives, paints, pharmaceuticals, cosmetics, mineral processing, drug delivery, tissue engineering and more recently as reducing/stabilizing agent in preparation of silver nanoparticles (Shukur et al., 2013c; Abdul Khalil et al., 2012; Varshney and Naithani, 2011; Li et al., 2009; He et al., 2007). Pure CMC appears as a white, granular and odorless powder (Figure 2.1(a)). CMC is a water-soluble polysaccharide and appears as a viscous clear liquid (Figure 2.1(b)). The solid CMC film is obtained by evaporating the water content (Figure 2.1(c)).



Figure 2.1 The physical appearance of pure CMC, (a) powder, (b) liquid, and (c) solid film.

Figure 2.2 represents the chemical structure of pure CMC (Ibrahim et al., 2011; Li et al., 2009; Biswal and Singh, 2004). CMC satisfies the basic requirements to serve as a host polymer matrix which include low glass transition temperature, low cohesive energy, flexible backbone and the presence of polar groups (Srivasta and Chandra, 2000). CMC has a polar functional group, CH_2COONa in its polymer chain

that exhibits a high affinity for cations and plasticizing solvents. The oxygen atom from carbonyl group of CMC is expected to form a coordinate bond with the cations from the doping salts/acids (Samsudin et al., 2012c; Chai and Isa, 2012), thus favour the ionic conduction in polymer electrolytes. Hence, it's show one of essential characteristics of a potential polymer electrolyte material.

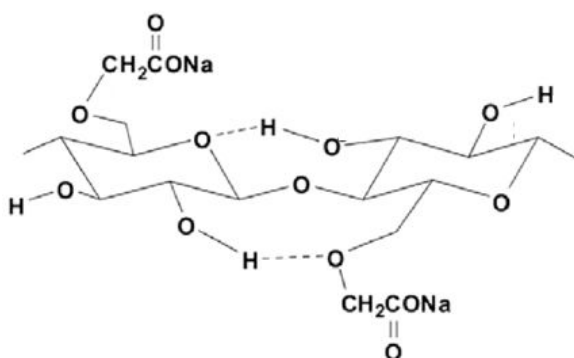


Figure 2.2 The chemical structure of pure CMC.

2.2 Solid polymer electrolytes

Polymer electrolytes can be defined as ionic conductors formed by dissolving salts in suitable high molecular weight polymers. In 1973, Fenton, Parker and Wright first discovered conductive polymer of poly(ethylene oxide (PEO)-alkaline metal ion complex with the ionic conductivity of $\sim 10^{-7} \text{ Scm}^{-1}$ (Wright, 1975; Fenton et al., 1973). Years later, Armand and co-workers proposed the application of solid polymer electrolyte (SPE) in lithium batteries (Armand and Trascon, 2008; Armand, 1994; Armand, 1986). Since then, the research and development on SPE widely expanded, in particular for the improvement of the ionic conductivity, understanding the ionic transport mechanism as well as discovering other conducting polymers with superior properties.

2.2.1 Types of solid polymer electrolytes

In general, SPE can be classified into three (3) types; dry, gelled and porous polymer electrolytes, based on the preparation routes employed during film casting and also their physical conditions (Agrawal and Pandey, 2008; Murata et al., 2000; Dias et al., 2000). The SPE films/membranes are generally cast either by solution cast method or hot-press (extrusion) technique.

Dry solid polymer electrolytes or conventional polymer-salt complexes are prepared by dissolving/complexing ionic salts into coordinating polar polymer hosts such as poly(ethylene oxide) (PEO), methyl cellulose (MC), chitosan, etc. The other category of dry SPEs is plasticized polymer-salt complexes, prepared by adding appropriate liquid plasticizers into the polymer-salt complexes. The magnitude of ambient ionic conductivity is significantly enhanced by this approach as a result of the increase of the polymer chain flexibility, and the decrement of both the crystallinity and the glass transition temperature.

Gelled or polymer gel electrolytes or also known as polymer hybrids are basically obtained by incorporating a large amount of organic liquid solvent/liquid plasticizer into the polymer matrix which resulted in the formation of a stable gel with the polymer host structure. A high ambient ionic conductivity close to those of the liquid electrolytes can be achieved following this method due to the similar conductivity mechanisms occur in both systems.

Porous or composite polymer electrolytes are prepared by introducing high surface area inert particulate ceramic fillers (inorganic solid) such as ZrO_2 , SiO_2 , TiO_2 , Al_2O_3 , etc. in proportion with a dry SPE or gelled SPE systems (polymer

matrices/SPE hosts). The composite formation substantially enhanced the ionic conductivity, mechanical stability and the interfacial activity of SPEs.

2.2.2 Basic properties of solid polymer electrolytes

SPEs based on natural biodegradable polymers have received considerable attention from academia and industry due to their vast practical applications in solid-state electrochemical devices such as solid-state batteries, electric double layer capacitors, fuel cells and solar cells (Bai et al., 2014; Vaghari et al., 2013; Markoulidis et al., 2012; Kadir et al., 2010; Bhargav et al., 2009; Xu et al., 2009). This also owing to their superior characteristics for instance leakage free, flame resistance, light weight, flexible, good electrodes-electrolyte surface contact, good dimensional and adhesive property (Shit and Shah, 2014; Gray, 1991). Thus, for the purpose of practical applications, the SPE materials should possess the following characteristics (Agrawal and Pandey, 2008; Dias et al., 2000; Gray, 1991):

- i. *Ionic conductivity*, $\sigma \geq 10^{-4} \text{ Scm}^{-1}$ at room temperature. This is crucial to gain performance level close to the liquid electrolyte-based devices.
- ii. *Ionic transference number*, $T_{ion} \sim 1$. The polymer electrolyte should perfectly serve as an ion conducting medium and also as a separator to enable use for battery applications. The polymer electrolyte should also preferably be a single-ion (e.g. cation) conducting system. Thus, the cationic transference number should be ≥ 0.5 to indicate the potential transporting ions in the polymer electrolyte, only a negligible contribution from electronic conduction. To achieve higher power density in the battery, a large cationic transference

number (close to unity) is required to minimize the concentration effect in the electrolyte during charge-discharge cycles.

- iii. *High mechanical strength, chemical, and thermal stabilities.* The SPE is sandwiched between the cathode and anode materials for the fabrication of solid state electrochemical devices. Thus, the SPE should possess a high mechanical strength to endure the chemical-thermal instabilities during charge-discharge steps for a safe and enduring battery, and also for the scaling-up and large-scale manufacturing of the devices. High chemical and thermal stabilities are vital to prevent undesirable chemical reactions occur at the electrolyte-electrode interfaces and enable a battery operation at a wider temperature range, respectively.
- iv. *High electrochemical stability.* This is essential particularly for rechargeable batteries. The instability in the SPE may cause irreversible reactions and capacity fading in the battery.
- v. *Compatibility with the electrode materials.* The SPE should be compatible with the different active electrode materials. Thus, the performance level of the electrochemical devices can be improved.

As mention above, the SPEs play two principal roles in solid-state electrochemical cells. SPEs serve as the conventional electrolytes, i.e., the medium of ion transport between the cathode and anode during battery operation, and also function as the separator due to its rigid structure which isolates the cathode from the anode. Therefore, the SPEs must sustain sufficient mechanical strength to endure electrode stack pressure and stresses caused by dimensional changes during charge/discharge cycling of rechargeable electrodes i.e. battery operation (Arora and

Zhang, 2004). For this reason, the materials that will be used in the preparation of solid polymer electrolytes should be cautiously selected.

2.2.3 Ion-conduction mechanism

Since the earliest breakthrough of ion conducting polymer (PEO-alkaline metal salt complexes) in 1973 (Fenton et al., 1973), the prime intention of the research and development of SPEs are focused on the preparation/synthesis of SPEs with room temperature ionic conductivity close to that of liquid/aqueous counterparts. A large number of polymer electrolyte systems have been reported for the past few decades, involving a variety of transporting ions, such as Li^+ , H^+ , Na^+ , K^+ , Ag^+ , Mg^{2+} , etc. as mobile species (Agrawal and Pandey, 2008).

There are two possible charge carrier/mobile ionic species in polymer-ammonium salt systems, namely cation and anion. The cation mobile species could be either NH_4^+ , NH_3^+ or H^+ . Srivastava and Chandra (2000) reported that H^+ ion is the only cation which contributes to the ionic transport in the PESC- NH_4ClO_4 system using alternating current (AC)/direct current (DC) impedance and Coulometric techniques. Similar observation has been found by other authors. Kadir et al. (2010), Shuhaimi et al. (2010), Samsudin and Isa (2012b), and Samsudin and Isa (2012b) claimed that the charge carrier that responsible for ionic conduction in the polymer-salt/acid complexes, namely chitosan- NH_4NO_3 , MC- NH_4NO_3 , CMC- NH_4Br and CMC-DTAB systems is proton, H^+ ion originates from the ammonium ions and the conduction occurs via Grotthus mechanism (i.e. conduction occurs through the exchange of H^+ ions between complexed sites) (Bai et al., 2014; Ma and Sahai, 2013;

Sheha, 2009; Jiang et al., 2008) as evidenced by FTIR and AC impedance techniques.

Several approaches of physical-chemical modifications have been suggested in the literature to enhance the ionic conductivity of polymer-salt complexes, including the use of blend polymers for grafted systems, the addition of ceramic fillers and carbon nanotubes for composites-based systems, the addition of plasticizers for plasticized systems, the cross-linking of polymers using UV and thermal radiation, etc (Dias et al., 2000). Hence, various theoretical approaches have been implemented to understand the ion transport mechanism in the SPEs and the physical-chemical processes that occur at the polymer electrolyte-electrode interfaces (Christie and Bruce, 1995; Gray, 1991).

The fast ion transport in SPEs was reported significantly due to the amorphous phase and highly structured of polymer electrolytes (Agrawal and Pandey, 2008; Andreev and Bruce, 2000). A good flexibility of the polymer chains can be achieved at a lower T_g of the amorphous phase of polymer host. Hence, the larger the degree of amorphosity of polymer host, the higher the ionic conductivity can be obtained i.e. faster ion transport. Therefore, an understanding to the interactions of the various species in the polymer electrolytes are necessary to ensure appropriate polymer hosts, complexing salts and salt/plasticizer concentrations are selected in order to optimize the ionic conductivity. In addition, Pandey et al. (2013) reported that the ionic conductivity of polymer electrolytes not only governs by the crystallinity of the material, other factors such as simultaneous cation and anion motion, and the formation of ion-pair (anion complex-cation interaction) should also be considered.

AC impedance

In DC technique, the electrical resistance, R is the ratio of voltage, V to the current, I or can be described as a property in which a material resists the flow of electrical current as expressed by Ohm's law (Finkenstadt, 2005).

$$R = V/I \quad (2.1)$$

For AC technique, the ratio gives an analogous quantity, the impedance, Z . The Ohm's law describes the behaviour of an ideal resistor, which is unlikely to the most of polymers, thus impedance is used. Similar to resistance, impedance is a measure of the ability of an electric circuit to resist the flow of an electrical current when voltage is applied (i.e. the complex ratio of the voltage to the current in an AC circuit). The AC impedance can also be expressed in terms of the real (Z_r) and imaginary (Z_i) parts with $j = \sqrt{-1}$ as follows,

$$Z = V/I = Z_r + jZ_i \quad (2.2)$$

Impedance spectra are plotted with $-Z_i$ against Z_r at a series of frequency range and affected by several aspects such as electron transfer, mass transport and chemical reactions. The AC impedance spectroscopy is commonly used to measure the complex components of the impedance response of the material. The impedance data are represented by a Nyquist (Cole-Cole) plot or Bode plot and typically analyzed in terms of an equivalent electrical circuit model. The complex impedance plot gives information on the different resistive contributions such as bulk, grain boundary and electrode/electrolyte interfacial resistance (Agrawal and Pandey, 2008).

Ionic conductivity

The DC ionic conductivity, σ is a crucial characteristic of SPEs and can be calculated by the following equation,

$$\sigma = \frac{t}{(R_b \times A)} \quad (2.3)$$

Here, t (cm) is the thickness, R_b (Ω) is the bulk resistance, and A (cm^2) is the surface area of electrolyte-electrodes contact of the SPE. The R_b of SPE can be retrieved from the intercept of high frequency semicircle or the low frequency spike on the Z_r -axis of the Nyquist plot.

The influence of temperature on the ion transport in SPEs can be described by means of the temperature-dependent ionic conductivity. The ionic conductivity of a thermally activated ion-transport process in amorphous phase below the T_g is expressed by a simple Arrhenius relation (Petrowsky and Frech, 2009),

$$\sigma = \sigma_0 e^{-(E_a / k_b T)} \quad (2.4)$$

Here, σ_0 is the exponential prefactor, E_a is the activation energy, k_b is the Boltzmann's constant ($1.38 \times 10^{-23} \text{ J.K}^{-1}$) and T is the temperature. The plot of the conductivity versus the reciprocal temperature displays a straight line where E_a can be retrieved from the gradient of the linear fit plot. The linear Arrhenius relation indicates the conduction mechanism (ion transport) via a simple hopping mechanism. In contrast, the temperature dependence of ionic conductivity in amorphous SPEs above the T_g can be explained by 'Free-Volume Theory' of the non-Arrhenius relationship (Pai et al., 2005; Pas et al., 2005). This relationship elucidates the fitted

conductivity data to an empirical equation such as Vogel-Tamman-Fulcher (VTF), Williams-Landel-Ferry (WLF), etc. The conductivity versus the reciprocal temperature plot shows a non-linear curve.

Effect of ammonium salts

The doping of salts can increase the amorphousity and improve the ionic conductivity of SPEs. Ammonium salts such as NH_4Cl , NH_4Br , NH_4SCN , NH_4NO_3 , and NH_4F , have been considered as good proton (H^+) donors to the polymer matrices since it rendered a high efficiency of proton conduction, thus were selected as doping salts (Samsudin and Isa, 2012b; Du et al., 2010). Among these salts, ammonium nitrate with chemical formula NH_4NO_3 is widely and frequently investigated for utilization in solid-state electrochemical applications.

NH_4NO_3 salt is an odorless, white crystalline solid and highly soluble in water. NH_4NO_3 salt exists in five stable polymorphic forms below its melting point of 169–170°C (Lang and Vyazovkin, 2008; Wu et al., 2007). NH_4NO_3 salt has a low lattice energy (637 kJmol^{-1}) and small NH_4^+ radius (1.4 \AA) which is beneficial for the polymer-salt complexation (Damle et al., 2009 and 2008). The chemical structure of NH_4NO_3 salt is shown in Figure 2.3.

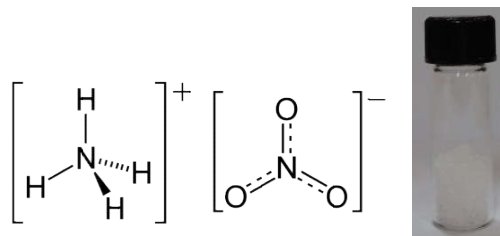


Figure 2.3 The chemical structure of NH_4NO_3 salt.

Effect of plasticizers

Plasticization is a simple technique used to increase the flexibility of the polymer chain and enhance the ionic conductivity by reducing the crystallinity and increasing the amorphous nature of the polymer electrolytes. The addition of a plasticizer to the polymer electrolyte decreases the T_g of the polymer, reduces the elastic modulus and softens the polymer backbone, leading to an increase in the segmental motion and subsequently enhanced the ionic conductivity (Varshney and Gupta, 2011). Many theories have been proposed to describe the plasticizer mechanism in polymer electrolytes. According to 'Lubricity Theory', the plasticizers serve as a lubricant to assist movements of charge carriers among themselves, while 'Gel Theory' explains it as the disruption of polymer-polymer interaction (Pandey et al., 2013; Ali et al., 2005). The 'Free-Volume Theory' describes the role of plasticizers to increase free volume, and thus lowering the T_g of the polymer (Pandey et al., 2013; Pai et al., 2005).

The effect of plasticizer on the polymer electrolytes greatly depends on the compatibility between plasticizer and polymer, and the specific nature of the plasticizer, indicated by the dielectric constant, donor number, viscosity, hydrogen bonding, etc. (Vieira et al., 2011; Shuhaimi et al., 2010a). The high dielectric constant of plasticizer weakens the Coulomb force between the cation and anion, thus resulting in the dissolution of salt and dissociation of ion pairs/aggregates into free cations or anions (Shukur et al., 2014). Whereas, the low viscosity of plasticizer reduces the T_g and increases the amorphous content of polymer electrolytes, which leads to the enhancement in ionic conductivity (Pradhan et al., 2007, 2008). For these reasons, ethylene carbonate (EC), propylene carbonate (PC) and glycerol are among the most

used plasticizers in SPE systems. Hence, ethylene glycol (EG) can be another alternative to be used as a natural-based plasticizer.

EG is a clear, odorless, low vapour pressure and biodegradable liquid plasticizer (Hudson et al., 2005). EG has similar physical properties and uses as propylene glycol (PG). Their chemical structures differ by only one methyl group (EG: HOCH₂CH₂OH; PG: CH₃CH[OH]CH₂OH). EG can dissolve in water and alcohol, and is vastly found in many household products, including antifreeze, deicing products, detergents, paints, and cosmetics. Figure 2.4 shows the chemical structure of EG plasticizer.

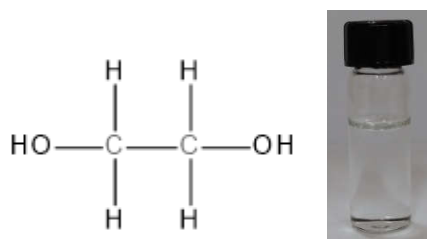


Figure 2.4 The chemical structure of EG plasticizer.

Proton or hydrogen ion (H⁺) is believed to play a vital role in ionic conduction in polymer-ammonium salt system. CMC has lone pair electrons at its oxygen (O) atoms originated from carbonyl groups (C=O) which serve as complexation sites with the cation of the doping salt. H⁺ ions have a tendency to coordinate with O atoms since the negatively charged O atoms can donate electrons to the cations to form dative bonds (Hema et al., 2008). Thus, showed that CMC polymer plays as a host for ionic conduction to take place through the presence of lone pair electrons.

CMC polysaccharide polymer has been intensively studied by Isa group since 2012 to investigate the effect of ammonium salts and acids on the ionic conductivity

of SPEs. The pure CMC film exhibits a low room temperature ionic conductivity between 10^{-7} and 10^{-8} Scm^{-1} (Ahmad and Isa, 2015; Isa and Noor, 2015; Kamarudin and Isa, 2013). The addition of doping salts and plasticizers significantly enhanced the ionic conductivity values to a higher magnitude orders. Table 2.2 lists the values of ionic conductivity obtained by implementing different amount of dopant into CMC-based SPEs as reported by several authors to date. Most of the works show the ionic conductivity was enhanced by the addition of the ionic dopants.

Table 2.2 Ionic conductivity of SPEs based on CMC-ammonium salt/acid systems as reported in the literature.

| Polymer (D.S.) | Ammonium salt / acid (wt.%) | Plasticizer (wt.%) | σ (Scm^{-1}) | Reference |
|----------------|---|--------------------|--------------------------------|-----------------------|
| CMC (0.7) | NH ₄ Br (25) | - | 1.12×10^{-4} | Samsudin & Isa, 2012b |
| CMC (0.7) | NH ₄ Br (25) | EC (8) | 3.31×10^{-3} | Samsudin & Isa, 2014b |
| CMC (0.7) | DTAB (35) | - | 7.72×10^{-4} | Samsudin & Isa, 2012c |
| CMC (0.7) | DTAB (35) | EC (10) | 2.37×10^{-3} | Isa & Samsudin, 2013 |
| CMC (0.7) | NH ₄ Cl (16) | - | 1.43×10^{-3} | Ahmad & Isa, 2015 |
| CMC (0.7) | NH ₄ SCN (25) | - | 6.48×10^{-5} | Noor & Isa, 2015 |
| CMC (0.7) | NH ₄ F (9) | - | 2.68×10^{-7} | Ramlli & Isa, 2015 |
| CMC (0.7) | (NH ₄) ₂ CO ₃ (7) | - | 7.71×10^{-6} | Sohaimy & Isa, 2015 |
| CMC (1.49) | CH ₃ COONH ₄ (20) | - | 5.77×10^{-4} | Rani et al., 2014 |
| CMC (0.7) | Salicylic acid (7) | - | 9.50×10^{-8} | Rozali et al., 2015 |
| CMC (0.7) | Adipic acid (5) | - | 6.12×10^{-7} | Rozali & Isa, 2014 |
| CMC (0.7) | Citric Acid (40) | - | 4.38×10^{-7} | Ng et al., 2014 |
| CMC (0.7) | Oleic acid (20) | - | 2.11×10^{-5} | Chai & Isa, 2012 |
| CMC (0.7) | Oleic acid (20) | PC (10) | 2.52×10^{-7} | Chai et al., 2013 |
| CMC (0.7) | Oleic acid (20) | Gly (40) | 1.64×10^{-4} | Chai & Isa, 2015 |

Note: D.S. – degree of substitution (purity); σ - DC ionic conductivity at room temperature; NH₄Br - ammonium bromide; DTAB - dodecyltrimethyl ammonium bromide; NH₄Cl - ammonium chloride; NH₄SCN - ammonium thiocyanate; NH₄F - ammonium fluoride; (NH₄)₂CO₃ - ammonium carbonate; CH₃COONH₄ - ammonium acetate; EC - ethylene carbonate; PC - propylene carbonate; Gly - glycerol.

The introduction of plasticizer further increases the values of ionic conductivity in SPEs. The ionic conductivity can be achieved as high as $\sim 10^{-3}$ Scm^{-1} for both plasticizer-free and plasticized CMC-based SPE systems. The ionic conductivity of single polymer-NH₄NO₃ salt complexes at room temperature have been reported

between 10^{-6} to 10^{-3} Scm^{-1} , depending on their specific nature of polymer hosts as listed in Table 2.3.

Table 2.3 Ionic conductivity of SPEs based on single polymer- NH_4NO_3 salt systems from literature compared to the present work.

| Polymer | NH_4NO_3 (wt.%) | Plasticizer (wt.%) | Solvent | σ (Scm^{-1}) | Reference |
|----------------|------------------------------------|-----------------------|-----------------|--------------------------------|---------------------------------|
| Tapioca Starch | 25 | - | Oxalic acid | 2.15×10^{-6} | Azlan & Isa, 2011 |
| Tapioca Starch | 25 | - | Distilled water | 2.83×10^{-5} | Khlar and Arof, 2010 |
| Chitosan | 40 | - | Acetic acid | 8.38×10^{-5} | Ng & Mohamad, 2006 |
| Chitosan | 40 | EC (70) | Acetic acid | 9.93×10^{-3} | Ng & Mohamad, 2008 |
| PVA | 20 | - | DMSO | 7.50×10^{-3} | Selvasekarapandian et al., 2010 |
| PAN | 20 | - | DMF | 2.74×10^{-6} | Nithya et al., 2013 |
| PAN | 20 | PC (0.02) | DMF | 7.48×10^{-3} | Nithya et al., 2015 |
| MC | 25 | - | Distilled water | 2.10×10^{-6} | Shuhaimi et al., 2010b |
| MC | 25 | PEG200 (15) | Distilled water | 1.14×10^{-4} | Shuhaimi et al., 2010a |

Note: PVA - poly(vinyl alcohol); PAN - polyacrylonitrile; MC - methyl cellulose; CMC - carboxymethyl cellulose; EC - ethylene carbonate; PC - propylene carbonate; PEG200 - poly(ethylene glycol) (200); MSO - dimethyl sulfoxide; DMF - dimethyl formamide.

Ionic transport mechanism

Generally, the ionic conductivity of polymer electrolytes relies on the number of the charge carriers and their mobility in the electrolyte system and can be explained as follows (Woo et al., 2013):

$$\sigma = \sum_i n_i z_i e \mu_i \quad (2.5)$$

Here, i , n_i , z_i , e and μ_i represent a charge carrier species (cation/anion), the number density (concentration) of charge carriers (cm^{-3}), the valency of the charge carriers,

the elementary electron charge and the mobility of charge carriers ($\text{cm}^2\text{V}^{-1}\text{s}^{-1}$), respectively. Thus, the enhancement of ionic conductivity can be attributed to the increase in the number density of free ions and their mobility by increasing the salt concentration.

Several approaches to evaluate the ionic transport parameters (i.e. the number density (n), mobility (μ) and diffusion coefficient (D) of charge carriers) of polymer electrolytes have been reported in the literature. This includes using impedance spectroscopy combined with the conventional Rice and Roth model (restricted to the Arrhenius-type behaviour of conductivity-temperature relationship) (Rice and Roth, 1972), dielectric measurements and a space charge relaxation model or known as broadband dielectric response (BDR) method (Bandara et al., 2011), impedance spectroscopy with the new developed equations (Arof et al., 2014) and Fourier transform infrared (FTIR) spectroscopy based on the deconvolution of IR-spectra (Abdul Rahaman et al., 2014).

Among those approaches, FTIR method has been applied to determine the ionic species in solid (Abdul Rahaman et al., 2014; Arof et al., 2013), gel (Arof et al., 2013; Petrowsky and Frech, 2008) and liquid (Ericson et al., 2000) electrolytes. Based on this method, the percentage of each ionic species (i.e. free ions, contact ion pairs and ion aggregates) can be estimated following the equations (Abdul Rahaman et al., 2014; Arof et al., 2013),

$$\text{Ionic species (\%)} = \frac{A_{\text{ionic species}}}{A_{\text{total}}} \times 100\% \quad (2.6)$$

or

$$Free\ ions\ (\%) = \frac{A_f}{(A_f + A_p + A_a)} \times 100\% \quad (2.7)$$

Here, A_f is the area under the peak denoting the free ions region, A_p is the area under the peak denoting the ion pairs (contact ions) region, and A_a is the area under the peak denoting the aggregated ions region. From the percentage variation of ionic species with the respect to the salt/plasticizer concentration obtained from the FTIR deconvolution, the transport parameters (i.e. n , μ , and D) can be calculated using equations (Abdul Rahaman et al., 2014; Arof et al., 2014),

$$n = \left(\frac{M \times N_A}{V_{total}} \right) \times Free\ ions\ (\%) \quad (2.8)$$

$$\mu = \frac{\sigma}{ne} \quad (2.9)$$

$$D = \frac{\mu k_b T}{e} \quad (2.10)$$

From the above equations, M is the number of moles of salt used in each electrolyte, N_A is the Avogadro's number ($6.02 \times 10^{23} \text{ mol}^{-1}$), V_{total} is the total volume of the SPE, σ is the DC ionic conductivity, e is the electric charge ($1.60 \times 10^{-19} \text{ C}$), k_b is the Boltzmann's constant ($1.38 \times 10^{-23} \text{ JK}^{-1}$) and T is the absolute temperature.

Ionic transference number

Another important characteristic of SPE is the ionic transference (transport) number. It is essential to identify the type of charge carrier in the SPE as either ions or electrons. In solid electrolytes, the total conductivity (σ_{tot}) is the sum of the ionic, (σ_{ion}) and electronic contributions (σ_{ele}) (Subba Reddy et al., 2003; Gray, 1991),

$$\sigma_{tot} = \sigma_{ion} + \sigma_{ele} \quad (2.11)$$

The Γ_{ion} quantitatively estimates the ionic contribution to the total of conductivity.

The fraction of conductivity due to ions or electrons can be expressed as

$$\Gamma_{ion} = \frac{\sigma_{ion}}{\sigma_{tot}} = \frac{I_{ion}}{I_{tot}} \quad (2.12)$$

$$\Gamma_{ele} = \frac{\sigma_{ele}}{\sigma_{tot}} = \frac{I_{ele}}{I_{tot}} \quad (2.13)$$

where I_{tot} is the total current, I_{ion} and I_{ele} are the partial currents carried by ionic and electronic contributions, respectively. In a pure ionic conductor, $\Gamma_{ion} = 1$, whereas a pure electronic conductor, $\Gamma_{ele} = 1$. However, for a mixed system, the Γ_{ion} varies between 0 and 1. Ideally, the value of Γ_{ion} should be unity for practical application in electrochemical devices which is almost impossible to obtain in SPEs. However, several works have been reported with the Γ_{ion} approximately close to unity. According to Agrawal and Pandey (2008), the performance of the electrolytes depends on the cationic transference number which is one of the crucial characteristics of SPEs. The relation of ionic conductivity and the ionic transference number has been described by Dias et al. (2000). The maximum power achieved in a battery can be associated to the ionic conductivity gained by the electrolyte, whereas, the maximum limiting current that can be acquired from the battery and the battery cycle ability can be related to the Γ_{ion} .

The Γ_{ion} can be directly measured via DC polarization technique by monitoring the polarization current as a function of time (Gray, 1991). The charge carrier species

as either cation or anion can also be determined using this technique. Other alternative techniques used to determine the Γ_{ion} includes Hittorf (Tubandt), NMR and radio tracer, concentration cell, AC impedance (electrochemical) and combination of AC/DC impedance techniques (Srivastava and Chandra, 2000; Olsen et al., 1995; Bruce et al., 1992).

The Γ_{ion} and Γ_{ele} can be calculated using the following equations,

$$\Gamma_{ion} = \frac{I_i - I_f}{I_i} \quad (2.14)$$

$$\Gamma_{ele} = \frac{I_f}{I_i} = 1 - \Gamma_{ion} \quad (2.15)$$

where, I_i is the initial current and I_f is the final residual current. In order to identify the species of the charge carrier in SPE system, the diffusion coefficient and mobility of cation and anion can be determined according to the relations (Ng et al., 2014; Park et al., 2010),

$$\mu = \mu_+ + \mu_- = \frac{\sigma}{ne} \quad (2.16)$$

$$D = D_+ + D_- = \frac{k_b T \sigma}{ne^2} \quad (2.17)$$

$$\Gamma_{ion} = \frac{\mu_+}{\mu_+ + \mu_-} = \frac{D_+}{D_+ + D_-} \quad (2.18)$$

where μ_+ is the diffusion coefficient of cation, μ_- is the diffusion coefficient of anion, D_+ is the mobility of cation and D_- is the mobility of anion.

Hopping mechanism

Ionic conduction mechanism of SPEs can be determined by applying Universal Power Law or also known as Universal Dielectric Response as originally proposed by Jonscher (1996, 1977) which describes the AC response of various different types of disordered solid materials (Dyre and Schröder, 2009; Psarras, 2006). The law stated that at the constant temperature, the total AC conductivity, $\sigma(\omega)$ is the sum of the frequency independent DC conductivity (σ_{DC}) and the AC conductivity (σ_{AC}), where σ_{DC} is the $\omega \rightarrow 0$ limiting value of $\sigma_{DC}(\omega)$.

$$\sigma(\omega) = \sigma_{DC}(\omega) + \sigma_{AC}(\omega) \quad (2.19)$$

The σ_{AC} is obtained via relation

$$\sigma_{AC} = A \omega^s \quad (2.20)$$

and also can be expressed as

$$\sigma_{AC} = \varepsilon_0 \varepsilon_i \omega \quad (2.21)$$

by substituting $\varepsilon_i = \varepsilon_r \tan \delta$. Here, A is the pre-exponential factor/temperature dependent parameter, s is the power law exponent (temperature dependent exponent), $\omega = 2\pi f$ is the angular frequency, ε_i is the dielectric loss and ε_0 is the permittivity of free space = $8.85 \times 10^{-12} \text{ Fm}^{-1}$. According to the law, the value of s is in the range of ($0 < s < 1$) (Ramesh et al., 2011) and this behaviour is correlated to the hopping of ions. Kumar et al. (2012c) stated that for good ion conductors, s is supposed to be ≈ 0.5 . The value of $s \approx 1$ can be described as long range hopping and the value of s less than that is explained as increasing tortuous path for ion-conduction. In addition,

the jump relaxation model (Funke, 1997) ascribes the power exponent s via the relation

$$s = (\text{back hop rate})/(\text{site relaxation time}) \quad (2.22)$$

If $s < 1$, the backward hopping is slower than the site relaxation, thus results in the translational motion of the charge carrier. It also due to the formation of free sites for charge carrier transport (Ravi et al., 2013). Given in Equation 2.19 - 2.21, the value of s can be estimated from the slope of the following relations.

$$\text{Ln } \sigma_{AC} = \text{Ln} A + (s) \text{Ln} \omega \quad (2.23)$$

$$\text{or } \text{Ln } \frac{\varepsilon_i}{\varepsilon_0} = \text{Ln} \frac{A}{\varepsilon_0} + (s-1) \text{Ln} \omega \quad (2.24)$$

To correlate the temperature dependence of s behaviour with the ionic conduction behaviour in polymer electrolyte systems, four (4) well-known theoretical hopping/tunneling models have been proposed (Ondo-Ndong et al., 2003; Chakraborty et al., 1997) and employed by several authors. In the small polaron hopping (SPH) model, the power exponent s is temperature dependent, where s increases with the increasing of temperature (Samsudin and Isa, 2012b; Chai and Isa, 2012). Correlated barrier hopping (CBH) model is the reverse to the SPH model where s in the range of 0.7 to 1.0 decreases with the increasing of temperature (Shukur et al., 2013c; Buraidah et al., 2009). In the quantum mechanical tunneling (QMT) model, the exponent s is independent of temperature and almost equal to 0.8 (Kamarudin et al., 2015; Samsudin and Isa, 2015; Shukur et al., 2013b). The exponent s is temperature dependent according to overlapping large polaron tunneling (OLPT) model. In the OLPT model, s declines to a minimum value and raises again as temperature increases (Deraman et al., 2013; Ravi et al., 2013).

2.3 Solid-state electrochemical cell

To investigate the potential of SPEs to be employed in the solid-state electrochemical cells (i.e. proton batteries), the fundamental theories and basic characteristics of a battery is briefly elucidated.

2.3.1 Fundamental theories of battery

A battery is an electrochemical device, which converts stored chemical energy directly to electrical energy in a process called electrochemical reactions. Battery can be classified into two types; primary and secondary. For the primary (single-use or non-rechargeable) battery, electrode materials undergo irreversible chemical reactions and disposed or discarded once used, whereas secondary (rechargeable) battery undergo reversible reactions and can be used repeatedly upon being recharged. A battery generally consists of three main components; a conductive electrolyte and two electrodes namely cathode (positive terminal) and anode (negative terminal). During the battery operation, the anode undergoes an oxidation reaction, while the cathode undergoes a reduction reaction by accepting the electrons released at the anode through the external circuit. The electrolyte acts as a medium for the transfer of charge between the anode and cathode in the form of ions inside the cell (Schwartz, 2009). Figure 2.5 shows a diagram of secondary solid-state electrochemical cell.

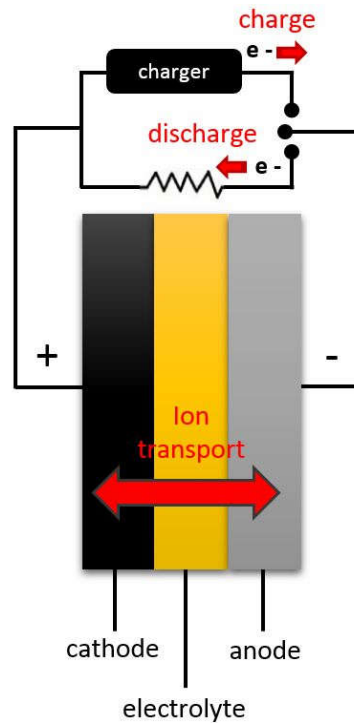


Figure 2.5 A diagram of the secondary solid-state electrochemical cell.

According to Pratap et al., (2006), the capability of an anode to supply or inject H^+ ions into the battery electrolyte, a proton conducting electrolyte and a reversible cathode is an essential criteria for a successful proton battery. Most of the secondary (rechargeable) proton batteries were fabricated by applying Zn metal and $ZnSO_4 \cdot 7H_2O$ as the anode electrode, whereas MnO_2 as the cathode electrode (Samsudin et al., 2014c; Ng and Mohamed, 2008; Bansod et al., 2007; Pandey et al., 1998). Theoretically, the chemical reactions that possibly occurred in a proton battery using Zn and $ZnSO_4 \cdot 7H_2O$ as anode, and MnO_2 as cathode electrodes can be described as follows (Alias et al., 2014; Shukur et al., 2013b; Botte and Muthuvel, 2012; Ng and Mohamad, 2008; Ali et al., 1998):

At the negative (anode) electrode, Zn was oxidized with the release of two electrons, and $ZnSO_4 \cdot 7H_2O$ provided the H^+ ions:



At the positive (cathode) electrode, MnO_2 was reduced with the acceptance of electrons:



Thus, the overall proton battery reactions was calculated based on the standard electrode potential and expressed as follows:

$$E_{\text{cell}}^{\circ} = E_{\text{red}}^{\circ} - E_{\text{ox}}^{\circ} = 1.22 - (0.76 + (-0.82)) = 1.28\text{V} \quad (2.28)$$

2.3.2 Battery characteristics

The battery performance is characterized by several electrochemical factors which involves the materials that built-up the battery components and the engineering required in designing and fabricating the battery. Open-circuit voltage (OCV) is one of the prominent of battery performance. OCV is performed to verify the self-discharge over the time. The self-discharge in secondary batteries is usually a result of decomposition of the cell due to water, electrode material solubility or reaction with the electrolyte (Gray, 1991). Hence, the total standard electrode potential, E_{cell}° gives the estimation voltage value of a cell to that of the OCV value.

The capacity, Q (Ah) of a battery can be defined as the amount of charge available or the number of electrons, n involved in the reaction as explained by

$$Q = It = nFN_m \quad (2.29)$$

where I , t , F and N_m are the current, time, Faraday constant and the number of moles of the anode and cathode materials, respectively. The specific capacity is the capacity delivered by the mass or area of electrode materials, and can be expressed as Ah/g or Ah/cm².

The cycle life (cycle number) of a battery is the number of times it can be charged and discharged repeatedly before the cell capacity falls below a limiting value around 80% of the nominal capacity. It gives information on the charge-discharge stability (rechargeability) of the cell over the time. The cycle life relies on several factors such as the reversible characteristics (structural and chemical stability) of the electrode materials, cell engineering and operating conditions (i.e. temperature, current density and depth of the discharge). For rechargeable solid-state proton battery, the number of cycles was reported to be lower than the lithium-ion battery (Dias et al., 2000). Pratap et al (2006) and Pandey et al. (1998) reported rechargeability of solid-state proton battery over 9 - 10 cycles and 20 - 30 cycles, respectively. This is due to the energy density of Li-ion battery is higher than in proton battery. Thus, proton batteries have a tendency to be applied in low energy density applications.

CHAPTER 3

METHODOLOGY

This chapter explains the methodology and characterization techniques employed in this research. The research mainly concerns to prepare SPE films and employ it into the development of rechargeable proton battery. The research was conducted in the Postgraduate Research Laboratory (Physics), School of Fundamental Science, Material Physics Laboratory, School of Ocean Engineering and Central Laboratory of Universiti Malaysia Terengganu. Solution casting technique was selected to be used in the preparation of SPE films due to the ease of preparation, simple, well-established technique and was proven to produce films with good structure and mechanically stable.

3.1 Method of research

The research was divided into four (4) main phases as shown in Figure 3.1. This includes; (I) preparation of solid polymer electrolytes, (II) characterization of solid polymer electrolytes, (III) fabrication of battery, and (IV) characterization of battery.

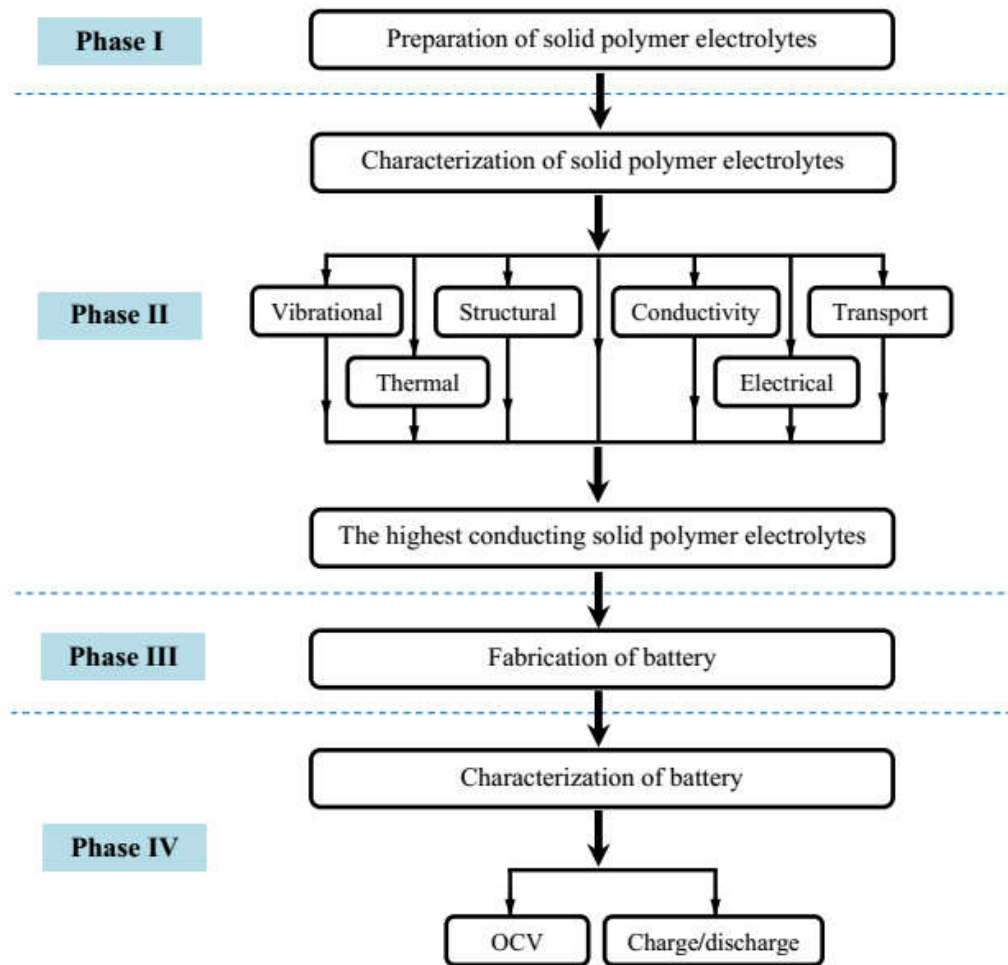


Figure 3.1 Flow chart of research methodology.

3.2 Phase I: Preparation of solid polymer electrolytes

The sodium salt of CMC was procured from Acros Organics (purity >99.9%; average M.W. = 90,000 and D.S. = 0.7), and both NH_4NO_3 (purity 99%) and EG (purity 99%) were purchased from Sigma Aldrich. All materials were directly used without further treatment. CMC, NH_4NO_3 and EG are water-soluble. The SPE films having three (3) different systems were prepared via classical/conventional solution casting technique according to the procedures below:

- i. *Single polymer:* Pure CMC film was prepared to act as a control. In a clean glass beaker, 2.0 g of CMC powder was dissolved in 75 ml distilled water. Complete dissolution was achieved after several hours using a magnetic stirrer on a plate stirrer at room temperature. The final clear CMC solution was then poured into Petri dishes and left to dry at room temperature to form a highly translucent and flexible film.
- ii. *System I (CMC-NH₄NO₃ system):* A set of SPE films were prepared with varied amount of NH₄NO₃ concentration. To the CMC solution in (i), NH₄NO₃ was added in varying ratios to prepare the polymer-salt system. The CMC-NH₄NO₃ mixture solution was magnetically stirred for several hours under mild stirring until a clear and homogenous solution resulted. The final clear solution was then casted into Petri dishes and left to dry at room temperature to form a highly translucent and flexible film. Ten (10) SPE films were produced in these conditions corresponding to CMC and NH₄NO₃ in different weight ratios (5 - 50 wt.% NH₄NO₃).
- iii. *System II (CMC-NH₄NO₃-EG system):* A set of plasticized SPE films were prepared following the procedures to prepare the most conductive SPE film (45 wt.% NH₄NO₃) in (ii). To the CMC-NH₄NO₃ solution containing 55 wt.% CMC and 45 wt.% NH₄NO₃, EG plasticizer was syringed and dropwised in varying ratios to produce polymer-salt-plasticizer system. This CMC-NH₄NO₃-EG mixture solution was magnetically stirred for several hours at room temperature until the solutions completely dissolved. The final clear solutions were then casted into Petri dishes and left to dry at room temperature to form translucent films. Eight (8) SPE films were carried out in these

conditions corresponding to CMC-NH₄NO₃ and EG in different weight ratios (5 - 40 wt.% EG).

The final SPE films were then kept in a dessicator filled with silica gel desiccants for a week for further drying to remove any traces of water (moisture) before films characterization. Table 3.1 and Table 3.2 show the designation and composition of materials used in preparation of single polymer, System I and System II films.

Table 3.1 The designation and NH₄NO₃ concentration of pure CMC film and System I films.
*Calculation to obtain weight percentage of NH₄NO₃ concentration.

| Designation | NH ₄ NO ₃ concentration | |
|---|---|--------------|
| | (wt.%) * | (± 0.0001 g) |
| Pure CMC | 0 | 0.0000 |
| 5 wt.% NH ₄ NO ₃ | 5 | 0.1053 |
| 10 wt.% NH ₄ NO ₃ | 10 | 0.2222 |
| 15 wt.% NH ₄ NO ₃ | 15 | 0.3529 |
| 20 wt.% NH ₄ NO ₃ | 20 | 0.5000 |
| 25 wt.% NH ₄ NO ₃ | 25 | 0.6667 |
| 30 wt.% NH ₄ NO ₃ | 30 | 0.8571 |
| 35 wt.% NH ₄ NO ₃ | 35 | 1.0769 |
| 40 wt.% NH ₄ NO ₃ | 40 | 1.3333 |
| 45 wt.% NH ₄ NO ₃ | 45 | 1.6363 |
| 50 wt.% NH ₄ NO ₃ | 50 | 2.0000 |

$$* \text{NH}_4\text{NO}_3 \text{ concentration (wt. \%)} = [\text{NH}_4\text{NO}_3 \text{ (g)} / (\text{CMC (g)} + \text{NH}_4\text{NO}_3 \text{ (g)})] \times 100\%$$

Table 3.2 The designation and EG concentration of System II films.
**Calculation to obtain weight percentage of EG concentration.

| Designation | EG concentration | |
|-------------|------------------|-------------|
| | (wt.%) ** | (± 0.01 ml) |
| 5 wt.% EG | 5 | 0.20 |
| 10 wt.% EG | 10 | 0.36 |
| 15 wt.% EG | 15 | 0.65 |
| 20 wt.% EG | 20 | 0.81 |
| 25 wt.% EG | 25 | 1.22 |
| 30 wt.% EG | 30 | 1.39 |
| 35 wt.% EG | 35 | 1.97 |
| 40 wt.% EG | 40 | 2.16 |

$$** \text{EG concentration (wt. \%)} = [\text{EG (g)} / (\text{CMC (g)} + \text{NH}_4\text{NO}_3 \text{ (g)} + \text{EG (g)})] \times 100\%$$

3.3 Phase II: Characterization of solid polymer electrolytes

Several techniques have been applied to characterize the prepared SPE films, namely X-ray diffraction, Fourier transform infrared spectroscopy, thermogravimetric analyzer, electrical impedance spectroscopy, transference number measurement and potentiostat-galvanostat.

3.3.1 Fourier transform infrared spectroscopy

Fourier transform infrared (FTIR) spectra were recorded using Thermo Nicolet 380 FTIR spectrometer equipped with an attenuated total reflection (ATR) accessory with a germanium crystal as shown in Figure 3.2. The SPE film was placed on germanium crystal and infrared light was passed through the sample with the frequency ranging from 700 – 4000 cm^{-1} and spectra resolution of 4 cm^{-1} . The FTIR data were recorded in the transmittance mode.

The FTIR technique is important to investigate SPEs structure, as it renders information on chemical bonding such as complexation and interactions between various elements in the SPE system. This technique also provides information on the fraction of ionic species (%) and transport properties of SPEs by deconvoluting selected FTIR peaks and has been detailed in Chapter 4 and Chapter 5, respectively. The procedure implies estimating the approximate peak positions of the component bands determined using second-order derivatives. The deconvolution analysis of FTIR spectra was performed based on the Gaussian-Lorentz function using non-linear least squares fitting OriginPro 8.0 software.

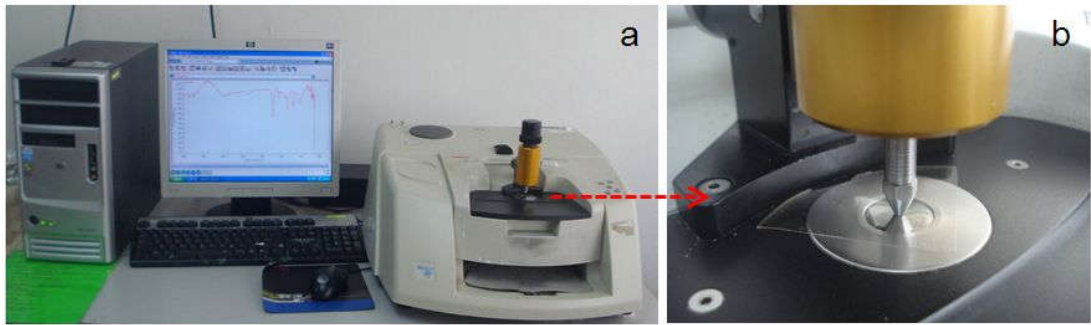


Figure 3.2 (a) The FTIR spectrometer used in this study and (b) the enlargement of SPE film position during measurement.

3.3.2 X-ray diffraction

X-ray diffraction (XRD) technique was performed on rectangular specimens (area = $2 \times 2 \text{ cm}^2$) using a MiniFlex II Rigaku (Figure 3.3) with CuK_α radiation (wavelength, $\lambda = 1.542 \text{ \AA}$) and operated at an acceleration voltage of 40 kV. The room temperature XRD patterns were recorded at Bragg angle, $2\theta = 10^\circ - 60^\circ$ with a scan speed of $2^\circ/\text{min}$. This technique was employed to investigate the amorphousity of SPE films.



Figure 3.3 The MiniFlex II Rigaku X-ray diffraction spectrometer used in this study.

In addition, Debye-Scherrer equation was used to estimated the crystallite size, L of SPE films (Monshi et al., 2012; Bushroa, 2012; Akbari, 2012),

$$L (\text{\AA}) = \frac{k \lambda}{\beta \cos \theta} \quad (3.1)$$

where k is the Scherrer constant = 0.9 and β is the full-width half maximum (FWHM) in degrees.

3.3.3 Thermogravimetric analyzer

Thermal stability of SPE films in a nitrogen atmosphere were carried out using a METTLER TOLEDO Thermogravimetric analyzer (TGA) which comprised of TGA/SDTA851^e as the main unit as shown in Figure 3.4. The TGA-DTG plots have been displayed using STARe software. SPE films weighing ~10 mg were loaded in an aluminium crucible pan and heated from room temperature to 400°C at a heating rate of 10°C/min under nitrogen flow rate of 30 ml/min.



Figure 3.4 The thermogravimetric analyzer used in this study.

3.3.4 Electrical impedance spectroscopy

Impedance measurements were performed to determine the ionic conductivity of SPE films over a wide range of frequency. The measurements were carried out with an electrical impedance spectroscopy (EIS) HIOKI 3532–50 LCR Hi Tester (Figure 3.5) interfaced to a personal computer in 50 Hz – 1M Hz frequency range and over temperature range of ambient temperature (30°C) to 80°C. A round piece of

SPE film in 2 cm diameter was pressed between two stainless steel (SS) electrodes of sample holder and placed in a temperature controlled MEMMERT oven.



Figure 3.5 The EIS (HIOKI 3532–50 LCR Hi Tester) equipped with a MEMMERT oven and interfaced to a personal computer.

The thickness of SPE films were measured using a digital micrometer. The Nyquist plots automatically display in the Microsoft Excel file format after each measurement using LCR sample program version 4.03E software. The impedance measurement on each SPE film was recorded in triplicate. The measured impedance data were used to calculate the real, Z_r and imaginary, Z_i parts of the impedances. The ionic conductivity of SPE films was considered from the average of ionic conductivity values obtained and calculated based on Equation 2.3.

The values of dielectric constant (ϵ_r) and dielectric loss (ϵ_i) can be estimated using relations (Rani et al., 2015a),

$$\epsilon_r = \frac{Z_i}{\omega C_0 (Z_r^2 + Z_i^2)} \quad (3.2)$$

$$\epsilon_i = \frac{Z_r}{\omega C_0 (Z_r^2 + Z_i^2)} \quad (3.3)$$

where $\omega = 2\pi f$ = angular frequency, $C_0 = \varepsilon_0 A/t$ = the capacitance of empty measuring cell of electrode area A and sample thickness t , and ε_0 = permittivity of free space = $8.85 \times 10^{-12} \text{ Fm}^{-1}$. The relation of the real (M_r) and imaginary (M_i) parts of electrical modulus is given by (Rani et al., 2015a),

$$M_r = \frac{\varepsilon_r}{(\varepsilon_r^2 + \varepsilon_i^2)} \quad (3.4)$$

$$M_i = \frac{\varepsilon_i}{(\varepsilon_r^2 + \varepsilon_i^2)} \quad (3.5)$$

The relaxation time, τ can be calculated from the frequency of maximum relaxation peak, f_m according to relation (Woo et al., 2012),

$$\omega \cdot \tau = (2\pi f_m) \cdot \tau = 1 \quad (3.6)$$

3.3.5 Transference number measurement

Transference number measurement (TNM) was carried out using DC polarization technique by monitoring the polarization current as a function of time at room temperature as shown in Figure 3.6. The current decays gradually with the time and approaches steady state (saturated). This technique was employed by sandwiching SPE film between two stainless steel (SS) blocking electrodes connected to a fixed DC voltage source and True RMS Multimeter UT803 RS232 in the configuration cell of SS/SPE film/SS. The plot of current over time was recorded using UT803 interface program version 1.10 software. The measurement was performed to obtain the transference (transport) numbers of the majority of charge carrier by correlating the diffusion phenomena to the conductivity behaviour of the SPE film (Gray, 1991).

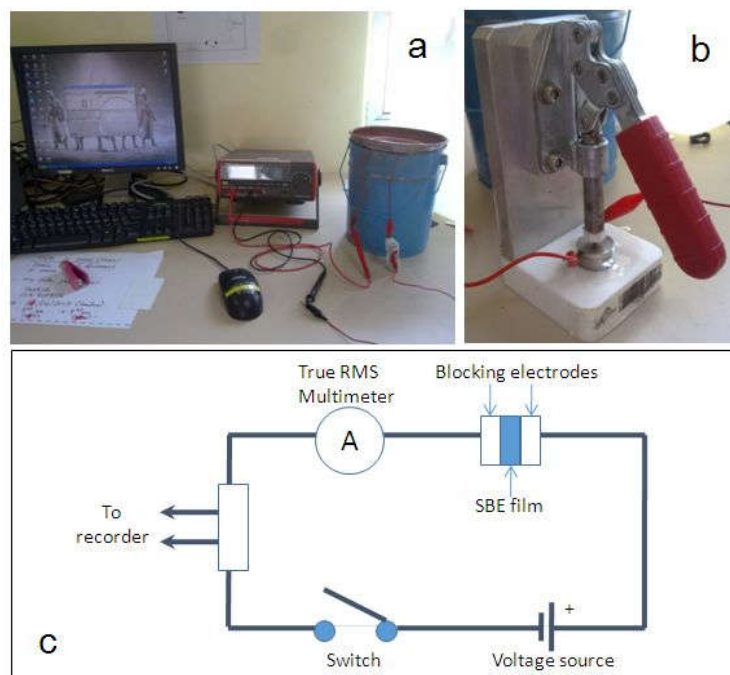


Figure 3.6 (a) The experimental arrangement of TNM apparatus, (b) the illustration of a SPE film sandwiched between two blocking electrodes inside the blue pail, and (c) the block diagram of the experimental arrangement in Figure 3.7(a).

3.3.6 Potentiostat-galvanostat

To study the potential of SPE film for electrochemical device application, linear sweep voltammetry (LSV) was employed. This technique measures the electrochemical window stability of SPE films using potentiostat-galvanostat Autolab PGSTAT302 (Eco Chemie, Netherlands) at room temperature (Figure 3.7).

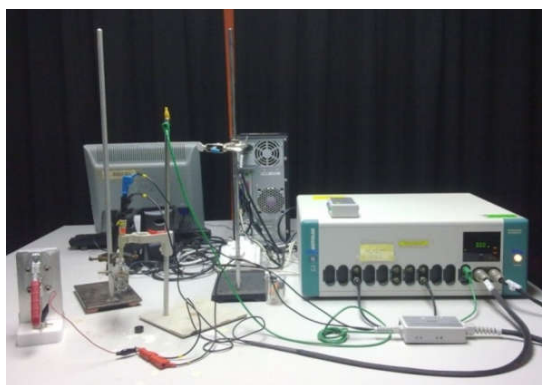


Figure 3.7 The potentiostat-galvanostat Autolab PGSTAT302.

The measurements were carried out at a scan rate of 1.0 mV/s in a potential range of 0 - 3 V. The SPE films were cut into a suitable size (diameter = 2.0 cm) and sandwiched between stainless steel electrodes and MnO_2 , which served as working electrode (WE) and counter electrode (CE), respectively. Plot of current versus voltage has been revealed using GPES program software.

3.4 Phase III: Fabrication of battery

Fabrication of a battery involves the preparation of electrodes (anode and cathode) and battery assembly. The cathode and anode were prepared according to the method proposed by Isa (2005) and weighted using an electronic balance. There are two (2) type of battery configurations have been used to prepare coin cell-type rechargeable solid-state proton batteries using the highest conducting SPE films for System I and System II:

Cell I - Anode/ SPE film containing 45 wt.% NH_4NO_3 /Cathode

Cell II - Anode/ SPE film containing 20 wt.% EG/Cathode

3.4.1 Preparation of electrodes

The cathode electrode was prepared by mixing manganese oxide, MnO_2 (Sigma Aldrich) as active material, Super-P carbon black (Kuraray Chemical Co.), poly(vinylidene) fluoride, PVDF (Sigma Aldrich) as binder, and dibutyl phthalate, DBP (Sigma Aldrich) as additive at a weight ratio of 65:7:10:18 in acetone for 24 hours. The mixture was stirred until homogenous cathode slurry was obtained. The cathode slurry was then cast uniformly on a piece of flat glass using a Biuge film applicator (Doctor blade or tape casting technique was used to obtain a uniform and adherent thin slurry layer with a controlled thickness) and left to dry before soaked in methanol solution to remove DBP. Prior to dry, the cathode electrode was hot pressed on both sides of the as-treated aluminium mesh (current collector) to ensure a good electrode-grid surface contact.

For anode electrode preparation, zinc metal (Merck), zinc sulfate heptahydrate, $\text{Zn.SO}_4.7\text{H}_2\text{O}$ (Merck), Super-P carbon black, PVDF and DBP at a weight ratio of 55:10:3:10:22 were mixed in acetone for 24 hours. Copper mesh was used as current collector. The later steps follow the procedures to prepare cathode electrode. Figure 3.8 illustrates the preparation of electrodes for solid-state rechargeable proton battery.

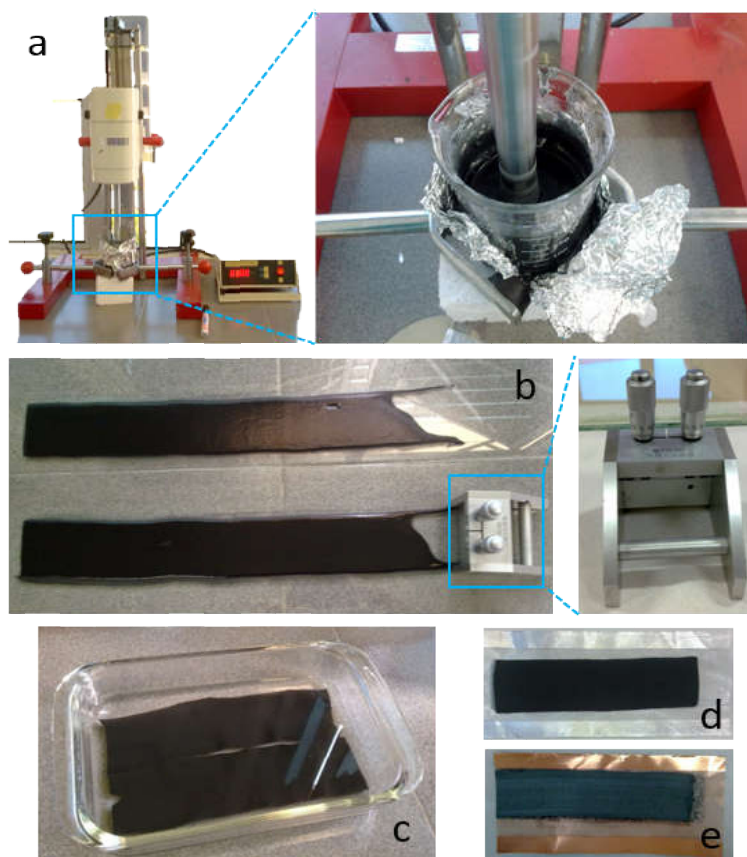


Figure 3.8 The preparation of electrodes. (a) A stand mixer was used to mix electrode slurry, (b) electrode slurry was cast on a flat glass using a Biuge film applicator, (c) dried electrodes were soaked and rinsed in methanol to remove DBP, and dried electrodes were then hot pressed on treated Al mesh for cathode (d) and Cu grid for anode (e).

3.4.2 Battery assembly

Cell assembly includes stacking/pressing anode, SPE film and cathode in a CR2032 coin cell casing and crimped to produce a complete rechargeable battery. Coin cell-type rechargeable proton batteries are tested for electrochemical performance based on open-circuit voltage and charge-discharge characteristics. Figure 3.9 shows the arrangement of components inside a rechargeable proton battery. Several cells were assembled for the purpose of different measurements to ensure reproducibility.

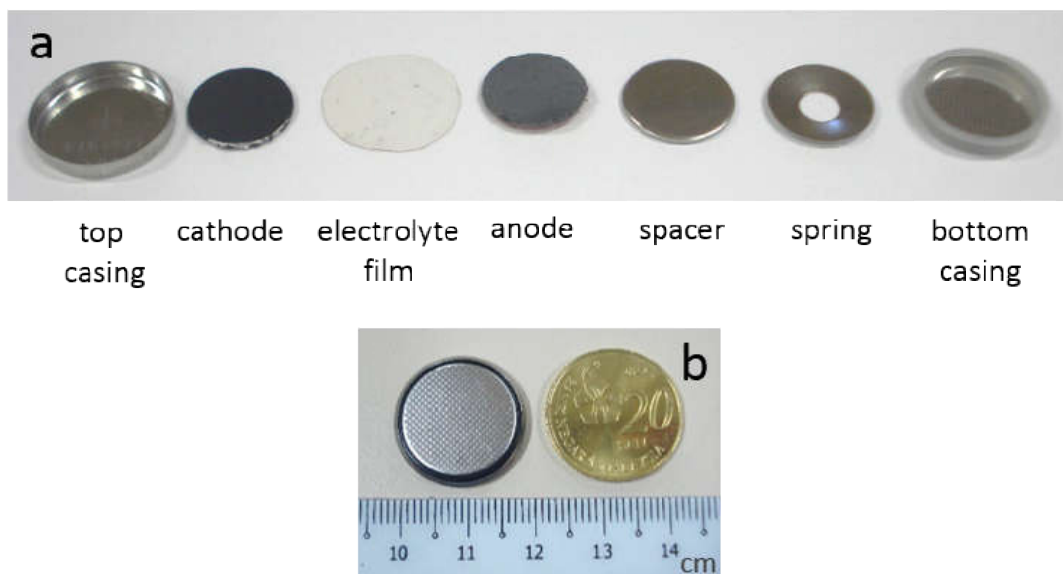


Figure 3.9 (a) The arrangement of components inside a coin cell-type rechargeable proton battery and (b) the actual size of that completely assembled battery.

3.5 Phase IV: Characterization of battery

Electrochemical characterization was performed to investigate the performance of proton batteries which involves open-circuit voltage (OCV) and charge/discharge characteristics. OCV was recorded using UT803 RMS multimeter attached to a personal computer performed at zero current for 24 hours measurement (Figure 3.10). Charge/discharge characteristics were carried out using a NEWARE high accuracy battery tester (Figure 3.11) at different constant input currents (i.e. 0.02 mA, 0.04 mA and 0.06 mA) within 50 cycles measured at room temperature.



Figure 3.10 Experimental set up for OCV test.

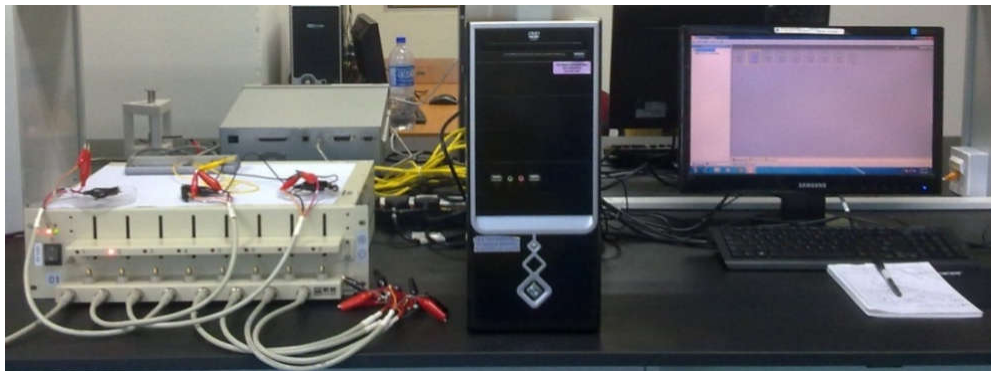


Figure 3.11 Experimental set up for charge/discharge characteristics using NEWARE high accuracy battery tester.

The cell capacity, Q was calculated using Equation 2.29, whereas energy density, E and power density, P of the cell were estimated using the following equations,

$$E = QV = ItV \quad (3.7)$$

$$P = \frac{E}{t} = IV \quad (3.8)$$

Here, t is the discharge time, V is the voltage and I is the current of the cell.

CHAPTER 4

VIBRATIONAL, STRUCTURAL AND THERMAL PROPERTIES OF SOLID POLYMER ELECTROLYTES

This chapter is concerned with the effect of the addition of NH_4NO_3 salt and EG plasticizer to the vibrational, structural and thermal properties of solid biopolymer electrolyte films. These properties are important to determine the ionic conductivity, electrical and transport behaviours of SPEs which is described in Chapter 5. Several techniques have been conducted to achieve the goal of the studies including FTIR, XRD and TGA. The solvent-free SPE films were prepared by solution casting technique at room temperature as described in Section 3.2 of Chapter 3.

4.1 Physical appearance of solid polymer electrolytes

Figure 4.1 shows a highly translucent and flexible SPE films obtained at room temperature. The thickness of SPE films was observed to increase with the addition of NH_4NO_3 salt and EG, where System I films ranging from $50\mu\text{m}$ to $180\mu\text{m}$, and System II films ranging from $200\mu\text{m}$ to $270\mu\text{m}$. The thickness of pure CMC film is $35\mu\text{m}$.



Figure 4.1 A highly translucent and flexible SPE films obtained at room temperature.

4.2 FTIR analysis

The IR vibration technique can be utilized to investigate the possible intermolecular interactions that occur between polymer and salt, and also between polymer and plasticizer. IR spectra yield information regarding various constituents in polymer electrolytes through vibration band properties, such as intensity, bandwidth, shift of the bands, emergence of new bands or/and disappearance of band, and have been employed by numerous researchers for vibration studies in the polymer electrolyte systems. In this work, by the addition of NH_4NO_3 salt and EG plasticizer in the CMC polymer matrix, the IR-spectra are expected to show some changes in the vibration patterns.

4.2.1 Molecular interaction of CMC and NH_4NO_3 salt

In order to study the interaction between CMC and NH_4NO_3 , Figure 4.2 is plotted. This figure represents the FTIR spectra of System I between wavenumber of 1800 cm^{-1} and 800 cm^{-1} .

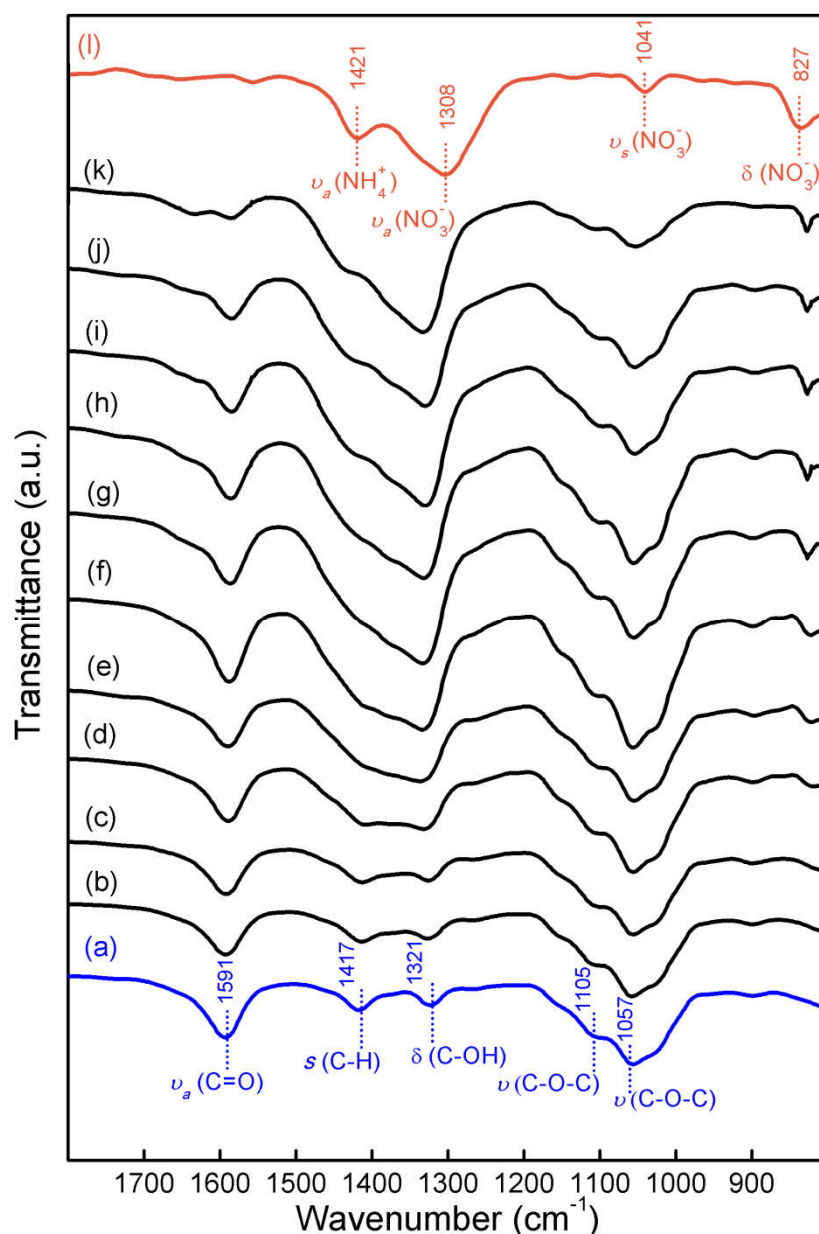


Figure 4.2 FTIR spectra of (a) pure CMC film and System I films incorporated with (b) 5 wt.% NH_4NO_3 , (c) 10 wt.% NH_4NO_3 , (d) 15 wt.% NH_4NO_3 , (e) 20 wt.% NH_4NO_3 , (f) 25 wt.% NH_4NO_3 , (g) 30 wt.% NH_4NO_3 , (h) 35 wt.% NH_4NO_3 , (i) 40 wt.% NH_4NO_3 , (j) 45 wt.% NH_4NO_3 , (k) 50 wt.% NH_4NO_3 , and (l) pure NH_4NO_3 salt.

Pure CMC shows a strong peak of asymmetric stretching mode of carboxylic group, $\nu_a(\text{C}=\text{O})$ at 1591 cm^{-1} as depicted in Figure 4.2(a). The bands located at 1417 cm^{-1} and 1321 cm^{-1} correspond to CH_2 scissoring, $\delta(\text{C}-\text{H})$ and bending mode of C-OH bonding, $\delta(\text{C}-\text{OH})$, respectively. The doubled stretching mode of C-O-C in β -

(1→4)-glucosidic and -CH₂-O-CH₂ linkage, $\nu(\text{C-O-C})$ were observed at 1105 cm⁻¹ and 1057 cm⁻¹. This result is in agreement as reported by several researchers (Sugama et al., 2015; Yadollahi et al., 2013; Mishra et al., 2012; Ibrahim et al., 2011; Bao et al., 2011; Peng et al., 2011; Pushpamalar et al., 2006).

Pure NH₄NO₃ exhibits intense vibration bands in the range of 800 - 1500 cm⁻¹ as exemplified in Figure 4.2(1). Wu et al. (2007) observed the asymmetric stretching and deformation modes of both $\nu(\text{NH}_4^+)$ and $\nu(\text{NO}_3^-)$ to appear between 1300 cm⁻¹ and 1500 cm⁻¹. Nik Aziz and Isa (2012) reported asymmetric and symmetric modes of ammonium ions, $\nu(\text{NH}_4^+)$ in the range of 1850 – 1500 cm⁻¹. In another work, Zhao et al. (2008) reported the asymmetric deformation mode of ammonium ions, $\nu(\text{NH}_4^+)$ occurs at 1470 cm⁻¹. The rest of the vibration bands from pure NH₄NO₃ at the lower wavenumber belongs to the stretching $\nu(\text{NO}_3^-)$ and bending $\delta(\text{NO}_3^-)$ modes of nitrate ions (Kadir et al., 2011; Wu et al., 2007; Majid and Arof, 2005).

CMC polymer plays as a host for ionic conduction to take place through the presence of lone pair electrons. In order to confirm the complexation occurs between $\nu_a(\text{C=O})$ of CMC and $\nu(\text{NH}_4^+)$ of NH₄NO₃, the FTIR spectra were deconvoluted in the region between 1700 cm⁻¹ and 1500 cm⁻¹ as shown in Figure 4.3. From the figure, it can be observed that upon the addition of NH₄NO₃, the $\nu_a(\text{C=O})$ band located at 1591 cm⁻¹ for pure CMC film (Figure 4.2(a)) has shown a shifting of band to the lower wavenumber. The $\nu_a(\text{C=O})$ band shifted around 10 cm⁻¹ from 1593 cm⁻¹ to 1583 cm⁻¹ with the addition of 5 - 50 wt.% NH₄NO₃.

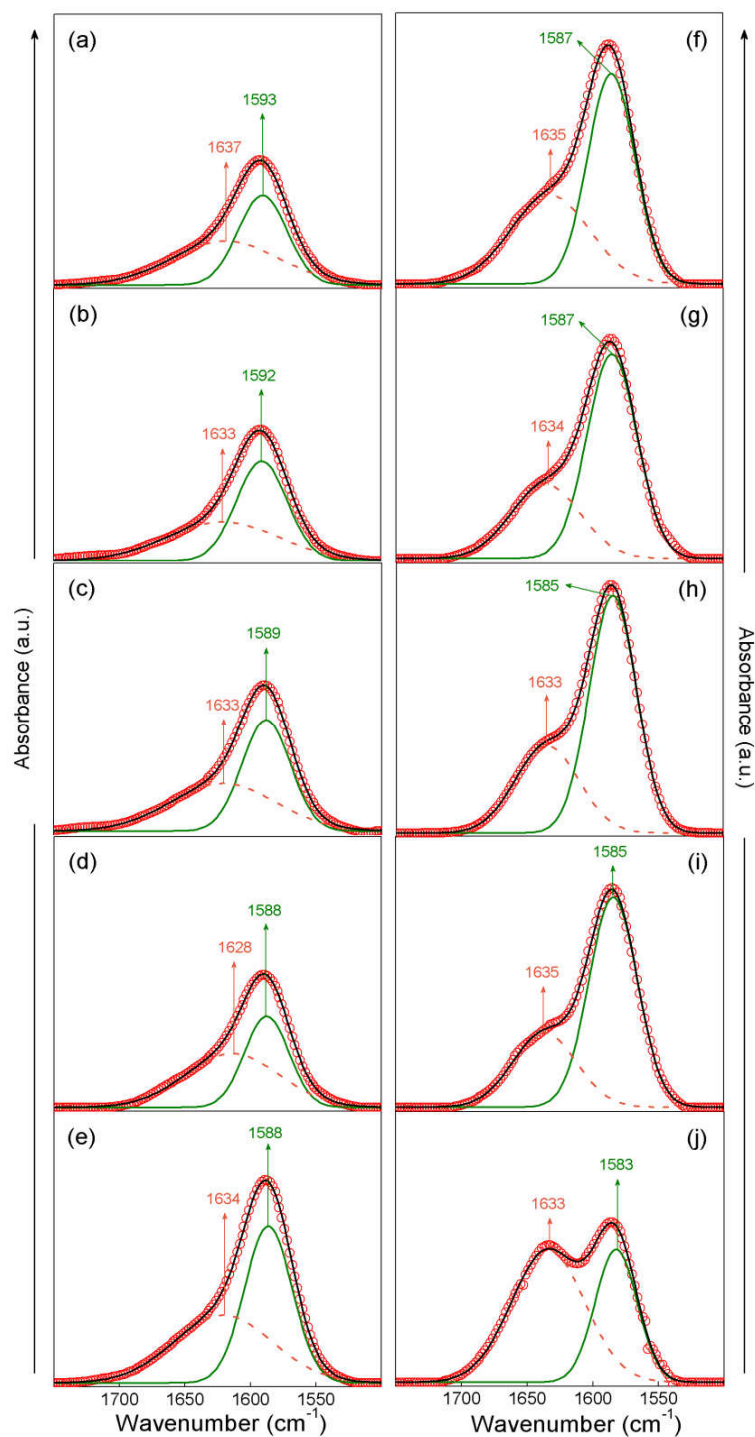


Figure 4.3 Gaussian fit for FTIR spectra between 1700 cm^{-1} and 1500 cm^{-1} for System I films incorporated with (a) (5 wt.% NH_4NO_3), (b) (10 wt.% NH_4NO_3), (c) (15 wt.% NH_4NO_3), (d) (20 wt.% NH_4NO_3), (e) (25 wt.% NH_4NO_3), (f) (30 wt.% NH_4NO_3), (g) (35 wt.% NH_4NO_3), (h) (40 wt.% NH_4NO_3), (i) (45 wt.% NH_4NO_3), and (j) (50 wt.% NH_4NO_3). *Note:* **Green** solid line - vibrational bands from CMC polymer, **orange** dash line - vibrational bands from NH_4NO_3 salt, **red** open circles - experimental data and **black** solid line - fitted sum data.

A shoulder can be seen to appear upon the addition of NH_4NO_3 in the system between $1637 - 1628 \text{ cm}^{-1}$ which belongs to $\delta(\text{NH}_4^+)$ of NH_4NO_3 salt. The $\nu(\text{NH}_4^+)$ peak becomes more obvious as more NH_4NO_3 salt was added. The growth of this intensity peak also can be clearly seen in the deconvoluted FTIR spectra. The $\nu(\text{NH}_4^+)$ band located at 1637 cm^{-1} (5 wt.% NH_4NO_3) gradually grew in intensity and almost reached the same level of intensity with the $\nu_a(\text{C=O})$ band at 1633 cm^{-1} (50 wt.% NH_4NO_3). Thus, it is suggested that more NH_4^+ ions from NH_4NO_3 salt have been supplied in the system and could have contributed to the growth of this peak. The shifting of the $\nu(\text{NH}_4^+)$ band also was discovered. The $\nu(\text{NH}_4^+)$ band at 1637 cm^{-1} (5 wt.% NH_4NO_3) has merged to 1633 cm^{-1} (10 wt.% NH_4NO_3), 1633 cm^{-1} (15 wt.% NH_4NO_3), 1628 cm^{-1} (20 wt.% NH_4NO_3), 1634 cm^{-1} (25 wt.% NH_4NO_3), 1635 cm^{-1} (30 wt.% NH_4NO_3), 1634 cm^{-1} (35 wt.% NH_4NO_3), 1633 cm^{-1} (40 wt.% NH_4NO_3) and 1635 cm^{-1} (45 wt.% NH_4NO_3). At 50 wt.% NH_4NO_3 , this band showed a slightly decline in wavenumber at 1633 cm^{-1} .

The changes in the wavenumbers and the emergence of the new band which comprised of $\nu_a(\text{C=O})$ of CMC and $\nu(\text{NH}_4^+)$ of NH_4NO_3 salt suggest that the coordination of H^+ ions has occurred at the oxygen atoms in the carbonyl group of CMC. This findings also have been discovered by other researchers (Ahmad and Isa, 2015; Shukur et al., 2013a; Samsudin et al., 2012c).

The $\nu(\text{C-O})$ stretching on polysaccharide skeletons of CMC backbone are expected to interact with the symmetric stretching mode of $\delta(\text{NO}_3^-)$ anions within $1200 - 900 \text{ cm}^{-1}$ region. In pure CMC film, only two $\nu(\text{C-O})$ peaks obviously present

within this region. The deconvolution of FTIR spectra in this region gave a better view the overlapping of FTIR bands in System I films and are depicted in Figure 4.4.

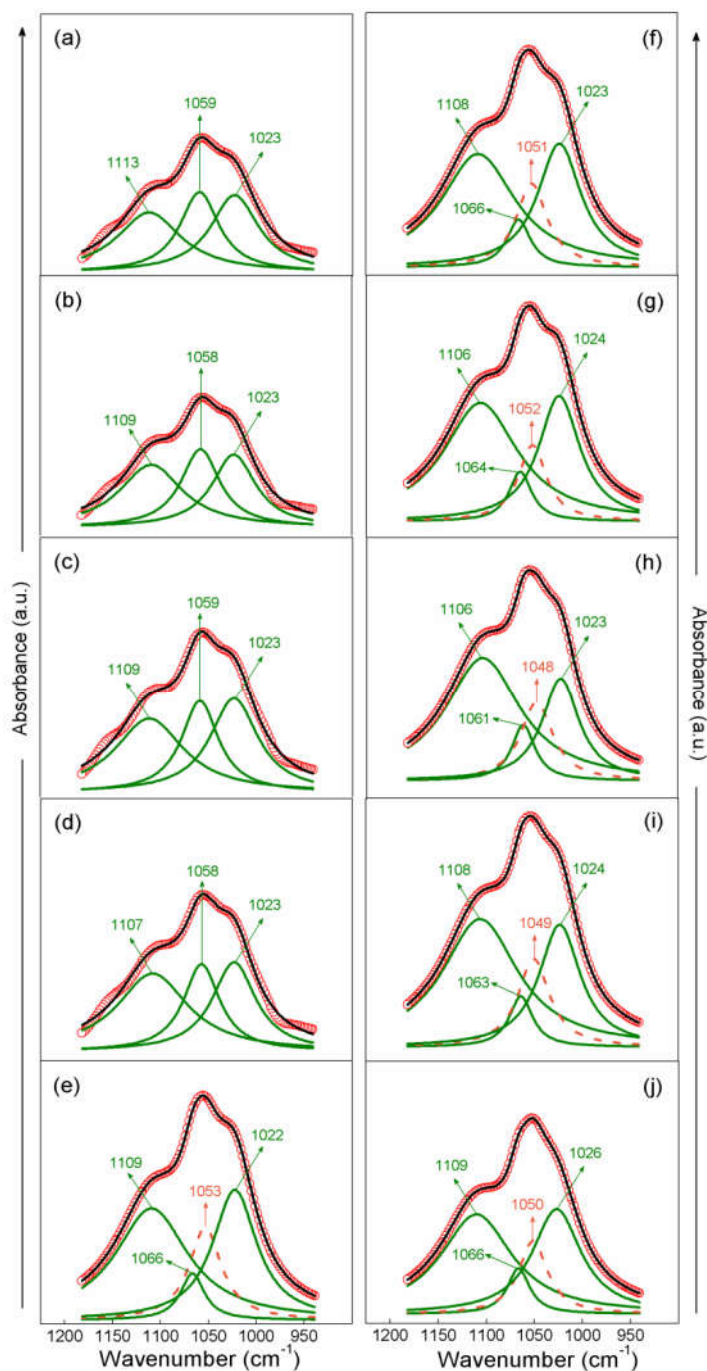


Figure 4.4 Deconvoluted FTIR spectra between 1200 cm^{-1} and 900 cm^{-1} for System I films incorporated with (a) (5 wt.% NH_4NO_3), (b) (10 wt.% NH_4NO_3), (c) (15 wt.% NH_4NO_3), (d) (20 wt.% NH_4NO_3), (e) (25 wt.% NH_4NO_3), (f) (30 wt.% NH_4NO_3), (g) (35 wt.% NH_4NO_3), (h) (40 wt.% NH_4NO_3), (i) (45 wt.% NH_4NO_3), and (j) (50 wt.% NH_4NO_3). *Note:* Green solid line - vibrational bands from CMC polymer, orange dash line - vibrational bands from NH_4NO_3 salt, red open circles - experimental data and black solid line - fitted sum data.

Three component bands of $\nu(\text{C-O})$ originated from CMC can be clearly observed in the polymer-salt complexes at $1113 - 1107 \text{ cm}^{-1}$, $1059 - 1058 \text{ cm}^{-1}$, and 1023 cm^{-1} when 5 - 20 wt.% NH_4NO_3 were added, hence no ammonium salt peak was observed. At 25 wt.% NH_4NO_3 , a small peak begins to appear. This peak was believed to be $\delta(\text{NO}_3^-)$ anions from NH_4NO_3 salt located at 1066 cm^{-1} , a slightly higher wavenumber than reported in Kadir et al. (2011), and Majid and Arof (2005) due to overlap with the $\nu(\text{C-O})$ peaks.

As more NH_4NO_3 salt was added (30 - 50 wt.% NH_4NO_3), this NO_3^- peak shows shifting in peak position ranging from $1066 - 1061 \text{ cm}^{-1}$. The C-O bands on both shoulders show less changes in peak position between $1106 - 1109 \text{ cm}^{-1}$, and $1023 - 1026 \text{ cm}^{-1}$, compared to the third C-O band (middle peak). This outweigh peak of C-O band maintained the peak intensity between $1059 - 1058 \text{ cm}^{-1}$ with the addition of 5 - 20 wt.% NH_4NO_3 . At 25 wt.% NH_4NO_3 , this peak shows a drop of peak intensity compared to the other two peaks at 1053 cm^{-1} band (Figure 4.4(e)). Increasing the amount of NH_4NO_3 salt to 50 wt.% NH_4NO_3 , the peak shows further decline in intensity with the peak position shifting in the range of $1052 - 1048 \text{ cm}^{-1}$.

At lower wavenumber between 870 cm^{-1} and 800 cm^{-1} , a new peak emerges and becomes more obvious as more NH_4NO_3 salt was added. This indicates that NH_4NO_3 salt possibly could have contributed to the growth of this peak. As illustrated in Figure 4.5, the new peak starts to emerge at 827 cm^{-1} band with the addition of 30 wt.% NH_4NO_3 (Figure 4.5(f)) and can be assigned to the symmetric bending mode of nitrate ions, $\delta(\text{NO}_3^-)$. The $\delta(\text{NO}_3^-)$ occurred at 827 cm^{-1} for pure NH_4NO_3 . The similar peak also has been detected by other authors (Kadir et al., 2011; Majid and Arof, 2005). Thus, it can be observed that with the increasing of

NH_4NO_3 salt, the intensity of $\delta(\text{NO}_3^-)$ anions peak steadily increases, hence, no shifting of peak occurs, thus implying that NO_3^- anions did not complex with the CMC in this region.

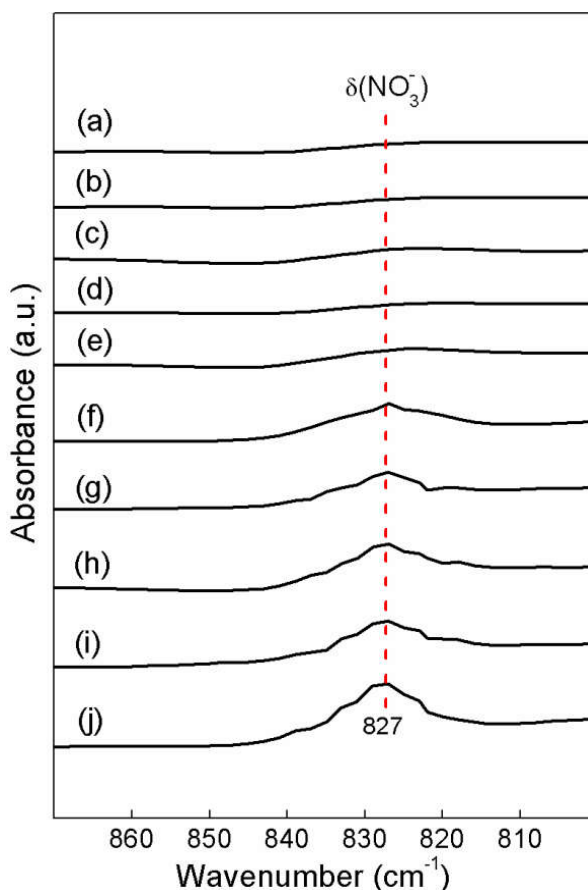


Figure 4.5 FTIR spectra within $870 - 800 \text{ cm}^{-1}$ wavenumber for System I films incorporated with (a) (5 wt.% NH_4NO_3), (b) (10 wt.% NH_4NO_3), (c) (15 wt.% NH_4NO_3), (d) (20 wt.% NH_4NO_3), (e) (25 wt.% NH_4NO_3), (f) (30 wt.% NH_4NO_3), (g) (35 wt.% NH_4NO_3), (h) (40 wt.% NH_4NO_3), (i) (45 wt.% NH_4NO_3), and (j) (50 wt.% NH_4NO_3).

4.2.2 Molecular interaction of CMC- NH_4NO_3 and EG plasticizer

In this work, System II films were subjected to the FTIR analysis with the present of EG as plasticizer. In order to determine the existence of interactions/complexes of EG-plasticized films, the FTIR spectra at various EG concentration and pure EG were plotted as shown in Figure 4.6.

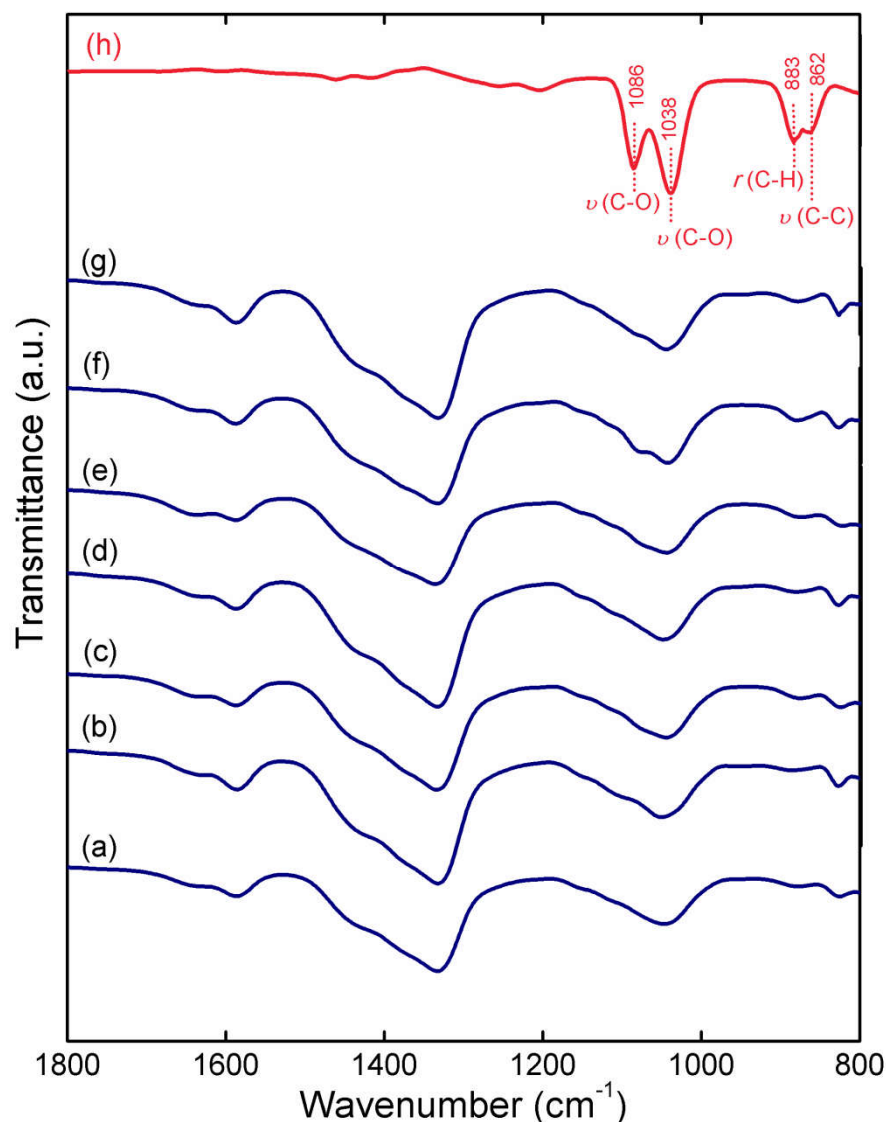


Figure 4.6 FTIR spectra of System II films incorporated with (a) 5 wt.% EG, (b) 10 wt.% EG, (c) 15 wt.% EG, (d) 20 wt.% EG, (e) 25 wt.% EG, (f) 30 wt.% EG and (g) 35 wt.% EG, and (h) pure EG plasticizer.

From the figure, the bands due to pure EG are obtained at 1086 cm^{-1} and 1038 cm^{-1} which can be assigned to twin peaks of stretching mode of the C-O band, and the bands at 883 cm^{-1} and 862 cm^{-1} correspond to CH_2 rocking mode and stretching mode of C-C bonds, respectively (Amarasinghe et al., 2014; Hudson et al., 2005; Huang et al., 1995). No obvious peaks can be detected for CH_2 twisting and wagging bands of pure EG.

The Gaussian fit for FTIR spectra of EG-added films between 1700 cm^{-1} and 1500 cm^{-1} are shown in Figure 4.7. In SPE film incorporating 5 wt.% EG, the $\nu(\text{NH}_4^+)$ of NH_4NO_3 and $\nu_a(\text{C}=\text{O})$ stretching modes were found at 1636 cm^{-1} and 1585 cm^{-1} , respectively. With the addition of 10 wt.% EG, the ammonium and carbonyl bands did not exhibit any position change which may indicate that EG did not interact either at the $\nu(\text{NH}_4^+)$ or $\nu_a(\text{C}=\text{O})$ bands.

Upon the incorporation of 20 - 35 wt.% EG, those bands are slightly shifted to higher wavenumbers. The $\nu(\text{NH}_4^+)$ band shifted from 1638 cm^{-1} to 1639 cm^{-1} , whereas the $\nu_a(\text{C}=\text{O})$ band moved from 1586 cm^{-1} to 1588 cm^{-1} . The slight upshift of $\nu(\text{NH}_4^+)$ and $\nu_a(\text{C}=\text{O})$ with the addition of a higher amount of EG could be assigned to the weaker coordination of H^+ ions onto the oxygen of the $\text{C}=\text{O}$ group, instead of EG molecules onto the $\text{C}=\text{O}$ or NH_4^+ groups. No EG vibrational bands were observed in this region for pure EG. Since H^+ ions are weakly coordinated to the carbonyl group, the cations are more mobile and can be transported easily from coordinating site to another. Thus, the plasticization of System II films should exhibit higher ionic conductivity.

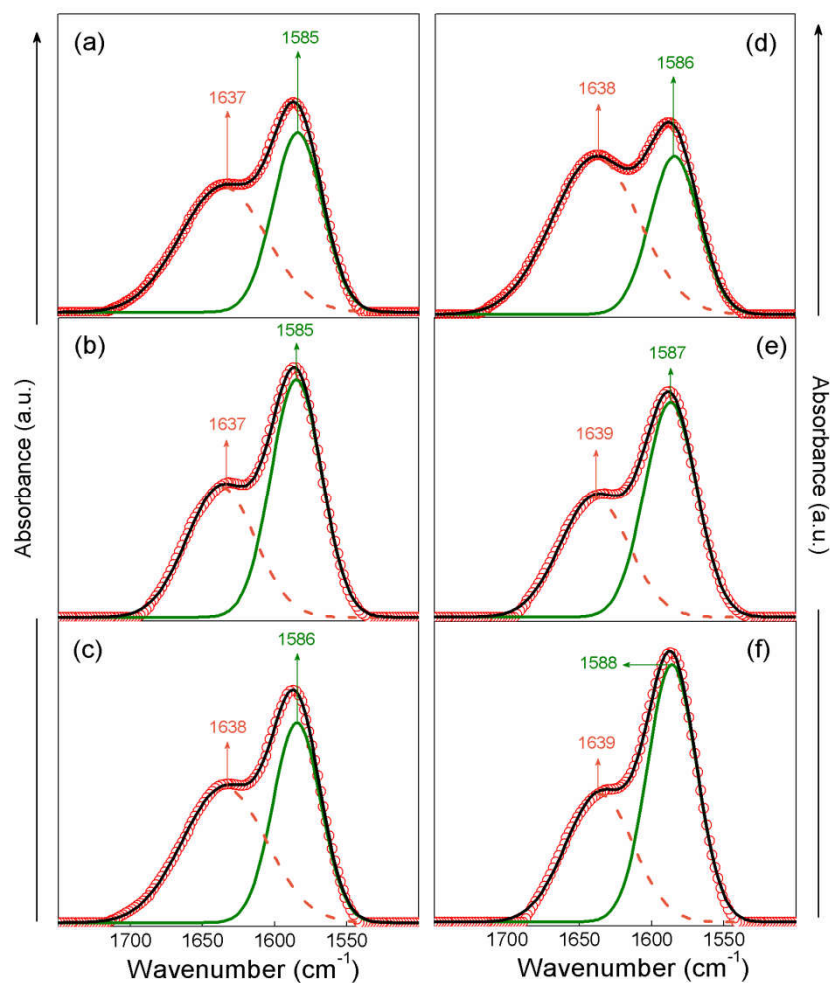


Figure 4.7 Gaussian fit for FTIR spectra between 1700 cm^{-1} and 1500 cm^{-1} for System II films incorporated with (a) (5 wt.% EG), (b) (10 wt.% EG), (c) (20 wt.% EG), (d) (25 wt.% EG), (e) (30 wt.% EG), and (f) (35 wt.% EG). *Note:* **Green** solid line - vibrational bands from CMC polymer, **orange** dash line - vibrational bands from NH_4NO_3 salt, **open** circles - experimental data and **black** solid line - fitted sum data.

In the region between 1200 cm^{-1} and 950 cm^{-1} , several bands correspond to the $\nu(\text{C-O})$ stretching of CMC, $\nu(\text{NO}_3^-)$ of NH_4NO_3 and $\nu(\text{C-OH})$ stretching of EG overlapped with each other. To segregate the overlapping bands, the deconvoluted FTIR spectra of selected System II films incorporating various EG concentration are plotted in Figure 4.8. The complexation of $\text{CMC-NH}_4\text{NO}_3$, CMC-EG , and $\text{EG-NH}_4\text{NO}_3$ was believed to be established in this region.

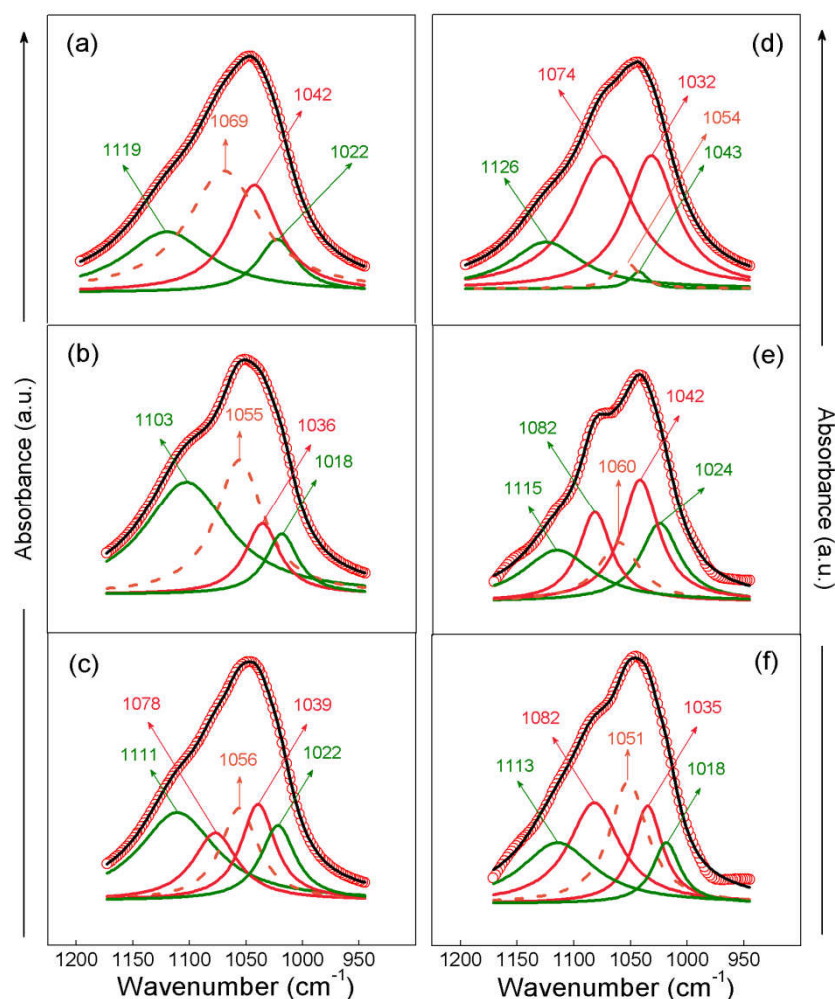


Figure 4.8 Deconvoluted FTIR spectra between 1200 cm^{-1} and 950 cm^{-1} for System II films incorporated with (a) (5 wt.% EG), (b) (10 wt.% EG), (c) (20 wt.% EG), (d) (25 wt.% EG), (e) (30 wt.% EG), and (f) (35 wt.% EG). *Note:* **Green** solid line - vibrational bands from CMC polymer, **red** solid line - vibrational bands from EG plasticizer, **orange** dash line - vibrational bands from NH_4NO_3 salt, **red** open circles - experimental data and **black** solid line - fitted sum data.

Upon the addition of 5 wt.% EG, the stretching of the C-O bond of CMC shifted from 1119 cm^{-1} to 1103 cm^{-1} . Further addition of plasticizer from 10 to 35 wt.% EG resulted in the upshift of the band at 1113 cm^{-1} . Another C-O bond of CMC was observed between 1022 cm^{-1} and 1018 cm^{-1} . The characteristic band of $\nu(\text{NO}_3^-)$ of NH_4NO_3 was present in the region between 1069 cm^{-1} (5 wt. % EG) and 1051 cm^{-1} (35 wt. % EG). The vibration modes corresponding to the $\nu(\text{C-OH})$ stretching of EG can be found within ($1078 - 1082\text{ cm}^{-1}$) and ($1035 - 1042\text{ cm}^{-1}$)

bands, respectively. The addition of EG in the system results in the emergence of new peaks corresponds to EG bands and shifting of position in CMC and NH_4NO_3 bands.

The interaction of NH_4NO_3 and EG also can be seen at the lower wavenumber between 870 cm^{-1} and 800 cm^{-1} as depicted in Figure 4.9. It can be observed that the CH_2 deformation band of EG was detected in this region. The CH_2 band of EG maintains at 879 cm^{-1} for all System II films except for 10 wt.% EG, the peak shifted about 6 cm^{-1} to 885 cm^{-1} .

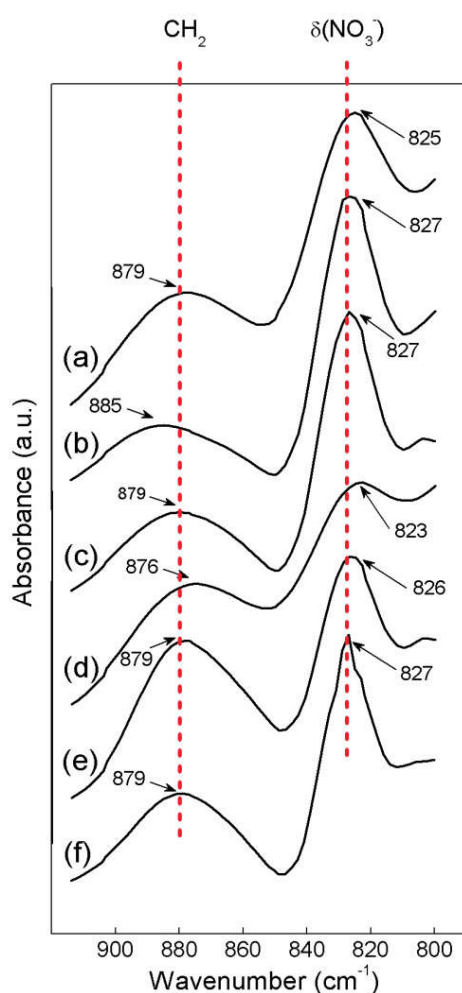


Figure 4.9 FTIR spectra of within $920 - 800\text{ cm}^{-1}$ wavenumber for System II films incorporated with (a) (5 wt.% EG), (b) (10 wt.% EG), (c) (20 wt.% EG), (d) (25 wt.% EG), (e) (30 wt.% EG), and (f) (35 wt.% EG).

The $\delta(\text{NO}_3^-)$ vibrational mode of NH_4NO_3 did not show distinct changes in its position with the addition of EG. At 5 wt.% EG, the 825 cm^{-1} band was relocated to $826 - 827\text{ cm}^{-1}$ when 10 - 35 wt.% EG added. Both individual bands can be seen did not overlap with each other, signifying that no interaction between NH_4NO_3 salt and EG plasticizer establishes within this region.

4.2.3 Proton transfer mechanism

Several authors reported that the coordination of H^+ ion occurs at the C=O band in CMC-based ammonium salt/acid system (Chai and Isa, 2015; Samsudin et al., 2014c; Rani et al., 2014; Ramlli et al., 2015b; Sohaimy and Isa, 2015; Ahmad and Isa, 2015), which support the results from the present work where the greatest downshift of C=O band around $\sim 10\text{ cm}^{-1}$ was discovered upon incorporation of NH_4NO_3 salt in System I. However, weaker coordination of H^+ ions onto the oxygen of the C=O group has been observed in System II films with $\sim 3\text{ cm}^{-1}$ upshift of wavenumber.

H^+ ion (or also known as a proton) which originates from ammonium ion (NH_4^+) of NH_4NO_3 salt is believed to be responsible for the ionic conduction in the System I and System II. Although there are two more possible conducting cations in the system, namely NH_3^+ and NH_4^+ , conduction from H^+ ion is more likely to occur in the polymer-ammonium salt system as proven by Sheha (2009) and Norby et al. (1999). The conduction of lone proton migration in the present systems occur through the exchange of H^+ ions between complexation sites and carried out by the structural diffusion (Grotthus mechanism) or also known as a free-proton mechanism (Bai et al., 2014; Ma and Sahai, 2013; Jiang et al., 2008). This proton transfer mechanism can be explained as follow. The NH_4^+ cations of NH_4NO_3 salt have an

ideal tetrahedral structure where two of the four hydrogen atoms are identically bound. These two hydrogen atoms either strictly or weakly bound. The weakly bound of hydrogen atom can easily be dissociated under the influence of an electric field. This H^+ ion can hop from one site to another leaving a vacancy which will be filled by another H^+ ion from a neighbouring site (Yusof et al., 2014).

Based on this interpretation, the H^+ ions from the NH_4^+ ion of NH_4NO_3 salt in System I is presumed to coordinate with the oxygen atom of the carboxyl group in CMC as proposed in Figure 4.10. As EG plasticizer added into System I, the possible interactions that occur in CMC- NH_4NO_3 -EG of System II are illustrated in Figure 4.11. In System II, the changes of band positions indicate that the EG plays a significant role in the complexation of CMC polymer and NH_4NO_3 salt. With the addition of EG in the system, more NH_4NO_3 dissolves, and more H^+ ion dissociates in the polymer matrix. Thus, create a weak bonding between H^+ ion and EG. This weaker coordination creates a new pathway of hopping of charge carrier, H^+ ion (i.e. proton mobility). It also believed that the short distance between transit sites where the H^+ ions hop are provided by the polymer and plasticizer. From these FTIR results, it can be summarized that the protonation has occurred in the present polymer-salt complexes and the interactions between CMC and NH_4NO_3 salt and between CMC- NH_4NO_3 and EG plasticizer have been established.

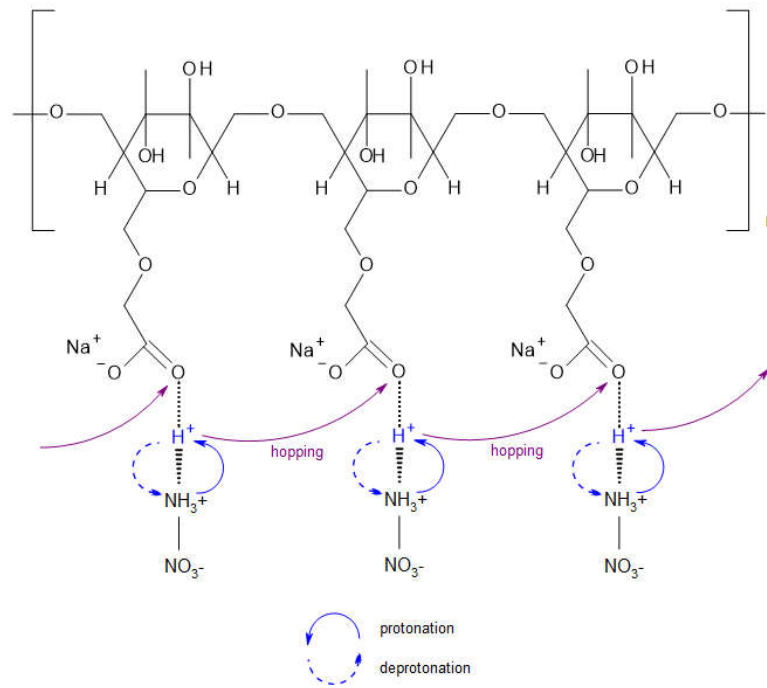


Figure 4.10 Possible interactions of CMC- NH_4NO_3 in System I.

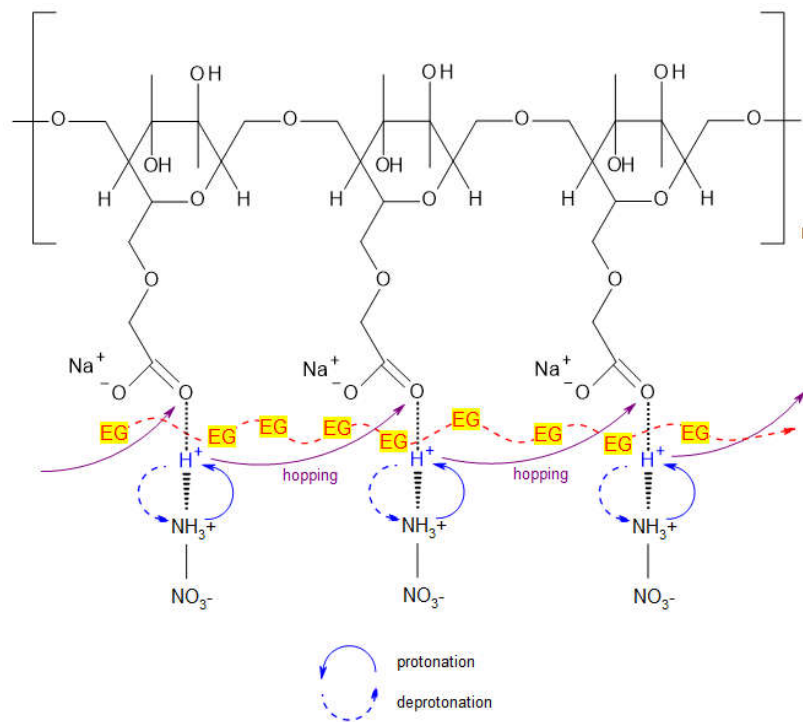


Figure 4.11 Possible interactions of CMC- NH_4NO_3 -EG in System II.

4.3 XRD analysis

XRD measurements were performed to investigate the structural changes in System I and System II films. Figure 4.12 shows the XRD patterns of pure CMC and System I films. Pure CMC powder is reported to inherit a broad diffused hump centred at $2\theta = 20.7^\circ$ and a small shoulder between 35° and 45° corresponding to the amorphous nature of pure CMC (Kamarudin and Isa, 2013). Pure NH_4NO_3 is reported to exhibit four intense polycrystalline peaks with the strongest intensity peak located at 2θ angles of 20.4° (Wu et al., 2007).

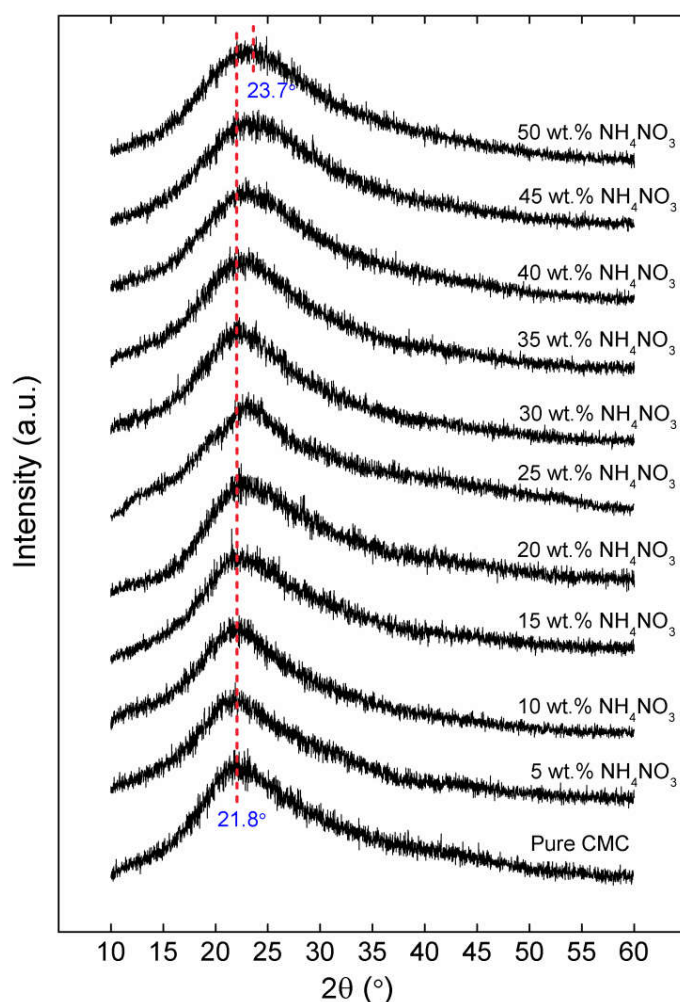


Figure 4.12 XRD patterns of pure CMC and System I films incorporating 5 - 50 wt.% NH_4NO_3 .

Based on the figure, no obvious diffraction peak of NH_4NO_3 appears, since NH_4NO_3 is uniformly dispersed in CMC polymer matrix. A shifting of $2\theta = 1.1^\circ$ to 21.8° has been observed in pure CMC film. Upon addition of NH_4NO_3 salt, the diffused hump tends to broaden and shifted to a higher Bragg angle from $2\theta = 22.2^\circ$ (5 wt.% NH_4NO_3) to 23.4° (50 wt.% NH_4NO_3) as can be seen in Figure 4.12. A similar feature to that of System I was observed with the addition of EG in System II as displayed in Figure 4.13. The addition of EG results in the decrement of diffused hump centred from $2\theta = 24.9^\circ$ (5 wt% EG) to 23.4° (40 wt% EG).

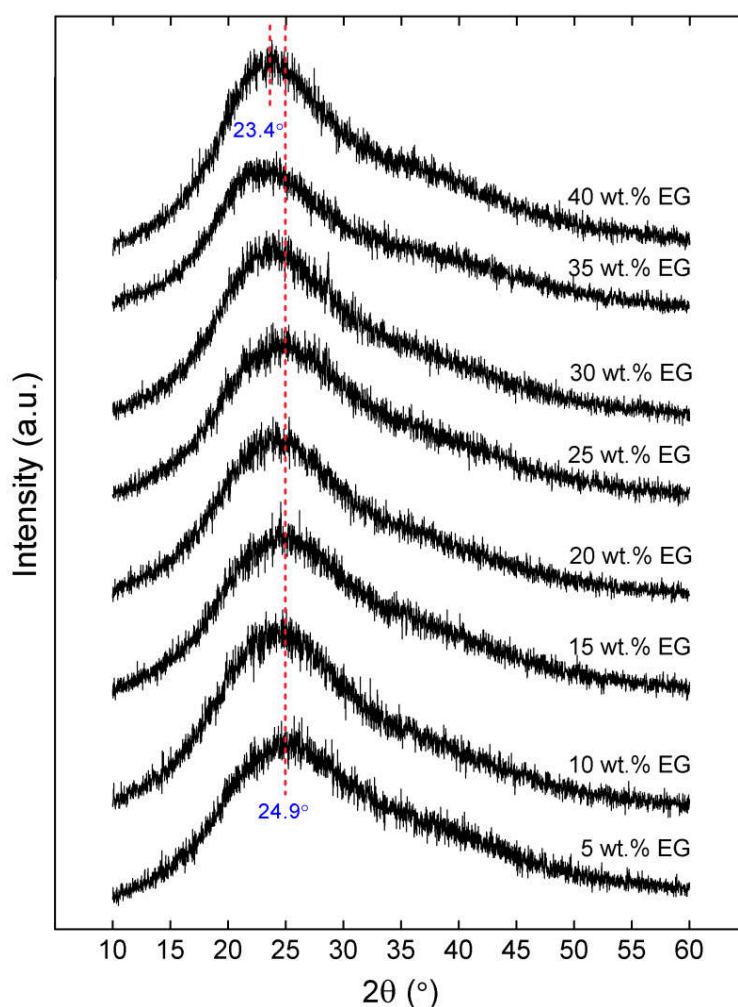


Figure 4.13 XRD patterns of System II films incorporating 5 - 40 wt.% EG.

The shifting of diffused hump (amorphous peak position) in Figure 4.12 and Figure 4.13 indicates the interaction/formation of polymer-salt and polymer-salt-plasticizer complexes. This also may be due to the rearrangement in the morphology of the polymeric chain after adding NH_4NO_3 salt and EG plasticizer to CMC host polymer. The appearance of characteristic amorphous hump/halo in the XRD pattern showed the domination of amorphous structure in the System I and System II. Thus, confirmed that ionic conduction mechanism was obtained mostly in the amorphous region (Nithya et al., 2013; Rosli et al., 2012; Vijaya et al., 2012).

The broadness (width at the half of maximal intensity) of diffused hump can be calculated from Debye-Scherrer equation (Equation 3.1). The calculated values of full-width at half maximum (FWHM), crystallite size, L with peak centre and height, are presented in Table 4.1. The FWHM and height (intensity) of peaks shows a variation trend between decreasing and increasing of its values. According to Nouh et al. (2007), and Selvasekarapandian et al. (2010), the regions which increase in broadness (lower in intensity) imply a decrease in the crystallinity (degree of disordering) of the polymer complexes. This can be attributed to the cross linking which eliminates the crystalline structure. In contrast, the increase regions in broadness (higher in intensity), signify an increase in the amount of crystalline phase (degree of ordering) of the polymer complexes due to the dissociation of ions induced by salt or plasticizer addition.

The average crystallite size of pure CMC film is 7.0 \AA . The average crystallite size of System I films was found to be in the range of $6.4 - 7.9 \text{ \AA}$, whereas lower average crystallite size was observed in the System II films between 5.4 \AA and 6.8 \AA . The smaller crystallite size $<7.9 \text{ \AA}$ in both systems and no additional or obvious

sharp crystalline peaks in the polymer complexes indicating a complete dissociation of NH_4NO_3 salt and EG plasticizer in the polymer matrix. Thus, confirmed the amorphous nature of all SBE films.

Table 4.1 Centre peak, FWHM and crystallite size for single polymer, System I and System II films.

| SPE film | Diffused hump peak | | | Crystallite size, L (Å) |
|----------------------------------|--------------------|--------------|----------|------------------------------|
| | Centre (°) | Height (cps) | FWHM (°) | |
| Pure CMC | 21.8 | 554.7 | 13.4 | 7.0 |
| System I | | | | |
| 5 wt.% NH_4NO_3 | 22.2 | 495.9 | 14.1 | 6.7 |
| 10 wt.% NH_4NO_3 | 22.3 | 581.8 | 13.2 | 7.1 |
| 15 wt.% NH_4NO_3 | 22.5 | 477.6 | 12.0 | 7.8 |
| 20 wt.% NH_4NO_3 | 22.5 | 432.7 | 11.9 | 7.9 |
| 25 wt.% NH_4NO_3 | 22.6 | 536.6 | 12.9 | 7.3 |
| 30 wt.% NH_4NO_3 | 22.7 | 608.7 | 12.9 | 7.3 |
| 35 wt.% NH_4NO_3 | 22.7 | 611.7 | 13.4 | 7.0 |
| 40 wt.% NH_4NO_3 | 23.0 | 595.9 | 14.2 | 6.6 |
| 45 wt.% NH_4NO_3 | 23.4 | 679.8 | 14.5 | 6.5 |
| 50 wt.% NH_4NO_3 | 23.7 | 699.0 | 14.8 | 6.4 |
| System II | | | | |
| 5 wt.% EG | 24.9 | 550.8 | 17.6 | 5.4 |
| 10 wt.% EG | 24.6 | 642.7 | 15.7 | 6.0 |
| 15 wt.% EG | 24.5 | 563.8 | 16.7 | 5.6 |
| 20 wt.% EG | 24.4 | 644.4 | 15.1 | 6.2 |
| 25 wt.% EG | 24.1 | 558.4 | 16.6 | 5.7 |
| 30 wt.% EG | 23.9 | 672.5 | 14.9 | 6.3 |
| 35 wt.% EG | 23.6 | 563.3 | 14.7 | 6.4 |
| 40 wt.% EG | 23.4 | 720.9 | 13.9 | 6.8 |

4.4 Thermal behaviour

In order to verify the thermal behaviour of biopolymer electrolyte films, TGA was performed. TGA is a method to decompose a material/substance by heat, which results in bonds within the molecules to be broken (El-Sayed et al., 2011). The TGA curves of pure CMC, and System I films are illustrated in Figure 4.14(a-f), whereas

Figure 4.15(a-d) represents the TGA curves of System II films. The stage of weight loss can be clearly distinguishable by the first derivative of TGA curves or known as DTG, which were achieved from the built-in software of the TGA instrument as depicted in Figure 4.14(g-l) and Figure 4.15(e-h). The maximum thermal degradation temperature or peak temperature, T_p can be retrieved from the DTG curves.

The first slight weight loss at low temperature is due to the present of small amount of moisture in the SPE films (Han et al., 2010; Li et al., 2009; Biswal and Singh, 2004). Polysaccharide such as CMC is a hydrophilic substance and water content always present in the sample. Water content in the film was found to be higher than in the dry state of CMC. Similar result has been reported in Li et al (2009). According to Li et al. (2009), the high water content was detected in both CMC powder and film due to the strong hydrophilicity of CMC. This is caused by hydrogen bonds, which formed between water molecules and hydrophilic OH and COONa bands of polymer chains. The subsequent appearing of latter weight loss in TGA curves could be attributed to the thermal degradation due to decomposition of CMC (melting point temperature, $T_m \sim 300^\circ\text{C}$), and NH_4NO_3 ($T_m \sim 169^\circ\text{C}$) and EG ($T_m \sim -13^\circ\text{C}$) complexes. For clarity of presentation, several films in System I and System II were selected and analyzed. The remaining results of films in both systems can be found in Appendix 1 and 2.

Figure 4.14(a-l) shows the TGA-DTG curves for System I films. Apparently from the figure, the introduction of NH_4NO_3 salt into the CMC polymer matrix substantially affect the thermal behaviour of SPE films based on the changes of TGA-DTG pattern. At the initial stage, the weight loss about 10.4% below 243°C for CMC powder and 17% below 244°C for CMC film can be attributed to the

evaporation of water content, dehydration of saccharide rings in the CMC chains (Han et al., 2010; Yang et al., 2009).

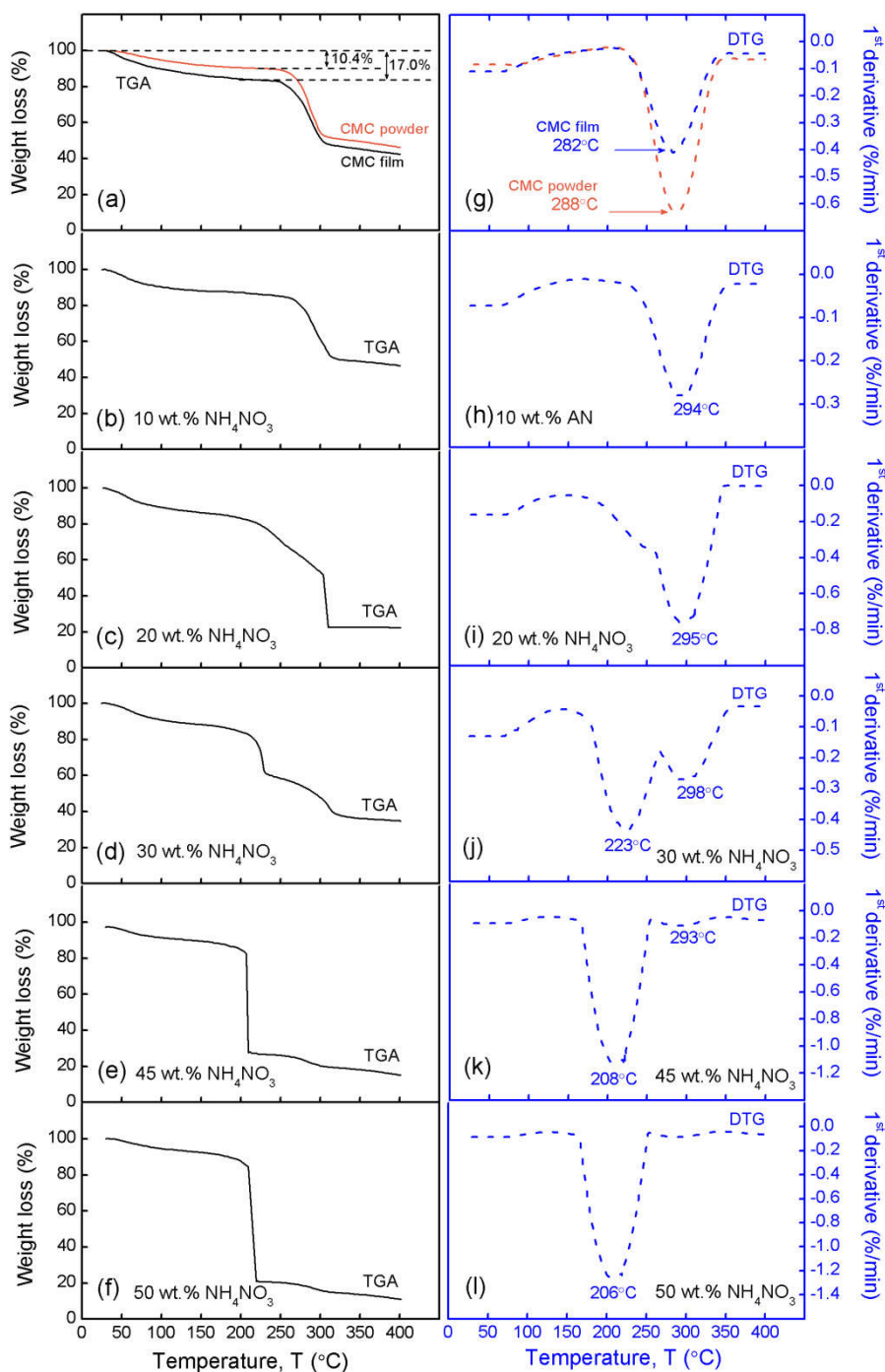


Figure 4.14 (a-f) TGA and (g-l) DTG curves for System I films obtained at room temperature to 400°C.

According to Li et al. (2009), the phase transition at 220°C can be explained by the dissociation of intra chain of hydrogen bonds. The following weight loss about 41% (243 - 305°C) for CMC powder and 23% for CMC film can be explained due to the loss of CO₂ molecules from the polysaccharide chain (Su et al. 2010; Biswal and Singh, 2004). The COO⁻ group for CMC film detected at 1591 cm⁻¹ band of FTIR analysis was decarboxylated in this temperature range. The weight loss was subsequently growing up till 400°C with CMC powder and film retains a total weight loss of 54% and 58%, respectively. A similar behaviour is observed in the film incorporating 10 wt.% NH₄NO₃ with a total weight loss of 53%.

As more NH₄NO₃ salt was added in System I, the thermal stability of the films shift in their degradation temperatures and can be clearly seen in DTG curves. At 30 wt.% NH₄NO₃ (Figure 4.14(j)), the T_p intensity corresponding to the decomposition of the CMC polymer i.e. the breaking of C-O-C bonds of CMC chains (Wang et al., 2011) weakens at the higher temperature. Hence, a new T_p emerged which corresponding to the decomposition of NH₄NO₃ salt at the lower temperature. Gunawan et al. (2006) reported that NH₄NO₃ starts to melt at ~170°C, after which the decomposition occurs. The T_p due to the decomposition of NH₄NO₃ salt merged from 223°C to 206°C. Whereas, the T_p for CMC decomposition shifted from 298°C to 293°C. The cross-linking of CMC with NH₄NO₃ resulted in the decrease in the maximum degradation temperature. This also indicates that thermal decomposition process in this region was assisted by the introducing of NH₄NO₃ in the system.

A remarkable drop of weight loss can be observed in film containing 45 wt.% NH_4NO_3 , which show rapid decomposition of NH_4NO_3 within a small temperature range of 207 - 209°C, with a residue of 15% at 400°C. This trend can also be seen in film containing 50 wt.% NH_4NO_3 . The total weight loss was found to increase from 65 – 89% with the increment of NH_4NO_3 concentration from 30 - 50 wt.% NH_4NO_3 .

TGA-DTG curves for System II films are displayed in Figure 4.15(a-h). The initial weight loss at lower temperature from TGA curves is suggested due to the free water removal or evaporation of residual solvent from the surface of SPE films (Ma et al., 2008). At 10 wt.% EG, the significant weight loss of 43% between 205°C and 219°C ($T_p = 207^\circ\text{C}$) is implied to the decomposition of CMC- NH_4NO_3 complexes. This can be attributed to the elimination of carboxylic groups embedded NH_4NO_3 moieties (via H^+ of NH_4^+), decarboxylation of CMC from the polymeric backbone. The successive weight loss about 11% within the temperature of 219 - 316°C is associated with the breaking of C-O-C bonds in CMC chains. The subsequent weight loss greater than this temperature range ($> 316^\circ\text{C}$) can be assigned to the destruction of main-chain scission (C-C bonds) and the termination of cross linked network structure (Lin et al., 2013).

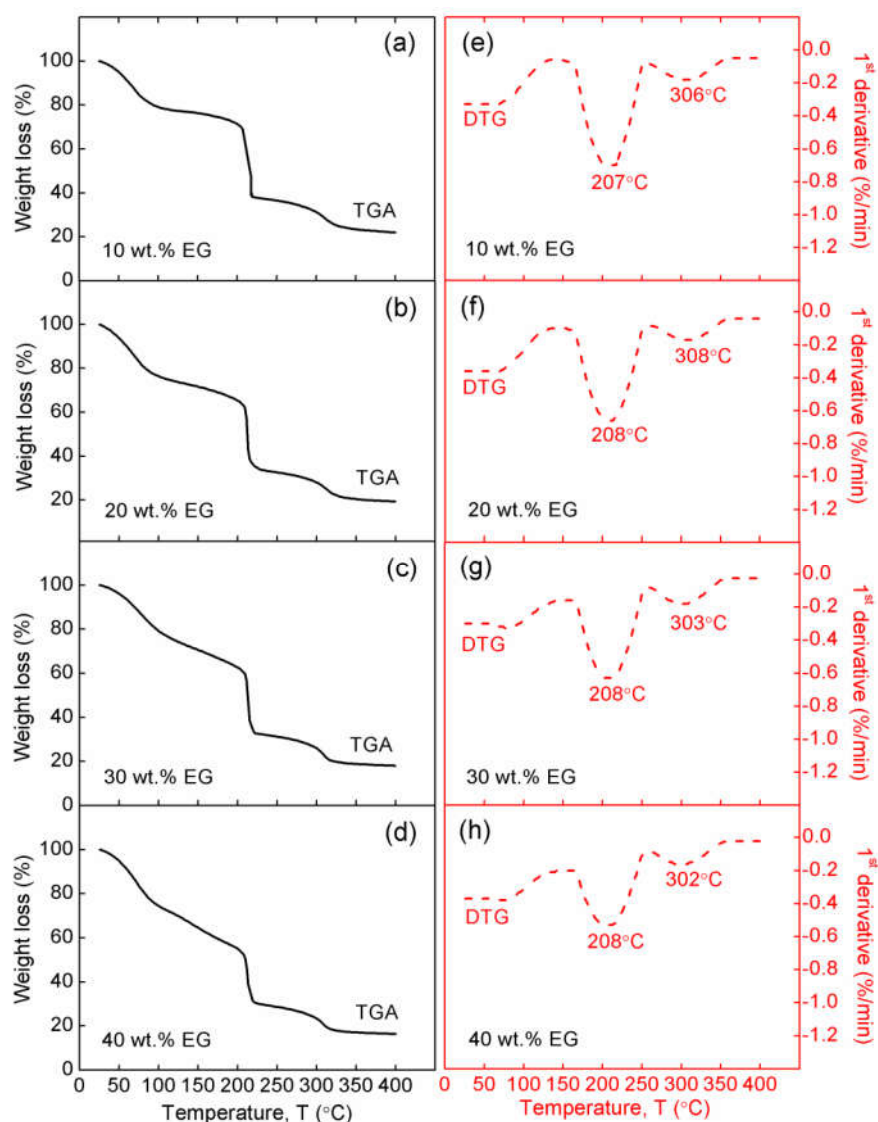


Figure 4.15 (a-d) TGA and (e-h) DTG curves for System II films obtained at room temperature to 400°C.

Table 4.2 summarized the results obtained from TGA analysis of pure CMC, System I and System II films under the nitrogen environment. The overall weight loss (%) increases linearly with the addition of NH_4NO_3 and EG contents. The introduction of NH_4NO_3 and EG in System I and System II resulted in the decrease of thermal stability, which was ascribed to the low thermal stability of both System I and System II films compared to pure CMC film. However, System II films were

observed to demonstrate a higher thermal stability or better heat-resistance than System I films based on the slower total weight loss over temperature.

Table 4.2 The total weight loss and degradation temperatures of pure CMC film, System I and System II films obtained from TG analysis.

| SPE film | T (°C) | WL (%) ^a | T _p (°C) ^b |
|---|---------|---------------------|----------------------------------|
| Pure CMC | 25-71 | 7 | - |
| | 71-244 | 10 | - |
| | 244-303 | 33 | 282 |
| | 303-400 | 8 [Total: 58] | - |
| System I | | | |
| 10 wt.% NH ₄ NO ₃ | 25-69 | 7 | - |
| | 69-263 | 9 | - |
| | 263-315 | 33 | 294 |
| | 315-400 | 4 [Total: 53] | - |
| 20wt.% NH ₄ NO ₃ | 25-71 | 8 | - |
| | 71-204 | 9 | - |
| | 204-303 | 31 | 295 |
| | 303-310 | 29 | - |
| | 310-400 | 1 [Total: 78] | - |
| 30 wt.% NH ₄ NO ₃ | 25-72 | 6 | - |
| | 72-189 | 8 | - |
| | 189-231 | 25 | 223 |
| | 231-315 | 21 | 298 |
| | 315-400 | 5 [Total: 65] | - |
| 45 wt.% NH ₄ NO ₃ | 25-73 | 7 | - |
| | 73-207 | 10 | - |
| | 207-209 | 55 | 208 |
| | 209-300 | 8 | 293 |
| | 300-400 | 5 [Total: 85] | - |
| 50 wt.% NH ₄ NO ₃ | 25-74 | 3 | - |
| | 74-210 | 12 | 206 |
| | 210-220 | 64 | - |
| | 220-305 | 6 | - |
| | 305-400 | 4 [Total: 89] | - |
| System II | | | |
| 10 wt. % EG | 25-90 | 19 | - |
| | 90-205 | 11 | - |
| | 205-219 | 32 | 207 |
| | 219-316 | 11 | 306 |
| | 316-400 | 5 [Total: 78] | - |
| 20 wt.% EG | 25-93 | 22 | - |
| | 93-207 | 15 | - |
| | 207-221 | 27 | 208 |
| | 221-317 | 12 | 308 |
| | 317-400 | 5 [Total: 81] | - |
| 30 wt.% EG | 25-98 | 2 | - |
| | 98-210 | 20 | 208 |
| | 210-221 | 27 | - |
| | 221-315 | 12 | 303 |
| | 315-400 | 3 [Total: 82] | - |
| 40 wt.% EG | 25-97 | 25 | - |
| | 97-204 | 21 | - |
| | 204-221 | 23 | 208 |
| | 221-313 | 12 | 302 |
| | 313-400 | 3 [Total: 84] | - |

a - Weight loss in percentage during the specific temperature ranges, and

b - Peak temperatures on DTG curves.

CHAPTER 5

IONIC CONDUCTIVITY, TRANSPORT AND ELECTRICAL PROPERTIES OF SOLID POLYMER ELECTROLYTES

This chapter discusses the effect of NH_4NO_3 salt and EG plasticizer addition on the ionic conductivity, transport and electrical properties of SPE films at selected temperatures and over a wide range of frequencies. AC impedance technique and transference number measurement have been utilized to investigate those properties. Besides, transport parameters of SPE films have been determined by the deconvolution of FTIR spectra. These properties are crucial for practical application in solid-state electrochemical cells.

5.1 Ionic conductivity studies

The ionic conductivity of SPEs has been attributed in the amorphous phases and can be investigated by several different techniques. One of the techniques is by dissolving the salt in a suitable polymer matrix. Plasticization is another technique to increase the amorphous phases, thus resulting in the enhancement of ionic conductivity.

5.1.1 Nyquist plots

The Nyquist (Cole-Cole) plots were derived from the AC impedance analysis. Figure 5.1(a-g) shows the Nyquist plots of the pure CMC film and SPE films incorporated

with varied NH_4NO_3 salt concentration in System I at ambient temperature. Pure CMC film shows an incomplete semicircle curve at the higher frequency region as depicted in Figure 5.1(a). The value of bulk resistance, R_b is determined from the intercept of the high-frequency semicircle or the low-frequency spike on the Z_r -axis.

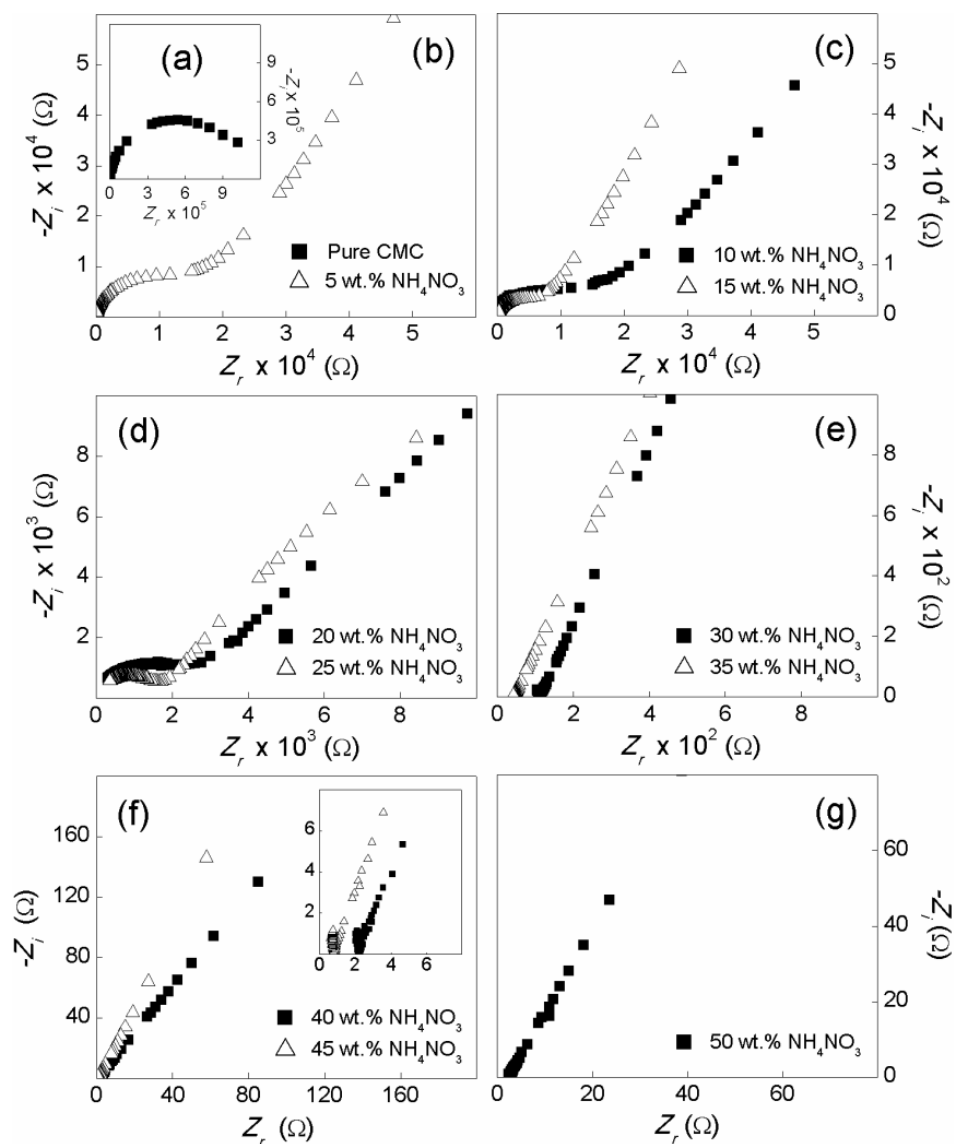


Figure 5.1 Nyquist plots of the real impedance, Z_r versus imaginary impedance, $-Z_i$ of (a) pure CMC film, and System I films incorporated with (b) 5 wt.% NH_4NO_3 , (c) 10 wt.% NH_4NO_3 and 15 wt.% NH_4NO_3 , (d) 20 wt.% NH_4NO_3 and 25 wt.% NH_4NO_3 , (e) 30 wt.% NH_4NO_3 and 35 wt.% NH_4NO_3 , (f) 40 wt.% NH_4NO_3 and 45 wt.% NH_4NO_3 (Inset: Enlargement of (f) in high-frequency region), and (g) 50 wt.% NH_4NO_3 , measured at ambient temperature.

With the addition of 5 - 15 wt.% NH_4NO_3 , the Nyquist plots comprise of a depressed semicircular arc at the higher frequency region and an inclined spike at the lower frequency region as illustrated in Figure 5.1(b-c). At 20 and 25 wt.% NH_4NO_3 , the semicircle part was observed to lessen towards the higher frequency region as shown in Figure 5.1(c). As the salt concentration further increases from 30 to 50 wt.% NH_4NO_3 , the semicircle part completely disappeared and left with only the inclined spikes (Figure 5.1(e-g)). It is also observed that the R_b decreases as salt concentration increases to 45 wt.% NH_4NO_3 . This can be attributed to the increase of mobile charge carriers in the system (Rani et al., 2015a; Chai and Isa, 2013). The SPE film incorporating with 45 wt.% NH_4NO_3 has the lowest value of R_b , thus exhibit the highest ionic conductivity (Equation 2.3).

According to Shukur et al. (2015a), the semicircle part is ascribed to the ionic conduction in the bulk sample. The high-frequency semicircle is associated to the parallel combination of the bulk resistance and bulk capacitance as a result of mobile charge carriers migration through the free volume of the polymer matrix and immobile polymer chains, respectively (Selvasekarapandian et al., 2010; Subban et al., 2005). The inclined spike is attributed to the effect of electrode polarization due to the diffusion process (Shukur et al., 2015a).

Since the blocking electrodes have been used in the impedance measurement, the electrode–electrolyte interface could be regarded as a capacitance. An ideal capacitance shows a vertical spike in the impedance plot. However, the inclination of the spike at an angle less than 90° with the real axis instead of the vertical spike can be caused by the roughness of the electrode–electrolyte interface or inhomogeneous distribution of salt in the polymer matrix (Shukur et al., 2014). Subban et al. (2005)

reported that the depressed semicircle and inclined spikes implies that the mobile charge carriers have different relaxation times.

The complete picture of the system can be represented by the electrical equivalent circuit which is typically used in impedance analysis. Pure CMC film has a sole semicircle curve (Figure 5.1(a)) which can be assigned to the parallel combination of R_b and constant phase element (CPE) (Mohamed et al., 2014; Shukur et al., 2014) as shown in Figure 5.2(a). Generally, a CPE or also known as a leaky capacitor, is used in a model rather than a capacitor to compensate for inhomogeneity in the system (Shukur et al., 2014), which has an intermediate characteristic between a resistor and a capacitor (Pradhan et al., 2007).

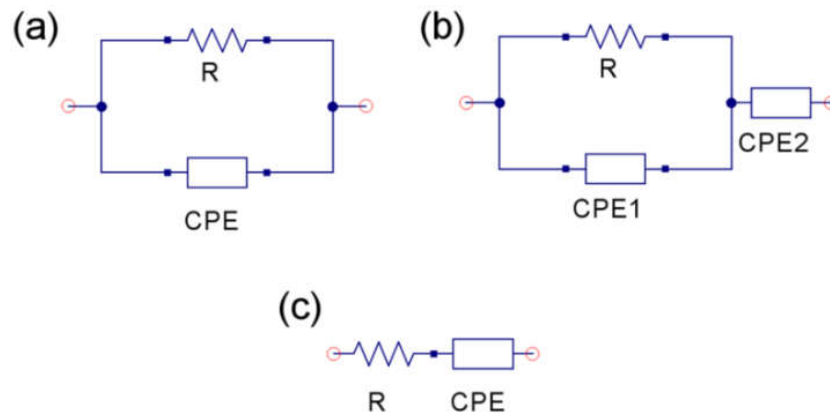


Figure 5.2 The corresponding electrical equivalent circuit for Nyquist plots in Figure 5.1.

The Nyquist plots of SPE films incorporating with 5 - 25 wt.% NH_4NO_3 consist of a semicircle and an inclined spike (Figure 5.1(b-d)). The equivalent circuit can be represented by a parallel combination of R_b and CPE with another CPE in series (Kumar et al., 2014; Woo et al., 2013; Hema et al., 2009) as illustrated in Figure 5.2(b). The appearance of low-frequency spike indicates that only the resistive component of the SPE film predominates (Figure 5.1(e-g)) (Selvasekarapandian et

al., 2010). The equivalent circuit for SPE films incorporating with 30 - 50 wt% NH_4NO_3 is represented by a combination of R_b and CPE in series (Sikkanthar et al., 2015; Rudhziah et al., 2015; Shukur et al., 2014) as depicted in Figure 5.2(c).

Figure 5.3 shows the Nyquist plots of System II films at ambient temperature. With the addition of 5 - 40 wt.% EG, only the inclined spikes prevail. The R_b decreases as the EG content increases to 20 wt.% EG and raises thereafter. Thus, the equivalent circuit for System II films at all EG content is represented by a combination of R_b and CPE in series.

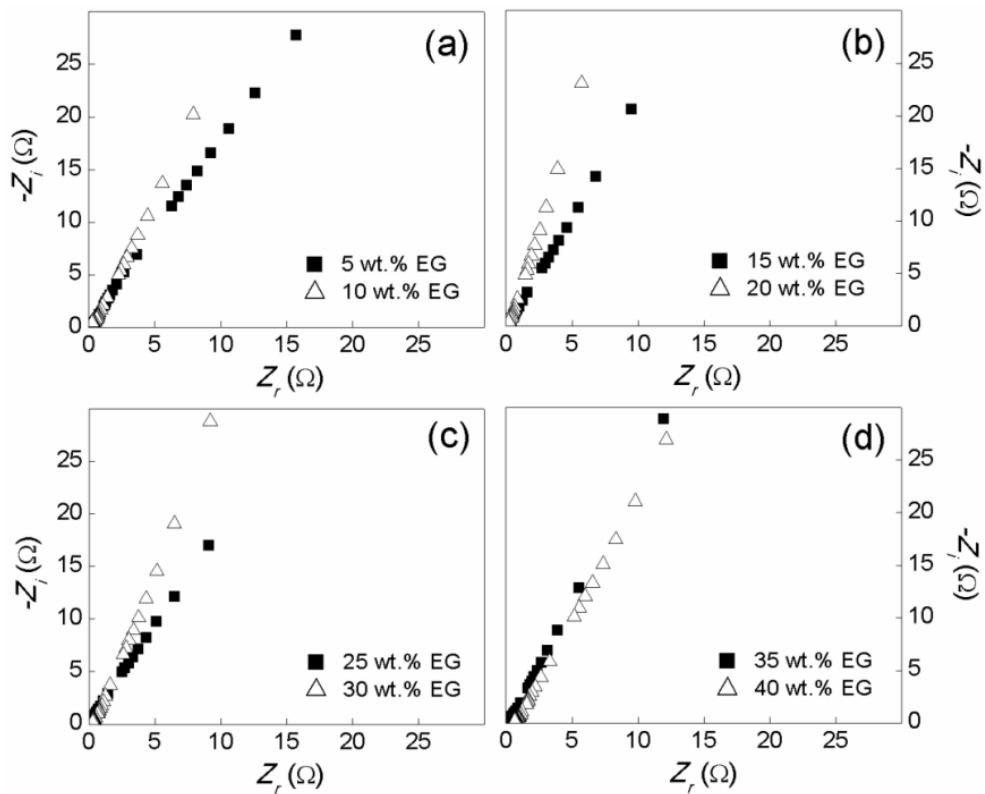


Figure 5.3 Nyquist plots of the real impedance, Z_r versus imaginary impedance, $-Z_i$ of System II films incorporated with (a) 5 wt.% EG and 10 wt.% EG, (b) 15 wt.% EG and 20 wt.% EG, (c) 25 wt.% EG and 30 wt.% EG, and (d) 35 wt.% EG and 40 wt.% EG obtained at ambient temperature.

To investigate the effect of temperature on impedance behaviour, the selected System I and System II films have been subjected to impedance measurements at elevated temperatures. For clarity of presentation, several films in System I and System II were selected and analyzed as shown in Figure 5.4(a-d) and Figure 5.5(a-d), respectively. The remaining results of films in both systems are attached in Appendix 3 and 4. Figure 5.4(a) demonstrates the Nyquist plots for 15 wt.% NH_4NO_3 at 303K - 353K. It can be seen that the semicircle part is lessening and the inclined spike shifting to the higher frequency region with the increasing of temperature.

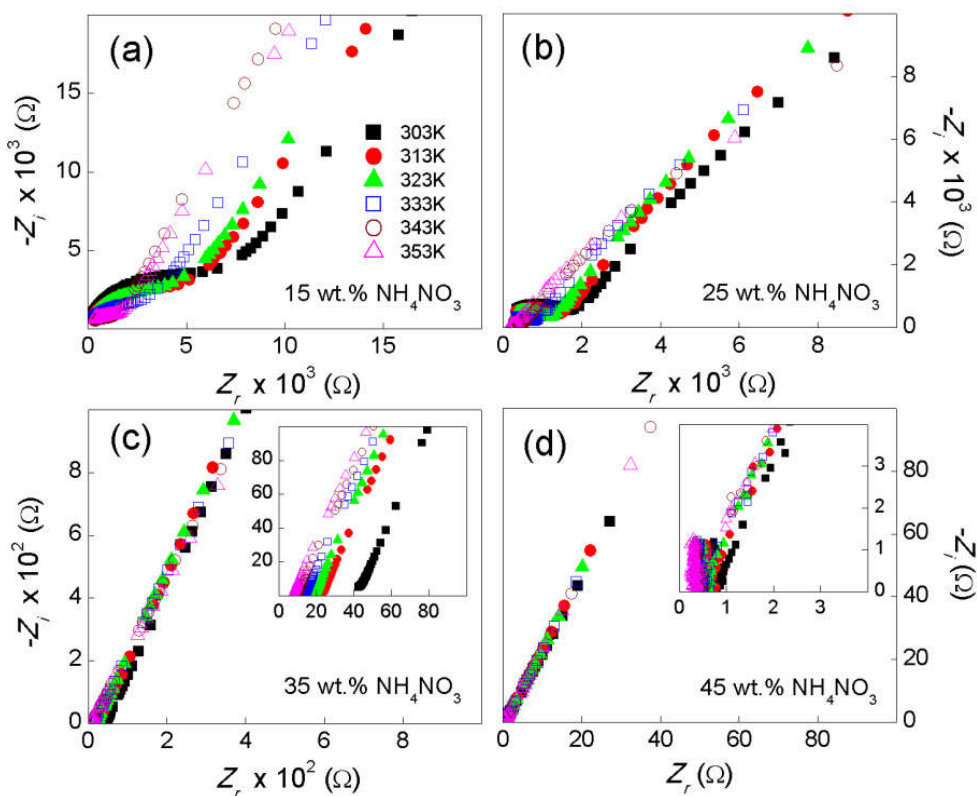


Figure 5.4 Nyquist plots of temperature dependence for System I films at elevated temperatures of 303K - 353K. (a) 15 wt.% NH_4NO_3 , (b) 25 wt.% NH_4NO_3 , (c) 35 wt.% NH_4NO_3 , and (d) 45 wt.% NH_4NO_3 , with a magnified high-frequency region (inset) for (c) and (d).

A similar result is observed for 25 wt.% NH_4NO_3 in Figure 5.4(b). The addition of 35 wt.% NH_4NO_3 and 45 wt.% NH_4NO_3 (Figure 5.4(c-d) reveal the

inclined spikes shifting to the higher frequency region as the temperature increases. This can be explained as the temperature increases, the segmental motion of the polymer chain and the dissociation of the NH_4NO_3 concentration increases, thus leading to the decrease in R_b value (Kumar et al., 2012a).

In addition, a similar trend can be observed for System II (Figure 5.5(a-d)), where the inclined spikes slightly shifting to the high-frequency region with the increasing of temperature. This is due to the plasticizer creates and promotes more free volume in the electrolyte system. Thus, decrease the viscosity of the electrolyte. Hence, enhance the segmental motion of polymer chain and dissociation of NH_4NO_3 salt in polymer matrix as the temperature increases. Consequently, increase the R_b value.

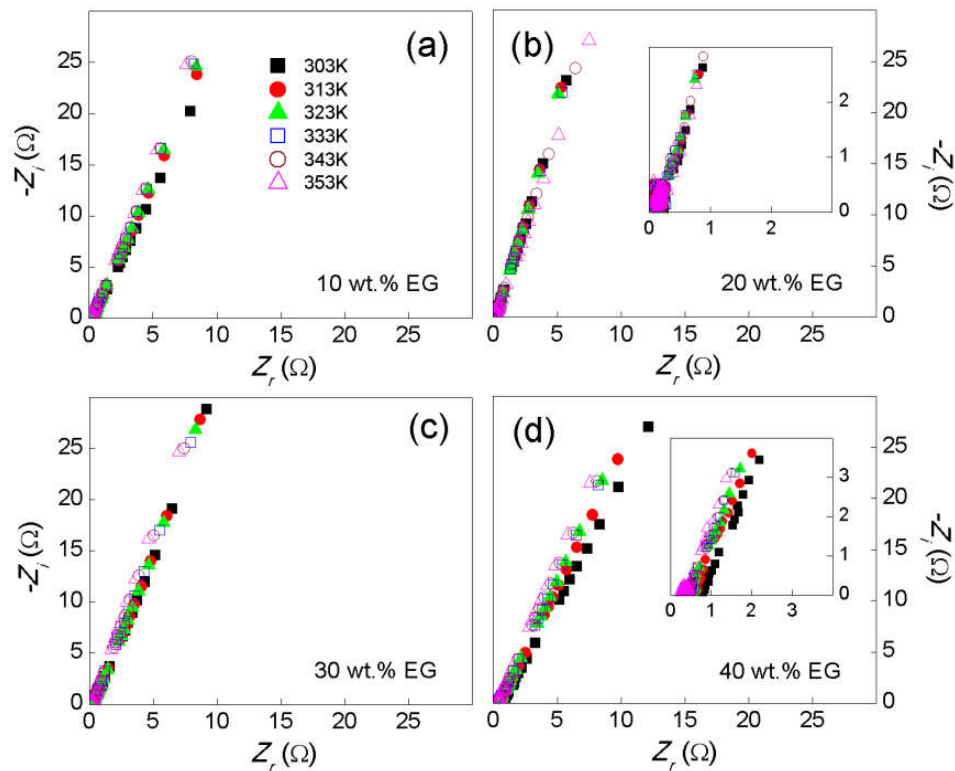


Figure 5.5 Nyquist plots of temperature dependence for System II films at elevated temperatures of 303K - 353K.. (a) 10 wt.% EG, (b) 20 wt.% EG, (c) 30 wt.% EG, and (d) 40 wt.% EG, with a magnified high-frequency region (inset) for (d).

The Nyquist plots for both systems revealed that the bulk resistance, R_b decreases with temperatures for all films. The absence of the high-frequency semicircle in System I and System II implies that the total conductivity is mainly due to the ion conduction (Hema et al., 2007; Selvasekarapandian et al., 2005).

5.1.2 Ionic conductivity

As presented in Chapter 2, SPEs based on CMC have been reported to exhibit excellent ionic conductivity (refer to Table 2.2) and are potentially employed in the application of secondary solid-state proton batteries (Samsudin et al., 2014c; Samsudin and Isa, 2012c). In the present work, the effect of adding NH_4NO_3 salt and EG plasticizer as well as the temperature on ionic conductivity of CMC-based SPEs has been investigated. The ionic conductivity can be calculated based on Equation 2.3.

Figure 5.6 depicts the variation of salt concentration-dependent ionic conductivity of System I films at ambient temperature (303K). The figure shows that the ionic conductivity increases gradually with the addition of NH_4NO_3 concentration up to 45 wt.% NH_4NO_3 (Region I), and then slightly decreases at 50 wt.% NH_4NO_3 (Region II). In Region I, the pure CMC film shows the lowest ionic conductivity of $(1.86 \pm 0.03) \times 10^{-8} \text{ Scm}^{-1}$. The highest ionic conductivity was achieved at $(7.71 \pm 0.04) \times 10^{-3} \text{ Scm}^{-1}$ with the addition of 45 wt.% NH_4NO_3 concentration. The optimized ionic conductivity value of System I in the present work is quite similar with that obtained by Selvasekarapandian et al. (2010) for PVA- NH_4NO_3 system. They reported the highest ionic conductivity of $7.50 \times 10^{-3} \text{ Scm}^{-1}$ at 20 wt.% NH_4NO_3 concentration. At NH_4NO_3 concentration greater than

45 wt.%, the ionic conductivity was observed to slightly drop to $(2.64 \pm 0.05) \times 10^{-4} \text{ Scm}^{-1}$ (Region II).

The increment of ionic conductivity with increasing NH_4NO_3 concentration in Region I can be related to the increasing number of mobile charge carriers and/or their mobility (Khiar and Arof, 2010; Shuhaimi et al., 2010a). This may also attributed to an increase of the amorphous nature of SPE films as confirmed by the XRD analysis. The subsequent decrease at NH_4NO_3 concentration of 50 wt.% in Region II could be caused by the formation of ion clusters due to the creation of ion pairs and ion aggregates. Thus, reduce the number of mobile charge carriers and limits its mobility in the SPE film (Woo et al., 2011; Yahya and Arof, 2003). Ferry et al. (1998) described the decrement of ionic conductivity beyond the optimized salt concentration could be induced by the reduction in film flexibility as a consequence of rapid increase in viscosity.

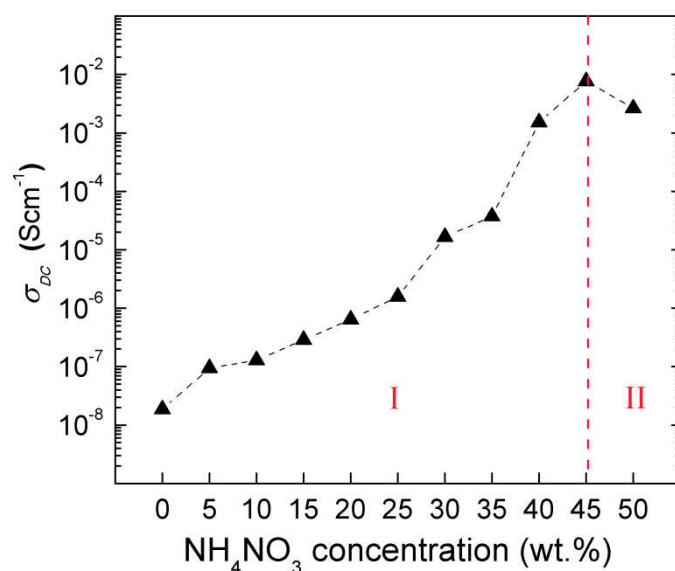


Figure 5.6 The salt-dependent ionic conductivity of System I films measured at ambient temperature.

Figure 5.7 represents the variation of plasticizer-dependent ionic conductivity of System II films at ambient temperature. The maximum ionic conductivity was attained at $(3.80 \pm 0.06) \times 10^{-2} \text{ Scm}^{-1}$ with 20 wt.% EG. With the addition of more plasticizer, the ionic conductivity was observed to decrease to $(1.19 \pm 0.08) \times 10^{-2} \text{ Scm}^{-1}$ (40 wt.% EG). A similar observation has been reported by Ng and Mohamad (2008) for chitosan- NH_4NO_3 system. The ionic conductivity was increased from $\sim 10^{-5} \text{ Scm}^{-1}$ to $\sim 10^{-3} \text{ Scm}^{-1}$ with the addition of 70 wt.% EC.

In this work, the enhancement of ionic conductivity with the addition of EG content in Region I is ascribed to the increase in number density and/or possibly ionic mobility of the charge carriers. EG as plasticizer possesses a high dielectric constant which helps to dissociate the salt or ion aggregates (Pandey et al., 2013). The presence of EG plasticizer may weaken the Coulomb force between NH_4^+ cation and NO_3^- anion of the NH_4NO_3 salt that caused to ion dissociation (Pradhan et al., 2008 and 2007). The addition of plasticizer also can establish more new pathways or routes for ion conduction, thus increase the ionic mobility (Yusof et al., 2014; Mishra, 2013).

Furthermore, the low viscosity of plasticizer may reduce the cohesive forces between polymer chains. The addition of plasticizer decreases the T_g , softens the polymer backbones and increase the segmental motion of polymer, resulting in the increment of ionic conductivity (Pradhan et al., 2008; Osman et al., 2003). The decrement in ionic conductivity after addition of 20 wt.% EG in Region II can be attributed to the formation of microcrystalline junctions/linkages between the plasticizer itself which promote the recrystallization of salt (Shukur et al., 2013c).

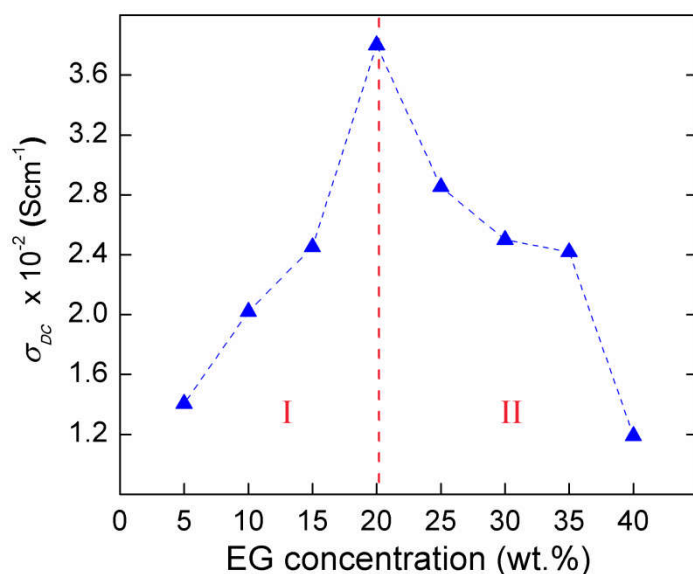


Figure 5.7 The plasticizer-dependent ionic conductivity of System II films measured at ambient temperature.

Figure 5.8 and Figure 5.9 exemplify the evolution of temperature-dependent ionic conductivity for System I and System II films obtained at elevated temperature between 303K and 353K. The linear variation of $\text{Ln } \sigma_{DC}$ versus $1000/T$ plots for System I and System II suggest the Arrhenius behaviour-thermally assisted process of ionic conductivity with regression, R^2 values close to unity (as tabulated in Table 5.1). Hence, the temperature dependence of ionic conductivity satisfies the Arrhenius relation as expressed by Equation 2.4. The plots also indicate no phase transition/sudden drop of ionic conductivity which confirms the amorphous structure of polymer electrolyte films within the measured temperature range. These results are consistent with those of other studies for various SPE systems reported by many authors (Nithya et al., 2015; Shukur et al., 2013d; Vijaya et al., 2012; Buraidah et al., 2011; Selvasekarapandian et al., 2010).

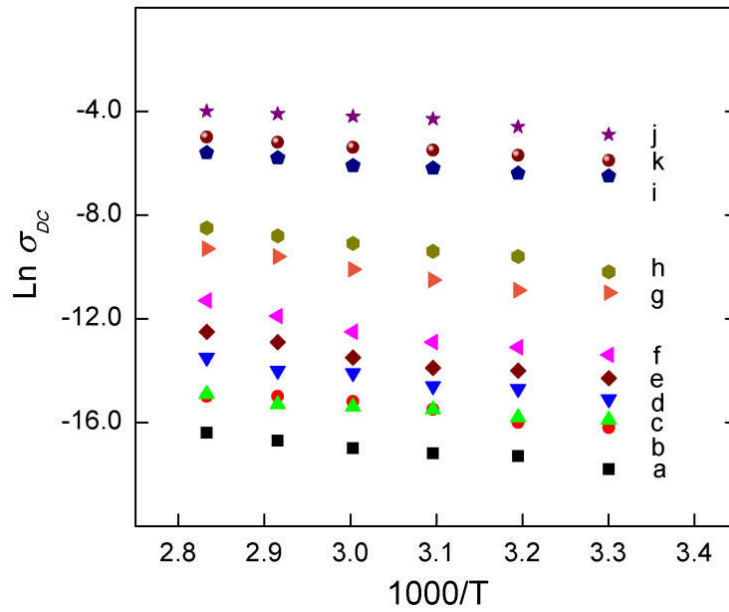


Figure 5.8 The temperature-dependent ionic conductivity of (a) pure CMC film, and System I films incorporated with (b) 5 wt.% NH_4NO_3 , (c) 10 wt.% NH_4NO_3 , (d) 15 wt.% NH_4NO_3 , (e) 20 wt.% NH_4NO_3 , (f) 25 wt.% NH_4NO_3 , (g) 30 wt.% NH_4NO_3 , (h) 35 wt.% NH_4NO_3 , (i) 40 wt.% NH_4NO_3 , (j) 45 wt.% NH_4NO_3 , and (k) 50 wt.% NH_4NO_3 .

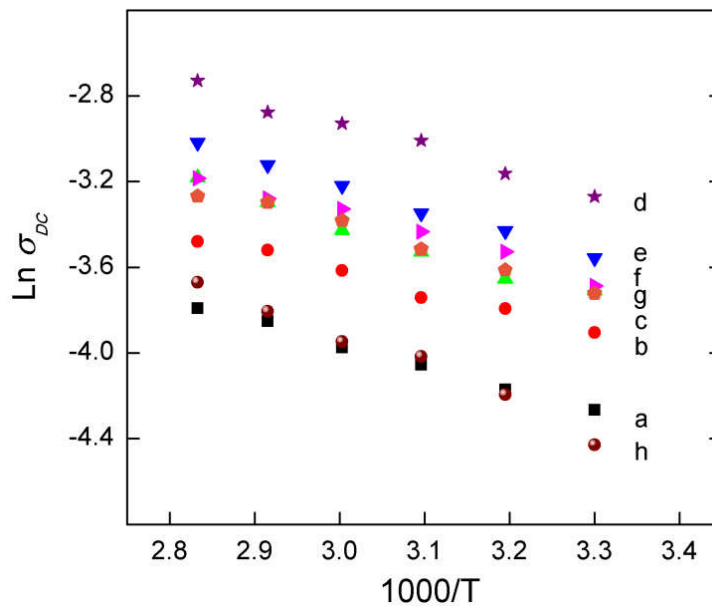


Figure 5.9 The temperature-dependent ionic conductivity of System II films incorporated with (a) 5 wt.% EG, (b) 10 wt.% EG, (c) 15 wt.% EG, (d) 20 wt.% EG, (e) 25 wt.% EG, (f) 30 wt.% EG, (g) 35 wt.% EG, and (h) 40 wt.% EG.

Further observations in System I show that the conductivity of optimum NH_4NO_3 salt concentration (45 wt.% NH_4NO_3) rise to one order of magnitude from

$(7.71 \pm 0.04) \times 10^{-3} \text{ Scm}^{-1}$ (303K) to $(1.84 \pm 0.04) \times 10^{-2} \text{ Scm}^{-1}$ (353K). Introducing heat to CMC film enhances the conductivity from $(1.86 \pm 0.01) \times 10^{-8} \text{ Scm}^{-1}$ to $(7.68 \pm 0.01) \times 10^{-8} \text{ Scm}^{-1}$. In System II, the maximum ionic conductivity (20 wt.% EG) was observed to slightly increase from $(3.80 \pm 0.06) \times 10^{-2} \text{ Scm}^{-1}$ (303K) to $(6.53 \pm 0.04) \times 10^{-2} \text{ Scm}^{-1}$ (353K). The increment of ionic conductivity with temperature in SPE films is attributed to the expansion of polymer matrix during heating which led to the segmental motion (inter- and intra chain ions hopping/movement) of polymer chain. This may create free volume and unoccupied space in the systems due to the lattice vibration and consequently resulting in H^+ ions to be conducted freely (Sohaimy and Isa, 2015; Selvasekarapandian et al., 2005). The segmental motion also allows the ions to hop from one site to another or provides a pathway for ions to move and hence increase the ionic conductivity (Kumar et al., 2012b; Baskaran et al., 2004; Subba et al., 2003).

Besides, another factor that affects the ionic conductivity in polymer-salt systems is activation energy (E_a). It is the minimum energy the ions (in this work, mobile charge carriers are known as H^+ ions) require to hop from one site to the neighbouring sites as elucidated in the FTIR analysis (See Section 4.2.3). The E_a is the combination of the energy of defect formation and the energy for migration of mobile charge carriers (Hema et al., 2008). From the linear fit of the Arrhenius plots retrieved from Equation 2.4, the E_a for all the prepared SPE films has been calculated and listed in Table 5.1. It can be observed that SPE films with the highest ionic conductivity for both systems do not necessarily possess the lowest activation energy. This observation is comparable with the findings reported by Ali et al. (1998) and Hashmi et al. (1990) for PEO- $(\text{NH}_4)_2\text{SO}_4$ system and PEO- NH_4ClO_4 system,

respectively, as a result of the polycrystalline nature of the materials. Furthermore, the observations for both systems in the present work show that the E_a values of the plasticized system (System II) were much lower than that in the plasticizer-free system (System I). This result implies that the H^+ ions in plasticized system required lower energy for migration or hop from one site to another neighbouring site than those in the plasticizer-free system for rapid ionic conduction. Lower activation energy could be caused by the short distance between transit sites yielded by the polymer and plasticizer. Further investigation on the ion conduction/transportation in both systems is explained in the following section.

Table 5.1 The thickness, regression values and activation energies of pure CMC film, and System I and System II films.

| SPE film | Thickness (± 0.0001 cm) | R^2 | E_a (eV) |
|-------------------------|---|-------------------------|------------------------------|
| Pure CMC | 0.0035 | 0.98 | 0.24 ± 0.02 |
| <i>System I</i> | | | |
| 5 wt.% AN | 0.0053 | 0.98 | 0.25 ± 0.03 |
| 10 wt.% AN | 0.0050 | 0.98 | 0.17 ± 0.02 |
| 15 wt.% AN | 0.0048 | 0.99 | 0.28 ± 0.03 |
| 20 wt.% AN | 0.0050 | 0.98 | 0.33 ± 0.04 |
| 25 wt.% AN | 0.0080 | 0.98 | 0.38 ± 0.05 |
| 30 wt.% AN | 0.0055 | 0.99 | 0.34 ± 0.03 |
| 35 wt.% AN | 0.0050 | 0.98 | 0.30 ± 0.02 |
| 40 wt.% AN | 0.0100 | 0.98 | 0.17 ± 0.02 |
| 45 wt.% AN | 0.0180 | 0.98 | 0.16 ± 0.02 |
| 50 wt.% AN | 0.0200 | 0.99 | 0.16 ± 0.02 |
| <i>System II</i> | | | |
| 5 wt.% EG | 0.0190 | 0.99 | 0.09 ± 0.01 |
| 10 wt.% EG | 0.0200 | 0.98 | 0.08 ± 0.01 |
| 15 wt.% EG | 0.0210 | 0.98 | 0.10 ± 0.01 |
| 20 wt.% EG | 0.0220 | 0.98 | 0.10 ± 0.01 |
| 25 wt.% EG | 0.0230 | 0.99 | 0.10 ± 0.01 |
| 30 wt.% EG | 0.0240 | 0.98 | 0.09 ± 0.01 |
| 35 wt.% EG | 0.0250 | 0.98 | 0.09 ± 0.01 |
| 40 wt.% EG | 0.0270 | 0.98 | 0.13 ± 0.01 |

5.2 Transport studies

The high ionic conductivity of SPEs is mainly governed by three important factors, i.e. the number density (concentration) of charge carrier, (n) and the mobility of charge carrier (μ) as expressed by Equation 2.5 as well as the diffusion coefficient of charge carrier (D) (Raphael et al., 2010; Hirankumar et al., 2005). The D can be determined from the Nernst-Einstein relation (Equation 2.10). These factors or known as transport parameters can be related to the ion association between cation and anion of doping salts in the polymer-salt systems.

The fraction of ionic species can be determined based on the area under the deconvoluted FTIR peak representing dissociated/associated ions. The area under peak is proportional to the relative concentration of the ionic species depicts in percentage (Abdul Rahaman et al., 2014; Arof et al., 2014). The percentage area of free ions, ion pairs and ion aggregates was estimated using Equation 2.6 and 2.7. In the present work for System I and System II, ion association occurs between NH_4^+ cation and NO_3^- anion. Thus, the possible dissociated ions were identified as NH_4^+ and NO_3^- free ions, whereas $\text{NH}_4^+\cdots\text{NO}_3^-$ ion pairs (contact ions) and highly aggregated ions/ion multiples were referred to the associated ions in both systems.

5.2.1 Ionic species analysis

FTIR spectra in the region between 1500 cm^{-1} and 1200 cm^{-1} has been investigated for ionic species analysis in System I as shown in Figure 5.10. This region was identified to show remarkable changes of FTIR pattern than other regions, thus was selected for this observation. The possible NH_4^+ and NO_3^- free ions, $\text{NH}_4^+\cdots\text{NO}_3^-$ ion

pairs (contact ions) and highly aggregated ions or ion multiples are expected to present within this region.

The band located at lower wavenumber around 1329 - 1319 cm^{-1} belongs to the $\delta(\text{C-OH})$ band of CMC. The weak peak at higher wavenumber between 1456 cm^{-1} and 1434 cm^{-1} is assigned to $\nu(\text{C-H})$ band of CMC which is shifted a bit further away from pure CMC film observed at 1417 cm^{-1} (refer to Figure 4.2). This is due to $\nu(\text{C-H})$ band overlapped with the NH_4NO_3 salt moieties. Kadir et al. (2011), Zhao et al. (2008), Wu et al. (2007), and Majid and Arof (2005) observed that asymmetric deformation mode, $\nu(\text{NH}_4^+)$ and asymmetric stretching mode, $\nu(\text{NO}_3^-)$ between 1500 cm^{-1} and 1300 cm^{-1} in their works. Thus, it can be suggested that free ions, ion pairs and ion aggregates from NH_4NO_3 salt may occur within this range. The shifting of $\delta(\text{C-OH})$ and $\nu(\text{C-H})$ band of CMC shows that the NH_4NO_3 salt has a great effect to those bands. Two component peaks attribute to the free ions and ion pairs vibrational modes could be spotted upon the deconvolution of FTIR spectra for SPE films containing 5 - 45 wt.% NH_4NO_3 (Figure 5.10(a)-(i)). The band of free ions is located at 1377 - 1341 cm^{-1} and the band at 1432 - 1413 cm^{-1} is ascribed to contact ion pairs. In addition, the formation of aggregated ions peak could be detected to emerge when 50 wt.% NH_4NO_3 (Figure 5.10(j)) was added. The ion aggregates of NH_4NO_3 salt is observed at 1383 cm^{-1} band.

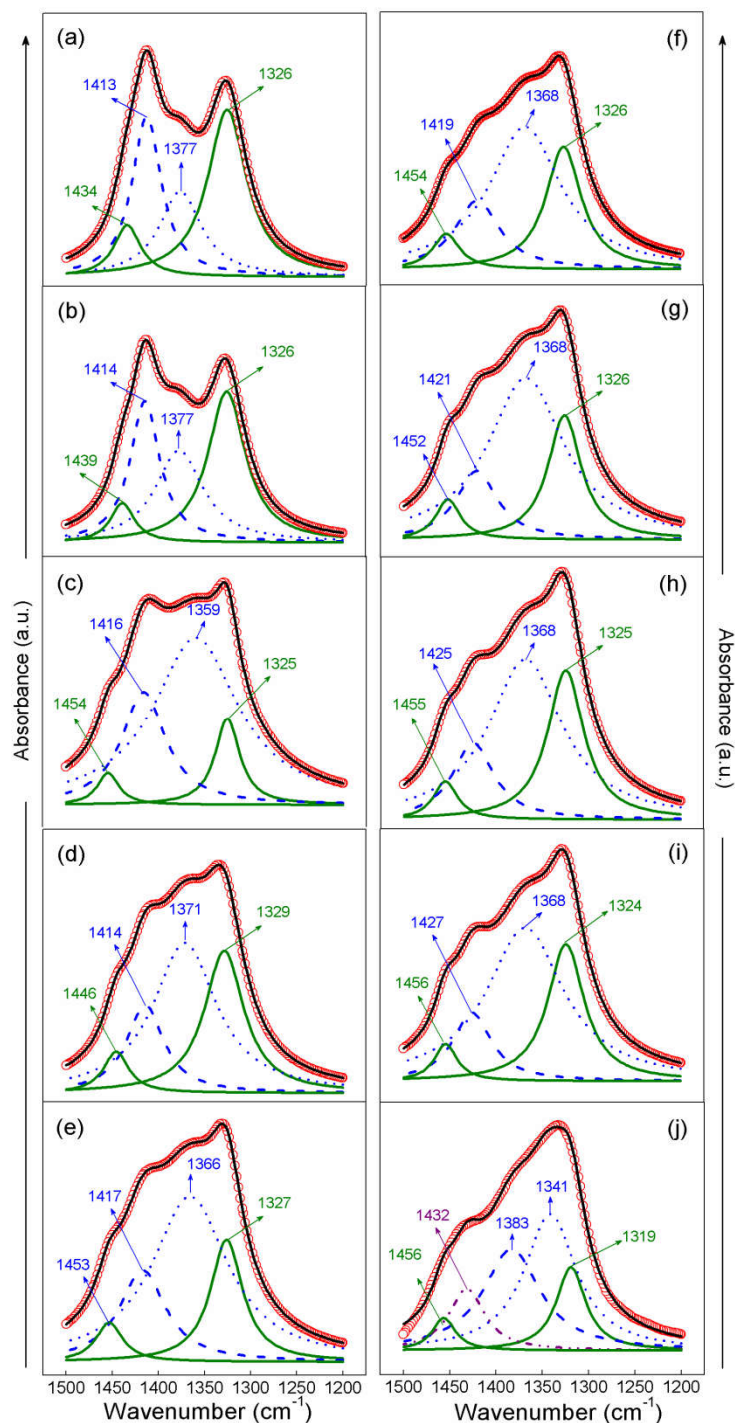


Figure 5.10 Deconvoluted FTIR spectra within 1500 – 1200 cm^{-1} wavenumber for System I films at varied NH_4NO_3 concentration. (a) 5 wt.% NH_4NO_3 , (b) 10 wt.% NH_4NO_3 , (c) 15 wt.% NH_4NO_3 , (d) 20 wt.% NH_4NO_3 , (e) 25 wt.% NH_4NO_3 , (f) 30 wt.% NH_4NO_3 , (g) 35 wt.% NH_4NO_3 , (h) 40 wt.% NH_4NO_3 , (i) 45 wt.% NH_4NO_3 , and (j) 50 wt.% NH_4NO_3 . *Note:* **Green** solid line (left) - (C-H) and (right) - (C-OH) characteristic bands of CMC. **Blue** dot line - free ions, dash line - ion pairs, and **purple** dash dot dot line - ion aggregates of NH_4NO_3 salt. **Red** open circles - experimental data and **black** solid line - fitted sum data.

Many researchers have been reported to correlate between the fraction of ionic species and the ionic conductivity of polymer electrolytes by using IR techniques such as Raman spectroscopy or FTIR spectroscopy (Ramya and Selvasekarapandian, 2014; Sim et al., 2012; Lim et al., 2012; Asmara et al., 2011; Holomb et al., 2006). Abdul Rahaman et al. (2014) and Arof et al. (2014) reported that the increment of ionic conductivity in polymer-salt systems was influenced by the fraction of free ions and ion pairs. In addition, the aggregation of ions may lead to the decrement of ionic conductivity in the polymer-salt system (Zainol et al., 2013).

The fraction of ionic species in System I was retrieved from the area under the peaks corresponding to each of constituents and plotted against NH_4NO_3 salt concentration as depicted in Figure 5.11. From the figure, it could be observed that the free ions dominated by more than half of the total ionic species (%). The ion pairs was found to be inversely proportional to the free ions with the addition of NH_4NO_3 salt. This also obviously can be seen from the intensity and area of the NO_3^- free ions which is greater than the ion pairs.

The maxima of free ions was achieved at 45 wt.% NH_4NO_3 . At 50 wt.% NH_4NO_3 , an abrupt drop of free ions can be discovered with a slight raise of ion pairs followed by a sudden grow of ion aggregates. This can be due to the formation/recombination of ions multiples from free ions and/or ion pairs, hence leading to neutralized aggregation of ions. This also may caused by the increasing of dipole interaction between H^+ and CMC bands (Rani et al., 2014). At the maxima of free ions (45 wt.% NH_4NO_3), it is believed to has the highest amount of free ions that may contribute to the conductivity. The existence of ion aggregates does not contribute to the conductivity enhancement. Similar results have been reported by

Sowthari et al. (2013), Lim et al. (2012) and Asmara et al. (2011). For that reason, SPE film incorporating with 45 wt.% NH_4NO_3 could be the most conducting film in System I and thus, this results confirmed the ionic conductivity analysis in Section 5.1.2 (Figure 5.6) determined by EIS technique.

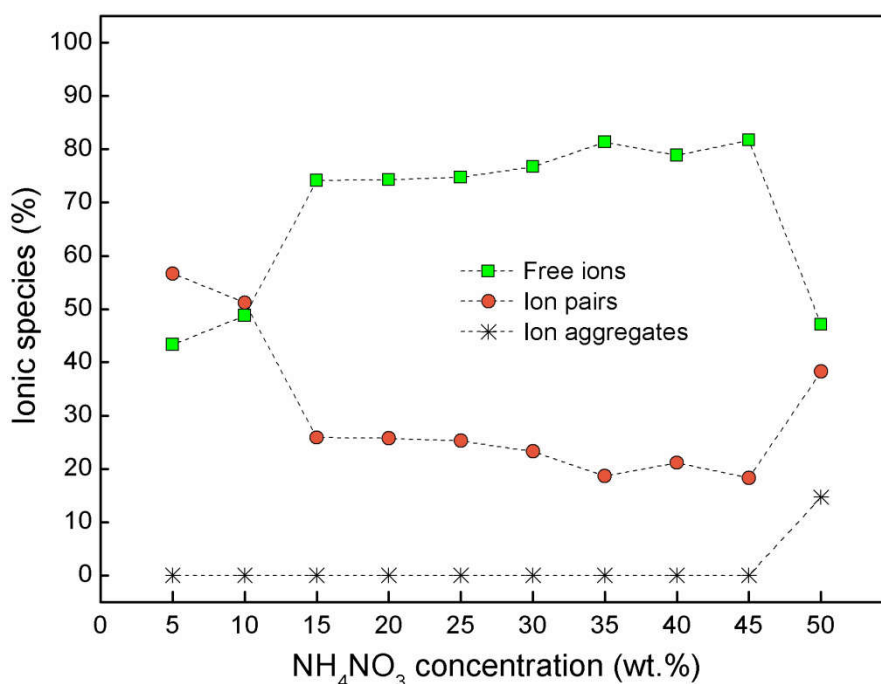


Figure 5.11 The percentage of ionic species of System I films at varied NH_4NO_3 salt concentration.

The ionic association was further investigated in System II. The deconvoluted FTIR spectra between 1500 cm^{-1} and 1200 cm^{-1} is exemplified in Figure 5.12. This region is expected to be affected due to the complexation of the system. In this region, no appreciable band corresponds to EG plasticizer is detected. Upon addition of EG in the System II, the two weak peaks assigned to the $\delta(\text{C-OH})$ and $\nu(\text{C-H})$ bands of CMC were observed to slightly shift in the peak positions. It can be seen that the $\delta(\text{C-OH})$ band was shifted to higher wavenumber from 1441 cm^{-1} to 1458

cm^{-1} , whereas the $\nu(\text{C-H})$ band tends to merge around $1321 - 1318 \text{ cm}^{-1}$ as EG was added into the system.

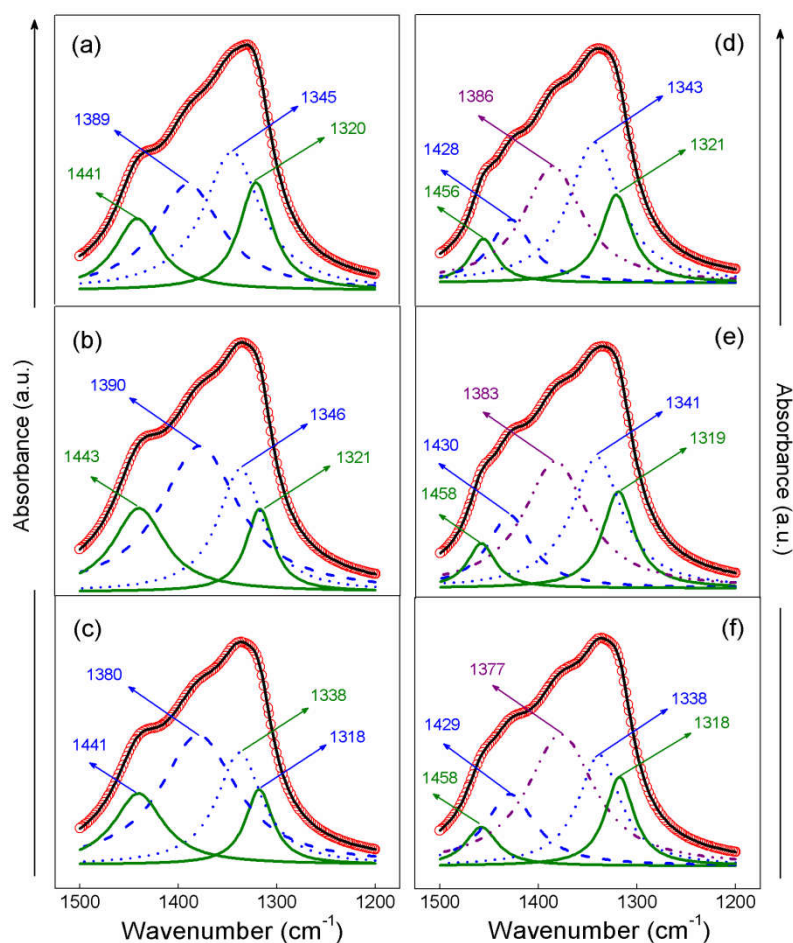


Figure 5.12 Deconvoluted FTIR spectra within $1500 - 1200 \text{ cm}^{-1}$ wavenumber for System II films at varied EG concentration. (a) 5 wt.% EG, (b) 10 wt.% EG, (c) 20 wt.% EG, (d) 25 wt.% EG, (e) 30 wt.% EG, and (f) 35 wt.% EG. *Note:* **Green** solid line (left) - (C-H) and (right) - (C-OH) characteristic bands of CMC. **Blue** dot line - free ions, dash line - ion pairs, and **purple** dash dot dot line - ion aggregates of NH_4NO_3 salt. **Red** open circles - experimental data and **black** solid line - fitted sum data.

The two intense peaks correspond to free ions and ion pairs were detected in the middle of $\delta(\text{C-OH})$ and $\nu(\text{C-H})$ bands of CMC. The free ions were discovered at 1345 cm^{-1} , 1346 cm^{-1} and 1338 cm^{-1} , whereas the ion pairs were located at 1389 cm^{-1} , 1390 cm^{-1} and 1380 cm^{-1} with the addition of 5 to 20 wt.% EG. The emergence of a new peak belongs to ion aggregates was spotted at 1386 cm^{-1} as 25

wt.% EG was added. Further addition of EG resulted in the change of the ion aggregates peak position to 1383 cm^{-1} (30 wt.% EG) and 1377 cm^{-1} (35 wt.% EG). At 35 wt.% EG, the peak intensity of ion aggregates was surpassed the peak intensity of free ions and ion pairs as shown in Figure 5.12(f).

The percentage of free ions, ion pairs and ion aggregates in System II was retrieved from the area under the peaks of corresponding constituents and represented in Figure 5.13. As can be seen in the figure, the free ions is inversely proportional to that of ion pairs, which is consistent with the result reported in the System I (Figure 5.11). The increment of ion aggregates can only be discovered beyond 20 wt.% EG addition, the similar increasing trend was detected for ion pairs. An abrupt jump of free ions about $\sim 30\%$ can be observed from 5 wt.% EG to 10 wt.% EG. After that, the free ions maintains at $\sim 82\%$ till 20 wt.% EG addition and eventually drop to $\sim 40\%$ at 25 wt.% EG. This fraction continually descending to $\sim 27\%$ at 35 wt.% EG. The maximum of free ions was obtained between 10 to 20 wt.% EG where it is expected to have the highest amount of free ions that may responsible to the high value of conductivity. 20 wt.% EG addition is likely the optimum EG concentration required in the System II to achieve the highest ionic conductivity. Beyond 20 wt.% EG addition, the free ions rapidly declined and the ion pairs and ion aggregates began to increase, signifying the formation of ion clusters/ion multiples and the increasing of dipole interaction between H^+ and CMC bands (Rani et al., 2014). Thus, further supported the ionic conductivity analysis in System II as elucidated in Section 5.1.2 (Figure 5.7) measured using EIS technique.

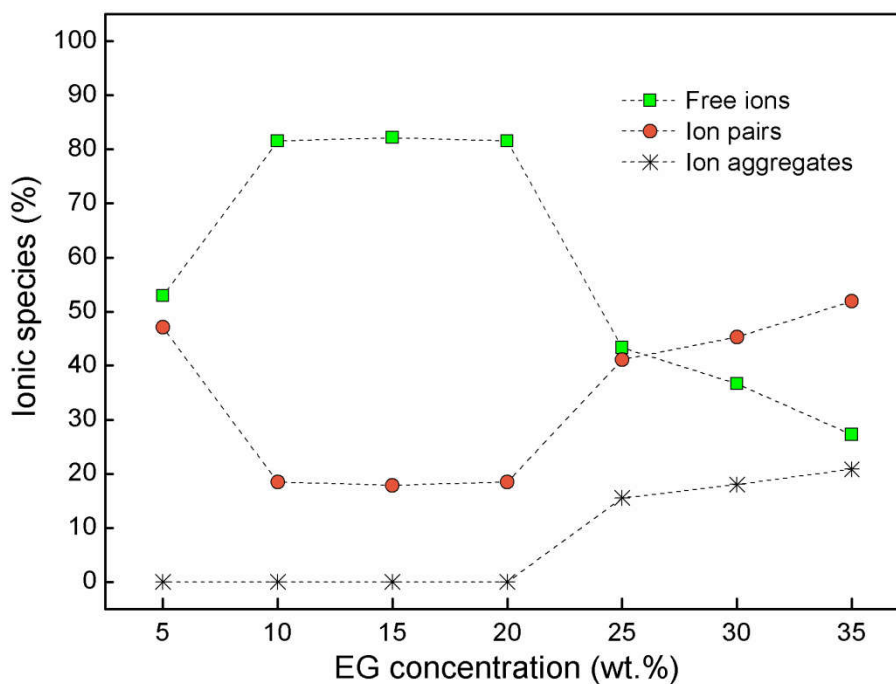


Figure 5.13 The percentage of ionic species of System II films at varied EG concentration.

Based on the observation on the fraction of ionic species in both systems, it can be inferred that the dependence of ionic conductivity with NH_4NO_3 and EG concentrations at ambient temperature is in agreement with the variation of the free ions. The fraction of free ions corresponds to the fraction of H^+ cation from NH_4NO_3 salt complexed with the oxygen atom of CMC polymer. The coordination of H^+ cation and $\text{C}=\text{O}$ bond of CMC was evidenced by FTIR analysis. A comparable behaviour can also be found in other polymer-salt systems by employing the similar method (Abdul Rahaman et al., 2014; Winie et al., 2014; Asmara et al., 2011; Wu and Chang, 2007; Rocco et al., 2004). Therefore, it can be deduced that the enhancement of ionic conductivity with the salt and plasticizer addition can be attributed to the increment in the number of free ions due to the greater dissociation of free ions.

5.2.2 Transport parameters

The conventional Rice and Roth method commonly applied to determine the transport parameters (i.e., n , μ and D) in various polymer electrolyte systems, strictly for Arrhenius-type systems. In the present work, the FTIR method which is applicable to Arrhenius and non-Arrhenius behaviour systems was employed to investigate the effect of NH_4NO_3 salt and EG plasticizer concentrations on the variation of transport parameters. This method utilized the information on the fraction of ionic species based on the deconvolution of FTIR spectra from the previous section. n can be related to the mass of mobile charge carriers, whereas μ and D can be regarded to the speed/velocity of mobile charge carriers and the distance/space between mobile charge carriers, respectively. The transport parameters in System I and System II were calculated according to Equation 2.8 - 2.10. The variation of transport parameters of mobile charge carriers in System I and System II is depicted in Figure 5.14 and Figure 5.15, respectively. The ionic transport behaviour in System I and System II can be explained as follows.

Figure 5.14 shows the dependence of σ on the n , μ and D with the addition of NH_4NO_3 salt in System I. It can be inferred that the increase in σ with NH_4NO_3 salt concentration could be assigned to an increase in the number of free ions or H^+ ions, leading to the fast movement of ions due to the increase of space/distance for ion migration. The slight increase of μ and D at 5 wt.% EG (Figure 5.14(b)) is ascribed to the high number of ion pairs compared to the free ions as shown in Figure 5.11. The decline of n , μ and D at higher NH_4NO_3 concentration (> 45 wt.% NH_4NO_3) is attributed to the recombination-ion association processes or formation of ion cluster due to the increase in ion pairs and ion aggregates in the system, which in turn reduce

the number of free ions. Hence, the dipole interaction between H^+ ions increase, resulting in the decrease of the σ (Srivastava and Chandra, 2000).

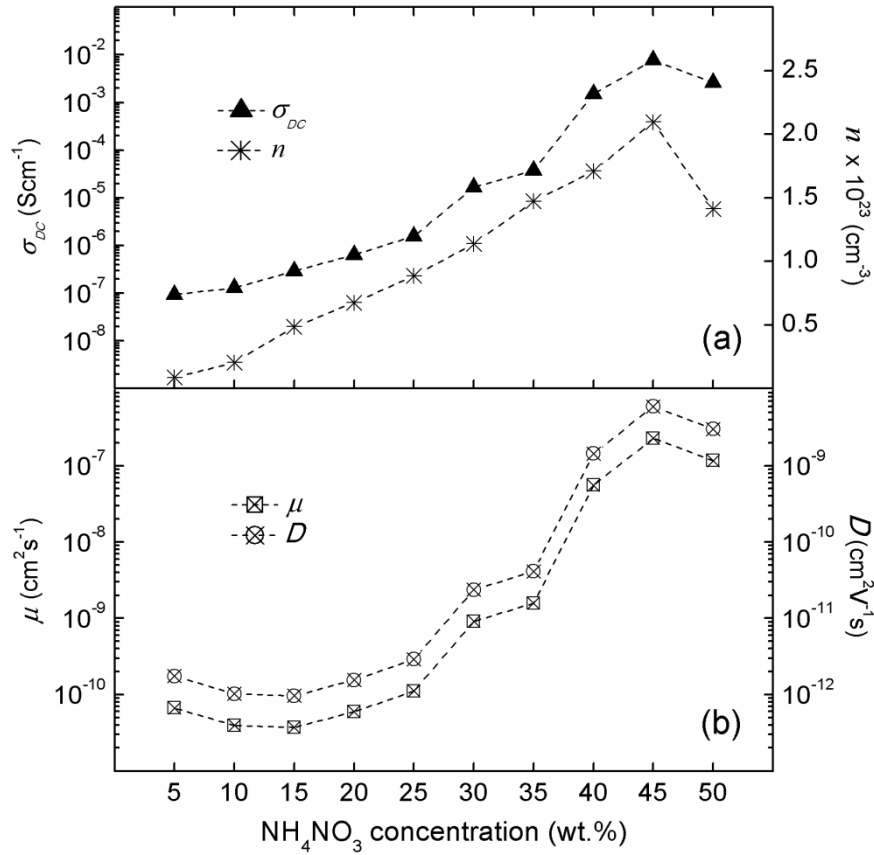


Figure 5.14 Transport parameters against NH_4NO_3 concentration of System I films. (a) Ionic conductivity, σ_{DC} , (b) number density of mobile ions, n , (c) mobility of ions, μ , and (d) diffusion coefficient, D .

Figure 5.15 represents the dependence of σ on n with the addition of EG plasticizer in System II. The trend in the variation of σ and n revealed in System II is quite similar to that in System I, which show the σ was controlled by n or σ is n dependence. However, μ and D do not favour the ion conduction in the system. A sudden drop of μ and D from 5 to 10 wt.% EG could be attributed to the greater dissociation of free ions as evidenced in Figure 5.13, thus reduce the association of ion pairs.

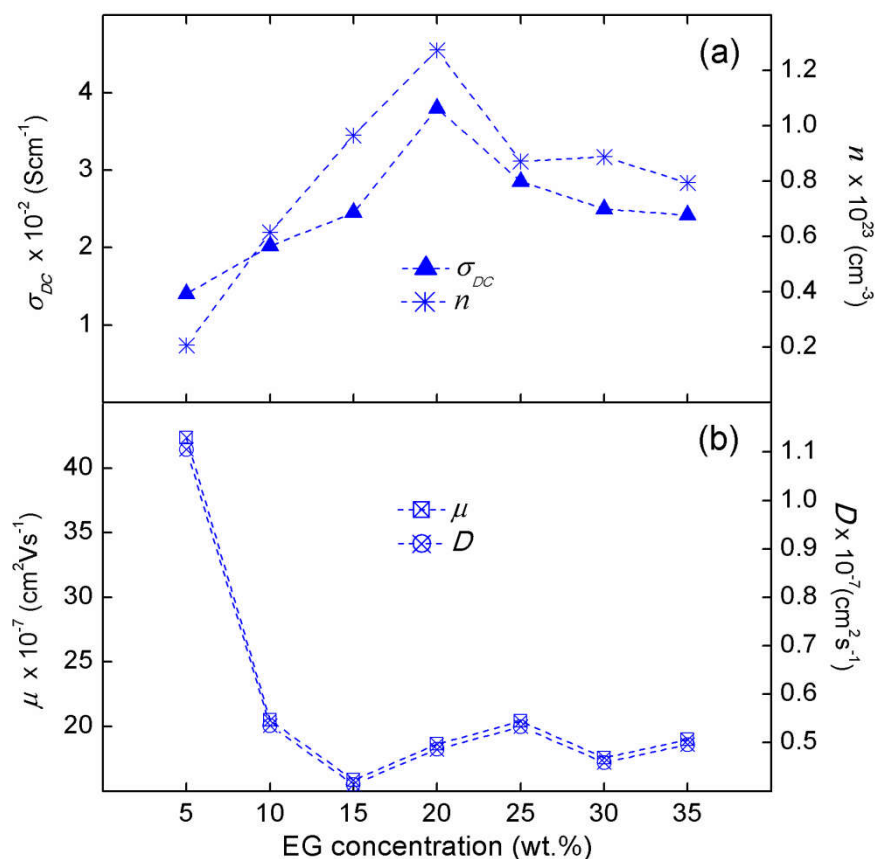


Figure 5.15 Transport parameters against EG concentration of System II films. (a) Ionic conductivity, σ_{DC} , (b) number of mobile ions, n , (c) mobility of ions, μ , and (d) diffusion coefficient, D .

Beyond > 10 wt.% EG concentration, the μ and D do not show an obvious trend signifying that the EG serves as a catalyst to promote ions movement and creating new pathways or routes for ions to hop from one site to another neighbouring site. In contrast, Yusof et al. (2014), and Mishra and Rai (2013) reported that the addition of plasticizer creates new pathways for ionic conduction, thus led to the increase in the ionic mobility. The decrement of σ at a higher EG concentration (> 20 wt.% EG) could be induced by the formation of ion pairs and ion aggregates, leading to the decrease in the number of free ions. However, in this case, the mobility and diffusion of ions did not show a significant impact to the decrease of

the σ . Further investigation on the effect of ionic mobility and diffusion coefficient of charge carriers are described in the following section.

5.2.3 Transference number

Ionic migration occurs when a voltage V , which is below the decomposition potential of the polymer electrolyte film, is applied to the cell until the steady state (saturated current) is achieved. At the steady state, the cell is polarized and any residual current flow is due to migration of electrons across the polymer electrolyte film and the interfaces (Nik Aziz et al., 2010). The transference numbers corresponding to the ionic, Γ_{ion} and electronic, Γ_{ele} constituents for System I and System II were determined based on the plot of normalized polarization current versus time via DC polarization technique. Figure 5.16 depicts the plots of normalized polarization current versus time for SPE film incorporating 45 wt.% NH_4NO_3 in System I and 20 wt.% EG in System II. The Γ_{ion} and Γ_{ele} were calculated based on Equation 2.14 and 2.15, respectively.

From the figure, it can be seen that the I_i decreases with time due to the depletion of the ionic contribution in the polymer electrolyte and becomes constant (saturated) in the fully-depletion stage. Saturated current is achieved after 60 minutes with Γ_{ion} about 0.67 for SPE film incorporating 45 wt.% NH_4NO_3 . While, SPE film incorporating 20 wt.% EG reaches saturated state within 15 minutes with a greater Γ_{ion} of 0.84. The shorter time required in the plasticized system may due to the rapid ionic migration of charge carriers in the host polymer facilitated by the plasticizer.

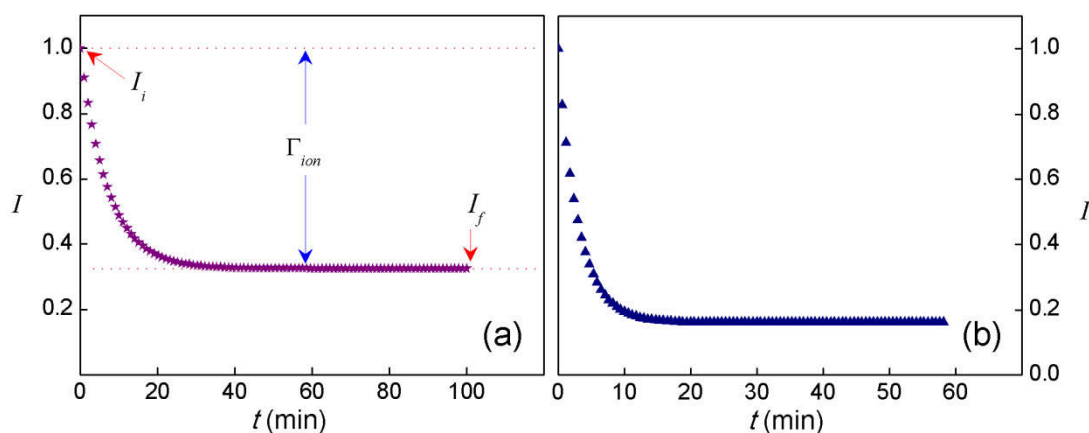


Figure 5.16 Normalized polarization current, I vs. time, t for the highest conducting SPE film incorporating (a) 45 wt.% NH_4NO_3 ($\Gamma_{ion} = 0.67$) and, (b) 20 wt.% EG ($\Gamma_{ion} = 0.84$) measured at room temperature.

Table 5.2 summarized the Γ_{ion} in System I and System II obtained at room temperature. Both systems show $\Gamma_{ion} > 0.5$ with the Γ_{ion} values in System II were found to be higher than those of System I. From the observation, the Γ_{ion} values suggest that the charge transport in both systems were predominantly due to ions accompanied by mass transport, the contribution of electronic species to the total current can be negligible. A similar observation has been found in CMC-ammonium salt based SPE systems as reported by Samsudin et al. (2014c and 2012c). The Γ_{ion} close to unity can be explained due to the cation of ammonium salt being closely attached to the CMC polymer backbone.

Table 5.2 Transference numbers of System I and System II films.

| SPE film | Transference number, F | | |
|---|--------------------------|-----------|-------------|
| | F_{ion} | F_{ele} | F_{total} |
| System I | | | |
| 5 wt.% NH ₄ NO ₃ | 0.83 | 0.17 | |
| 10 wt.% NH ₄ NO ₃ | 0.86 | 0.14 | |
| 15 wt.% NH ₄ NO ₃ | 0.83 | 0.17 | |
| 20 wt.% NH ₄ NO ₃ | 0.61 | 0.39 | |
| 25 wt.% NH ₄ NO ₃ | 0.60 | 0.40 | 1.0 |
| 30 wt.% NH ₄ NO ₃ | 0.72 | 0.28 | |
| 35 wt.% NH ₄ NO ₃ | 0.90 | 0.10 | |
| 40 wt.% NH ₄ NO ₃ | 0.78 | 0.22 | |
| 45 wt.% NH ₄ NO ₃ | 0.67 | 0.33 | |
| 50 wt.% NH ₄ NO ₃ | 0.65 | 0.35 | |
| System II | | | |
| 5 wt.% EG | 0.97 | 0.03 | |
| 10 wt.% EG | 0.98 | 0.02 | |
| 15 wt.% EG | 0.89 | 0.11 | |
| 20 wt.% EG | 0.84 | 0.16 | 1.0 |
| 25 wt.% EG | 0.95 | 0.05 | |
| 30 wt.% EG | 0.87 | 0.13 | |
| 35 wt.% EG | 0.95 | 0.05 | |
| 40 wt.% EG | 0.95 | 0.05 | |

In polymer electrolyte systems, there are two possible mobile ion/charge carrier species as either cations or anions. In order to identify the species of the charge carrier in System I and System II, the diffusion coefficient and mobility of cations and anions were determined based on Equation 2.16 - 2.18. The variation of μ_+ , μ_- , D_+ and D_- are depicted in Figure 5.17 and Figure 5.18 for System I and System II films, respectively.

In Figure 5.17, it can be observed that the μ_+ , μ_- , D_+ and D_- increase as the NH₄NO₃ concentration increase, the similar trend as that obtained by the μ and D of System I (Figure 5.14). In Figure 5.18, the μ_+ , μ_- , D_+ and D_- in System II shows the similar behaviour as the μ and D (Figure 5.15) except for 5wt.% EG. This can be ascribed to the low fraction of free ions in 5 wt.% NH₄NO₃ film than in 10 wt.%

NH_4NO_3 film as shown in Figure 5.11. In addition, μ_+ and D_+ were observed to be higher than μ_- and D_- for both systems. This indicates that the System I and System II films are more viable to be cationic (+) than anionic (-) conductor. Thus, confirmed that proton (H^+ ion) as charge species that responsible for ionic conduction to take place in both systems. This result also supports the possibility that the proton conduction in both systems is due to the Grotthuss mechanism as reported in FTIR analysis (refer to Section 4.2) since the oxygen atoms from the carbonyl group of CMC polymer can serve as good proton acceptor and thus provides free pathways for proton mobility.

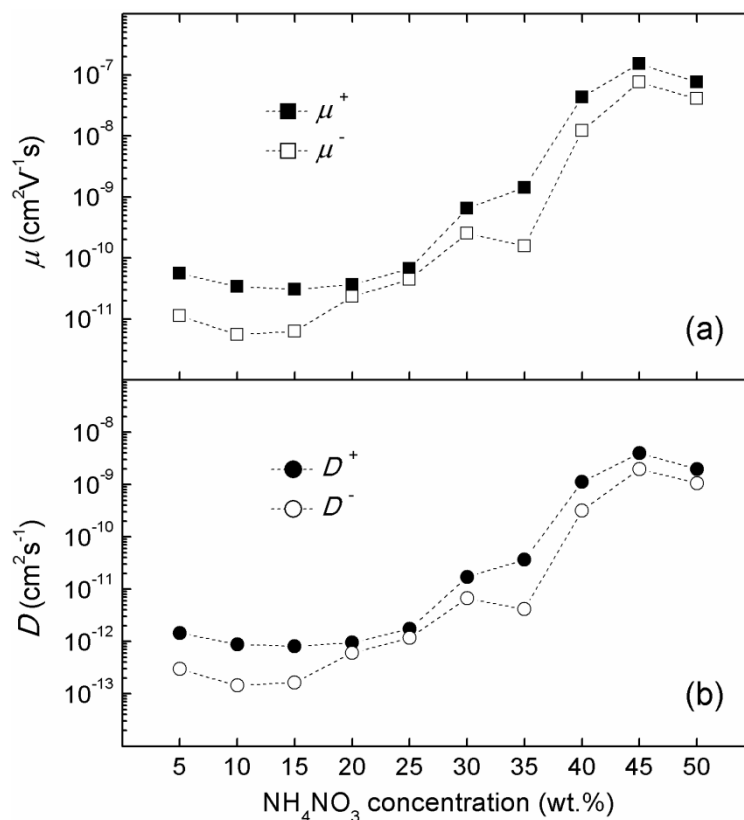


Figure 5.17 The relation of (a) mobility and, (b) diffusion coefficient of cations and anions against NH_4NO_3 concentration for System I films.

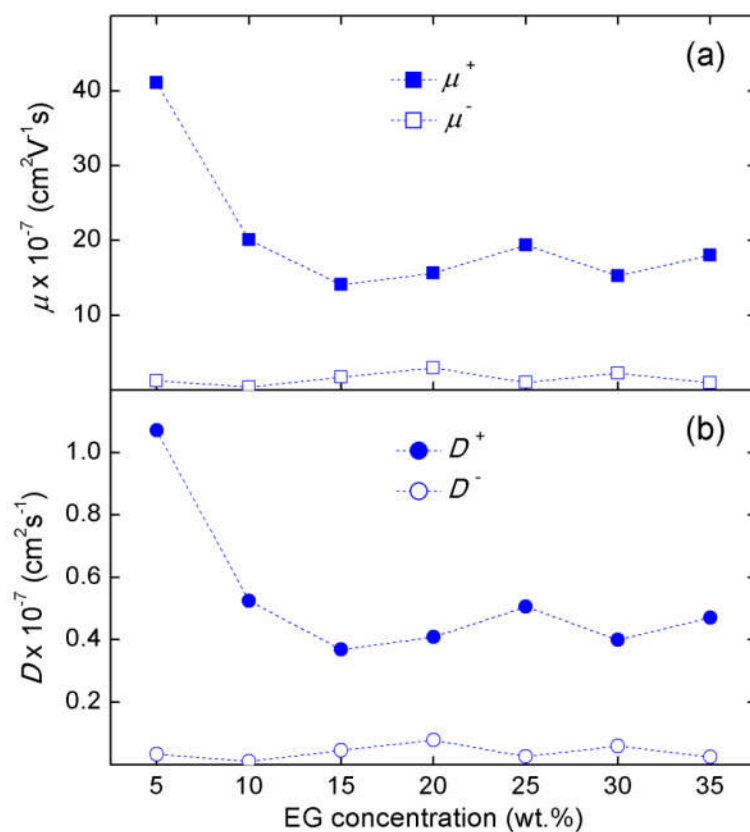


Figure 5.18 The relation of (a) mobility and, (b) diffusion coefficient of cations and anions against EG concentration for System II films.

5.3 Electrical studies

The conductivity behaviour of SPEs can be further studied by electrical studies. In this section, the effect of adding NH_4NO_3 salt and EG plasticizer on the electrical properties such as dielectric constant, dielectric loss, real modulus, and imaginary modulus with the applied electric field frequency at selected temperature range are presented and discussed.

5.3.1 Dielectric and modulus

The conductivity behaviour of SPEs can be understood from dielectric studies. The dielectric study is favourable due to the separable contribution of bulk materials and

interfacial effects at the electrodes (Woo et al., 2012). The dielectric constant, ϵ_r is a measure of the material's polarization, associated with the capacity to retain/store electric charge (i.e. stored energy) and also represents the amount of dipole alignment in a given volume, whereas the dielectric loss, ϵ_i is a measure of energy losses/dissipates during ions movement and dipoles alignment when the polarity electric field reverse rapidly (Shukur et al., 2014; Yusof et al., 2014a; Woo et al., 2012). Aziz and Abidin (2013) define ϵ_r as a measure of reduction of Coulomb interaction between the pair ions in polymer electrolytes. Thus, provides useful information on the ionic/molecular interaction of polymer electrolytes and ionic transport behaviour (Aziz and Abidin, 2013; Hema et al., 2008). The values of ϵ_r and ϵ_i can be calculated using Equation 3.2 and 3.3, respectively.

Figure 5.19 represents the variation of ϵ_r and ϵ_i as a function of frequency for pure CMC, System I and System II films at 303K. The ϵ_r and ϵ_i of pure CMC film (Figure 5.19(a-b)) decreases exponentially towards higher frequencies. A similar trend also can be seen for SPE films in System I (Figure 5.19(c-d)) and System II (Figure 5.19(e-f)), where ϵ_r and ϵ_i are very high at low frequencies and decrease with the increase of frequencies, and become close to zero or saturated at higher frequencies. The abrupt decrease of both ϵ_r and ϵ_i at low frequency region is a result of electrode polarization effects or blocking electrodes effects or also called space charge effects (Woo et al., 2013; Ramesh and Chai, 2007; Yahya and Arof, 2003). In this region, ions move along the direction of the electric field, but cannot be transported to the external circuit due to the blocking electrodes. Thus, results in the ions trapped near the electrode-electrolyte interface and causing the formation of a hetero-charge layer known as electrode polarization (Woo et al., 2013). As the frequency increases, the dielectric parameters decrease drastically and eventually

saturate in the high frequency region. At high frequency, ion diffusion in the electric field is unattainable due to periodic orientation/reversal of the applied electric field (Shukur et al., 2014). Consequently, leading to the decrease in both dielectric parameters as a result of free charges building up at the interface between the electrolyte and the electrode (i.e. charge accumulation at electrolyte-electrode interface) (Nithya et al., 2015; Vijaya et al., 2012; Vieira et al., 2007).

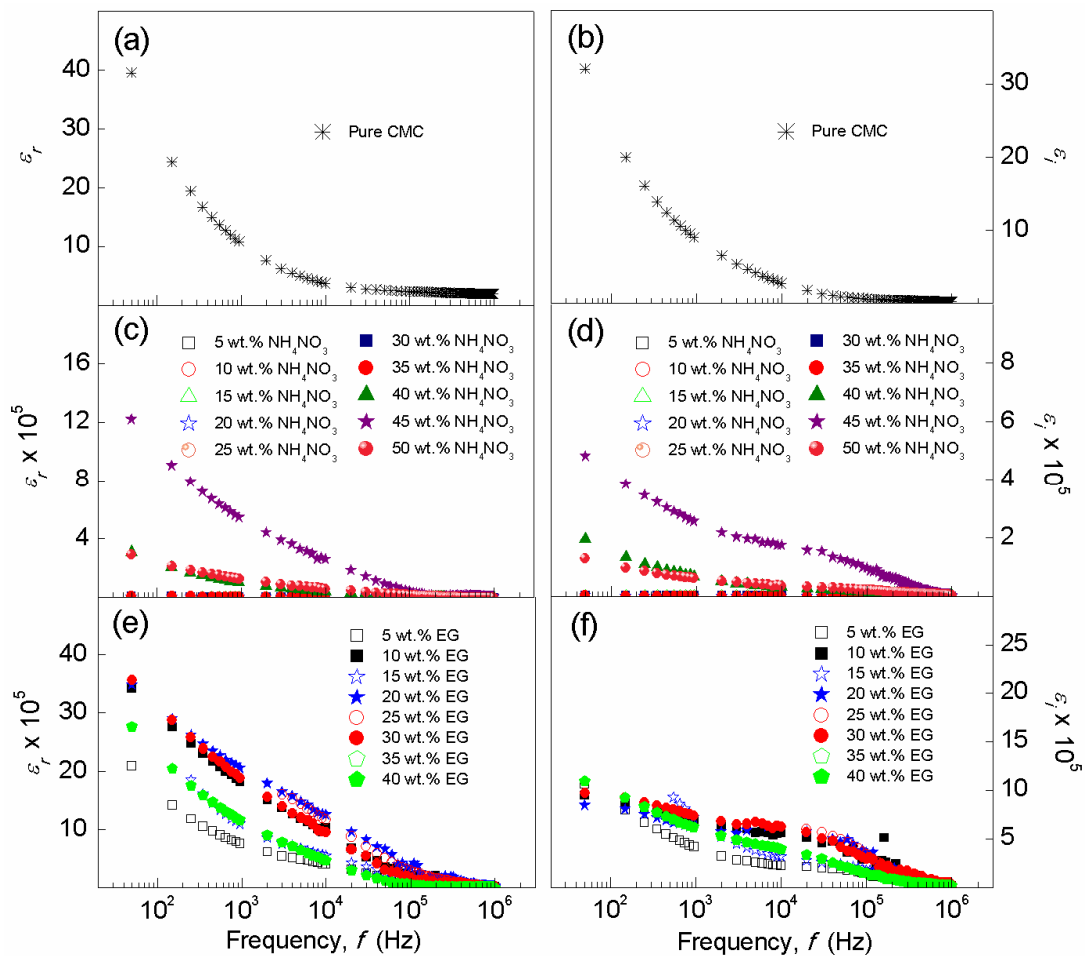


Figure 5.19 The dependence of ϵ_r and ϵ_i on frequency for (a-b) pure CMC, (c-d) System I, and (e-f) System II films at ambient temperature, 303K.

In addition, the values of ϵ_r and ϵ_i are observed to increase as NH_4NO_3 salt and EG plasticizer concentrations increase to 45 wt.% NH_4NO_3 and 20 wt.% EG, respectively. As the NH_4NO_3 concentration increases, the charge stored in the

electrolyte increases. Thus, increase the number density of mobile ions, n and subsequently increase the conductivity (Buraidah et al., 2009). The declining of ϵ_r and ϵ_i values for electrolytes incorporating with greater than 45 wt.% NH_4NO_3 is assigned to the re-association of ions, resulting in the decrement of conductivity (Woo et al., 2011). Nithya et al. (2013) and Samsudin and Isa (2012b) reported that both ϵ_r and ϵ_i results are in good agreement with the conductivity results of PAN- NH_4NO_3 and CMC- NH_4Br systems, respectively, which is comparable with the present work. When the EG plasticizer is added into the unplasticized system, the rate of ion dissociation raises (i.e., high dissociation ability to hinder ion-pair formation or high effectiveness on preventing the inter-ionic Coulomb attraction between cations and anions) (Woo et al., 2011; Yahya et al., 2003) due to the high ϵ_r value (37.0) of pure EG, leading to the enhancement of conductivity. As reported by similar authors, the PC-plasticized PAN- NH_4NO_3 system and EC-plasticized CMC- NH_4Br system with higher conductivity values exhibit higher ϵ_r values (Nithya et al., 2015; Samsudin and Isa, 2014b).

Figure 5.20 shows the variation of ϵ_r and ϵ_i as a function of frequency for pure CMC film, and the highest conducting SPE films in System I and System II, respectively at 303K - 353K. For clarity of presentation, several films in System I and System II were selected and analyzed. The remaining results of films in both systems are allocated in Appendix 5 - 8. As depicted in the figure, the values of ϵ_r and ϵ_i increase with the increasing of temperatures for all systems. This can be attributed to the migration of polarization of the mobile charge carriers, confirming the plurality relaxation mechanism and non-Debye behaviour of the polymer electrolytes. As the temperature increases, the degree of dissociation and re-

dissociation of ion aggregates increases, thus result in the increase of the number of free ions or charge carrier density, which assists in the increment of conductivity (Rani et al., 2015a; Nithya et al., 2015). The sharp decrease of ϵ_r and ϵ_i values towards higher frequencies indicates the occurrence of electrode polarization effects (Rani et al., 2015b). At the high frequency region, the rate of the periodic reversal of the applied field increases. Hence, no charge build up at the electrode-electrolyte interface due to the decrease of the polarization effect by the charge accumulated, leading to the drop of ϵ_r and ϵ_i values (Vieira et al., 2007).

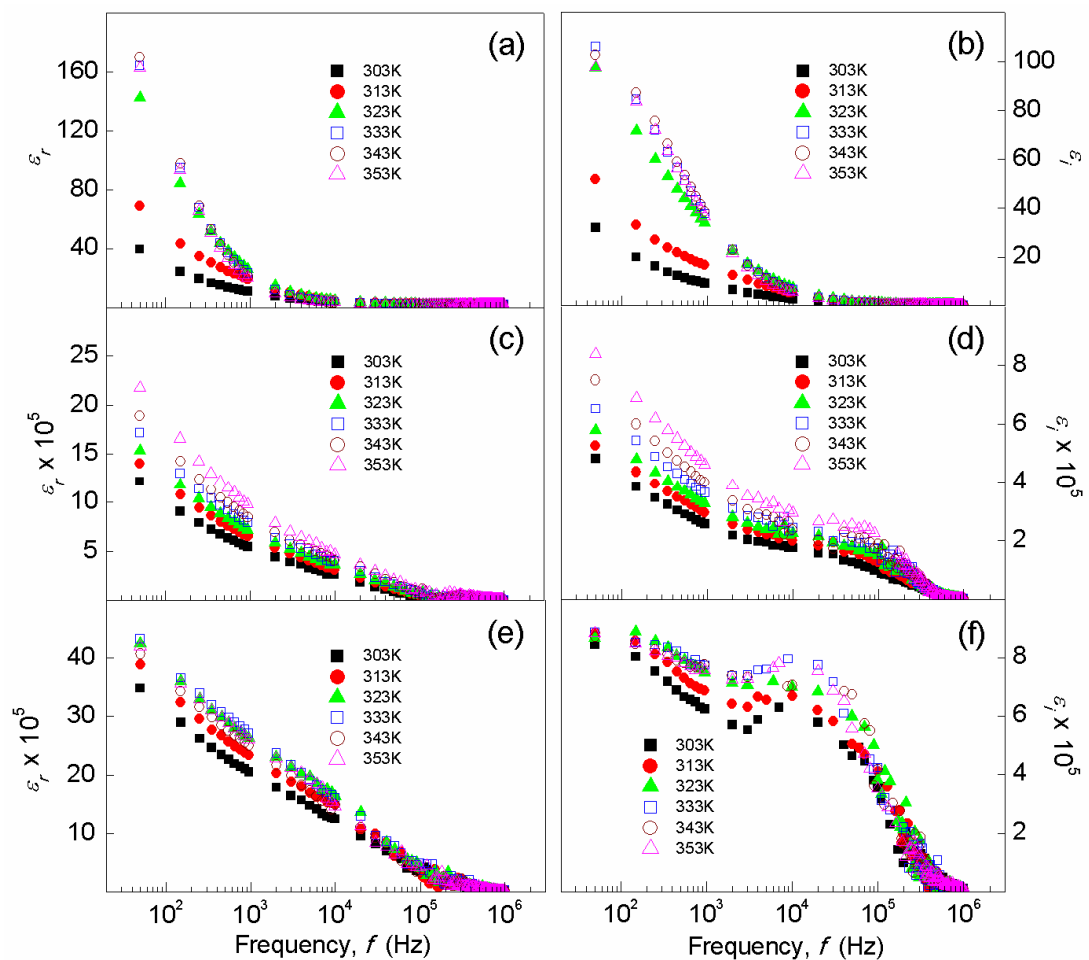


Figure 5.20 The dependence of ϵ_r and ϵ_i on frequency for (a-b) pure CMC film, and the highest conducting SPE film in (c-d) System I, and (e-f) System II at selected temperatures, 303K - 353K.

In addition, no appreciable relaxation peaks were observed in the frequency range employed in this study for ϵ_r , thus implying that the increment of conductivity can be assigned to the increase of the number of charge carrier density. However, the ϵ_i for the highest conducting in System I (Figure 5.20(d)) and System II films (Figure 5.20(f)) shows the appearance of a dominant dielectric relaxation peak with the maximum shifted upwards as the temperature increases. Nithya et al. (2015), Tamilselvi et al. (2014) and Vijaya et al. (2012) claimed that this peak belongs to the high-frequency β -relaxation peak as a result of the side group dipoles and the nearest part of the polymer backbone. In polymer, the influence of temperature affects the segmental motion and polymer chain which result in the occurrence of α -, β -, and γ -relaxations indicates by the emergence of ϵ_i relaxation peak as detailed in Ahmad (2012) and Damez et al. (2007). In addition, Das et al. (2014) reported that one of the main contributions to the energy loss/dissipation in polymer-salt system is the relaxation of the ionic species or dipoles (ion pairs). This involves two types of relaxation processes, (i) the low-frequency α -relaxation, arising due to the segmental relaxation of polymer chains and considered as a slow relaxation process, and (ii) the high-frequency β -relaxation, resulting from the local relaxation of an ion rich section of polymer matrix or dipoles in polymer chain and associated with a fast relaxation process. The occurrence of conductivity relaxation peak in this study implies that the SPE film is an ionic conductor (Shukur et al., 2014; Woo et al., 2012).

The dielectric behaviour was further explored by using the formulation of dielectric moduli, which restrain/suppress the electrode polarization effects (Ramesh and Wong, 2009) and also investigated the relaxation phenomena in the polymeric system. The relation of the real (M_r) and imaginary (M_i) parts of electrical modulus is

given by Equation 3.4 and 3.5. Figure 5.21 represents the variation of M_r and M_i as a function of frequency for pure CMC, System I and System II films at 303K.

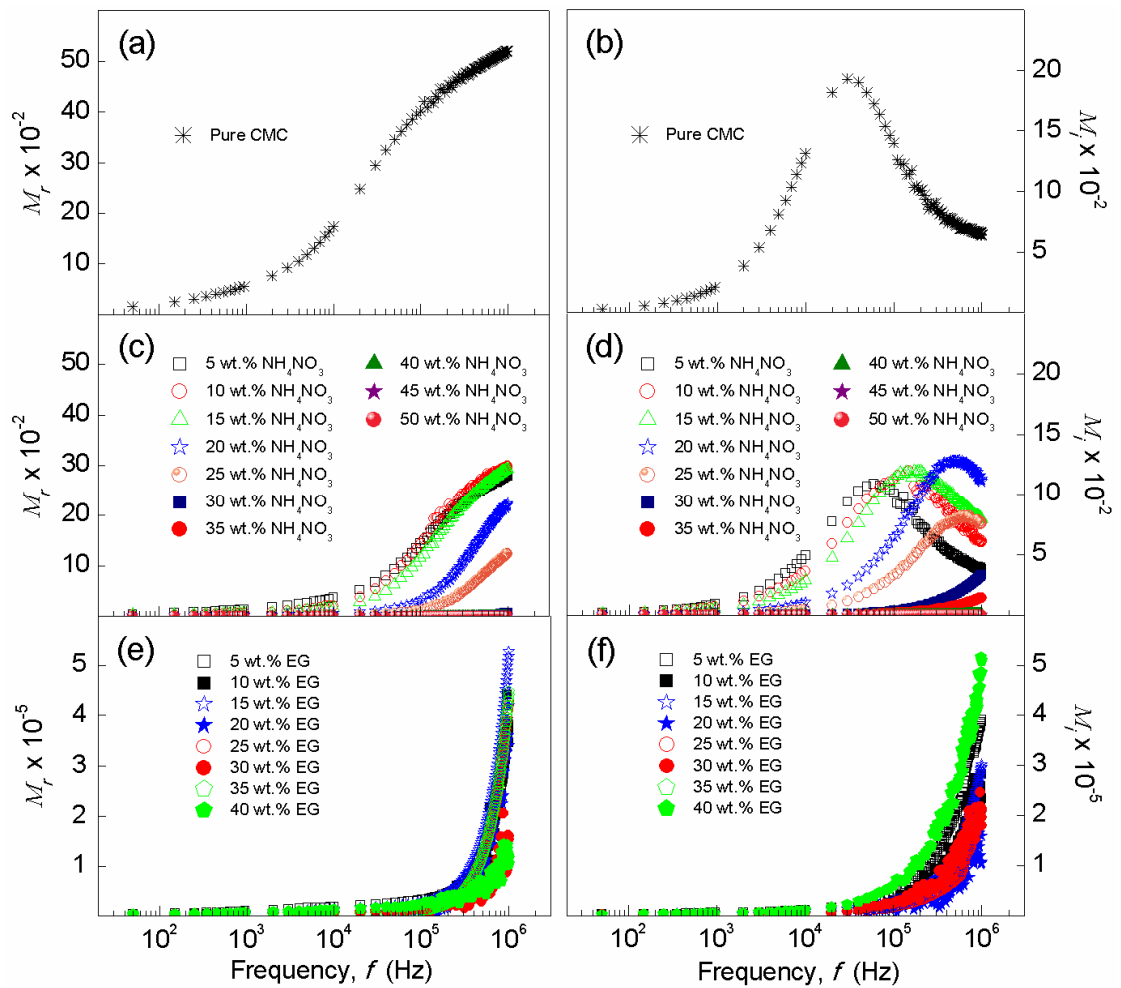


Figure 5.21 The dependence of M_r and M_i on frequency for (a-b) pure CMC, (c-d) System I, and (e-f) System II films at ambient temperature, 303K.

The M_r of pure CMC film (Figure 5.21(a)) was revealed to increase gradually towards higher frequencies. A similar trend of M_r was observed with the addition of NH_4NO_3 salt and EG plasticizer (Figure 5.21(c) and (e)). The long tail approaching zero at the low frequency region reflects the suppression of electrical double layer effect (high capacitance value) at the electrode-electrolyte interface, showing a negligible contribution of electrode polarization phenomena (Ramesh et al., 2011; Ramesh and Chai, 2007). The M_r shows an increase at the high-frequency end with

sigmoid shapes/curves appear in most of the films, however no well-defined dispersion peaks were observed. The curves at the higher frequency can be assigned to the bulk effect and the decrease of curve height with the NH_4NO_3 salt and EG plasticizer concentration, indicating a plurality of the relaxation mechanism (Ramesh et al., 2011; Mishra and Rao, 1998).

The long tail at the low-frequency region of M_i (Figure 5.21(b), (d) and (f)) is attributed to the large capacitance associated with the electrode and small contribution from electrode polarization can be negligible (Ramesh et al., 2011; Ramesh and Chai, 2007). As the frequency increases, pure CMC film shows an asymmetric peak broadening centred at 30k Hz. With the addition of NH_4NO_3 salt into the System I, 5 - 20 wt% NH_4NO_3 films show incomplete distribution peaks centred at 60k Hz (5 wt.% NH_4NO_3), 170k Hz (10 wt.% NH_4NO_3), 520k Hz (15 wt.% NH_4NO_3), 630k Hz (20 wt.% NH_4NO_3) and 650k Hz (25 wt.% NH_4NO_3), respectively which represent the conductivity relaxation peaks for the distribution of relaxation times of the free charge (Yahya and Arof, 2003; Mishra and Rao, 1998). However, beyond 25 wt.% NH_4NO_3 , the value of M_i is close to zero. The relaxation time, τ can be calculated from Equation 3.6. The shifting of the relaxation peaks to a higher frequency range with the addition of NH_4NO_3 concentration indicates the shorter relaxation time (i.e., faster relaxation process), resulting in the increase of conductivity. The presence of relaxation peaks signify that the SPE films are ionic conductors (Woo et al., 2012; Ramesh and Wong, 2009; Yahya and Arof, 2003).

When EG was added into System II, only M_i curves appear, hence, no well-defined distribution peaks have been observed prior to the increase of M_i at the high-frequency end. Thus, no conductivity relaxation was observed within the specific frequency range. This may be due to the experimental frequency limitation, therefore no well-defined peak can be seen.

Figure 5.22 shows the variation of M_r and M_i as a function of frequency for pure CMC film, and the highest conducting SPE films in System I and System II, respectively at 303K - 353K. For clarity of presentation, several films in System I and System II were selected and analyzed. The remaining results of films in both systems are assigned in Appendix 9 - 12. The long tail in the M_r and M_i versus f plots correspond to the capacitive nature of films and the occurrence of the relaxation peaks observed in M_i against f plot for pure CMC film (Figure 5.22(a)) implies the distribution of relaxation times of the ionic conductors (Woo et al., 2012). In addition, the intensity of the peak decreases with the increasing of temperature suggesting a plurality of relaxation mechanism which also confirmed the non-Debye dependence of film (Shukur et al., 2014). No relaxation peak was observed in the highest conducting System I and System II films as shown in Figure 5.22(d) and Figure 5.22(f), respectively.

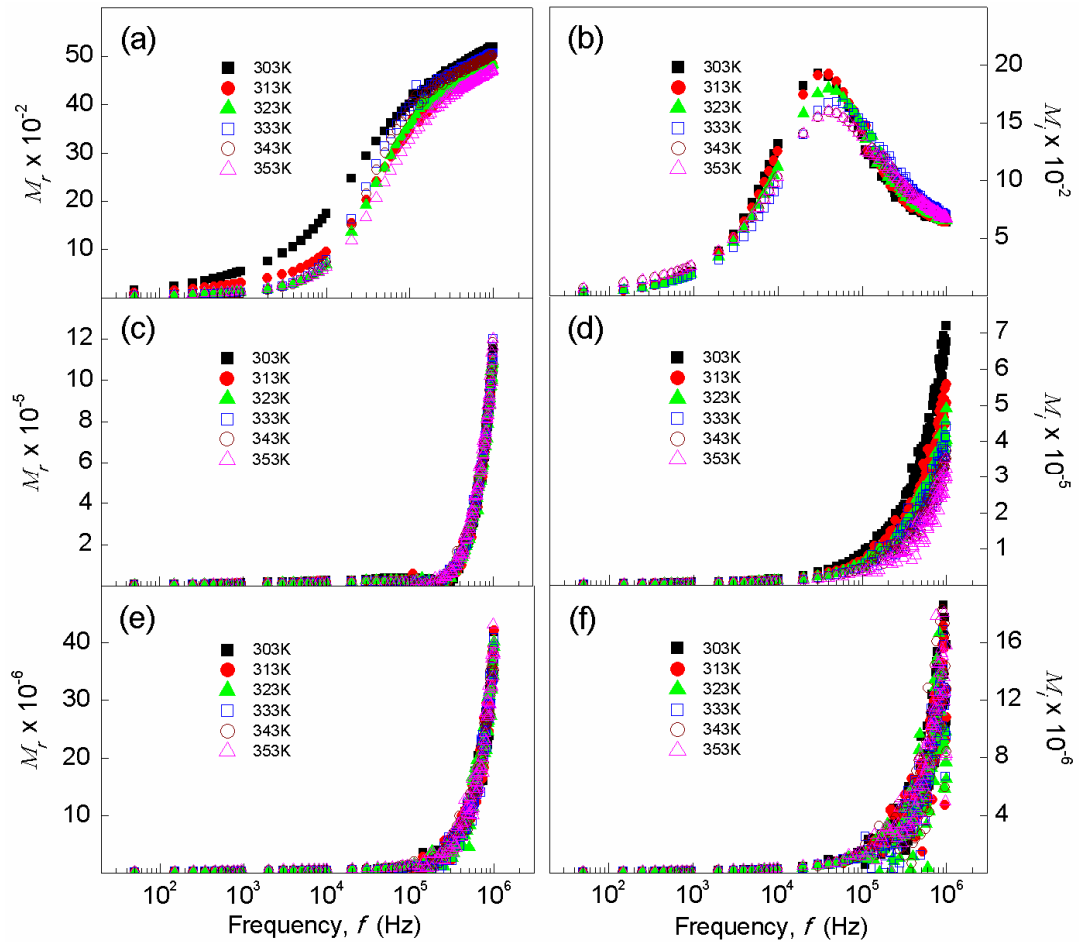


Figure 5.22 The dependence of M_r and M_i on frequency for (a-b) pure CMC film, and the highest conducting SPE film in (c-d) System I, and (e-f) System II at selected temperatures, 303K - 353K.

5.3.2 Hopping mechanism

According to Ravi et al. (2013), for polymer electrolyte system inherited an Arrhenian behaviour of conductivity-temperature relationship, the ionic conduction is by a hopping mechanism. As the temperature increases, the polymer chain requires faster internal modes in which bond rotations cause segmental motion. This subsequently results in the movement of ions via inter-chain and intra-chain hopping, leading to the increasing of conductivity with temperature in the polymer electrolyte.

In the present systems, this hopping phenomena has been proposed and illustrated in Figure 4.10 and Figure 4.11.

To further investigate the possible hopping mechanism involves in the System I and System II, the highest conducting film in both systems were studied. Figure 5.23(a-f) depicts plots of σ_{AC} , $\ln \sigma_{AC}$ and power law exponent s for 45 wt.% NH_4NO_3 film, and 20 wt.% EG film. Based on the Jonscher's Universal Power Law (Equation 2.19 - 2.24), the values of s were procured from the gradient of $\ln \sigma_{AC}$ against $\ln \omega$ plots and the plots of exponent s against temperature are shown in Figure 5.23(c) and (f). It can be observed that the exponent s is approximate ~ 0.8 and ~ 0.9 for 45 wt.% NH_4NO_3 film and 20 wt.% EG film, respectively. The small gradient of 0.0004 (Figure 5.23(c)) and 0.0015 (Figure 5.23(f)) from the linear fitted plots signifies that the exponent s almost independent of temperature. The variation of exponent s with temperature suggests that the frequency dependence for both films can be inferred to quantum mechanical tunneling (QMT) which is more applicable in elucidating the conduction mechanism in plasticizer-free and plasticized systems. The various theoretical models for AC conductivity have been well detailed in Section 2.2.3.

The QMT model was first proposed by Pollak and Geballe (1961) to describe impurity conduction in n -type silicon where the exponent s is temperature independent and frequency dependent. In conduction mechanism of QMT, the polarons (i.e. the protons and their stress field) is capable to tunnel through the potential barrier that exists between two possible complexation sites (Shukur et al., 2013b; Buraidah and Arof, 2009; Majid and Arof, 2007). Psarras (2006) inferred that hopping as the movement of a charge carrier (H^+ ion) from one site to another

neighbouring site and occurs not only by jumping/hopping over a potential barrier, but also accompanied by quantum mechanical tunneling.

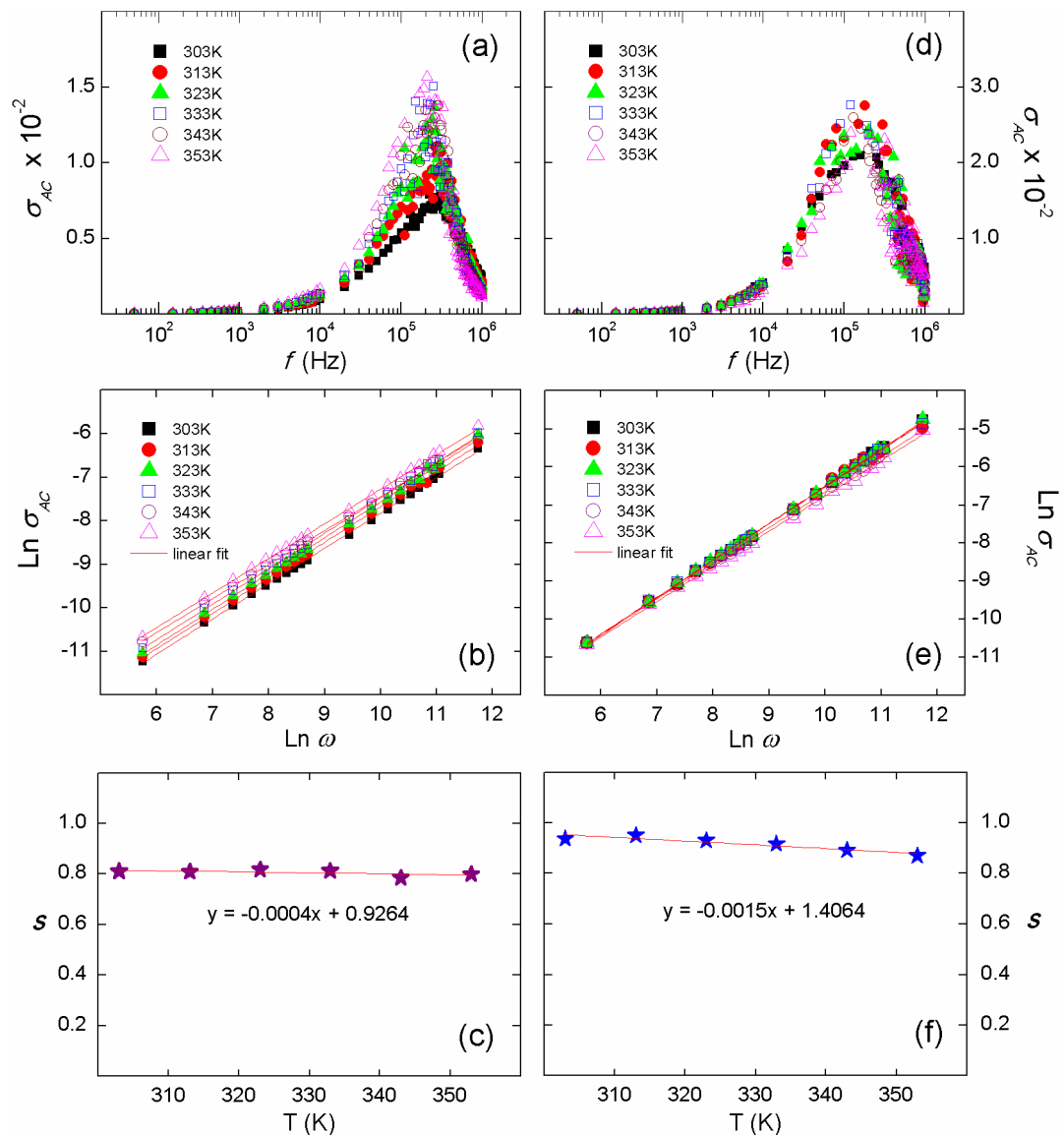


Figure 5.23 Plots of σ_{AC} , $\ln \sigma_{AC}$ and power law exponent s for (a-c) 45 wt.% NH₄NO₃ film in System I and (d-f) 20 wt.% EG film in System II obtained at elevated temperatures.

For plasticizer-free polymer-salt system, the present result for System I is comparable with the findings reported by Hafiza and Isa (2014) and Kamarudin et al. (2015) for the CMC-chitosan-NH₄Br and CMC-chitosan-NH₄NO₃ systems, respectively. However, the results obtained in the present work are disagreement

with the results demonstrated by Samsudin and Isa (2012a, 2012b) and Chai and Isa (2012a). The CMC system incorporating either with DTAB, NH_4Br or oleic acid, those systems follow SPH model where the exponent s increases linearly with the temperature due to a large degree of local lattice distortion as a result of small polarons formation.

For plasticized polymer-salt system, CMC- NH_4Br and CMC-DTAB systems using EC as plasticizer (Samsudin et al., 2015; Isa and Samsudin, 2013) were reported to follow QMT model, which is in agreement with the plasticized system (System II) in the present work using EG as plasticizer. According to Shukur and Kadir (2015a), the difference in the ionic conduction mechanism in plasticizer-free and plasticized systems can be ascribed to the difference of E_a value. In this work, the E_a value of the highest conducting film in System I ($E_a = 0.16$ eV) is quite close to the System II ($E_a = 0.10$ eV), thus it's consider to has similar conduction mechanism i.e., quantum mechanical tunneling.

CHAPTER 6

ELECTROCHEMICAL CELL PERFORMANCE

This chapter demonstrates the potential of SPEs to be employed in the solid-state electrochemical cells. For practical application in electrochemical devices as described in literature, the ionic conductivity of SPEs should possess $\sigma \geq 10^{-4} \text{ Scm}^{-1}$. Thus, the highest conducting SPE films in System I and System II were selected based on the ionic conductivity analysis in Chapter 5. The rechargeable proton batteries were fabricated following the method as mentioned in Chapter 3. Electrochemical characteristics are important to verify the performance and durability of solid-state rechargeable proton batteries that have been prepared. The electrochemical characterization was carried out using potentiostat-galvanostat and high accuracy battery tester.

6.1 Linear sweep voltammetry

In the present work, linear sweep voltammetry (LSV) measurement was carried out in order to study the electrochemical window stability of the SPE films and also to determine the maximum operating voltage an electrochemical device can achieve (Rudhziah et al., 2015; Subba Reddy et al., 2003). The LSV was performed on the highest conducting SPE films in the System I and System II. The corresponding LSV plots are shown in Figure 6.1. It can be observed that the breakdown/decomposition voltage of 45 wt.% NH_4NO_3 film and 20 wt.% EG film is 1.55 V and 1.50 V,

respectively. The divergence of LSV values for both films indicated that the plasticized film which has higher ionic conductivity is more stable and can be applied on high current application compared to the plasticizer-free film.

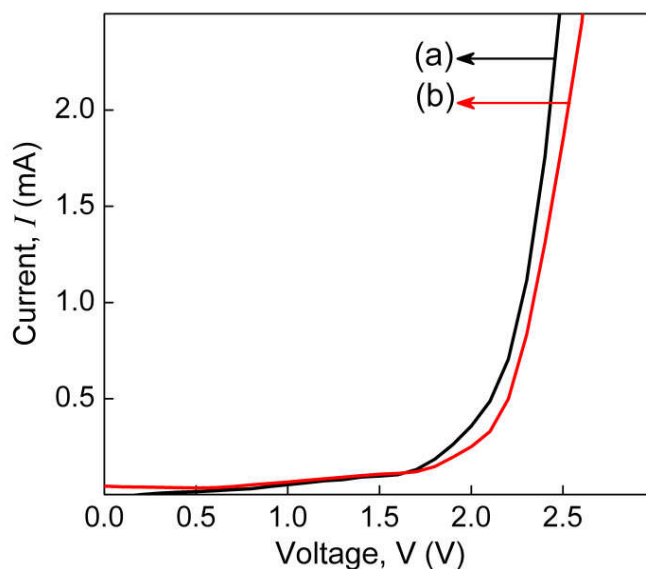


Figure 6.1 LSV for (a) 45 wt.% NH_4NO_3 and (b) 20 wt.% EG films measured at room temperature.

The standard electrochemical window for proton batteries is ~ 1 V (Pratap et al., 2006). Therefore, the LSV result suggests that both films are suitable to be used in the fabrication of electrochemical devices, particularly for proton batteries. Table 6.1 lists the LSV values for different polymer electrolyte systems as reported by several authors, which is comparable to the present work.

Table 6.1 The LSV values of different electrolyte systems as reported in literature compared to the present work.

| Electrolyte system | Rate (mVs ⁻¹) | LSV(V) | Potential application | Reference |
|--|---------------------------|--------|--------------------------------|-----------------------|
| CMKC-CMC blends | 1 | 2.75 | DSSC | Rudziah et al., 2015 |
| CMC-CH ₃ COONH ₄ | 1 | 2.50 | Solar cells/ Proton battery | Rani et al., 2014 |
| CMC- NH ₄ Br | 1 | 1.42 | Proton battery | Samsudin et al, 2014c |
| Chitosan-PEO-NH ₄ NO ₃ -EC | 10 | 1.75 | EDLC/ Proton battery | Shukur et al., 2013b |
| Phthaloyl chitosan-NH ₄ SCN | 5 | 2.07 | Proton battery | Aziz et al., 2012 |
| Chitosan-NH ₄ NO ₃ -EC | 1 | 1.80 | Proton battery | Ng and Mohamed, 2008 |
| CMC-NH ₄ NO ₃ | 1 | 1.50 | Proton battery | This work |
| CMC-NH ₄ NO ₃ -EG | 1 | 1.55 | Proton battery | This work |

Note: (CMKC) carboxymethyl κ-carrageenan; DSSC - dye-sensitized solar cells; EDLC - electrical double layer capacitor.

6.2 Solid-state rechargeable proton batteries

The rechargeable proton batteries were fabricated using the highest conducting SPE films in both System I and System II. The batteries were designed as follows,

Cell I : Zn + ZnSO₄.7H₂O | SBE film containing 45 wt.% NH₄NO₃ | MnO₂

Cell II : Zn + ZnSO₄.7H₂O | SBE film containing 20 wt.% EG | MnO₂

6.2.1 Open-circuit voltage

In order to examine the ability of a battery to self-discharge over the time, the open-circuit voltage (OCV) was performed. Cell I and Cell II were allowed to self-discharge until a constant voltage was obtained. Figure 6.2 illustrates the variation in OCV of both cells were monitored for 24 hours at room temperature. Cell I shows

initial OCV of (1.09 ± 0.02) V before gradually falls about $\sim 36\%$ to (0.70 ± 0.03) V. The similar trend also can be seen in Cell II with a slight dropped of $\sim 10\%$ OCV from (1.19 ± 0.01) V to (1.07 ± 0.02) V. From the observation, Cell I shows an obvious depleting behaviour within 24 hours compared to Cell II, indicating a rapid self-discharge with time due to the instability of the cell. The drop in OCV could be due to the oxidation of Zn at the surface of anode electrode.

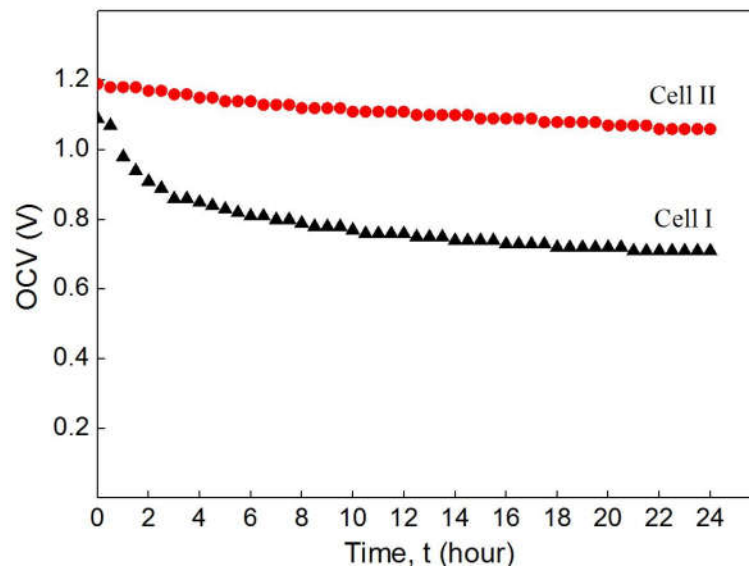


Figure 6.2 The OCV of Cell I and Cell II for 24 hours.

In addition, the OCV values of both cells were revealed to be lower than the theoretical calculation based on the standard electrode potential ($E_{\text{cell}}^0 = 1.28$ V). The slight drop of the voltage at the initial OCV could be due to the oxidation of negative (anode) electrode (Samsudin et al., 2014a). The disparity of OCV results between theoretical and present work could be influenced by the concentration and transport of charge carrier, H^+ ions (Shukur and Kadir, 2015b; Botte and Muthuvel, 2012). The OCV values attained from the previous works on proton batteries using the same cathode and anode active materials were listed in Table 6.2.

Table 6.2 The OCV value of proton batteries as reported by previous authors.

| Electrolyte system | OCV (V) | Time (hour) | Reference |
|--|---------|-------------|-------------------------|
| Chitosan-SiO ₂ -NH ₄ CH ₃ COO | 1.40 | 7 days | Alias et al., 2015 |
| Chitosan-starch-NH ₄ Cl-glycerol | 1.54 | 48 | Shukur and Kadir, 2015b |
| Chitosan-NH ₄ CH ₃ COO-EC | 1.60 | 48 | Alias et al., 2014 |
| Chitosan-PEO-NH ₄ NO ₃ -EC | 1.66 | 24 | Shukur et al., 2013b |
| Chitosan-NH ₄ NO ₃ -EC | 1.48 | 60 | Ng and Mohamad, 2008 |
| CMC-NH ₄ Br | 1.36 | 24 | Samsudin et al., 2014a |
| CMC-NH ₄ Br-EC | 1.48 | 24 | Samsudin, 2014 |
| CMC-DTAB | 1.33 | 24 | Samsudin et al., 2013 |
| PEO-(NH ₄) ₂ SO ₄ | 0.65 | Not stated | Ali et al., 1998 |
| CMC-NH ₄ NO ₃ | 0.70 | 24 | This work |
| CMC-NH ₄ NO ₃ -EG | 1.01 | 24 | This work |

6.2.2 Charge-discharge characteristics

Cell I and Cell II were subjected to charge-discharge at different constant current. The Cell I was charged to 0.70 V and then discharged to 0.2 V, whereas Cell II was charged to 1.07 V and then discharged to 0.2 V. The information obtained from charge-discharge characteristics were interpreted and discussed.

Discharge voltage at different constant current

The typical discharge curves of Cell I at a varied constant current of 0.02 mA, 0.04 mA and 0.06 mA are shown in Figure 6.3 - 6.5. It can be observed that the discharge period at 0.02 mA current is longer compared to that of 0.04 mA and 0.06 mA currents. At 0.02 mA, the cell discharge within 26 hours and 2 min 49 s (169 s) for the first and second cycles, respectively. The discharge process for cycle 4 and above took a short period of less than 2 min.

No obvious plateau region was observed from all discharge curves for Cell I indicating rapid discharge behaviour with time. This can be suggested due to the faster reduction of cathode materials. Besides, initial discharge voltage shows a decreasing trend with the increasing of current from 0.02 mA to 0.06 mA. This could be suggested that the cell requires a lower current in order to achieve the maximum voltage.

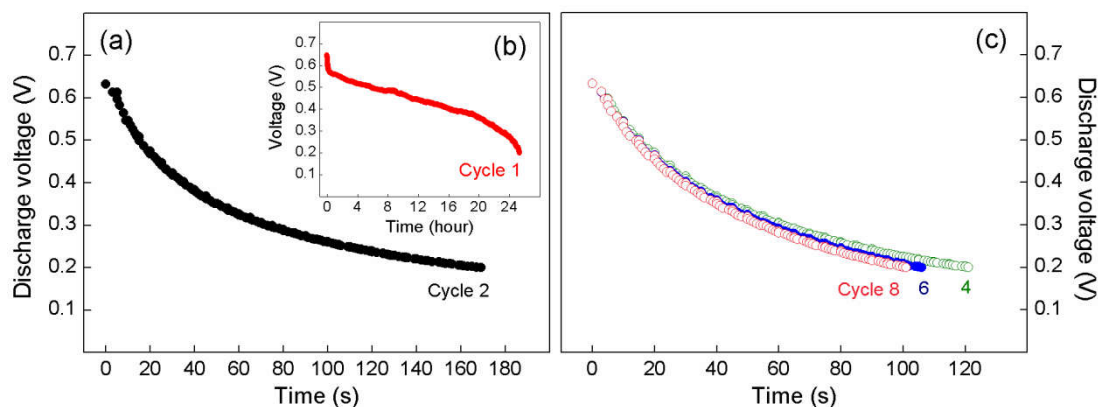


Figure 6.3 Discharge curves of Cell I for (a) cycle 1, (b) cycle 2, and (c) cycle 4, cycle 6 and cycle 8, measured at 0.02 mA constant current.

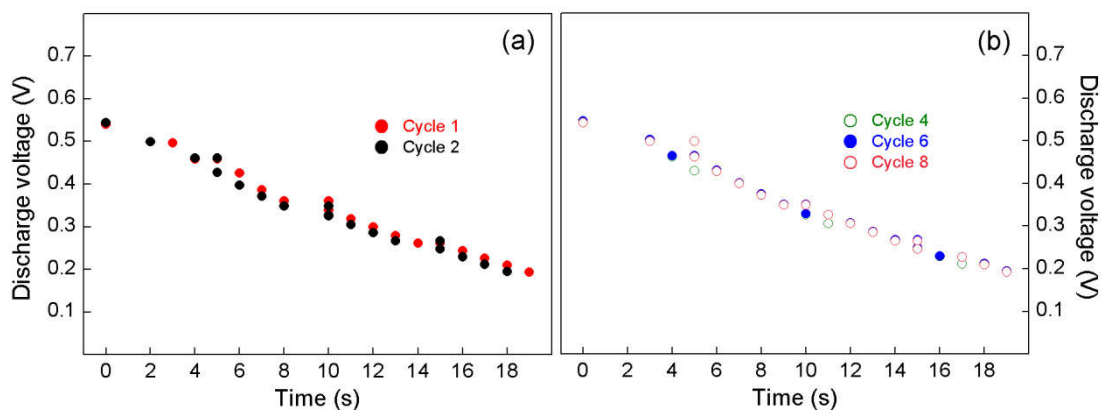


Figure 6.4 Discharge curves of Cell I for (a) cycle 1 and cycle 2, and (b) cycle 4, cycle 6 and cycle 8, measured at 0.04 mA constant current.

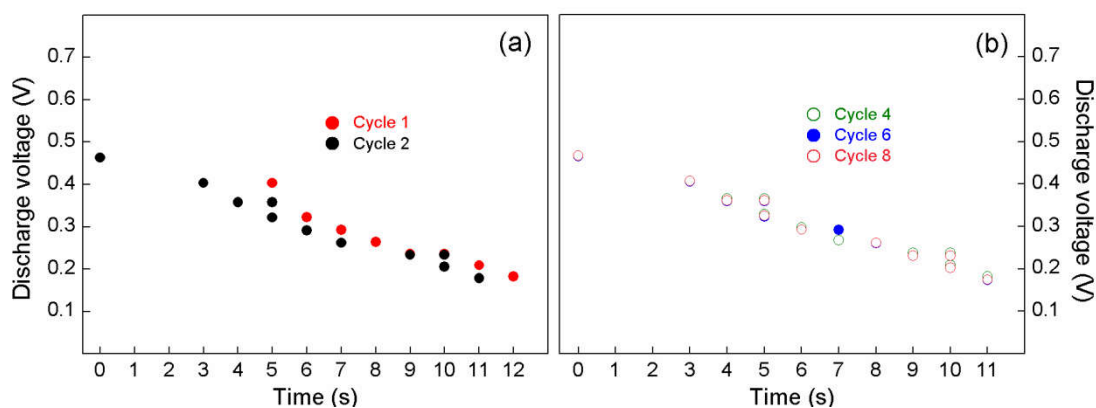


Figure 6.5 Discharge curves of Cell I for (a) cycle 1 and cycle 2, and (b) cycle 4, cycle 6 and cycle 8, measured at 0.06 mA constant current.

Figure 6.6 and 6.7 represent the typical discharge curves of Cell II at a varied constant current of 0.02 mA and 0.04 mA. An initial sharp decline of voltage was observed for all discharge cycles when discharge at 0.02 mA and 0.04 mA. This could be attributed to the polarization and/or formation of a thin layer of NH_4NO_3 salt at the electrode-electrolyte interface (Selvasekarapandian et al., 2010; Mohan et al., 2005). The initial voltage maintains at 1.07 V upon discharge at 0.02 mA. However, a slight decrease of initial voltage (~ 0.95 V) could be detected when cell discharged at 0.04 mA. The cell voltage remains constant for a particular duration, indicating by the discharge plateau region as clearly be seen in the inset of both figures.

Further discharge the cell leading to the drop of voltage to 0.2 V. The discharge period is higher at 0.02 mA compared to 0.04 mA. At 0.02 mA, cycle 1 and 2 discharged within 3.5 hr and 2.2 hr, respectively. Shorter discharge duration of less than 109 s (1 hr 49 min) was obtained for cycle 4 to 8.

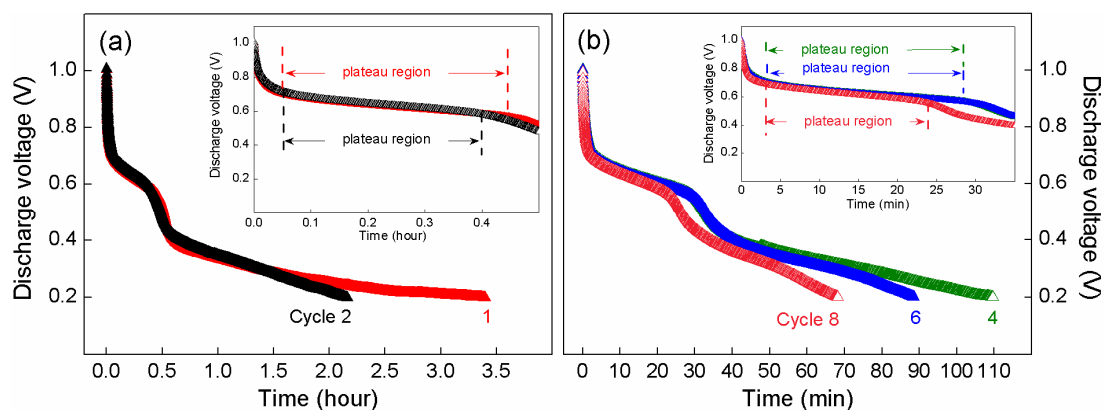


Figure 6.6 Discharge curves of Cell II for (a) cycle 1 and 2, and (b) cycle 4, cycle 6, and cycle 8 at 0.02 mA constant current. (Inset: Enlargement of the plateau region).

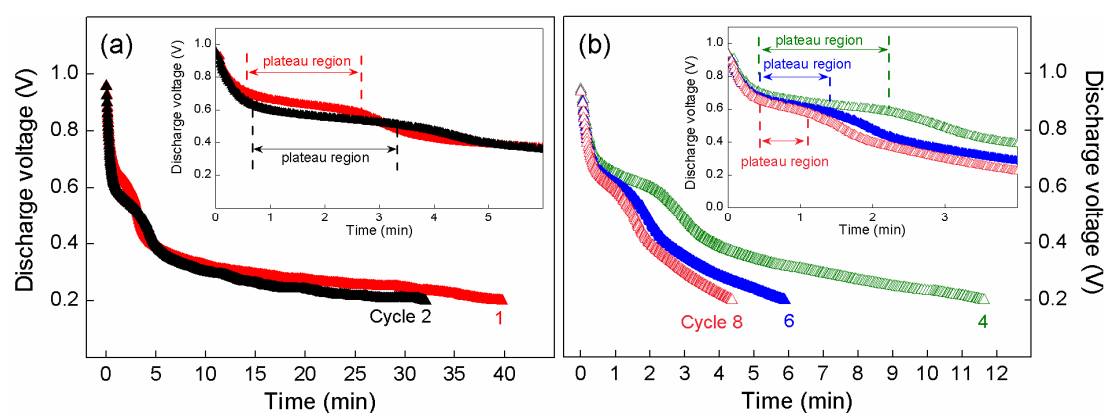


Figure 6.7 Discharge curves of Cell II for (a) cycle 1 and 2, and (b) cycle 4, cycle 6, and cycle 8 at 0.04 mA constant current. (Inset: Enlargement of the plateau region).

The plateau regions can only be observed in Cell II at 0.02 mA (Figure 6.6) and 0.04 mA (Figure 6.7). The cell parameters based on the plateau regions at 0.02 mA and 0.04 mA were summarized in Table 6.3 and 6.4, respectively. The 0.02 mA current of Cell II shows longer discharge plateau and higher capacity compared to 0.04 mA current. This may attributed to the ability of cell to endure low discharge current to complete the discharge cycles.

Table 6.3 Cell parameters calculated in the plateau region at 0.02 mA discharge current for Cell II.

| Cell parameter | Cycle | | | | |
|--|-------|-------|-------|-------|-------|
| | 1 | 2 | 4 | 6 | 8 |
| Cell weight, m (g) | 0.30 | 0.30 | 0.30 | 0.30 | 0.30 |
| Cell area, A (cm ²) | 1.00 | 1.00 | 1.00 | 1.00 | 1.00 |
| Current density, I (mA/cm ²) | 0.02 | 0.02 | 0.02 | 0.02 | 0.02 |
| Discharge plateau time, t (hour) | 0.40 | 0.35 | 0.42 | 0.42 | 0.34 |
| Discharge capacity, Q (μ Ah) | 8.00 | 7.00 | 8.40 | 8.40 | 6.80 |
| Energy density, E (μ Wh/cm ²) | 4.80 | 4.20 | 5.04 | 5.04 | 4.08 |
| Power density, P (μ W/cm ²) | 12.00 | 12.00 | 12.00 | 12.00 | 12.00 |

Table 6.4 Cell parameters calculated in the plateau region at 0.04 mA discharge current for Cell II.

| Cell parameter | Cycle | | | | |
|--|-------|-------|-------|-------|-------|
| | 1 | 2 | 4 | 6 | 8 |
| Cell weight, m (g) | 0.30 | 0.30 | 0.30 | 0.30 | 0.30 |
| Cell area, A (cm ²) | 1.00 | 1.00 | 1.00 | 1.00 | 1.00 |
| Current density, I (mA/cm ²) | 0.04 | 0.04 | 0.04 | 0.04 | 0.04 |
| Discharge plateau time, t (hour) | 0.04 | 0.05 | 0.03 | 0.02 | 0.01 |
| Discharge capacity, Q (μ Ah) | 1.60 | 2.00 | 1.20 | 0.80 | 0.40 |
| Energy density, E (μ Wh/cm ²) | 0.96 | 1.20 | 0.72 | 0.48 | 0.24 |
| Power density, P (μ W/cm ²) | 24.00 | 24.00 | 24.00 | 24.00 | 24.00 |

Upon discharge to a higher current of 0.06 mA of Cell II, the initial voltage dropped to ~0.88 V (Figure 6.8). The similar trend was observed in Cell I at different constant currents. No obvious plateau region can be observed within cycle 1 to 8. Cycle 1 took the longest discharge period of ~3.9 min, followed by 2 min for cycle 2. Cycle 4 to 8 complete their discharge process in less than 100 s (1.7 min).

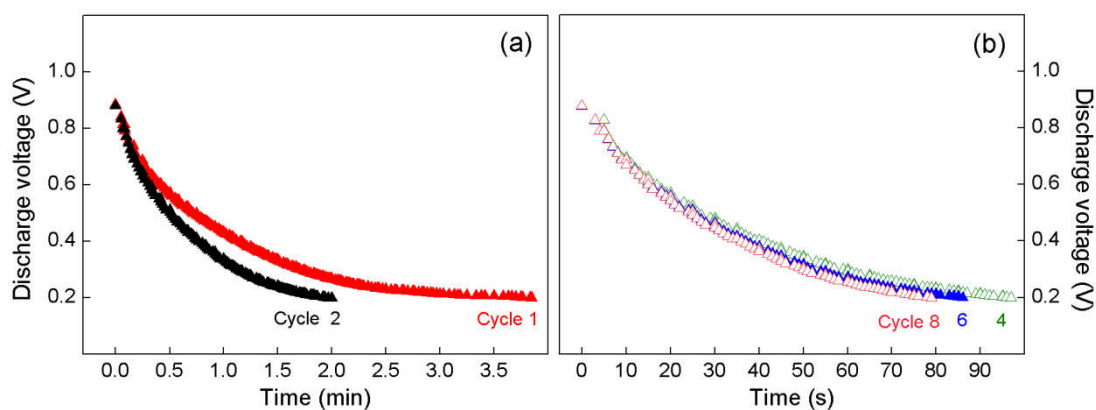


Figure 6.8 Discharge curves of Cell II for (a) cycle 1 and 2, (b) cycle 4, (c) cycle 6, and (d) cycle 8 at 0.06 mA constant current.

Specific capacity at different constant current

The discharge capacity of Cell I and Cell II at different constant current are exemplified in Figure 6.9 and 6.10, respectively. It can be observed that the discharge capacity gradually decreased with the increase of cycle number in both cells. Moreover, the discharge capacity was found higher in Cell II than in Cell I.

At 0.02 mA, Cell 1 demonstrates the highest discharge capacity of 1.79 mAhg^{-1} at the first cycle and the discharge capacity abruptly drops to $3.45 \text{ } \mu\text{Ahg}^{-1}$ at the second cycle. After that, the discharge capacity gradually decreases and remains constant at $\sim 2 \text{ } \mu\text{Ahg}^{-1}$ for cycle 4 and above. For Cell II, the initial discharge capacity was found at 0.23 mAhg^{-1} and followed by a decline of discharge capacity about 0.15 mAhg^{-1} . The discharge capacity slowly decreases to 0.06 mAhg^{-1} at cycle 8. The fade of capacity over cycle number could be attributed to the large interfacial resistance developed between the electrode and electrolyte. A similar observation has been reported in other rechargeable proton battery based polymer-salt systems (Samsudin et al., 2014c; Selvasekarapandian et al., 2010; Mohamad et al., 2003).

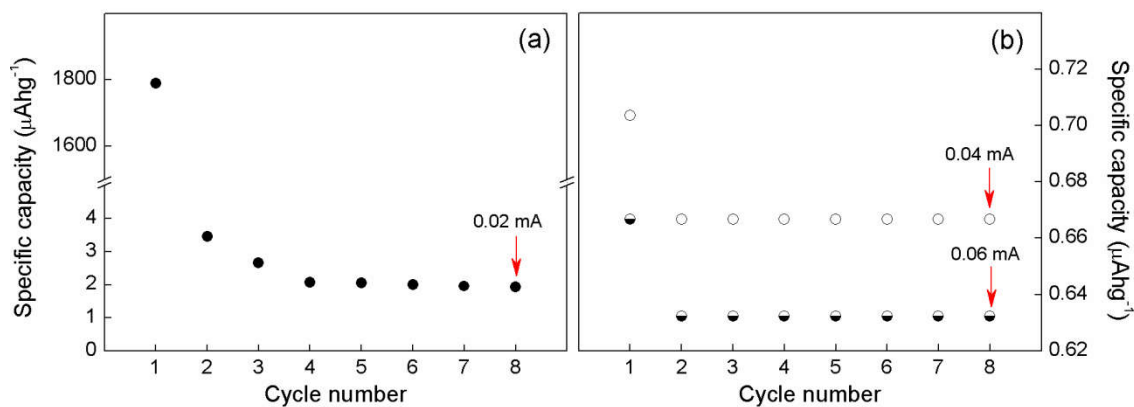


Figure 6.9 Discharge specific capacity of Cell I at different constant current of (a) 0.02 mA, and (b) 0.04 mA and 0.06 mA.

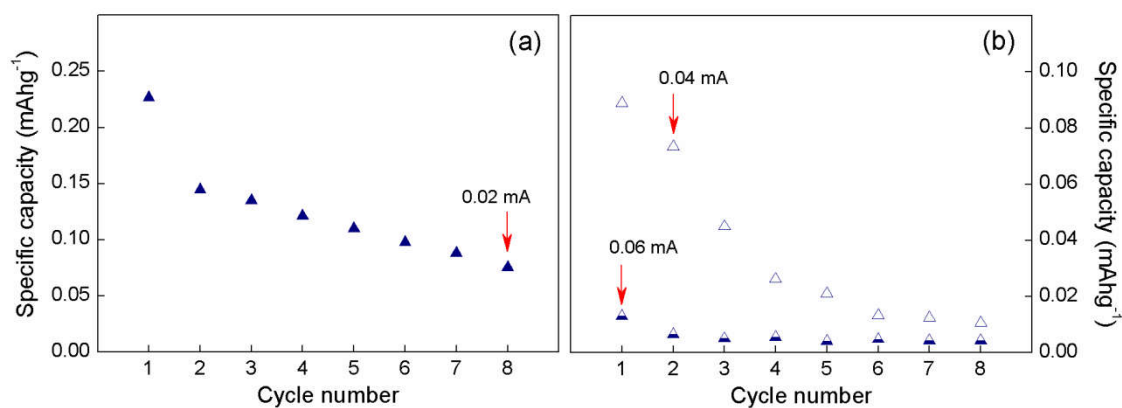


Figure 6.10 Discharge specific capacity of Cell II at different constant current of (a) 0.02 mA, and (b) 0.04 mA and 0.06 mA.

Rechargeability studies

The rechargeability of a cell acquires good cathode materials which show reversibility for the mobility of H^+ ion, in this case, MnO_2 was used as cathode layered material. The $\text{ZnSO}_4 \cdot 7\text{H}_2\text{O}$ anode layered material was acted as the source of H^+ ion for supplying or injecting H^+ ions into the electrolyte of proton battery (Pandey et al., 1998). Hence, the small ionic radii of H^+ ions could be intercalated into the layers of the layered materials (Pratap et al., 2006). The rechargeable proton battery chemical reactions have been detailed in Section 2.3.1.

The charge-discharge characteristic curves of Cell I and Cell II are shown in Figure 6.11 and Figure 6.12, respectively. The charge-discharge of both cells was measured within 10 cycles at 0.02 mA constant current without significant loss in the voltage. The discharge was terminated after both cells voltage fell to 0.2 V. The cells were then re-charged to the initial voltage using a constant current.

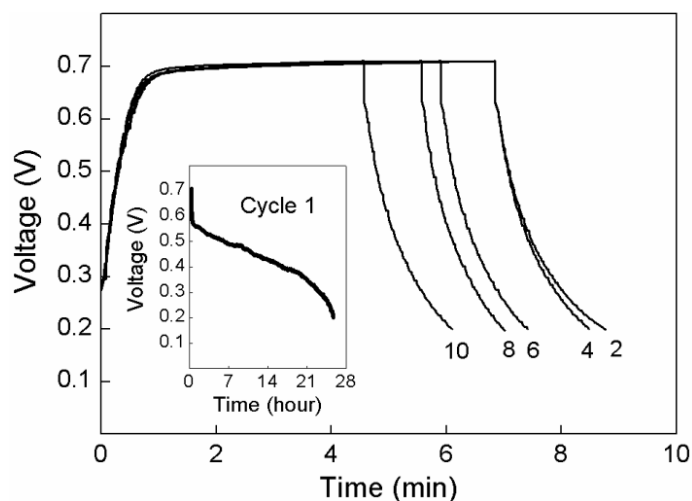


Figure 6.11 Charge-discharge characteristics of Cell I for 1 to 10 cycles at 0.02 mA constant current.

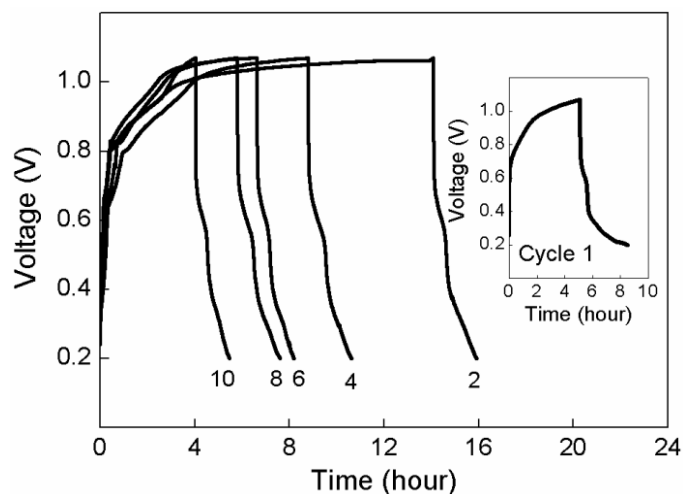


Figure 6.12 Charge-discharge characteristics of Cell II for 1 to 10 cycles at 0.02 mA constant current.

It can be seen from both figures the cells regain its initial voltage after recharging. Pandey et al. (1998) showed a good rechargeability which was tested for 20 - 30 cycles under different load conditions, whereas Pratap et al. (2006) demonstrated rechargeability of the cell up to 9 - 10 cycles without significant loss in the voltage. During the discharge cycle, the anode layered materials able to intercalate the mobile H^+ ions migrating from the electrolyte between its layers and de-intercalate during the charge cycle (Pratap et al., 2006). In addition, Samsudin (2014) reported higher charge-discharge current and a longer period of the cell cycle. The cell capable of completing 10 - 20 cycles within 201 hours to 382 hours.

From the observation of the OCV and charge-discharge characteristics, the poor/weak performance of cells can be suggested due to the low values of ionic transference number, Γ_{ion} of SPEs in both cells (Cell I ($\Gamma_{ion} = 0.67$) and Cell II ($\Gamma_{ion} = 0.84$). Γ_{ion} lower than unity may limit the current due to the development of concentration gradient at the electrode surfaces (Dias et al., 2000). According to Mohamed et al. (1995), the failure of batteries could be due to the $ZnOH_2$ formation at the electrode-electrolyte interfaces, and/or other low conducting discharge products. It may also attributed to the poor interfacial contact between the electrodes and electrolyte during cell assembly which may induce high internal resistance.

It also can be inferred that Cell I discharged at faster rate than in Cell II for all constant currents. The decay in the Cell II voltage could be suggested due to the polarization and the formation of the low ionic conductivity of 45 wt.% NH_4NO_3 film (System I) compared to 20 wt.% EG film (System II) at the electrode-electrolyte interface (Agrawal et al., 2004). The plateau region can only be observed in Cell II when discharged at 0.02 mA and 0.04 mA. The longer discharge plateau period was

achieved at 0.02 mA. In addition, Cell II performed much better than Cell I at 0.02 mA. Thus, the rechargeable proton batteries based SPEs in this work are suitable to be applied in low current density application.

CHAPTER 7

CONCLUSION AND FUTURE WORK

7.1 Conclusion

In this research, two series of cellulose based SPEs comprised of CMC-NH₄NO₃ (System I) and CMC-NH₄NO₃-EG (System II) were successfully prepared using the solution casting method (first research objective) and characterized using different physical techniques. The most conductive SPE film from each of the systems were then applied as an electrolyte for the development of solid-state rechargeable proton battery. The battery was fabricated using Zn-MnO₂ as electrodes and characterized using several techniques to test its performance.

In the first part of this research, the characterization of System I and System II was carried out at various NH₄NO₃ and EG concentrations, and temperatures. The effect of NH₄NO₃ salt and EG plasticizer on vibrational, structural and thermal properties of SPEs were investigated using FTIR, XRD and TGA techniques. The interaction or complexation in System I and System II was observed and confirmed by FTIR analysis. The H⁺ ion (proton) was identified to be the prominent ionic species/charge carriers in both systems and the ionic conduction occurs through the coordination site of an oxygen atom of a CMC polymer chain and a hydrogen atom of a NH₄⁺ ion from NH₄NO₃ salt. The possible proton transfer mechanism in both systems was suggested via structural diffusion or also known as the Grotthuss mechanism, in which a H⁺ ion hops from one coordinating site to another

neighbouring site. The XRD results revealed the complete dissolution of SPEs and confirmed the amorphous nature of SPEs in both systems. System II was observed to demonstrate a higher thermal stability or better heat-resistance than System I based on the thermal analysis. Therefore, proving that the second objective of this research was achieved.

The enhancement of ionic conductivity of SPEs was accomplished by the doping and plasticization approaches. The increasing and decreasing ionic conductivity in System I and System II followed the common features for most of the polymer-salt and polymer-salt-plasticizer complexes. Salt concentration dependence of ionic conductivity revealed that the ionic conductivity was increased to five magnitude orders with the addition of 0 to 45 wt.% NH_4NO_3 salt at ambient temperature. Pure CMC film exhibited $\sigma \sim 10^{-8} \text{ Scm}^{-1}$ and was increased to $\sim 10^{-3} \text{ Scm}^{-1}$ when 45 wt.% NH_4NO_3 was added. Further enhancement of ionic conductivity to one magnitude order was observed with the addition of 20 wt.% EG plasticizer ($\sigma \sim 10^{-2} \text{ Scm}^{-1}$) at ambient temperature. Temperature dependence studies on the ionic conductivity in both systems showed that the ion conduction follows the Arrhenius behaviour and the ionic conductivity occurs by a thermally assisted transport process.

The ion transport behaviour was investigated based on the deconvoluted FTIR spectra. The ionic species analysis revealed the dissociation behaviour of the free ions from NH_4NO_3 salt that significantly influenced the ionic conductivity behaviour of the SPE films in both systems. This analysis was also plausible with the ionic conductivity analysis of salt-dependent and plasticizer-dependent ionic conductivity obtained using AC impedance technique. TNM analysis confirmed that the charge

transport of the mobile charge carrier in both systems was purely ionic at room temperature and those systems can be regarded as cationic or protonic conductor.

The electrical studies demonstrated that System I and II were ionic conductors and occurred at a faster ionic conduction mechanism, evidenced by the β -conductivity relaxation behaviour at the high-frequency end. The ionic conduction mechanism for the highest conducting electrolyte in both systems were elucidated based on Jonscher's Universal Power Law and revealed to be best represented by the quantum mechanical tunnelling model. Therefore, the results obtained from ionic conductivity, ion transport and electrical studies verified the achievement of the third objective of this research.

In the second part of this research, the highest conducting SPE in both systems was used as an electrolyte in the fabrication of solid-state rechargeable proton battery. The electrochemical performance of solid-state rechargeable proton batteries was further investigated in terms of LSV, OCV and charge-discharge characteristics. Electrochemical analysis showed the promising features of CMC-based SPEs to be employed, particularly in a low current density rechargeable proton battery. These proton conducting electrolytes can be a good alternative to lithium ion conductors in proton battery and other electrochemical device applications. Therefore, the final objective of this research was accomplished.

7.2 Recommendations for future work

SPEs with a potential application in rechargeable proton batteries can be attained from this work. However, some recommendations are necessary to improve the present work and to obtain more information on SPEs and its relation to battery

performance. This includes a further study on the influence of temperature on the ionic species behaviour using FTIR-TGA technique. The present work only gives information on the effect of NH_4NO_3 and EG concentrations to the fraction of ionic species in SPEs at room temperature using the FTIR approach. Due to the lack of crystallinity information from XRD analysis, detailed observation on T_g and crystallinity of SPEs can be performed using differential scanning calorimetry (DSC) or dynamic mechanical analysis (DMA) techniques. These techniques also can be utilized to gain some information on the degradation of SPEs over the time and at higher temperatures. It was also suggested to investigate the mechanical integrity/strength in order to observe the capability of SPEs to endure pressure and temperature over time.

For further investigation on the performance of rechargeable proton battery, scanning electron microscopy (SEM) and energy dispersive X-ray (EDX) can be employed to observe the intimate contact between electrolyte-electrodes. These techniques can provide a glimpse of information on the surface morphology and cross-section of SPE as sandwiched between two electrodes. This is essential to investigate the weak battery performance due to high internal resistance between electrolyte and electrodes as well as corrosion and oxidation of electrodes during chemical reactions which may affect recyclability and battery capacity. Atomic force microscopy (AFM) may also be an alternative technique to examine the surface roughness and morphology of electrolyte and electrodes. In addition, the reversible electrode reaction and cell resistance can be evaluated using the cyclic voltammetry (CV) technique. It is also worthwhile to study the effect of temperature to that of battery performance. Detailed studies on Zn- MnO_2 electrodes and its compatibility

with the current SPEs are possible. The mechanism or chemical reaction during charge-discharge cycles requires a detailed explanation. Rechargeable proton batteries using other electrode systems or different electrode materials may be the subject of future work. SPEs could be applied in other electrochemical device applications such as primary batteries, electric double-layer capacitors (EDLC), dye-sensitized solar cells (DSSC), and fuel cells.

REFERENCES

- Abdul Khalil, H. P. S.; Bhat, A. H.; Ireana Yusra, A. F., Green composites from sustainable cellulose nanofibrils: A review. *Carbohydrate Polymers* **2012**, *87* (2), 963-979.
- Abdul Rahaman, M. H.; Khandaker, M. U.; Khan, Z. R.; Kufian, M. Z.; Noor, I. S. M.; Arof, A. K., Effect of gamma irradiation on poly(vinylidene difluoride)-lithium bis(oxalato)borate electrolyte. *Physical Chemistry Chemical Physics* **2014**, *16* (23), 11527-11537.
- Adinugraha, M. P.; Marseno, D. W.; Haryadi, Synthesis and characterization of sodium carboxymethylcellulose from cavendish banana pseudo stem (*Musa cavendishii* LAMBERT). *Carbohydrate Polymers* **2005**, *62* (2), 164-169.
- Agrawal, R. C.; Pandey, G. P., Solid polymer electrolytes: Materials designing and all-solid-state battery applications: an overview. *Journal of Physics D: Applied Physics* **2008**, *41* (22), 223001.
- Ahmad, N. H.; Isa, M. I. N., Structural and ionic conductivity studies of CMC based polymer electrolyte doped with NH_4Cl . *Advanced Materials Research* **2015**, *1107*, 247-252.
- Ahmad, Z., *Dielectric materials: Polymer dielectric materials*. InTech: Rijeka, Croatia, **2012**; p 3-26.
- Akar, E.; Altınışık, A.; Seki, Y., Preparation of pH- and ionic-strength responsive biodegradable fumaric acid crosslinked carboxymethyl cellulose. *Carbohydrate Polymers* **2012**, *90* (4), 1634-1641.
- Ali, A. M. M.; Mohamed, N. S.; Arof, A. K., Polyethylene oxide (PEO)-ammonium sulfate $((\text{NH}_4)_2\text{SO}_4)$ complexes and electrochemical cell performance. *Journal of Power Sources* **1998**, *74* (1), 135-141.
- Alias, S. S.; Ariff, Z. M.; Mohamad, A. A., Porous membrane based on chitosan-SiO₂ for coin cell proton battery. *Ceramics International* **2015**, *41*, 5484-5491.
- Alias, S. S.; Chee, S. M.; Mohamad, A. A., Chitosan-ammonium acetate-ethylene carbonate membrane for proton batteries. *Arabian Journal of Chemistry* **2014**. <http://dx.doi.org/10.1016/j.arabjc.2014.05.001>
- AlSalhi, M. S.; Alam, J.; Dass, L. A.; Raja, M., Recent advances in conjugated polymers for light emitting devices. *International Journal of Molecular Sciences* **2011**, *12*, 2036-2054.
- Andreev, Y. G.; Bruce, P. G., Polymer electrolyte structure and its implications. *Electrochimica Acta* **2000**, *45* (8-9), 1417-1423.
- Armand, M. B., Polymer Electrolytes. *Annual Review of Materials Science* **1986**, *16*, 245-261.
- Armand, M., The history of polymer electrolytes. *Solid State Ionics* **1994**, *69* (3-4), 309-319.
- Armand, M.; Tarascon, J. M., Building better batteries. *Nature* **2008**, *451* (7179), 652-657.
- Arof, A. K.; Amirudin, S.; Yusof, S. Z.; Noor, I. M., A method based on impedance spectroscopy to determine transport properties of polymer electrolytes. *Physical Chemistry Chemical Physics* **2014**, *16* (5), 1856-1867.
- Arof, A. K.; Jun, H. K.; Sim, L. N.; Kufian, M. Z.; Sahraoui, B., Gel polymer electrolyte based on LiBOB and PAN for the application in dye-sensitized solar cells. *Optical Materials* **2013**, *36* (1), 135-139.

- Arora, P.; Zhang, Z. J., Battery separators. *Chemical Reviews* **2004**, *104*, 4419-4462.
- Asmara, S. N.; Kufian, M. Z.; Majid, S. R.; Arof, A. K., Preparation and characterization of magnesium ion gel polymer electrolytes for application in electrical double layer capacitors. *Electrochimica Acta* **2011**, *57* (0), 91-97.
- Avérous, L.; Pollet, E., *Environmental Silicate Nano-Biocomposites*. Springer-Verlag London, UK: **2012**, p. 450.
- Aziz, N. A.; Majid, S. R.; Arof, A. K., Synthesis and characterizations of phthaloyl chitosan-based polymer electrolytes. *Journal of Non-Crystalline Solids* **2012**, *358* (12-13), 1581-1590.
- Aziz, S. B.; Abidin, Z. H. Z., Electrical conduction mechanism in solid polymer electrolytes: New concepts to arrhenius equation. *Journal of Soft Matter* **2013**, *2013*, 8.
- Baggetto, L.; Niessen, R. A. H.; Roozeboom, F.; Notten, P. H. L., High energy density all-solid-state batteries: a challenging concept towards 3D integration. *Advanced Functional Materials* **2008**, *18* (7), 1057-1066.
- Bai, H.; Zhang, H.; He, Y.; Liu, J.; Zhang, B.; Wang, J., Enhanced proton conduction of chitosan membrane enabled by halloysite nanotubes bearing sulfonate polyelectrolyte brushes. *Journal of Membrane Science* **2014**, *454*, 220-232.
- Bandara, T. M. W. J.; Dissanayake, M. A. K. L.; Albinsson, I.; Mellander, B. E., Mobile charge carrier concentration and mobility of a polymer electrolyte containing PEO and Pr₄N⁺I using electrical and dielectric measurements. *Solid State Ionics* **2011**, *189* (1), 63-68.
- Bansod, S. M.; Bhoga, S. S.; Singh, K.; Tiwari, R. U., The role of electrolyte in governing the performance of protonic solid state battery. *Ionics* **2007**, *13* (5), 329-332.
- Bao, Y.; Ma, J.; Li, N., Synthesis and swelling behaviors of sodium carboxymethyl cellulose-g-poly(AA-co-AM-co-AMPS)/MMT superabsorbent hydrogel. *Carbohydrate Polymers* **2011**, *84* (1), 76-82.
- Baskaran, R.; Selvasekarapandian, S.; Hirankumar, G.; Bhuvaneshwari, M. S., Dielectric and conductivity relaxations in PVAc based polymer electrolytes. *Ionics* **2004**, *10* (1-2), 129-134.
- Bhargav, P. B.; Mohan, V. M.; Sharma, A. K.; Rao, V. V. R. N., Investigations on electrical properties of (PVA:NaF) polymer electrolytes for electrochemical cell applications. *Current Applied Physics* **2009**, *9* (1), 165-171.
- Biswal, D. R.; Singh, R. P., Characterisation of carboxymethyl cellulose and polyacrylamide graft copolymer. *Carbohydrate Polymers* **2004**, *57* (4), 379-387.
- Bordes, P.; Pollet, E.; Avérous, L., Nano-biocomposites: Biodegradable polyester/nanoclay systems. *Progress in Polymer Science* **2009**, *34*, 125-155.
- Botte, G.G.; Muthuvel, M., *Electrochemical energy storage: Applications, processes, and trends, Handbook of Industrial Chemistry and Biotechnology*. Springer, Florida, USA, 2012, 1497-1539.
- Bruce, P. G.; Hardgrave, M. T.; Vincent, C. A., The determination of transference numbers in solid polymer electrolytes using the Hittorf method. *Solid State Ionics* **1992**, *53-56*, Part 2 (0), 1087-1094.
- Buraidah, M. H.; Arof, A. K., Characterization of chitosan/PVA blended electrolyte doped with NH₄I. *Journal of Non-Crystalline Solids* **2011**, *357* (16-17), 3261-3266.

- Buraidah, M. H.; Teo, L. P.; Majid, S. R.; Arof, A. K., Ionic conductivity by correlated barrier hopping in NH₄I doped chitosan solid electrolyte. *Physica B* **2009**, *404*, 1373-1379.
- Chai, M. N.; Isa, M. I. N., Electrical characterization and ionic transport properties of carboxyl methylcellulose-oleic acid solid polymer electrolytes. *International Journal of Polymer Analysis and Characterization* **2013**, *18* (4), 280-286.
- Chai, M. N.; Isa, M. I. N., Investigation on the conduction mechanism of carboxyl methylcellulose-oleic acid natural solid polymer electrolyte. *International Journal of Advanced Technology & Engineering Research* **2012**, *2* (6), 36-39.
- Chai, M. N.; Isa, M. I. N., Structural study of plasticized carboxy methylcellulose based solid biopolymer electrolyte. *Advanced Materials Research* **2015**, *1107*, 242-246.
- Chai, M. N.; Ramlli, M. A.; Isa, M. I. N., Proton conductor of propylene carbonate–plasticized carboxyl methylcellulose–based solid polymer electrolyte. *International Journal of Polymer Analysis and Characterization* **2013**, *18* (4), 297-302.
- Chakraborty, S.; Sadhukhan, M.; Chaudhuri, B. K.; Mori, H.; Sakata, H., Frequency dependent electrical conductivity and dielectric relaxation behavior in amorphous (90V₂O₅–10Bi₂O₃) oxide semiconductors doped with SrTiO₃. *Materials Chemistry and Physics* **1997**, *50* (3), 219-226.
- Charles, E. C. J., *Carraher's polymer chemistry*. CRC Press, Taylor and Franchis Group: Florida, USA, **2013**.
- Choi, B.-K.; Jang, B., Conductivity and thermal behavior of proton conductor based on poly(vinylpyrrolidone) complexed with ammonium perchlorate. *Macromolecular Research* **2010**, *18* (1), 35-39.
- Christie, L.; Los, P.; Bruce, P. G., The polymer electrolyte/electrode interface. *Electrochimica Acta* **1995**, *40* (13–14), 2159-2164.
- Damez, J.-L.; Clerjon, S.; Abouelkaram, S. d.; Lepetit, J., Dielectric behavior of beef meat in the 1–1500 kHz range: Simulation with the Fricke/Cole–Cole model. *Meat Science* **2007**, *77*, 512–519.
- Damle, R.; Kulkarni, P. N.; Bhat, S. V., Study of effect of composition, irradiation and quenching on ionic conductivity in (PEG)_x : NH₄NO₃ solid polymer electrolyte. *Bulletin of Materials Science* **2008**, *31* (6), 869-876.
- Damle, R.; Kulkarni, P. N.; Bhat, S. V., The effect of composition, electron irradiation and quenching on ionic conductivity in a new solid polymer electrolyte: (PEG)_xNH₄I. *Pramana-Journal of Physics* **2009**, *72* (3), 555-568.
- Das, A.; Thakur, A. K.; Kumar, K., Evidence of low temperature relaxation and hopping in ion conducting polymer blend. *Solid State Ionics* **2014**, *262*, 815-820.
- Dash, A.; Cudworth Ii, G., Therapeutic applications of implantable drug delivery systems. *Journal of Pharmacological and Toxicological Methods* **1998**, *40* (1), 1-12.
- Deraman, S. K.; Mohamed, N. S.; Subban, R. H. Y., Conductivity and dielectric properties of proton conducting poly (vinyl) chloride (PVC) based gel polymer electrolytes. *Sains Malaysiana* **2013**, *42* (4), 475-479
- Di Noto, V.; Lavina, S.; Giffin, G. A.; Negro, E.; Scrosati, B., Polymer electrolytes: Present, past and future. *Electrochimica Acta* **2011**, *57* (0), 4-13.
- Dias, F. B.; Plomp, L.; Veldhuis, J. B. J., Trends in polymer electrolytes for secondary lithium batteries. *Journal of Power Sources* **2000**, *88*, 169-191.

- Du, J. F.; Bai, Y.; Chu, W. Y.; Qiao, L. J., Synthesis and performance of proton conducting chitosan/NH₄Cl electrolyte. *Journal of Polymer Science Part B: Polymer Physics* **2010**, *48* (3), 260-266.
- Dyre, J. C.; Schröder, T. B., Hopping models and AC universality. *Physica Status Solidi (b)* **2002**, *230* (1), 5-13.
- El-Sayed, S.; Mahmoud, K. H.; Fatah, A. A.; Hassen, A., DSC, TGA and dielectric properties of carboxymethyl cellulose/polyvinyl alcohol blends. *Physica B: Condensed Matter* **2011**, *406* (21), 4068-4076.
- Ericson, H.; Svanberg, C.; Brodin, A.; Grillone, A. M.; Panero, S.; Scrosati, B.; Jacobsson, P., Poly(methyl methacrylate)-based protonic gel electrolytes: a spectroscopic study. *Electrochimica Acta* **2000**, *45* (8-9), 1409-1414.
- Fenton, D.; Parker, J.; Wright, P., Complexes of alkali metal ions with poly(ethylene oxide). *Polymer* **1973**, *14*, 589.
- Ferry, A.; Oradd, G.; Jacobsson, P., Ionic interactions and transport in a low-molecular-weight model polymer electrolyte. *Journal of Chemical Physics* **1998**, *108* (17), 7426-7433.
- Finkenstadt, V. L., Natural polysaccharides as electroactive polymers. *Applied Microbiology and Biotechnology* **2005**, *67*, 735-745.
- Gray, F. M., *Solid polymer electrolytes: Fundamentals and technological applications*. Wiley-VCH: Scotland, UK, **1991**.
- Gunawan, R.; Freij, S.; Zhang, D.-K.; Beach, F.; Littlefair, M., A mechanistic study into the reactions of ammonium nitrate with pyrite. *Chemical Engineering Science* **2006**, *61* (17), 5781-5790.
- Hafiza, M. N.; Isa, M. I. N., Ionic conductivity and conduction mechanism studies of CMC/chitosan biopolymer blend electrolytes. *Research Journal of Recent Sciences* **2014**, *3* (11), 50-56.
- Hallinan, D. T.; Balsara, N. P., Polymer Electrolytes. *Annual Review of Materials Research* **2013**, *43* (1), 503-525.
- Han, F. Q.; Shao, B.; Wang, Q. W.; Guo, C. G.; Liu, Y. X., Synthesis and characterization of carboxymethylcellulose and methyl methacrylate graft copolymers. *Pigment and Resin Technology* **2010**, *39* (3), 156-162.
- Hashmi, S. A.; Kumar, A.; Maurya, K. K.; Chandra, S., Proton-conducting polymer electrolyte. I. The polyethylene oxide + NH₄ClO₄ system. *Journal of Physics D: Applied Physics* **1990**, *23* (10), 1307.
- He, F.; Zhao, D.; Liu, J.; Roberts, C. B., Stabilization of Fe Pd Nanoparticles with sodium carboxymethyl cellulose for enhanced transport and dechlorination of trichloroethylene in soil and groundwater. *Industrial & Engineering Chemistry Research* **2007**, *46* (1), 29-34.
- Hema, M.; Selvasekarapandian, S.; Arunkumar, D.; Sakunthala, A.; Nithya, H., FTIR, XRD and AC impedance spectroscopic study on PVA based polymer electrolyte doped with NH₄X (X = Cl, Br, I). *Journal of Non-Crystalline Solids* **2009**, *355* (2), 84-90.
- Hema, M.; Selvasekerapandian, S.; Hirankumar, G., Vibrational and impedance spectroscopic analysis of poly(vinyl alcohol)-based solid polymer electrolytes. *Ionics* **2007**, *13*, 483-487.
- Hema, M.; Selvasekerapandian, S.; Sakunthala, A.; Arunkumar, D.; Nithya, H., Structural, vibrational and electrical characterization of PVA-NH₄Br polymer electrolyte system. *Physica B: Condensed Matter* **2008**, *403* (17), 2740-2747.

- Hirankumar, G.; Selvasekarapandian, S.; Kuwata, N.; Kawamura, J.; Hattori, T., Thermal, electrical and optical studies on the poly (vinyl alcohol) based polymer electrolytes. *Journal of Power Sources* **2005**, *144* (1), 262-267.
- Holmberg, S.; Perebikovskiy, A.; Kulinsky, L.; Madou, M., 3-D micro and nano technologies for improvements in electrochemical power devices. *Micromachines* **2014**, *5* (2), 171-203.
- Holomb, R.; Xu, W.; Markusson, H.; Johansson, P.; Jacobsson, P., Vibrational spectroscopy and ab initio studies of lithium bis(oxalato)borate (LiBOB) in different solvents. *The Journal of Physical Chemistry A* **2006**, *110* (40), 11467-11472.
- Ibrahim, A. A.; Adel, A. M.; El-Wahab, Z. H. A.; Al-Shemy, M. T., Utilization of carboxymethyl cellulose based on bean hulls as chelating agent. Synthesis, characterization and biological activity. *Carbohydrate Polymers* **2011**, *83* (1), 94-115.
- Isa, M. I. N.; Noor, N. A. M., Ionic conduction mechanism of solid biodegradable polymer electrolytes based carboxymethyl cellulose doped ammonium thiocyanate. *Applied Mechanics and Materials* **2015**, *719-720*, 114-118.
- Isa, M.I.N. Imittance responses of PMMA-salicylic acid gel electrolytes and other related studies. Ph.D. Thesis, University of Malaya, 2005.
- Isa, M.I.N.; Samsudin, A., Ionic conduction behavior of CMC based green polymer electrolytes. *Advanced Materials Research* **2013**, *802*, 194-198.
- Jiang, Z.; Zheng, X.; Wu, H.; Pan, F., Proton conducting membranes prepared by incorporation of organophosphorus acids into alcohol barrier polymers for direct methanol fuel cells. *Journal of Power Sources* **2008**, *185* (1), 85-94.
- Jonscher, A. K., *Dielectric Relaxation in Solids*. Chelsea Dielectrics Press: London, UK, 1996.
- Jonscher, A. K., *Universal Relaxation Law*. Chelsea Dielectrics Press: London, UK, 1996.
- Kadir, M. F. Z.; Aspanut, Z.; Majid, S. R.; Arof, A. K., FTIR studies of plasticized poly(vinyl alcohol)-chitosan blend doped with NH_4NO_3 polymer electrolyte membrane. *Spectrochimica Acta Part A: Molecular and Biomolecular Spectroscopy* **2011**, *78* (3), 1068-1074.
- Kadir, M. F. Z.; Majid, S. R.; Arof, A. K., Plasticized chitosan-PVA blend polymer electrolyte based proton battery. *Electrochimica Acta* **2010**, *55* (4), 1475-1482.
- Kamarudin, K. H.; Isa, M. I. N., Structural and dc ionic conductivity studies of carboxy methylcellulose doped with ammonium nitrate as solid polymer electrolytes. *International Journal of Physical Sciences* **2013**, *8* (31), 1581-1587.
- Kamarudin, K. H.; Rani, M. S. A.; Isa, M. I. N., Ionic Conductivity and conduction mechanism of biodegradable dual polysaccharides blend electrolytes. *American-Eurasian Journal of Sustainable Agriculture* **2015**, *9* (2), 8-14.
- Kato, Y.; Hori, S.; Saito, T.; Suzuki, K.; Hirayama, M.; Mitsui, A.; Yonemura, M.; Iba, H.; Kanno, R., High-power all-solid-state batteries using sulfide superionic conductors. *Nature Energy* **2016**, 16030.
- Khair, A. S. A.; Arof, A. K., Conductivity studies of starch-based polymer electrolytes. *Ionics* **2010**, *16* (2), 123-129.
- Kumar, D. A.; Selvasekarapandian, S.; Baskaran, R.; Savitha, T.; Nithya, H., Thermal, vibrational and ac impedance studies on proton conducting polymer electrolytes based on poly(vinyl acetate). *Journal of Non-Crystalline Solids* **2012a**, *358*, 531-536.

- Kumar, K. K.; Ravi, M.; Pavani, Y.; Bhavani, S.; Sharma, A. K.; Rao, V. V. R. N., Electrical conduction mechanism in NaCl complexed PEO/PVP polymer blend electrolytes. *Journal of Non-Crystalline Solids* **2012b**, 358 (23), 3205-3211.
- Kumar, M.; Sekhon, S. S., Role of plasticizer's dielectric constant on conductivity modification of PEO–NH₄F polymer electrolytes. *European Polymer Journal* **2002**, 38 (7), 1297-1304.
- Kumar, M.; Tiwari, T.; Chauhan, J. K.; Srivastava, N., Understanding the ion dynamics and relaxation behavior from impedance spectroscopy of NaI doped Zwitterionic polymer system. *Materials Research Express* **2014**, 1 (4), 045003.
- Kumar, M.; Tiwari, T.; Srivastava, N., Electrical transport behaviour of bio-polymer electrolyte system: Potato starch + ammonium iodide. *Carbohydrate Polymers* **2012**, 88 (1), 54-60.
- Lakshmi, N.; Chandra, S., Rechargeable solid-state battery using a proton-conducting composite as electrolyte. *Journal of Power Sources* **2002**, 108, 256-260.
- Lang, A. J.; Vyazovkin, S., Phase and thermal stabilization of ammonium nitrate in the form of PVP–AN glass. *Materials Letters* **2008**, 62 (12–13), 1757-1760.
- Li, W.; Sun, B.; Wu, P., Study on hydrogen bonds of carboxymethyl cellulose sodium film with two-dimensional correlation infrared spectroscopy. *Carbohydrate Polymers* **2009**, 78, 454-461.
- Li, Z. R., *Organic Light-Emitting Materials*. CRC Press, Taylor & Francis Group, USA: **2015**.
- Lim, Y.-J.; An, Y.-H.; Jo, N.-J., Polystyrene-Al₂O₃ composite solid polymer electrolyte for lithium secondary battery. *Nanoscale Research Letters* **2012**, 7 (1), 19.
- Lin, X.; Chen, Z.; Zhang, C.; Luo, X.; Du, X.; Huang, Y., Synthesis, characterization and electrospinning of new thermoplastic carboxymethyl cellulose (TCMC). *Chemical Engineering Journal* **2013**, 215-216, 709-720.
- Ma, J.; Sahai, Y., Chitosan biopolymer for fuel cell applications. *Carbohydrate Polymers* **2013**, 92 (2), 955-975.
- Ma, X.; Chang, P. R.; Yu, J., Properties of biodegradable thermoplastic pea starch/carboxymethyl cellulose and pea starch/microcrystalline cellulose composites. *Carbohydrate Polymers* **2008**, 72 (3), 369-375.
- Maanan, M.; Saddik, M.; Maanan, M.; Chaibi, M.; Assobhei, O.; Zourarah, B., Environmental and ecological risk assessment of heavy metals in sediments of Nador lagoon, Morocco. *Ecological Indicators* **2015**, 48, 616-626.
- Maitz, M. F., Applications of synthetic polymers in clinical medicine. *Biosurface and Biotribology* **2015**, 1 (3), 161-176.
- Majid, S. R.; Arof, A. K., Electrical behavior of proton-conducting chitosan-phosphoric acid-based electrolytes. *Physica B* **2007**, 390, 209-215.
- Majid, S. R.; Arof, A. K., Proton-conducting polymer electrolyte films based on chitosan acetate complexed with NH₄NO₃ salt. *Physica B: Condensed Matter* **2005**, 355 (1–4), 78-82.
- Markoulidis, F.; Lei, C.; Lekakou, C.; Figgemeier, E.; Duff, D.; Khalil, S.; Martorana, B.; Cannavaro, I., High-performance supercapacitor cells with activated carbon/MWNT nanocomposite electrodes. *IOP Conference Series: Materials Science and Engineering* **2012**, 40 (1), 012021.

- Maurya, K. K.; Hashmi, S. A.; Chandra, S., *Solid State Ionics: Materials and Application*. World Scientific: Singapore, 1992.
- Mishra, K.; Rai, D., Studies of a plasticized PEO + NH₄PF₆ proton-conducting polymer electrolyte system and its application in a proton battery. *Journal of the Korean Physical Society* **2013**, *62* (2), 311-319.
- Mishra, R.; Rao, K. J., Electrical conductivity studies of poly(ethyleneoxide)-poly(vinylalcohol) blends. *Solid State Ionics* **1998**, *106* (1-2), 113-127.
- Mishra, S.; Usha Rani, G.; Sen, G., Microwave initiated synthesis and application of polyacrylic acid grafted carboxymethyl cellulose. *Carbohydrate Polymers* **2012**, *87* (3), 2255-2262.
- Mohamad, A. A.; Mohamed, N. S.; Yahya, M. Z. A.; Othman, R.; Ramesh, S.; Alias, Y.; Arof, A. K., Ionic conductivity studies of poly(vinyl alcohol) alkaline solid polymer electrolyte and its use in nickel-zinc cells. *Solid State Ionics* **2003**, *156* (1-2), 171-177.
- Mohamed, N. S.; Subban, R. H. Y.; Arof, A. K., Polymer batteries fabricated from lithium complexed acetylated chitosan. *Journal of Power Sources* **1995**, *56*, 153-156.
- Mohamed, S. A.; Al-Ghamdi, A. A.; Sharma, G. D.; El-Mansy, M. K., Effect of ethylene carbonate as a plasticizer on CuI/PVA nanocomposite: Structure, optical and electrical properties. *Journal of Advanced Research* **2014**, *5*, 79-86.
- Mohan, V. M.; Raja, V.; Sharma, A. K.; Rao, V. V. R. N., Ionic conductivity and discharge characteristics of solid-state battery based on novel polymer electrolyte (PEO + NaBiF₄). *Materials Chemistry and Physics* **2005**, *94* (2-3), 177-181.
- Murata, K.; Izuchi, S.; Yoshihisa, Y., An overview of the research and development of solid polymer electrolyte batteries. *Electrochimica Acta* **2000**, *45*, 1501-1508.
- Ng, L. S.; Mohamad, A. A., Effect of temperature on the performance of proton batteries based on chitosan-NH₄NO₃-EC membrane. *Journal of Membrane Science* **2008**, *325* (2), 653-657.
- Ng, L. S.; Mohamad, A. A., Protonic battery based on a plasticized chitosan-NH₄NO₃ solid polymer electrolyte. *Journal of Power Sources* **2006**, *163* (1), 382-385.
- Ng, W. F.; Chai, M. N.; Isa, M. I. N., Proton conducting carboxy methyl cellulose solid polymer electrolytes doped with citric acid. *Advanced Materials Research* **2014**, *895*, 130-133.
- Nguyen, T. H.; Fraiwan, A.; Choi, S., Paper-based batteries: A review. *Biosensors and Bioelectronics* **2014**, *54*, 640-649.
- Nik Aziz, N. A.; Idris, N. K.; Isa, M. I. N., Proton conducting polymer electrolytes of methylcellulose doped ammonium fluoride: Conductivity and ionic transport studies. *International Journal of Physical Sciences* **2010**, *5* (6), 748-752.
- Nik Aziz, N. A.; Isa, M. I. N., FTIR and electrical studies of methylcellulose doped NH₄F solid polymer electrolytes. *Solid State Science and Technology Letters* **2012**, *19* (1&2), 37-47.
- Nithya, S.; Selvasekarapandian, S.; Karhikeyan, S.; Vinoth Pandi, D.; Rajeswari, N.; Sanjeeviraja, C., Proton conducting polymer electrolyte based on PAN. *Indian Journal of Applied Research* **2013**, *3* (10), 1-6.
- Nithya, S.; Selvasekarapandian, S.; Karhikeyan, S.; Vinoth Pandi, D., Effect of propylene carbonate on the ionic conductivity of polyacrylonitrile-based solid polymer electrolytes. *Journal of Applied Polymer Science* **2015**, *132* (14), 41743.

- Noor, N. A. M.; Isa, M. I. N., Ionic conductivity and dielectric properties of CMC doped NH_4SCN solid biopolymer electrolytes *Advanced Materials Research* **2015**, *1107*, 230-235.
- Notten, P. H. L.; Roozeboom, F.; Niessen, R. A. H.; Baggetto, L., 3-D Integrated all-solid-state rechargeable batteries. *Advanced Materials* **2007**, *19* (24), 4564-4567.
- Nouh, S. A.; Ibrahim El-Tayeb, N.; Said, A. F.; Radwan, M. M.; El-Fiki, S. A., Structural and optical studies of electron beam-irradiated Makrofol nuclear track detector. *Radiation Measurements* **2007**, *42* (1), 8-13.
- Ogawa, M.; Yoshida, K.; Harada, K., All-solid-state lithium batteries with wide operating temperature range. *SEI Technical Review* **2012**, *74*, 88-90.
- Olsen, I. I.; Koksang, R.; Skou, E., Transference number measurements on a hybrid polymer electrolyte. *Electrochimica Acta* **1995**, *40* (11), 1701-1706.
- Ondo-Ndong, R.; Ferblantier, G.; Pascal-Delannoy, F.; Boyer, A.; Foucaran, A., Electrical properties of zinc oxide sputtered thin films. *Microelectronics Journal* **2003**, *34* (11), 1087-1092.
- Osman, Z.; Arof, A. K., FTIR studies of chitosan acetate based polymer electrolytes. *Electrochimica Acta* **2003**, *48* (8), 993-999.
- Osswald, T. A.; Menges, G., *Material science of polymers for engineers*. Carl Hanser Verlag: Munich, Germany, **2010**.
- Pai, S. J.; Bae, Y. C.; Sun, Y. K., Ionic conductivities of solid polymer electrolyte/salt systems for lithium secondary battery. *Polymer* **2005**, *46* (9), 3111-3118.
- Pandey, K.; Asthana, N.; Dwivedi, M. M.; Chaturvedi, S. K., Effect of plasticizers on structural and dielectric behaviour of $[\text{PEO} + (\text{NH}_4)_2\text{C}_4\text{H}_8(\text{COO})_2]$ Polymer Electrolyte. *Journal of Polymers* **2013**, *2013*, 12.
- Pandey, K.; Lakshmi, N.; Chandra, S., A rechargeable solid-state proton battery with an intercalating cathode and an anode containing a hydrogen-storage material. *Journal of Power Sources* **1998**, *76* (1), 116-123.
- Park, M.; Zhang, X.; Chung, M.; Less, G. B.; Sastry, A. M., A review of conduction phenomena in Li-ion batteries. *Journal of Power Sources* **2010**, *195* (24), 7904-7929.
- Pas, S. J.; Ingram, M. D.; Funke, K.; Hill, A. J., Free volume and conductivity in polymer electrolytes. *Electrochimica Acta* **2005**, *50* (19), 3955-3962.
- Pasparakis, G.; Manouras, T.; Argitis, P.; Vamvakaki, M., Photodegradable polymers for biotechnological applications. *Macromolecular Rapid Communications* **2012**, *33* (3), 183-198.
- Peng, H.; Ma, G.; Ying, W.; Wang, A.; Huang, H.; Lei, Z., In-situ synthesis of polyaniline/sodium carboxymethyl cellulose nanorods for high-performance redox supercapacitors. *Journal of Power Sources* **2012**, *211*, 40-45.
- Petrowsky, M.; Frech, R., Concentration dependence of ionic transport in dilute organic electrolyte solutions. *The Journal of Physical Chemistry B* **2008**, *112* (28), 8285-8290.
- Petrowsky, M.; Frech, R., Temperature Dependence of Ion Transport: The compensated Arrhenius equation. *The Journal of Physical Chemistry B* **2009**, *113* (17), 5996-6000.
- Pollak, M.; Geballe, T. H., Low-frequency conductivity due to hopping processes in silicon. *Physical Review* **1961**, *122* (6), 1742-1753.

- Pradhan, D. K.; Choudhary, R. N. P.; Samantaray, B. K., Studies of dielectric relaxation and ac conductivity behavior of plasticized polymer nanocomposite electrolytes. *International Journal Electrochemical Science* **2008**, *3*, 597-608.
- Pradhan, D. K.; Choudhary, R. N. P.; Samantaray, B. K.; Karan, N. K.; Katiyar, R. S., Effect of plasticizer on structural and electrical properties of polymer nanocomposite electrolytes. *International Journal Electrochemical Science* **2007**, *2*, 861-871.
- Pratap, R.; Singh, B.; Chandra, S., Polymeric rechargeable solid-state proton battery. *Journal of Power Sources* **2006**, *161* (1), 702-706.
- Priya James, H.; John, R.; Alex, A.; Anoop, K. R., Smart polymers for the controlled delivery of drugs – A concise overview. *Acta Pharmaceutica Sinica B* **2014**, *4* (2), 120-127.
- Psarras, G. C., Hopping conductivity in polymer matrix-metal particles composites. *Composites Part A: Applied Science and Manufacturing* **2006**, *37* (10), 1545-1553.
- Pushpamalar, V.; Langford, S. J.; Ahmad, M.; Lim, Y. Y., Optimization of reaction conditions for preparing carboxymethyl cellulose from sago waste. *Carbohydrate Polymers* **2006**, *64* (2), 312-318.
- Quartarone, E.; Mustarelli, P., Electrolytes for solid-state lithium rechargeable batteries: recent advances and perspectives. *Chemical Society Reviews* **2011**, *40* (5), 2525-2540.
- Ramesh, S.; Chai, M. F., Conductivity, dielectric behavior and FTIR studies of high molecular weight poly(vinylchloride)–lithium triflate polymer electrolytes. *Materials Science and Engineering: B* **2007**, *139* (2–3), 240-245.
- Ramesh, S.; Liew, C.-W.; Arof, A. K., Ion conducting corn starch biopolymer electrolytes doped with ionic liquid 1-butyl-3-methylimidazolium hexafluorophosphate. *Journal of Non-Crystalline Solids* **2011**, *357* (21), 3654-3660.
- Ramesh, S.; Wong, K. C., Conductivity, dielectric behaviour and thermal stability studies of lithium ion dissociation in poly(methylmethacrylate)-based gel polymer electrolytes. *Ionics* **2009**, *15* (2), 249-254.
- Ramlli, M. A.; Isa, M. I. N., Solid biopolymer electrolytes based carboxymethyl cellulose doped with ammonium fluoride: Ionic transport and conduction mechanism *Polymers from Renewable Resources* **2015a**, *6* (2), 55-63.
- Ramlli, M. A.; Kamarudin, K. H.; Isa, M. I. N., Ionic conductivity and structural analysis of carboxymethyl cellulose doped with ammonium fluoride as solid biopolymer electrolytes. *American-Eurasian Journal of Sustainable Agriculture* **2015b**, *9* (2), 46-51.
- Ramya, C. S.; Selvasekarapandian, S., Spectroscopic studies on ion dynamics of PVP–NH₄SCN polymer electrolytes. *Ionics* **2014**, *20* (12), 1681-1686.
- Ramya, C. S.; Selvasekarapandian, S.; Savitha, T.; Hirankumar, G.; Angelo, P. C., Vibrational and impedance spectroscopic study on PVP–NH₄SCN based polymer electrolytes. *Physica B: Condensed Matter* **2007**, *393* (1–2), 11-17.
- Rani, M. S. A.; Dzulkurnain, N. A.; Ahmad, A.; Mohamed, N. S., Conductivity and dielectric behavior studies of carboxymethyl cellulose from kenaf bast fiber incorporated with ammonium acetate-BMATFSI biopolymer electrolytes. *International Journal of Polymer Analysis and Characterization* **2015a**, *20* (3), 250-260.
- Rani, M. S. A.; Mohamed, N. S.; Isa, M. I. N., Investigation of the ionic conduction mechanism in carboxymethyl cellulose/chitosan biopolymer blend electrolyte

- impregnated with ammonium nitrate. *International Journal of Polymer Analysis and Characterization* **2015b**, *20*, 491–503.
- Rani, M.; Rudhziah, S.; Ahmad, A.; Mohamed, N., Biopolymer electrolyte based on derivatives of cellulose from kenaf bast fiber. *Polymers* **2014**, *6* (9), 2371-2385.
- Raphael, E.; Avellaneda, C. O.; Manzolli, B.; Pawlicka, A., Agar-based films for application as polymer electrolytes. *Electrochimica Acta* **2010**, *55* (4), 1455-1459.
- Ravi, M.; Bhavani, S.; Kumar, K. K.; Rao, V. V. R. N., Investigations on electrical properties of PVP:KIO₄ polymer electrolyte films. *Solid State Sciences* **2013**, *19*, 85-93.
- Ravve, A., *Principles of Polymer Chemistry*. Springer New York: USA, **2012**; p 695-790.
- Rice, M. J.; Roth, W. L., Ionic transport in super ionic conductors: A Theoretical model. *Journal of Solid State Chemistry* **1972**, *4*, 294-310.
- Rocco, A. M.; Fonseca, C. P.; Loureiro, F. A. M.; Pereira, R. P., A polymeric solid electrolyte based on a poly(ethylene oxide)/poly(bisphenol A-co-epichlorohydrin) blend with LiClO₄. *Solid State Ionics* **2004**, *166* (1–2), 115-126.
- Rosli, N. H. A.; Chan, C. H.; Subban, R. H. Y.; Winie, T., Studies on the structural and electrical properties of hexanoyl chitosan/polystyrene-based polymer electrolytes. *Physics Procedia* **2012**, *25* (0), 215-220.
- Rozali, M. L. H.; Ahmad, Z.; Isa, M. I. N., Interaction between carboxy methylcellulose and salicylic acid solid biopolymer electrolytes *Advanced Materials Research* **2015**, *1107*, 223-229.
- Rozali, M. L. H.; Isa, M. I. N., Electrical behaviour of carboxy methylcellulose doped adipic acid solid biopolymer electrolyte. *International Journal of Material Science* **2014**, *4* (2), 59-64.
- Rudhziah, S.; Rani, M. S. A.; Ahmad, A.; Mohamed, N. S.; Kaddami, H., Potential of blend of kappa-carrageenan and cellulose derivatives for green polymer electrolyte application. *Industrial Crops and Products* **2015**, *72*, 133-141.
- Samsudin, A. S. Development of carboxymethyl cellulose based proton conducting biopolymer electrolytes and its application in solid-state proton battery. Ph.D. Thesis, Universiti Malaysia Terengganu, 2014.
- Samsudin, A. S.; Tham, J.; Isa, M., Investigation of a biodegradable polymer electrolytes based on carboxy methylcellulose and its potential application in solid-state batteries. *Advanced Materials Research* **2013**, *802*, 99-103.
- Samsudin, A. S.; Isa, M. I. N., Conduction mechanism of enhanced CMC–NH₄Br biopolymer electrolytes *Advanced Materials Research* **2015**, *1108*, 27-32.
- Samsudin, A. S.; Isa, M. I. N., Structural and electrical properties of carboxy methylcellulose- dodecyltrimethyl ammonium bromide-based biopolymer electrolytes system. *International Journal of Polymeric Materials* **2012a**, *61* (1), 30-40.
- Samsudin, A. S.; Isa, M. I. N., Structural and ionic transport study on CMC doped NH₄Br: A new types of Biopolymer Electrolytes. *Journal of Applied Sciences* **2012b**, *12* (2), 174-179.
- Samsudin, A. S.; Isa, M. I. N., Study of the ionic conduction mechanism based on carboxymethyl cellulose biopolymer electrolytes. *Journal of the Korean Physical Society* **2014a**, *65* (9), 1441-1447.

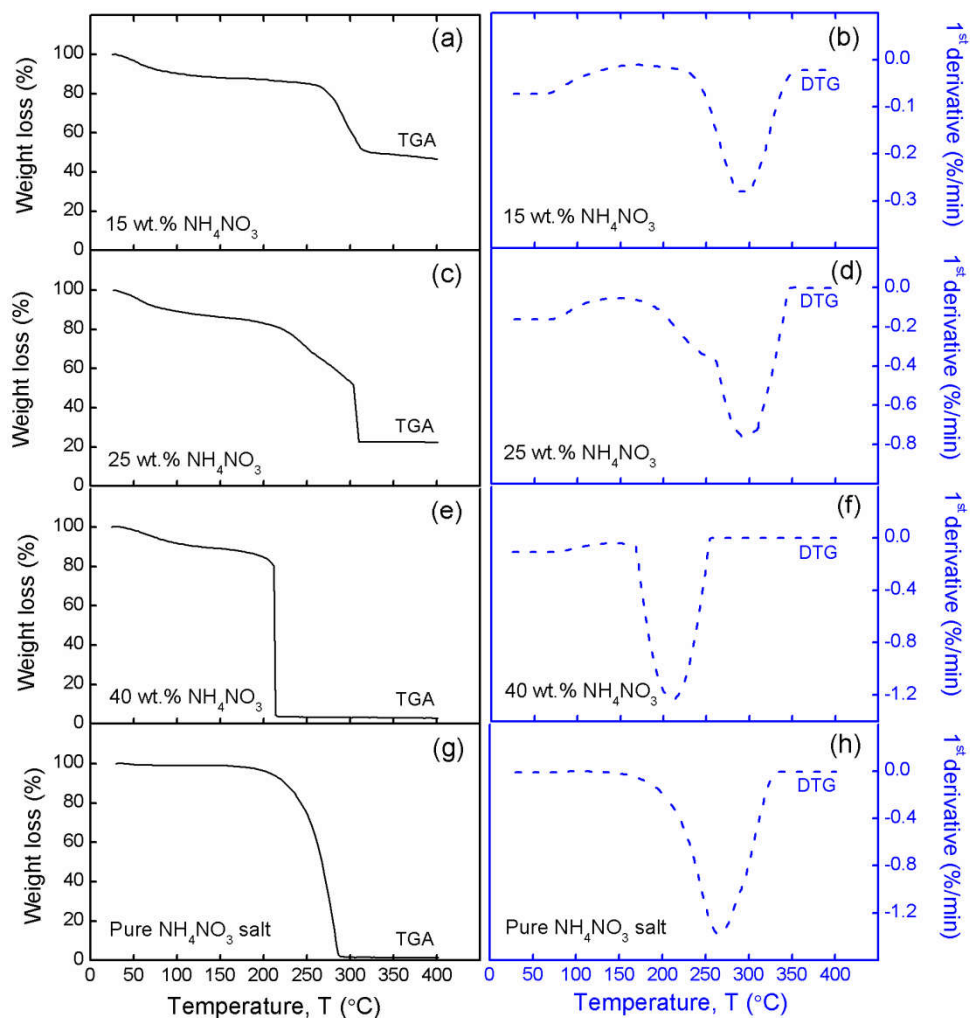
- Samsudin, A. S.; Isa, M. I. N.; Conductivity and transport properties study of plasticized carboxymethyl cellulose (CMC) based solid biopolymer electrolytes (SBE). *Advanced Materials Research* **2014b**, 856, 118-122.
- Samsudin, A. S.; Khairul, W. M.; Isa, M. I. N., Characterization on the potential of carboxy methylcellulose for application as proton conducting biopolymer electrolytes. *Journal of Non-Crystalline Solids* **2012c**, 358 (8), 1104-1112.
- Samsudin, A. S.; Lai, H. M.; Isa, M. I. N., Biopolymer materials based carboxymethyl cellulose as a proton conducting biopolymer electrolyte for application in rechargeable proton battery. *Electrochimica Acta* **2014c**, 129 (0), 1-13.
- Schwartz, M., *Smart Materials*. CRC Press: US, **2009**.
- Selvasekarapandian, S.; Baskaran, R.; Hema, M., Complex AC impedance, transference number and vibrational spectroscopy studies of proton conducting PVAc–NH₄SCN polymer electrolytes. *Physica B* **2005**, 357 (412-419).
- Selvasekarapandian, S.; Hema, M.; Kawamura, J.; Kamishima, O.; Baskaran, R., Characterization of PVA-NH₄NO₃ polymer electrolyte and its application in rechargeable proton battery. *Journal of the Physical Society of Japan* **2010**, 79SA, 163-168.
- Sequeira, C. A. C.; Santos, D. M. F., *Polymer Electrolytes: Fundamentals and Applications*. Woodhead Publishing: Cambridge, UK, **2010**.
- Shit, S. C.; Shah, P. M., Edible Polymers: Challenges and Opportunities. *Journal of Polymers* **2014**, 2014, 13.
- Shuhaimi, N. E. A.; Alias, N. A.; Kufian, M. Z.; Majid, S. R.; Arof, A. K., Characteristics of methyl cellulose-NH₄NO₃-PEG electrolyte and application in fuel cells. *Journal of Solid State Electrochemistry* **2010a**, 14 (12), 2153-2159.
- Shuhaimi, N. E. A.; Teo, L. P.; Majid, S. R.; Arof, A. K., Transport studies of NH₄NO₃ doped methyl cellulose electrolyte. *Synthetic Metals* **2010b**, 160 (9-10), 1040-1044.
- Shukur, M. F.; Ibrahim, F. M.; Majid, N. A.; Ithnin, R.; Kadir, M. F. Z., Electrical analysis of amorphous corn starch-based polymer electrolyte membranes doped with LiI. *Physica Scripta* **2013a**, 88 (025601), 1-9.
- Shukur, M. F.; Ithnin, R.; Illias, H. A.; Kadir, M. F. Z., Proton conducting polymer electrolyte based on plasticized chitosan–PEO blend and application in electrochemical devices. *Optical Materials* **2013b**, 35 (10), 1834-1841.
- Shukur, M. F.; Ithnin, R.; Kadir, M. F. Z., Electrical properties of proton conducting solid biopolymer electrolytes based on starch–chitosan blend. *Ionics* **2014**, 20 (7), 977-999.
- Shukur, M. F.; Ithnin, R.; Sonsudin, F.; Yahya, R.; Ahmad, Z.; Kadir, M. F. Z., Conduction mechanism and dielectric properties of solid biopolymer electrolyte incorporated with silver nitrate. *Advanced Materials Research* **2013c**, 701, 115-120.
- Shukur, M. F.; Kadir, M. F. Z., Electrical and transport properties of NH₄Br-doped cornstarch-based solid biopolymer electrolyte. *Ionics* **2015a**, 21 (1), 111-124.
- Shukur, M. F.; Kadir, M. F. Z., Hydrogen ion conducting starch-chitosan blend based electrolyte for application in electrochemical devices. *Electrochimica Acta* **2015b**, 158, 152-165.
- Shukur, M. F.; Majid, N. A.; Ithnin, R.; Kadir, M. F. Z., Effect of plasticization on the conductivity and dielectric properties of starch–chitosan blend biopolymer electrolytes infused with NH₄Br. *Physica Scripta* **2013d**, 2013 (T157), 014051.

- Sikkanthar, S.; Karthikeyan, S.; Selvasekarapandian, S.; Pandi, D. V.; Nithya, S.; Sanjeeviraja, C., Electrical conductivity characterization of polyacrylonitrile-ammonium bromide polymer electrolyte system. *J Solid State Electrochem* **2015**, *19* (4), 987-999.
- Sim, L. N.; Majid, S. R.; Arof, A. K., Characteristics of PEMA/PVdF-HFP blend polymeric gel films incorporated with lithium triflate salt in electrochromic device. *Solid State Ionics* **2012**, *209–210*, 15-23.
- Sohaimy, M. I. H.; Isa, M. I. N., Effect of ammonium carbonate salt concentration on structural and ionic conductivity of cellulose based solid polymer electrolytes. *Fibers and Polymers* **2015**, *16* (5), 1031-1034.
- Song, Q.; Li, J., A review on human health consequences of metals exposure to e-waste in China. *Environmental Pollution* **2015**, *196*, 450-461.
- Sownthari, K.; Suthanthiraraj, S. A., Synthesis and characterization of an electrolyte system based on a biodegradable polymer. *eXPRESS Polymer Letters* **2013**, *7* (6), 495–504.
- Srivastava, N.; Chandra, S., Studies on a new proton conducting polymer system: poly(ethylene succinate) + NH₄ClO₄. *European Polymer Journal* **2000**, *36* (2), 421-433.
- Su, J.-F.; Huang, Z.; Yuan, X.-Y.; Wang, X.-Y.; Li, M., Structure and properties of carboxymethyl cellulose/soy protein isolate blend edible films crosslinked by Maillard reactions. *Carbohydrate Polymers* **2010**, *79* (1), 145-153.
- Subba Reddy, C. V.; Sharma, A. K.; Narasimha Rao, V. V. R., Conductivity and discharge characteristics of polyblend (PVP + PVA + KIO₃) electrolyte. *Journal of Power Sources* **2003**, *114* (2), 338-345.
- Subban, R. H. Y.; Ahmad, A. H.; Kamarulzaman, N.; Ali, A. M. M., Effects of plasticiser on the lithium ionic conductivity of polymer electrolyte PVC-LiCF₃SO₃. *Ionics* **2005**, *11* (5-6), 442-445.
- Sugama, T.; Pyatina, T., Effect of sodium carboxymethyl celluloses on water-catalyzed self-degradation of 200°C-heated alkali-activated cement. *Cement and Concrete Composites* **2015**, *55*, 281-289.
- Tamilselvi, P.; Hema, M., Conductivity studies of LiCF₃SO₃ doped PVA:PVdF blend polymer electrolyte. *Physica B: Condensed Matter* **2014**, *437*, 53-57.
- Ulaganathan, M.; Mathew, C. M.; Rajendran, S., Highly porous lithium-ion conducting solvent-free poly(vinylidene fluoride-co-hexafluoropropylene)/poly(ethyl methacrylate) based polymer blend electrolytes for Li battery applications. *Electrochimica Acta* **2013**, *93*, 230-235.
- Ulaganathan, M.; Nithya, R.; Rajendran, S., Surface analysis studies on polymer electrolyte membranes using scanning electron microscope and atomic force microscope In *Scanning Electron Microscopy*, Kazmiruk, V., Ed. InTech: Croatia, **2012**; p 830.
- Vaghari, H.; Jafarizadeh-Malmiri, H.; Berenjian, A.; Anarjan, N., Recent advances in application of chitosan in fuel cells. *Sustainable Chemical Processes* **2013**, *1* (16), 1-12.
- Varshney, P.; Gupta, S., Natural polymer-based electrolytes for electrochemical devices: a review. *Ionics* **2011**, *17* (6), 479-483.
- Varshney, V. K.; Naithani, S., Chemical functionalization of cellulose derived from nonconventional sources cellulose fibers: Bio- and nano-polymer composites. Kalia, S.; Kaith, B. S.; Kaur, I., Eds. Springer Berlin Heidelberg: **2011**; pp 43-60.

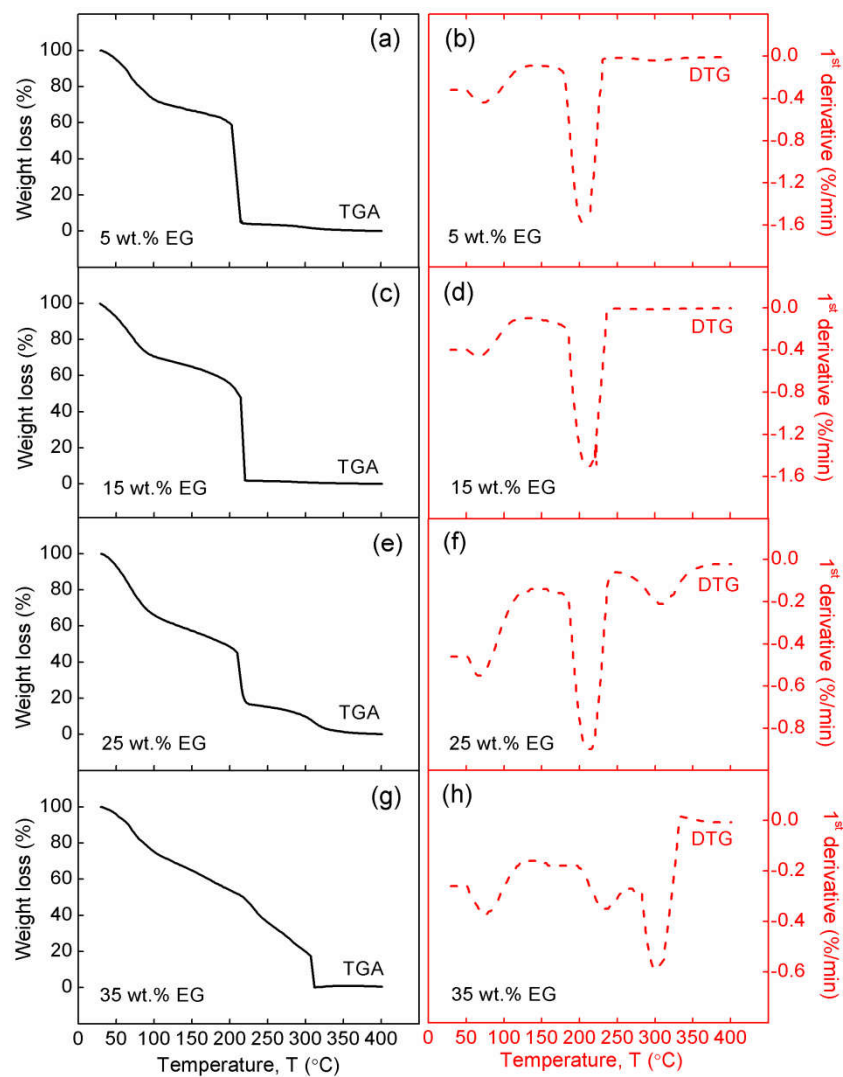
- Vieira, M. G. A.; da Silva, M. A.; dos Santos, L. O.; Beppu, M. M., Natural-based plasticizers and biopolymer films: A review. *European Polymer Journal* **2011**, *47* (3), 254-263.
- Vijaya, N.; Selvasekarapandian, S.; Hirankumar, G.; Karthikeyan, S.; Nithya, H.; Ramya, C. S.; Prabu, M., Structural, vibrational, thermal, and conductivity studies on proton-conducting polymer electrolyte based on poly (N-vinylpyrrolidone). *Ionics* **2012**, *18* (1-2), 91-99.
- Vroman, I.; Tighzert, L., Biodegradable Polymers. *Materials* **2009**, *2* (2), 307.
- Wang, W. B.; Xu, J. X.; Wang, A. Q., A pH-, salt- and solvent-responsive carboxymethylcellulose -g-poly(sodium acrylate)/medical stone superabsorbent composite with enhanced swelling and responsive properties. *eXPRESS Polymer Letters* **2011**, *5* (5), 385-400.
- Winie, T.; Shahril, N. S. M.; Chan, C. H.; Arof, A. K., Selective localization of lithium trifluoromethanesulfonate in the blend of hexanoyl chitosan and polystyrene. *High Performance Polymers* **2014**, *26* (6), 666-671.
- Woo, H. J.; Majid, S. R.; Arof, A. K., Conduction and thermal properties of a proton conducting polymer electrolyte based on poly (ϵ -caprolactone). *Solid State Ionics* **2011**, *199–200* (0), 14-20.
- Woo, H. J.; Majid, S. R.; Arof, A. K., Dielectric properties and morphology of polymer electrolyte based on poly(ϵ -caprolactone) and ammonium thiocyanate. *Materials Chemistry and Physics* **2012**, *134* (2–3), 755-761.
- Woo, H. J.; Majid, S. R.; Arof, A. K., Effect of ethylene carbonate on proton conducting polymer electrolyte based on poly(ϵ -caprolactone) (PCL). *Solid State Ionics* **2013**, *252* (0), 102-108.
- Wright, P., Electrical conductivity in ionic complexes of poly (ethylene oxide). *British Polymer Journal* **1975**, *7*, 319 - 327.
- Wu, H. B.; Chan, M. N.; Chan, C. K., FTIR characterization of polymorphic transformation of ammonium nitrate. *Aerosol Science and Technology* **2007**, *41* (6), 581-588.
- Wu, I. D.; Chang, F.-C., Determination of the interaction within polyester-based solid polymer electrolyte using FTIR spectroscopy. *Polymer* **2007**, *48* (4), 989-996.
- Wu, Q.; Leung, J. Y. S.; Geng, X.; Chen, S.; Huang, X.; Li, H.; Huang, Z.; Zhu, L.; Chen, J.; Lu, Y., Heavy metal contamination of soil and water in the vicinity of an abandoned e-waste recycling site: Implications for dissemination of heavy metals. *Science of The Total Environment* **2015**, *506–507*, 217-225.
- Xu, B.; Wu, F.; Chen, S.; Zhou, Z.; Cao, G.; Yang, Y., High-capacitance carbon electrode prepared by PVDC carbonization for aqueous EDLCs. *Electrochimica Acta* **2009**, *54* (8), 2185-2189.
- Yadollahi, M.; Namazi, H., Synthesis and characterization of carboxymethyl cellulose/layered double hydroxide nanocomposites. *Journal of Nanoparticles Research* **2013**, *15* (4), 1-9.
- Yahya, M. Z. A.; Arof, A. K., Effect of oleic acid plasticizer on chitosan–lithium acetate solid polymer electrolytes. *European Polymer Journal* **2003**, *39* (5), 897-902.
- Young, R. J.; Lovell, P. A., *Introduction to polymers*. CRC Press, Taylor and Franchis Group: Florida, USA, **2011**.
- Yu, J. C.; Jang, J. I.; Lee, B. R.; Lee, G.-W.; Han, J. T.; Song, M. H., Highly efficient polymer-based optoelectronic devices using PEDOT:PSS and a GO composite layer

- as a hole transport layer. *ACS Applied Materials & Interfaces* **2014**, 6 (3), 2067-2073.
- Yusof, Y. M.; Majid, N. A.; Kasmani, R. M.; Illias, H. A.; Kadir, M. F. Z., The effect of plasticization on conductivity and other properties of starch/chitosan blend biopolymer electrolyte incorporated with ammonium iodide. *Molecular Crystals and Liquid Crystals* **2014a**, 603 (1), 73-88.
- Yusof, Y. M.; Shukur, M. F.; Illias, H. A.; Kadir, M. F. Z., Conductivity and electrical properties of corn starch–chitosan blend biopolymer electrolyte incorporated with ammonium iodide. *Physica Scripta* **2014b**, 89 (3), 035701.
- Zainol, N. H.; Osman, Z.; Othman, L.; Isa, K. B. M., Transport and morphological properties of gel polymer electrolytes containing $\text{Mg}(\text{CF}_3\text{SO}_3)_2$. *Advanced Materials Research* **2013**, 686, 137-144.
- Zhao, S.; Wang, C.-Y.; Chen, M.-M.; Sun, J.-H., Mechanism for the preparation of carbon spheres from potato starch treated by NH_4Cl . *Carbon* **2008**, 47 (1), 331-333.
- Zugenmaier, P., *Crystalline Cellulose and Derivatives: Characterization and Structures*. Springer Berlin Heidelberg: Germany, **2008**; p 285.

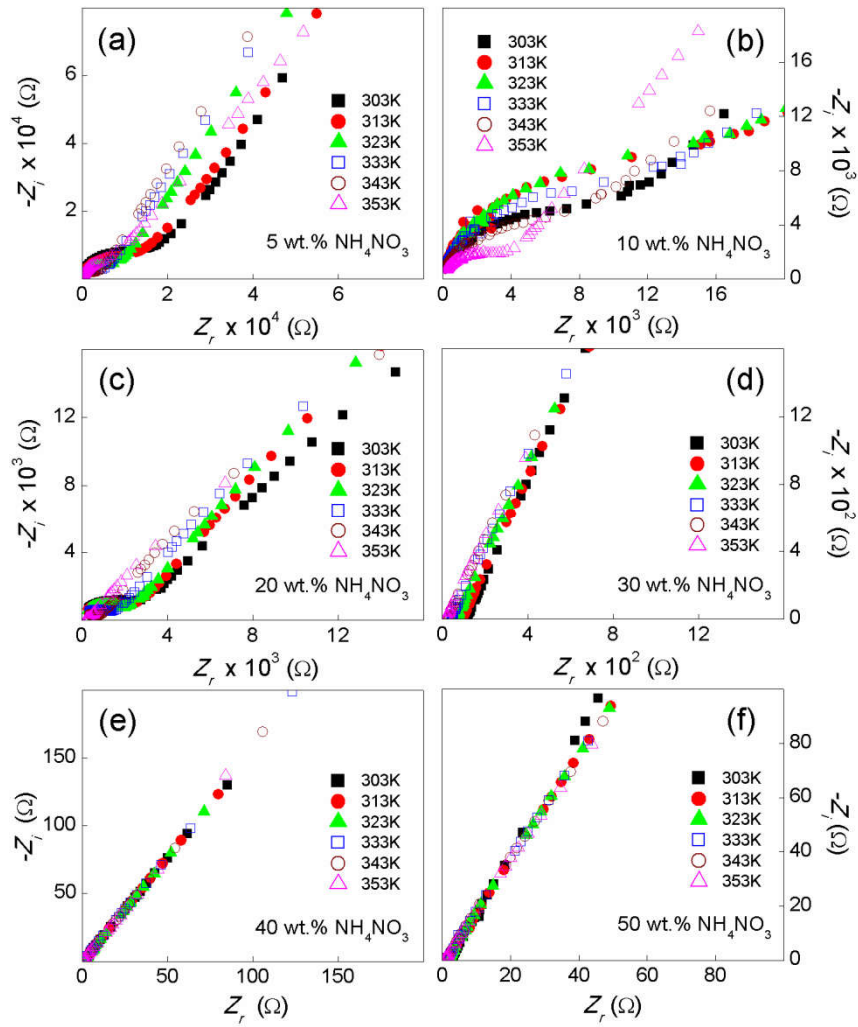
APPENDICES



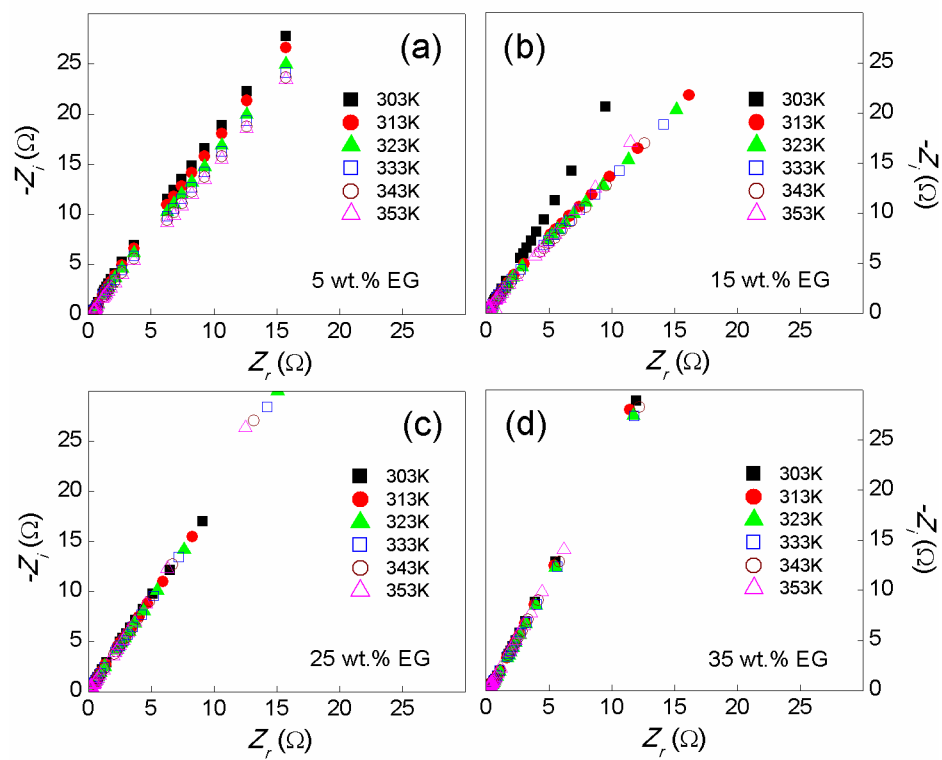
Appendix 1 TGA and DTG curves for System I films with (a-b) 15 wt.% NH₄NO₃, (c-d) 25 wt.% NH₄NO₃, (e-f) 40 wt.% NH₄NO₃, and (g-h) pure NH₄NO₃ salt, obtained at room temperature to 400°C.



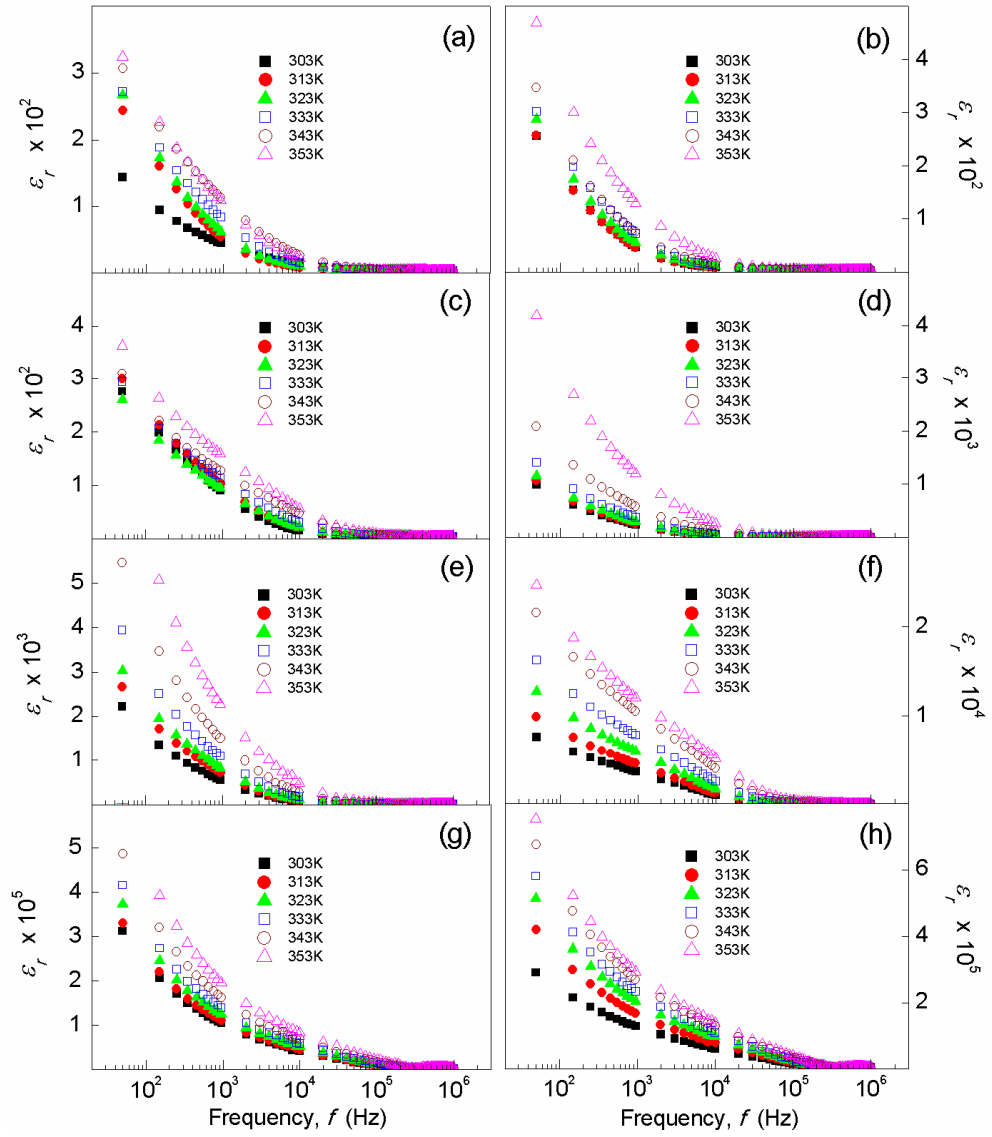
Appendix 2 TGA and DTG curves for System II films with (a-b) 5 wt.% EG, (c-d) 15 wt.% EG, (e-f) 25 wt.% EG, and (g-h) 35 wt.% EG, obtained at room temperature to 400°C.



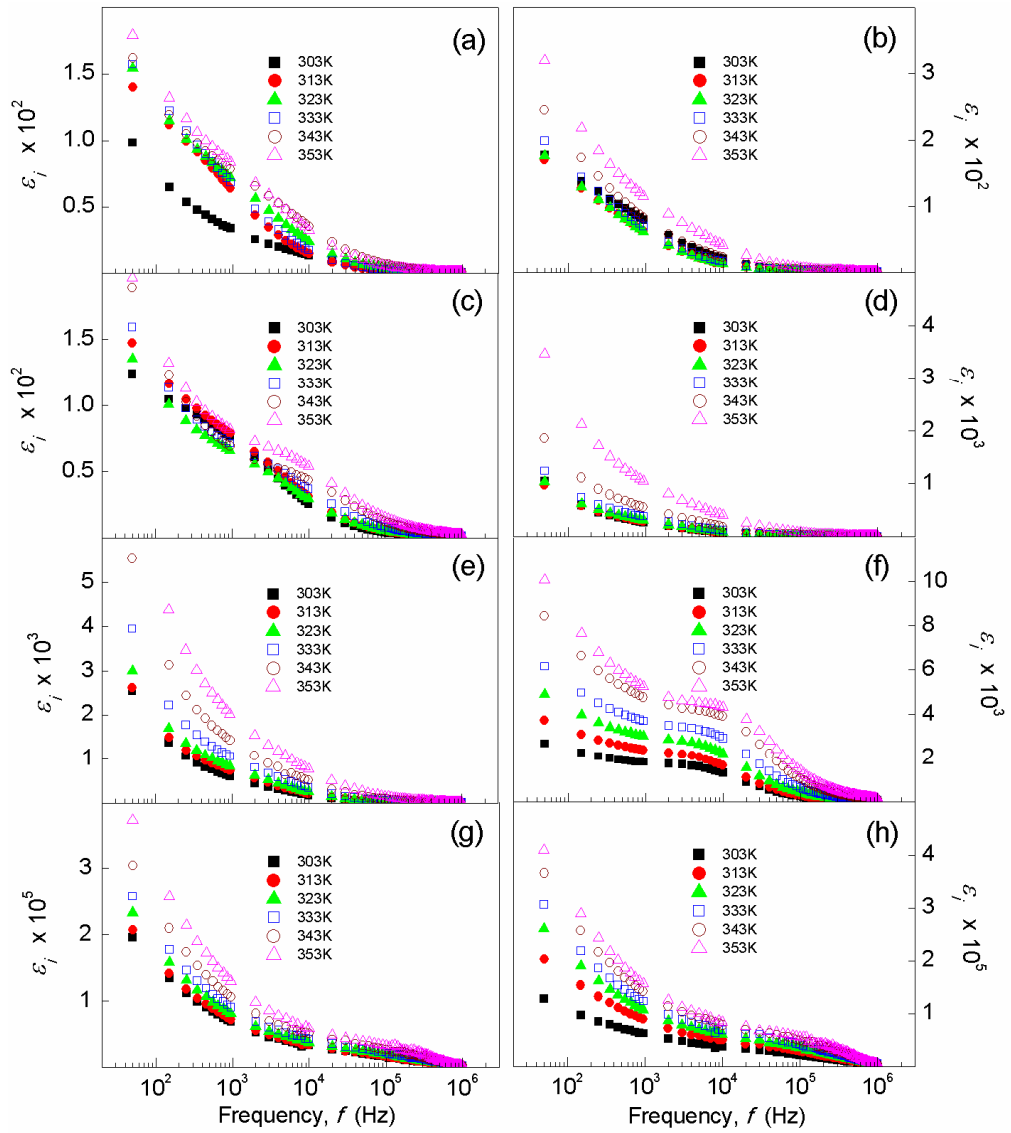
Appendix 3 Nyquist plots of temperature dependence for System I films at 303K - 353K. (a) 5 wt.% NH_4NO_3 , (b) 10 wt.% NH_4NO_3 , (c) 20 wt.% NH_4NO_3 , (d) 30 wt.% NH_4NO_3 , (e) 40 wt.% NH_4NO_3 , and (f) 50 wt.% NH_4NO_3 .



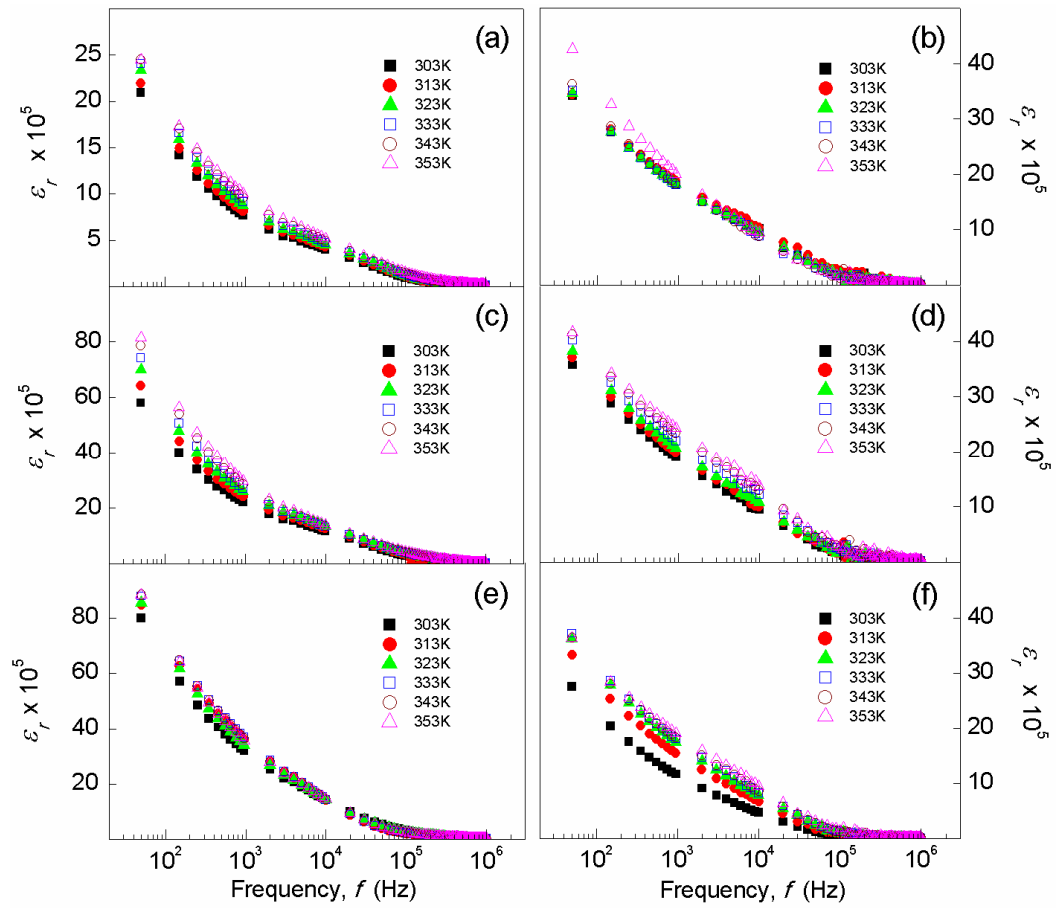
Appendix 4 Nyquist plots of temperature dependence for System II films at 303K - 353K. (a) 5 wt.% EG, (b) 15 wt.% EG, (c) 25 wt.% EG, and (d) 35 wt.% EG.



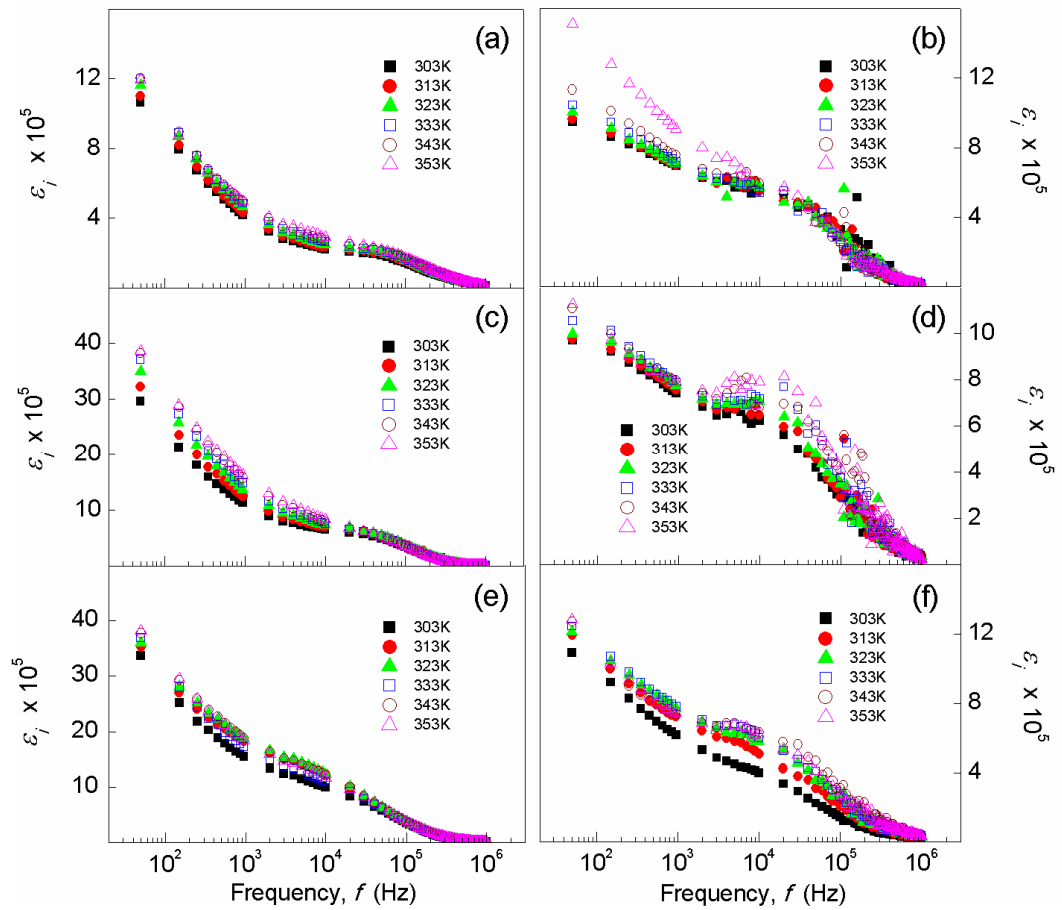
Appendix 5 Dielectric constant, ϵ_r of System I films at different temperatures. (a) 5 wt.% NH_4NO_3 , (b) 10 wt.% NH_4NO_3 , (c) 15 wt.% NH_4NO_3 , (d) 20 wt.% NH_4NO_3 , (e) 25 wt.% NH_4NO_3 , (f) 30 wt.% NH_4NO_3 , (g) 40 wt.% NH_4NO_3 , and (h) 50 wt.% NH_4NO_3 .



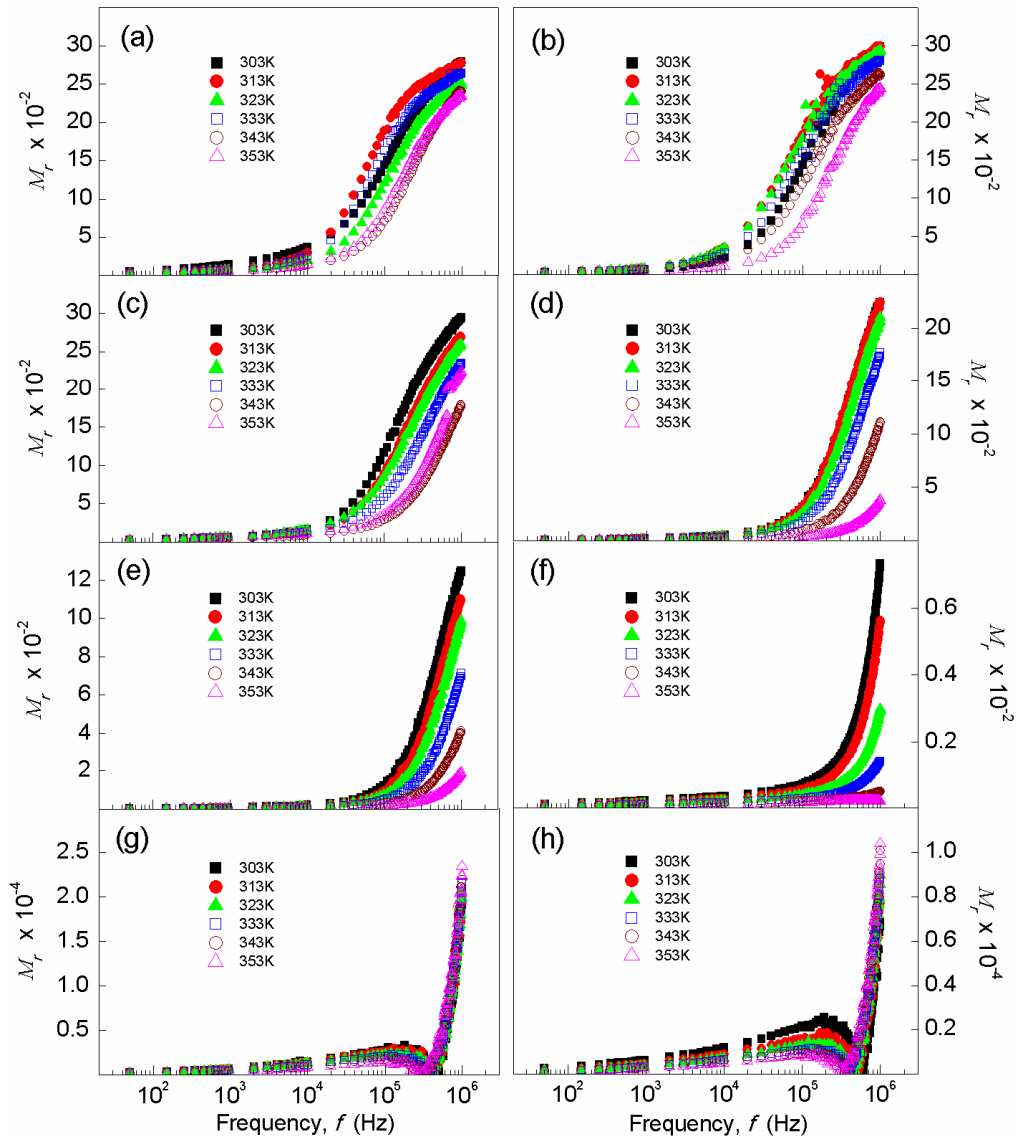
Appendix 6 Dielectric loss, ϵ_i of System I films at different temperatures. (a) 5 wt.% NH_4NO_3 , (b) 10 wt.% NH_4NO_3 , (c) 15 wt.% NH_4NO_3 , (d) 20 wt.% NH_4NO_3 , (e) 25 wt.% NH_4NO_3 , (f) 30 wt.% NH_4NO_3 , (g) 40 wt.% NH_4NO_3 , and (h) 50 wt.% NH_4NO_3 .



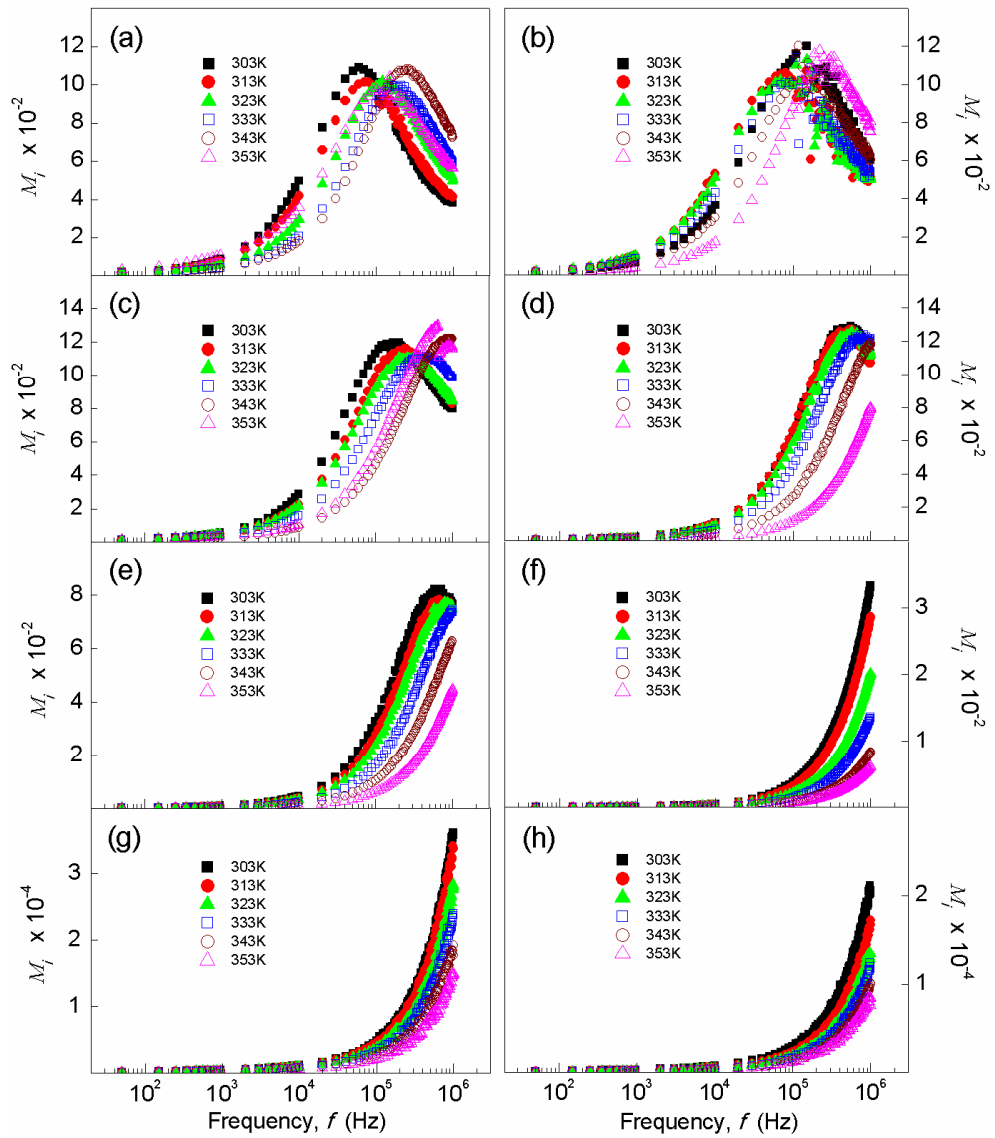
Appendix 7 Dielectric constant, ϵ_r , of System II films at different temperatures. (a) 5 wt.% EG, (b) 10 wt.% EG, (c) 25 wt.% EG, (d) 30 wt.% EG, (e) 35 wt.% EG, and (f) 40 wt.% EG.



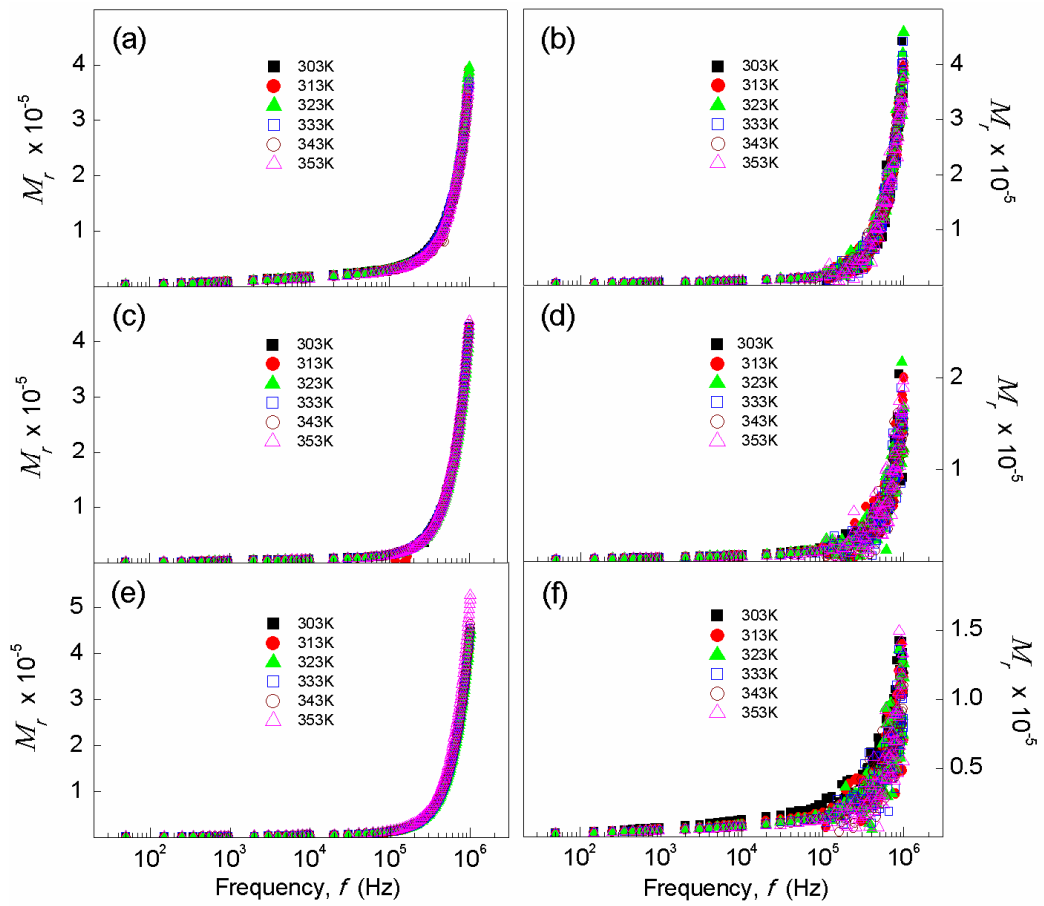
Appendix 8 Dielectric loss, ϵ_i of System II films at different temperatures. (a) 5 wt.% EG, (b) 10 wt.% EG, (c) 25 wt.% EG, (d) 30 wt.% EG, (e) 35 wt.% EG, and (f) 40 wt.% EG.



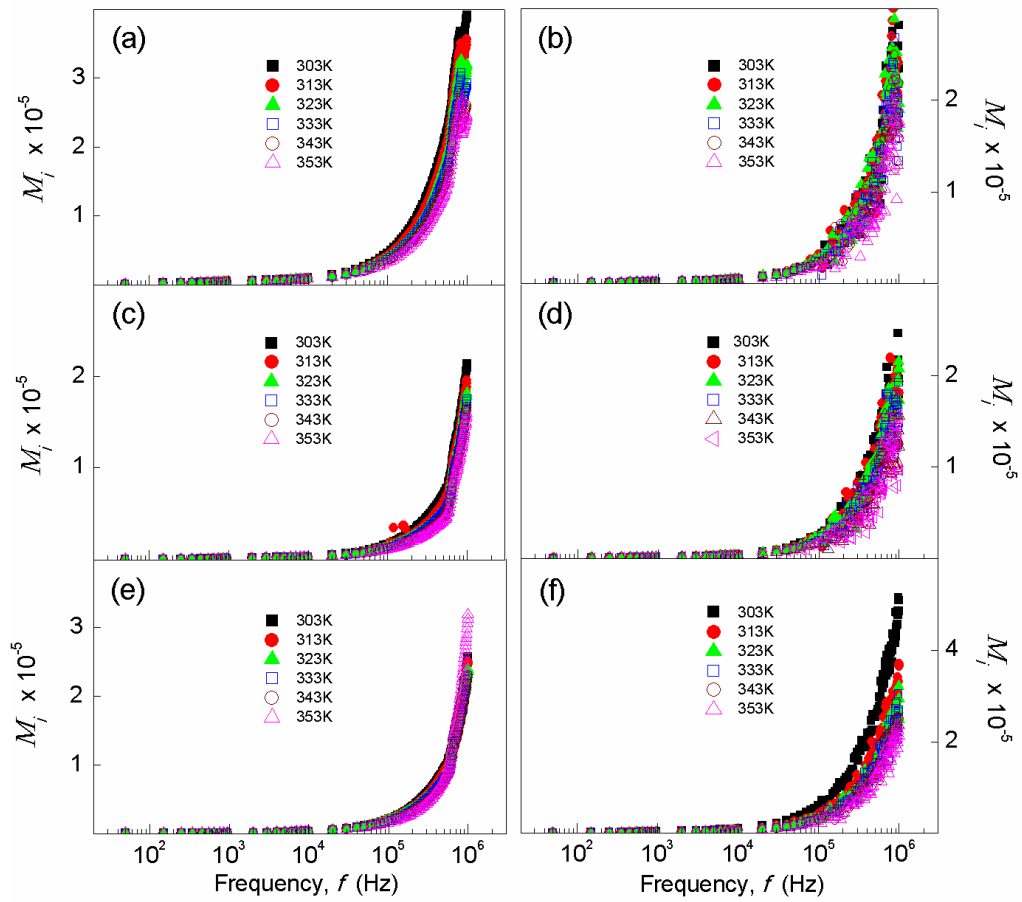
Appendix 9 Real part of electrical modulus, M_r of System I films at different temperatures.
 (a) 5 wt.% NH_4NO_3 , (b) 10 wt.% NH_4NO_3 , (c) 15 wt.% NH_4NO_3 , (d) 20 wt.% NH_4NO_3 ,
 (e) 25 wt.% NH_4NO_3 , (f) 30 wt.% NH_4NO_3 , (g) 40 wt.% NH_4NO_3 , and (h) 50 wt.% NH_4NO_3 .



Appendix 10 Imaginary part of electrical modulus, M_i of System I films at different temperatures. (a) 5 wt.% NH_4NO_3 , (b) 10 wt.% NH_4NO_3 , (c) 15 wt.% NH_4NO_3 , (d) 20 wt.% NH_4NO_3 , (e) 25 wt.% NH_4NO_3 , (f) 30 wt.% NH_4NO_3 , (g) 40 wt.% NH_4NO_3 , and (h) 50 wt.% NH_4NO_3 .



Appendix 11 Real part of electrical modulus, M_r of System II films at different temperatures. (a) 5 wt.% EG, (b) 10 wt.% EG, (c) 25 wt.% EG, (d) 30 wt.% EG, (e) 35 wt.% EG, and (f) 40 wt.% EG.



Appendix 12 Imaginary part of electrical modulus, M_i of System II films at different temperatures. (a) 5 wt.% EG, (b) 10 wt.% EG, (c) 25 wt.% EG, (d) 30 wt.% EG, (e) 35 wt.% EG, and (f) 40 wt.% EG.

BIODATA OF THE AUTHOR



Khadijah Hilmun Kamarudin was born and brought up in Terengganu. She received her early education at Sekolah Rendah Kebangsaan Bukit Perah and later Sekolah Menengah Agama Tok Jiring in Terengganu. She continued her foundation study at Kolej Matrikulasi Melaka under Kementerian Pendidikan

Malaysia in 2000. Due to her great interest in science and astronomy, she further her study in Physics at Universiti Kebangsaan Malaysia (UKM), where she graduated with a Bachelor of Science (Honours) in Physics in 2004. She obtained her Master of Science in Medical Physics from Universiti Sains Malaysia (USM) in 2006. She pursued her Ph.D. in Physics at Universiti Malaysia Terengganu (UMT) on September 2012. Currently, she serves as a tutor at the School of Fundamental Science, Universiti Malaysia Terengganu.